The Radical Ion Chemistry of Electron Capture Dissociation Mass Spectrometry of Modified Peptides

by

ANDREW JONES

A Thesis submitted to

The University of Birmingham

for the degree of

DOCTOR OF PHILOSOPHY

School of Bioscience

University of Birmingham

July 2012

Abstract

The introduction of electron capture dissociation mass spectrometry in 1998 has provided a unique technique for the analysis of peptides and proteins, especially for the identification and localisation of posttranslational modifications. Despite many successes debate continues on the radical-based mechanism of ECD. This thesis explores ECD behaviour in a wide range of PTMs with the intention of furthering our knowledge of the radical-based mechanism.

Studies were undertaken on the effect of 3-nitrotyrosine, which is an electron withdrawing group, on ECD. The presence of nitration dramatically decreases peptide backbone sequence coverage but results in the presence of abundant small neutral losses. The key finding is the insight provided into the hierarchy of the various proposed ECD mechanisms.

ECD of cysteine bound modifications is shown to result in the fragmentation of the sulfur-modification bond and backbone sequence coverage is highly diminished when analysing *S*-nitrosopeptides. ECD behaviour of hydrogen-deficient radical peptides is highly dependent on gas-phase peptide structure, with electron capture typically resulting in an increase in charge-reduced precursor intensity.

Comparisons of the intermolecular phospho-guanidinium bond strengths between phospho-serine, -threonine and -tyrosine were undertaken. ECD of these complexes results in the retention of the noncovalent bond allowing backbone sequence coverage.

Acknowledgements

I would like to acknowledge and express my gratitude to the following people for their help and support throughout my PhD.

Firstly, I would like to thank my supervisor, Helen Cooper, whose continued supervision and guidance allowed me to complete this work. Helen's continued encouragement also allowed me to have three publications as well as presenting my work at numerous international conferences, I am extremely grateful.

Peter Winn for introducing me into the field of molecular dynamics and provided assistance for the generation and analysis of the peptide structures used in this work. Logan Mackay for allowing use of the FT-ICR at the University of Edinburgh to complete MS^3 experiments I would otherwise have been unable to complete. All the members of Helen Cooper's research group, past and present, especially Andrew Creese, Steve Sweet and Cleidiane Zampronio for providing day-to-day advice on instrumentation and problem solving. I would like to thank all members of the fifth floor who have led to an extremely enjoyable period of my life, usually due to tea and cake consumption.

Finally, I would like to thank my parents who never let me give up and always believed in me, and Sylwia whose calming influence has aided the writing of this thesis immeasurably.

I would also like to thank EPSRC for funding this work.

Table of Contents

Chapter 1: Introduction

Chapter 3: Electron Capture Dissociation Mass Spectrometry of Nitrated Peptides

Chapter 4: Origin of Ammonia Loss Formed Following ECD of Nitrated Peptides

Chapter 5: Electron Capture Dissociation Mass Spectrometry of Alkylated Peptides

Chapter 6: Electron Capture Dissociation Mass Spectrometry of Nitrosylated and Radical Cysteine

Chapter 7: Electron Capture Dissociation Mass Spectrometry of Noncovalent Phospho-Guanidinium Complexes

Appendix

List of Figures

List of Equations and Tables

List of Abbreviations

AI ECD	Activation ion electron capture dissociation
CID	Collision induced dissociation
ECD	Electron capture dissociation
ESI	Electrospray ionisation
ETD	Electron transfer dissociation
FT-ICR	Fourier transform ion cyclotron resonance
HPLC	High performance liquid chromatography
IRMPD	Infrared multiphoton dissociation
IT	Ion trap
LIT	Linear ion trap
MD	Molecular dynamics
MS	Mass spectrometry
MS/MS	Tandem mass spectrometry
PTM	Posttranslational modification
saETD	Supplemental activation electron transfer dissociation

Amino Acid Abbreviations

A	Ala	Alanine
C	Cys	Cysteine
D	Asp	Aspartic Acid
E	Glu	Glutamic Acid
F	Phe	Phenylalanine
G	Gly	Glycine
H	His	Histidine
I	Ile	Isoleucine
K	Lys	Lysine
L	Leu	Leucine
M	Met	Methionine
N	Asn	Asparagine
P	Pro	Proline
Q	Gln	Glutamine
R	Arg	Arginine
S	Ser	Serine
T	Thr	Threonine
V	Val	Valine
W	Trp	Tryptophan
Y	Tyr	Tyrosine

Chapter 1: Introduction

Overview

Since its first documentation in 1998 [1], electron capture dissociation (ECD) mass spectrometry has been shown to be extremely successful for the analysis of peptides, and along with the related electron transfer dissociation [2] has developed into a valuable tool in proteomic analysis. The success of ECD is perhaps most evident for the identification and localisation of labile posttranslational modifications, which are retained on the peptide backbone fragment ions [3]. In comparison, collisional induced dissociation (CID) [4, 5], the most commonly utilised tandem mass spectrometry technique, results in the favourable loss of labile posttranslational modifications whilst retaining the intact peptide backbone, thus preventing posttranslational modification localisation and limiting peptide backbone sequence coverage. These differences are due to the variation in fragmentation mechanisms; with CID being a thermal process in which the weakest bonds are broken, whereas ECD follows a radical-based mechanism resulting in more diverse fragmentation [6]. The exact mechanism of peptide and protein ECD is still of much debate and it is of great interest to elucidate the mechanism to further our understanding of how best to undertake a proteomics study.

Proteomics [7, 8] is the study of the entire complement of proteins expressed by a cell or tissue type. Unlike the genome, the proteome is dynamic, varying between cells depending on their type and state (*e.g.* stage of cell cycle), and sporadically (*e.g.* chemical imbalance or viral presence), and is further complicated by the presence and formation of posttranslational modifications. Posttranslational modification, in which a functional group may be covalently attached, cleaved or substituted, of a protein, is one of the final stages of protein biosynthesis and can come about through many different mechanisms, *e.g.* phosphorylation of any protein

through the action of enzymes [9] and formation of 3-nitrotyrosine in the presence of high levels of reactive oxygen species in the cell, *e.g.* superoxide and nitric oxide [10-12].

The goal of the work presented in this thesis was to further our knowledge of the radical-based mechanism of peptide with specific inference to modifications of amino acid side-chains. The rationale for the work was that by understanding the gas-phase ion chemistry, it should be possible to determine the most appropriate proteomics workflow for the study of a particular modification. The research considered both post-translational modifications (*i.e.* nitration, nitrosylation and phosphorylation) and process-induced modifications (*i.e.* carbamidomethylation and carboxymethylation).

1.1 Mass spectrometry

Mass spectrometry (MS) is an analytical technique which has long been used for the determination of the elemental composition of a sample or molecule by measuring the *m*/*z* (mass to charge) ratio of the ionised sample. A mass spectrometer comprises three main components: an ion source, where ions are generated, a mass analyser, which separates ions according to *m*/*z*, and a detector, where the ions are detected.

1.1.1 History

The first mass spectrometer was developed by J. J. Thomson [13] in the early 1910s (called the parabola spectrograph). Using this instrument he was able to measure the masses of O_2, N_2, CO, CO_2, $COCl_2$, observe negative and multiply charged ions, discover metastable ions,

and discover the isotopes ^{20}Ne and ^{22}Ne [14]. Prior to this work, Thomson was awarded the Nobel Prize in Physics in 1906 for "his theoretical and experimental investigations on the conduction of electricity by gases" which led directly to the development of the parabola spectrograph. Thomson's student Francis Aston continued the research and, in 1919, built the first fully functioning mass spectrometer which dispersed and focused ions by mass and velocity [15]. The use of electromagnetic focusing improved the resolution of the spectrum and allowed identification of 212 of the 287 naturally occurring isotopes [16] (*e.g.* ^{35}Cl and ^{37}Cl). For this work Aston was awarded the 1922 Nobel Prize in Chemistry "for his discovery, by the means of mass spectrograph, of isotopes, in a large number of non-radioactive elements, and for his enunciation for the whole-number rule."

Mass spectrometry was revolutionised during the 1940s, when both the linear time-of-flight (TOF) and ion cyclotron resonance (ICR) mass analysers were introduced. Stephens first proposed the TOF in 1946 [17], and was vindicated by Cameron and Eggers' results in 1948 [18]. Ions analysed by TOF-MS are separated by velocity across a specific distance, following acceleration by an electric field of known strength. ICR as a mass analyser for mass spectrometry was developed by Hipple *et al*. in 1949 [19]. ICR relies on the cyclotron motion of ions in a magnetic field. This was developed further by Comisarow and Marshall in 1974 [20] where they coupled ICR with Fourier transform (FT-ICR) – this is further explained in **Section 1.3.3.1**. In 1953, the quadrupole analyser and ion trap were developed by Paul and Steinwedel [21]. Ions were trapped in an oscillating RF electric field and ion traps are now commonly used as mass filters in hybrid instruments, as well as stand-alone instruments. Paul was later awarded the 1989 Nobel Prize in Physics "for the development of the ion trap technique." More recently, in 2000, Makarov [22] developed the orbitrap mass analyser with the principle originally developed in the 1920s, termed the Kingdon trap [23] – this is further

explained in **Section 1.3.3.2**. In the Kingdon trap and orbitrap, ions are trapped by their attraction to a central wire or electrode and, if they have sufficient velocity, will begin to orbit about the wire or electrode with their velocity being dependent on their *m*/*z*.

1.2 Ionisation

The earliest techniques of ionisation (*e.g.* electron ionisation (EI) [24], and chemical ionisation (CI) [25]) were, and still are, highly successful for analysis of isotopic elements and organic molecules; however, both EI and CI increase the internal energy of the analyte significantly, which for complex mixtures and molecules (*e.g.* fossil fuels, and biological samples) leads to significant fragmentation of the molecule and fails to produce stable ions of the molecular species.

The problems with EI and CI were partially rectified by Krone and Beckey in 1969 [26] with the development of field desorption (FD) which allowed the ionisation, and hence analysis, of non-volatile substances of up to 5 kDa. Significant steps were taken during the 1970s and 1980s in this field with the subsequent introduction of plasma desorption (PD) [27], secondary ion mass spectrometry (SIMS) [28], laser desorption (LD) [29], and fast atom bombardment (FAB) [30]. All of these techniques transformed mass spectrometry into a useful tool for the analysis of biomolecules but with a limit on *m*/*z*.

Despite these successes, it was not until the introduction of matrix assisted laser desorption ionisation (MALDI) [31, 32] and electrospray ionisation (ESI) [33, 34] during the late 1980s, that the analysis of certain biomolecules was enabled. The true advantage of these two

techniques is that they are both 'soft' ionisation techniques, thus allowing very large biomolecules to obtain a stable gas-phase structure when ionised and leading to very little, if any, fragmentation. For the development of MALDI and ESI, the 2002 Nobel Prize in Chemistry was awarded to Koichi Tanaka (MALDI) and John Fenn (ESI) "for their development of soft ionisation methods for mass spectrometric analyses of biological macromolecules."

MALDI, as the name suggests, uses a matrix to aid laser desorption. Prior to analysis the sample is dissolved in a solvent containing small organic molecules on an analysis plate and allowed to dry. The organic molecules in the matrix are variable, depending on the sample for analysis, but they must have a strong absorption at a specific laser wavelength. The sample is irradiated with a pulsed laser beam at this specific wavelength such that the matrix absorbs the energy and leads to analyte ionisation. Today MALDI is frequently used for imaging tissues, and for the identification, presence and distribution of proteins, peptides, lipids, metabolites, xenobiotics, and other biological molecules in intact tissues [35].

1.2.2 Electrospray ionisation

As mentioned above, the successful application of electrospray ionisation for protein analysis led to the award of the Nobel Prize to John Fenn; however, as with most scientific discoveries the theory behind the technique was documented many decades prior to this. Notable observations and contributions were made by John Zeleny – who first identified electric discharge from liquid points, *i.e.* a hemispherical drop forms by passing a liquid through a fine capillary tube [36] – and Malcolm Dole – who was able to successfully spray macroions

(specifically polystyrene) using electrospray [34] – although it was not until John Fenn successfully ionised a wider range of compounds, including proteins, that the technique was widely utilised.

Ionisation through ESI takes place on samples which have been dissolved into a solution, usually containing volatile organic solvents and an acidic or basic buffer. This solution becomes charged by passing through a capillary with a very fine tip which has a high charge (several kV) applied to it. Both positive and negative ions may be formed by applying either a positive or negative voltage, respectively. The ions in solution repel each other and the particles at the nozzle of the capillary form a Taylor cone. Formation of a Taylor cone occurs once a certain voltage, termed the 'onset voltage', is reached and the Coulombic repulsion becomes greater than the surface tension of the solution [37]. Once formed, the Taylor cone begins to divide and small droplets are released, which in turn divide further and eventually form a fine spray of charged particles. This continual division takes place because the charges are located on the surface of the droplets and as they decrease in size the Coulombic repulsion increases further. As this reaches the Rayleigh limit of the droplet a further stage of division (Coulombic fission) occurs [38]. This process ultimately produces multiply charged ions, a major advantage over other ionisation techniques (including MALDI which tends to form few multiply charged ions), the charge state of which is relative to both the size of the analyte and the composition. The process of ESI is shown in **Figure 1.1**.

The exact mechanism of ESI is still of some debate, with two main models proposed: the charge reduced model (CRM) [34] and the ion evaporation model (IEM) [39], both of which are shown in **Figure 1.1**. In both models it is assumed that a sequence of evaporation and

splitting stages of the charged droplets occur which are due to Rayleigh instabilities being reached, thus leading to smaller and smaller droplets. The CRM then proposes that this sequence continues until a droplet contains only one single solute molecule and, as the remaining solvent evaporates, the droplet's charge is retained on the molecule [34]. The IEM proposes that before each droplet becomes small enough that it contains only one solute molecule, the field strength at the surface of the droplet becomes large enough to allow a surface ion or ions to undergo field desorption into the gas phase [39].

While there is no definitive scientific proof, there is a general consensus among researchers that a combination of the two models takes place during ESI, with small ions typically being formed through the IEM and larger ions being liberated *via* the CRM. Fenn himself declared during his Nobel Lecture that "IEM is more consistent with more experimental observations than is CRM; however, sometimes the CRM seems more likely to apply, especially in the case of very large analyte molecules" [40].

Further optimisation of ESI has been undertaken with focus on development of smaller capillaries and adapted probe tips, which has been shown to increase sensitivity and allow a lower flow rate. Two such techniques are known as micro- [41] and nano-ESI [42]. Nano-ESI utilises narrower capillaries which produces a smaller Taylor cone and thus smaller charged droplets. The smaller charged particles require less fission steps than ESI to form gas-phase ions, resulting in a less negative effect of high salt concentration than for ESI [43]. These developments of nano-ESI have increased the sensitivity significantly, with successful detection being noted at zeptomole (10^{-21}) concentrations [44].

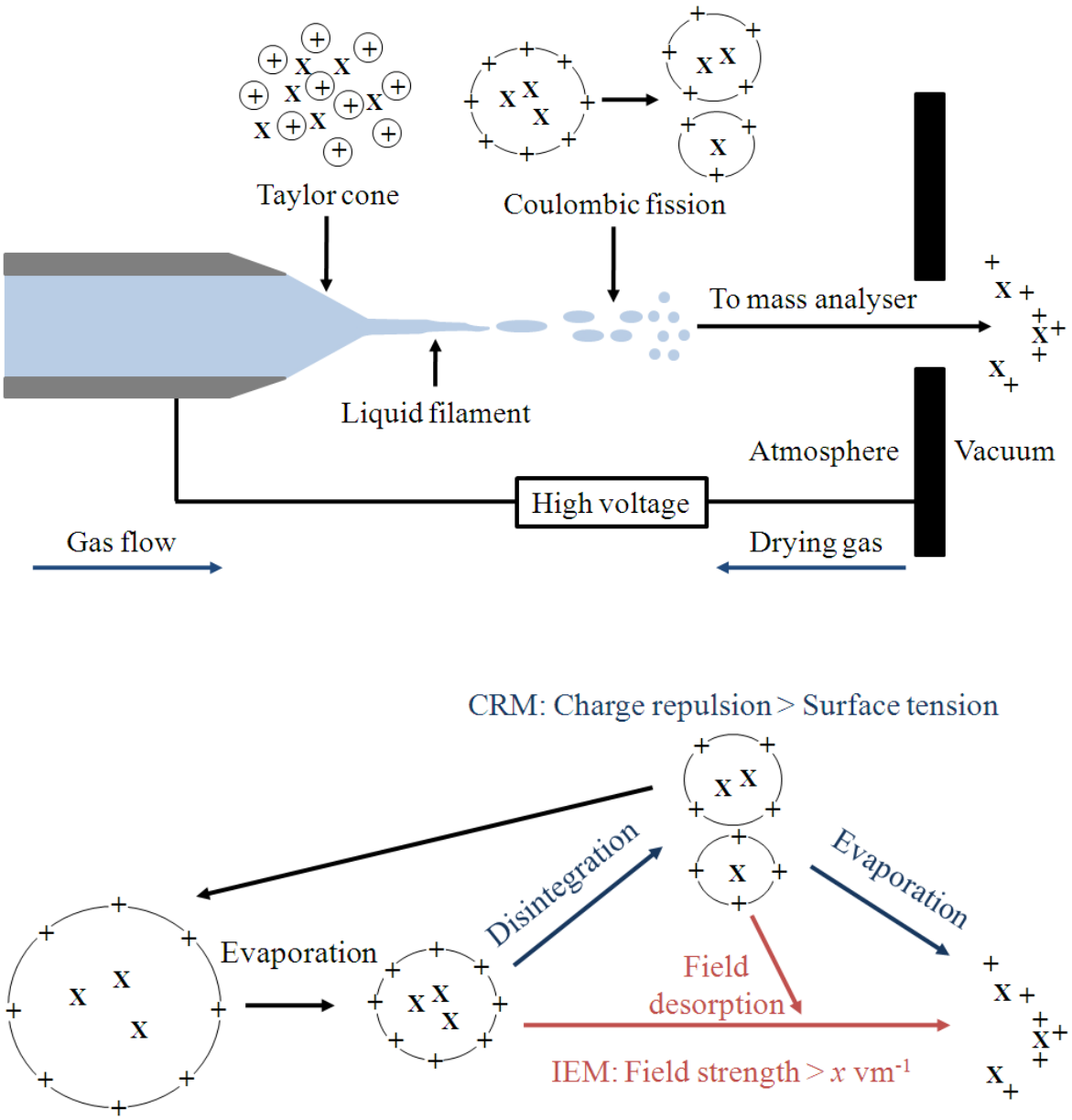

Figure 1.1: The process and proposed models of ESI

Upper: Schematic of the ESI process.

Lower: Schematic of the charge reduced model (CRM) and ion evaporation model (IEM), shown in blue and red, respectively. Adapted from [40].

1.3 Mass analysis

Once the ions have been converted into the gas-phase, be it through any of the available ionisation sources, they are separated with the use of mass analysers. Mass analysers have also been developed to isolate and separate ions prior to detection. An ion trap is a device that uses electric and/or magnetic fields to capture and store ions, these ions can then be analysed or transferred into another mass analyser for further detection. The types of ion traps which have been employed in this work and therefore are discussed in this thesis are the eponymously named Paul trap [21], Kingdon trap [23] and Penning trap [45]. The Paul trap is more commonly referred to as the three-dimensional (3D) quadrupole ion trap, and is discussed, along with the related linear quadrupole ion trap, in **Section 1.3.1**. The Penning trap is utilised in FT-ICR mass spectrometry and is discussed in significant detail in **Section 1.3.2**. The Kingdon trap has since been further developed into the orbitrap [22] and is discussed in **Section 1.3.3**.

1.3.1 Quadrupole ion trap

The quadrupole ion trap exists both in linear (LIT) [46] and 3D (also referred to as a Paul trap [21]) types, with both trapping ions by using constant direct currents and radio frequencies (RFs) and oscillating alternating current electric fields. The LIT is based upon the four-rod quadrupole, with variation of the electric field within the rods, allowing the ions to be repelled or attracted such that ions of interest may be retained. The Paul trap consists of a circular electrode with two ellipsoid caps on the top and bottom which creates a three dimensional quadrupolar field. In both the LIT and Paul traps, ions are detected by the use of an electron multiplier. A schematic of the LIT mass analyser is shown in **Figure 1.2**.

Advantage of LITs, in comparison to the Paul trap, are the >10-fold higher ion trapping capacity and the higher trapping efficiency, which increase both the sensitivity and dynamic range of the instrument [47]. Once introduced into the LIT ions are first cooled by colliding with an inert gas, typically helium, and transfer along the *z* axis of the electrodes, while oscillating in the *xy* plane, as shown in **Figure 1.2**. Ions are trapped along the *xy* plane by applying an RF voltage along the electrodes and a static electric field at the ends of the rods to trap along the *z* axis [48].

Once trapped, ions within an LIT can undergo either axial or radial ejection. Axial ejection, in which ions are ejected along the z axis of the electrodes, occurs following application of an AC voltage between the rods and the exit lens; whereas radial ejection, in which ions are ejected perpendicular to the electrodes, takes place by applying an AC voltage on two opposing rods [48]. Once ejected, ions can either be detected by electron multipliers, or allow isolation of non-ejected ions. These isolated ions can then be transferred to other mass analysers for analysis, *e.g.* FT-ICR, undergo fragmentation techniques within the ion trap, *e.g.* collision-induced dissociation (CID) or both fragmentation and analysis, *e.g.* analysis within a triple quadrupole (QqQ) undergoes isolation within the first LTQ (Q1) prior to transfer to the second quadrupole (q2) where CID may take place.

A major disadvantage of the LIT and the Paul trap is the loss of low-mass ions following certain dissociation techniques, *e.g.* CID (discussed in further detail in **Section 1.4.1**), referred to as the 'one-third' rule [49]. This issue arises from the necessity to apply an RF voltage for CID to take place, which directly affects the observable *m*/*z* limit (an increase in the applied

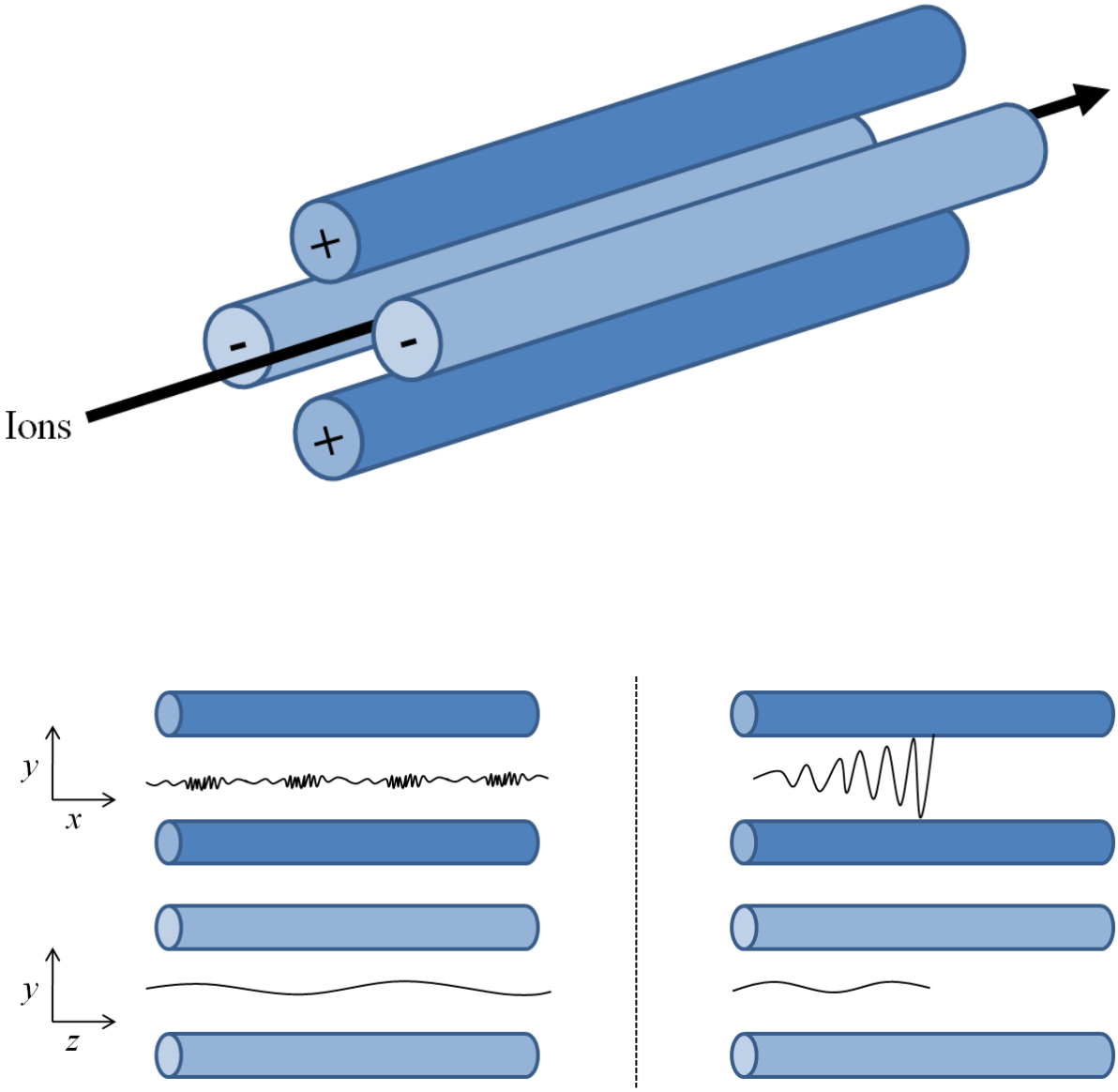

Figure 1.2: Schematic of a LIT mass analyser and ion trajectories within

Upper: A linear quadrupole ion trap.

Lower: Trajectory of a stable (left-hand) and unstable (right-hand) ion passing through an LIT. The ion in the left-hand schematic is stable along both the *x* and *z* planes, whereas the ion depicted on the right-hand figure is stable only along the *z* plane and unstable along the *x* place, leading to ion (radial) ejection.

voltage increases the *m*/*z* limit), resulting in the loss of ions with a mass of approximately one-third of the isolated ion [50].

1.3.3.2 Fourier transform ion cyclotron resonance

Fourier transform ion cyclotron resonance (FT-ICR) mass spectrometry was first developed in the early 1970s by Comisarow and Marshall [20] by coupling together Fourier transform with the pre-existing ion cyclotron resonance (ICR) mass analyser. Analysis is performed in a high field magnetic Penning trap which allows the ions to be held in a stable environment; this stability allows certain techniques to be completed which may not otherwise be possible, *e.g.* electron capture dissociation (see **Section 1.4.2**). Once the ions are trapped they are excited by an oscillating electric field increasing their cyclotron motion to a larger radius and allowing the ions to move in-phase. The in-phase ions are detected as they pass by a pair of plates, producing a time domain signal, known as a transient, which is extracted by performing fast Fourier transform to give a frequency spectrum which is calibrated to give a mass spectrum. A photograph and schematic of a hybrid LTQ FT-ICR mass spectrometer are shown in **Figure 1.3**, and this ion behaviour within the ICR cell is shown in **Figure 1.4**. In the work presented in this thesis, experiments were initially performed on a Thermo Finnigan LTQ FT and latterly on a Thermo Fisher LTQ FT Ultra

FT-ICR allows the greatest resolution and mass accuracy of all current mass spectrometers with resolving power greater than 8 000 000 and parts per billion mass accuracy being reported [51-53]; this is possible due to the use of superconducting magnets which have been found to be more stable than RF voltage [54]. These specifications have allowed FT-ICR to

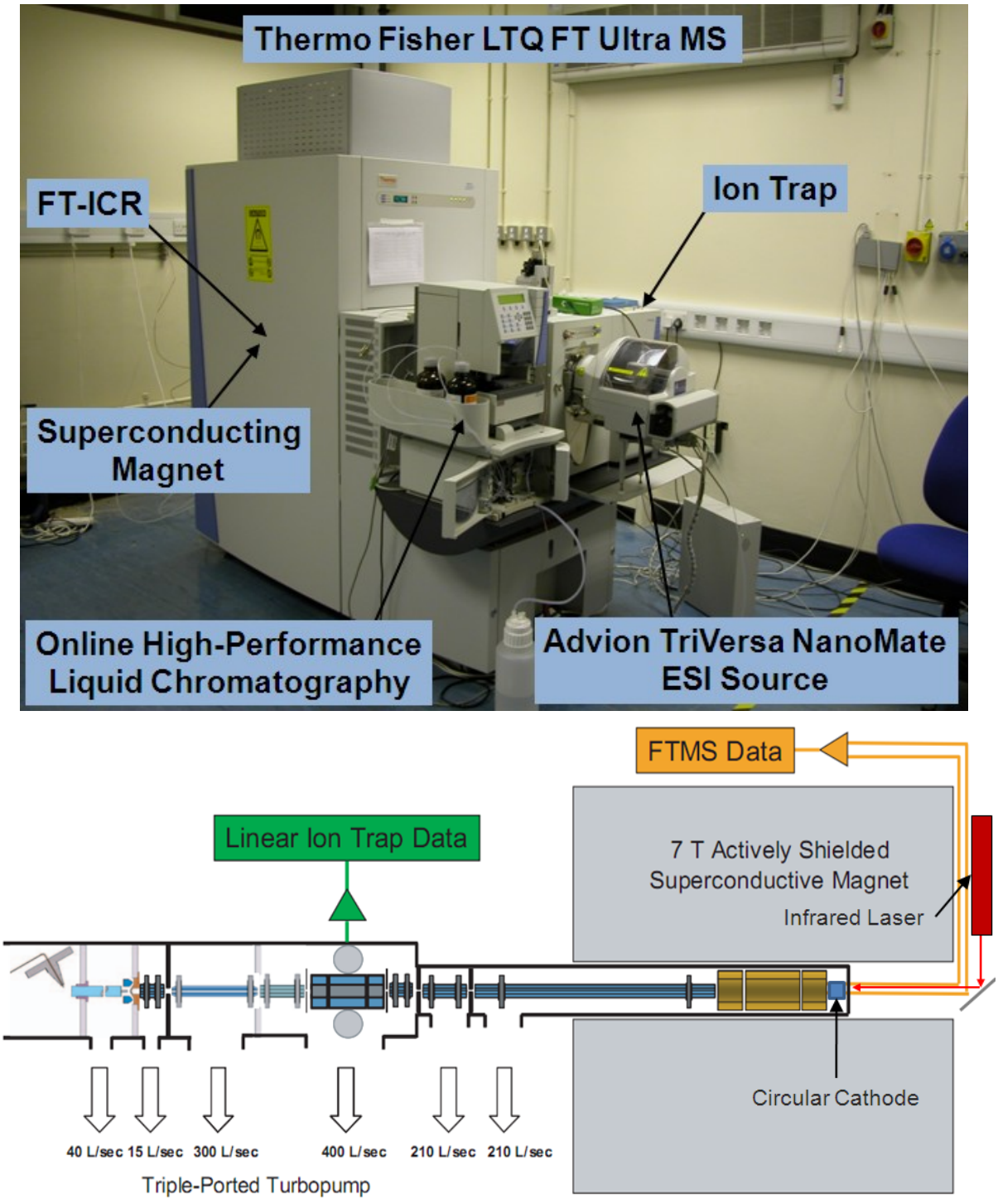

Figure 1.3: Photograph and schematic of an LTQ-FT-ICR mass spectrometer

Upper: Annotated photograph of a Thermo Fisher LTQ FT Ultra™ mass spectrometer with connected Advion TriVersa NanoMate® electrospray source.

Lower: Annotated schematic of the Thermo Finnigan™ LTQ FT™ mass spectrometer [61]. Note the presence of the infrared laser and the circular cathode allowing IRMPD and ECD experiments to be completed.

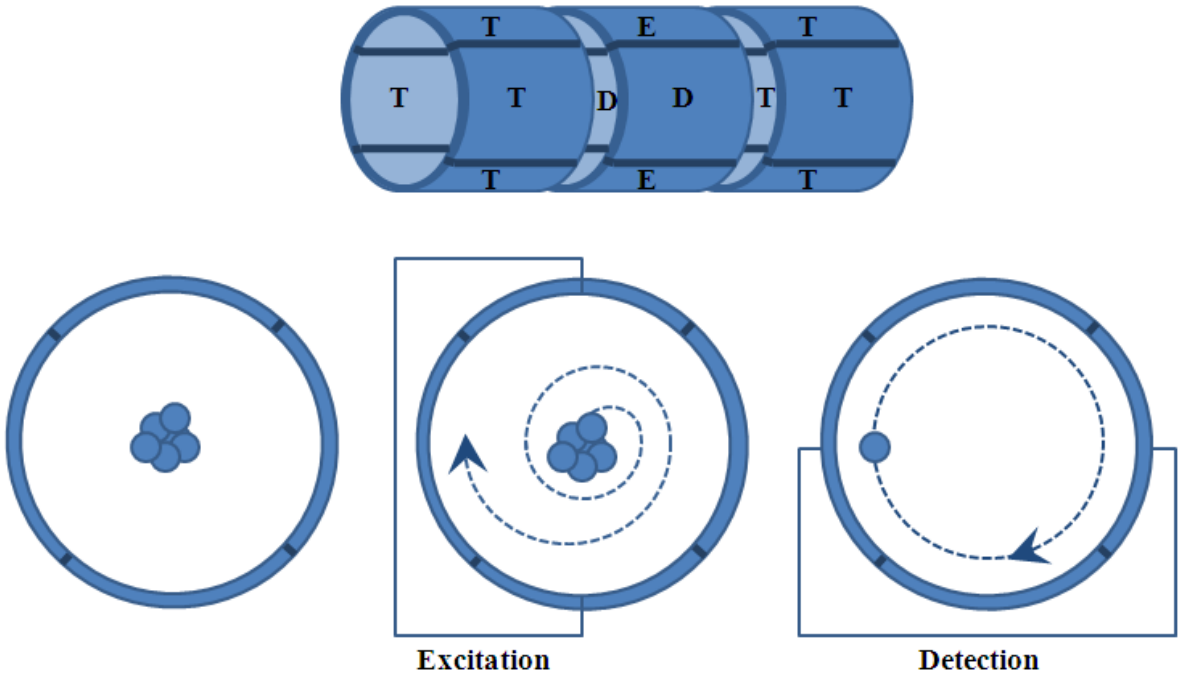

Figure 1.4: Schematic of an ICR mass spectrometer and ion trajectories within

Upper: Schematic of an open-ended ICR ion trap or 'cell', where T is Trapping, E is Excitation, and D is Detection.

Lower: Ion packet behaviour within an ICR cell. Out-of-phase ion packets of the same *m*/*z* trapped within the ICR (**left**). Excitation of the ion packets increases the radial orbit to result in coherent in-phase cyclotron motion (**centre**). Finally, the excitation plates are switched off and detection of the cyclotron motion of the in-phase ion packets is measured (**right**). As well as the cyclotron motion in the *xy* plane the ion packets undergo magnetron motion, and in the *z* plane the ion packets undergo trapping motion.

be used successfully for the identification and separation of many complex mixtures which may be limited in other mass analysers [55], these include petroleomic [56], metabolomic [57], and proteomic [58] samples. Currently, the largest magnet available has a 25 T field which leads to an increase in resolution, scan speed, and the mass range of detection [59]. These improvements are due to the direct correlation between magnetic field strength and ion movement within the ICR cell, specifically the cyclotron motion, as shown by **Equation 1.1** [60], where ω_c is the angular cyclotron frequency, q is the charge, B_0 is the magnetic field strength and m is the mass.

$$\omega_c = \frac{qB_0}{m}$$

Equation 1.1

Equation 1.1 is developed from the principle that any charged particle in a uniform and stable magnetic field will be influenced by the Lorentz magnetic force and will orbit in a perpendicular direction to a magnetic field. An increase in magnetic field results in an increase in cyclotron frequency, and as shown by **Equation 1.2**, where v_{xy} is the ion velocity in the two-dimensional *xy* plane, and r is the ion radius in the *xy* plane, the radius of the ion's motion is inversely proportional to the cyclotron frequency (*i.e.* an increase in cyclotron motion will lead to a decrease in radius of the ion) [60], thus the possible range of detection is increased.

$$\omega_c = \frac{v_{xy}}{r}$$

Equation 1.2

Once the ions enter the ICR cell, trapping must take place to prevent ion ejection; this is completed by applying voltages to the trapping plates, as shown in **Figure 1.4**. This trapping force is provided in the *z* plane and results in trapping motion at the trapping oscillation frequency, ω_z. **Equation 1.3** [60] shows this trapping motion with respect to the charge, q, trapping voltage, V_{trap}, mass, m, the cell length, a, and a constant specific to the cell type, α.

$$\omega_z = \sqrt{\frac{2qV_{trap}\alpha}{ma^2}}$$

Equation 1.3

The final force exerted onto the ions is the magnetron motion, ω_-, which takes place in the *xy* phase, shown by **Equation 1.4** [60].

$$\omega_- = \frac{\omega_c}{2} - \sqrt{\left(\frac{\omega_c}{2}\right)^2 - \frac{\omega_z^2}{2}}$$

Equation 1.4

Importantly, the cyclotron motion exhibited by the Lorentz force, as discussed above, is only applicable within a uniform and stable magnetic field (referred to as the unperturbed cyclotron motion), and due to the application of the trapping oscillation, in which a voltage is applied, a change in cyclotron motion of the ion results. This resultant force is called the reduced cyclotron frequency, ω_+, as shown in **Equation 1.5** [60].

$$\omega_+ = \frac{\omega_c}{2} + \sqrt{\left(\frac{\omega_c}{2}\right)^2 - \frac{\omega_z^2}{2}}$$

Equation 1.5

Once trapped within the ICR cell, an RF voltage is applied to the two excitation plates which excites the ions. Excitation of the ions will lead to an increase in ion radius, and will allow formation of ion 'packets'. In their ground state, ions of the same mass and charge tend to be 'out of phase' with each other, and would lead to signal destruction when detection takes place. Once excited to a suitable radius the excitation plates are switched off and as the ion packet passes by the detection plates an image current is inducted, and hence are detected. The reduced cyclotron frequency is typically greater than both the magnetron and trapping frequencies, and therefore is usually the parameter which is detected; however, in some instances of instrument fault small sidebands may be identified, *e.g.* if the ICR cell is misaligned with the magnet these sidebands are due to the magnetron motion [62].

As the RF voltage across the excitation plates is terminated the ions will begin to lose energy due to collisions with gases within the cell, and as the orbits of the ions decreases, the ion-to-detection plate charge induction is reduced and hence the signal decays. Importantly, image current detection is non-destructive, and therefore the ions are repeatedly detected. This allows the formation of an image current being a composite of sine waves of different frequencies. Fourier transform is applied to this time domain signal and is converted from a time-domain waveform to a frequency-domain waveform. This frequency-domain spectrum is ultimately converted into a mass spectrum by applying a calibration equation, shown in **Equation 1.6** where *A* and *B* are constants obtained through internal calibration [60].

$$\frac{m}{z} = \frac{A}{v_+} + \frac{B}{v_+^2}$$

Equation 1.6

1.3.3 Fourier transform orbitrap

Similarly to the FT-ICR, the FT-orbitrap (or simply 'orbitrap') detects ions *via* an induced image current and following detection the mass spectrum is generated by Fourier transform; however, whereas the FT-ICR ions are trapped and detected inside an ICR cell, orbitrap analyses are completed as the ions oscillate up and down along the outside of an electrode. A photograph and schematic of a hybrid LTQ orbitrap mass spectrometer is shown in **Figure 1.5**.

The orbitrap was first developed by Makarov in 2000 [22] with the principle behind the orbitrap being around since the 1920s [23]. The trap developed by Kingdon in 1923 consisted of a thin central wire encased in an outer cylindrical electrode, [23]. Makarov developed these results by converting the central wire into a shaped electrode. As ions are directed into the trap they are attracted to the electrode, and if they have sufficient velocity will begin orbiting about the electrode. This ion trapping is due to the electrostatic field about the shaped electrode, whereas in the case of FT-ICR mass analysers trapping occurs in the electromagnetic field. If the ion velocity is not within the detection range the ions are ejected. Once trapped, the ions undergo harmonic oscillations along the electrode with the frequency being proportional to $(m/z)^{-1/2}$, these oscillations are detected using image current detection and, as with FT-ICR mass spectrometry, converted using fast Fourier transform into a mass spectrum [22].

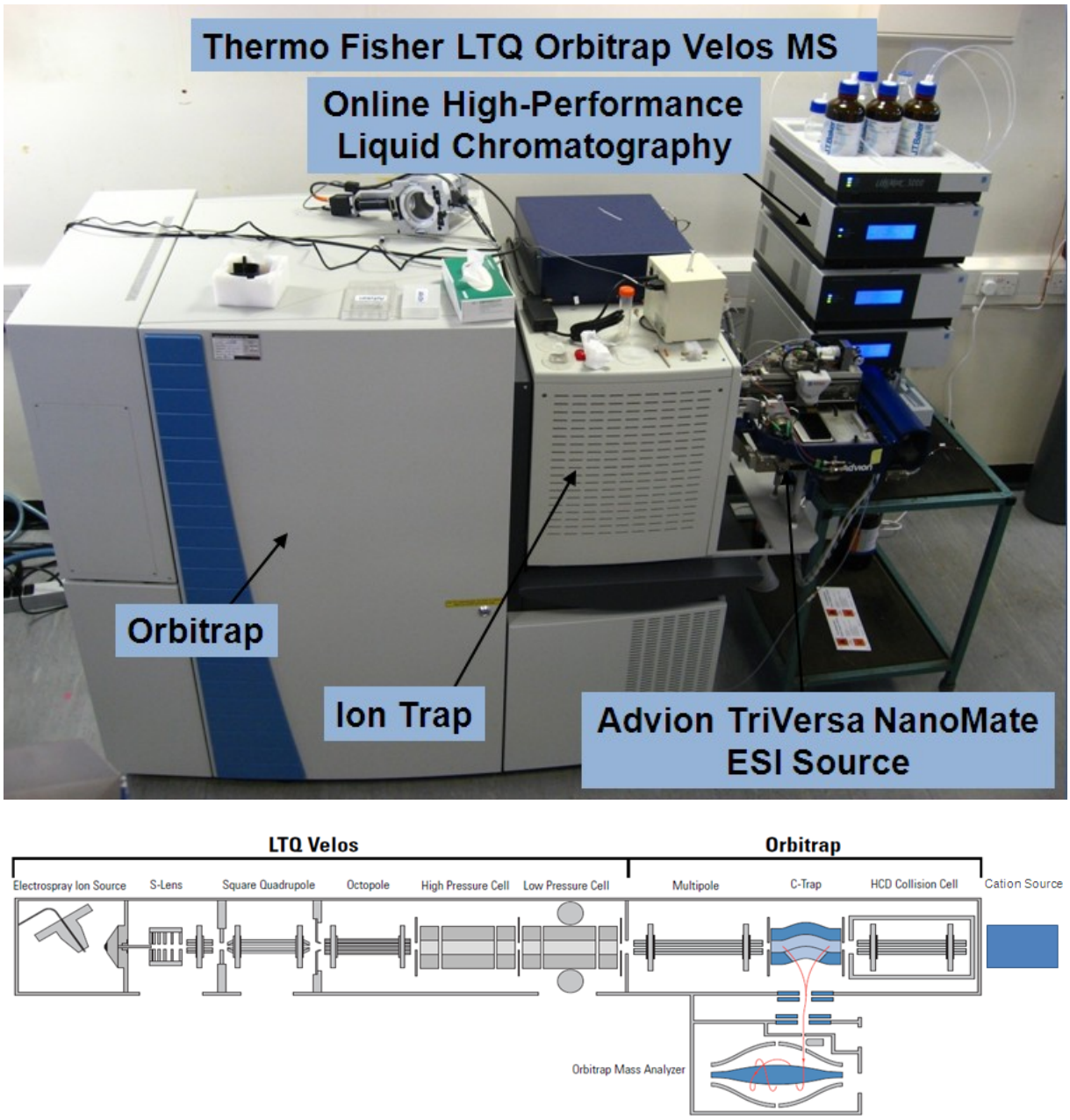

Figure 1.5: Photograph and schematic of an LTQ-FT-orbitrap mass spectrometer

Upper: Annotated photograph of a Thermo Fisher LTQ Orbitrap Velos™ mass spectrometer with connected Advion TriVersa NanoMate® electrospray source.

Lower: Annotated schematic of the Thermo Fisher LTQ Orbitrap Velos™ mass spectrometer [66]. Note the addition of the cation source at the rear of the instrument allowing heating and electron ionisation of chemicals for ion-ion experiments, *e.g.* fluoranthene for ETD.

Initial reports showed that a mass accuracy of 1-2 ppm, resolving power of up to 200 000 and a dynamic range of around 5 000 [63, 64] could all be obtained. More recent developments have decreased the gap between the inner and outer electrodes, thus providing a higher field strength, and leading to an increase in resolving power of >600 000 and a dynamic range of 25 000 [65]. Interestingly, the development of the high-field orbitrap mass analyser also identifies that space charge of ions within the orbitrap appear to make very little difference to mass shifts, a issue identified in the original orbitrap and in FT-ICR mass analysis [65].

1.4 Tandem mass spectrometry

Tandem mass spectrometry (MS/MS), in which a precursor ion is characterised according to its fragments, is widely used in structural analyses. MS/MS involves isolation of a precursor ion followed by exposure to an external stimulus to induce controlled fragmentation. In mass spectrometry-based proteomics, digested peptides are frequently analysed using MS/MS to identify the intact protein and, if present, posttranslational modifications. In this thesis, work has focused on the use of the radical-based electron capture dissociation and electron transfer dissociation for the analysis of a wide array of biological and synthetically modified peptides, for comparison the widely utilised thermal-based collision-induced dissociation and infrared multiphoton dissociation were also used. The purpose of which was to identify how best to analyse biological samples in future and to further investigate the much debated radical ion chemistry of electron capture dissociation.

1.4.1 Collision-induced dissociation and infrared multiphoton dissociation

Collision-induced dissociation (CID), also referred to as collisionally activated dissociation (CAD), was first described by Jennings [4], and McLafferty [5]. In CID, isolated ions of interest (termed "precursor ions") are accelerated to higher kinetic energies and undergo collisions with neutral gas atoms or molecules (typically helium, nitrogen or argon). Following this inelastic collision, some of the ion's kinetic energy is converted into internal vibrational energy resulting in bond cleavage. Infrared multiphoton dissociation (IRMPD) [67] is achieved by irradiating precursor ions with an infrared laser, again leading to an increase in internal vibrational energy and bond cleavage.

CID and IRMPD are classed as slow activation methods in which multiple separate collisions take place during the activation period, which itself is as long, or longer, than the timescale for unimolecular fragmentation of the ion. If these activation events are slow enough to result in competition with deactivation of the ion, the process is considered a 'slow-heating' method [68]. Slow-heating techniques, such as resonant excitation CID (within an ion trap, *e.g.* LIT), result in heating of the precursor ion to a higher Boltzmann temperature prior to fragmentation and, due to the slow energy conversion throughout the ion, leads to fragmentation *via* the lowest energy pathway(s). Other slow-heating techniques include blackbody infrared radiative dissociation (BIRD) [69]), , surface induced dissociation (SID) [70] and sustained off-resonance irradiation collision-induced dissociation (SORI-CID) [71]. Slow activation techniques which are not 'slow-heating', *i.e.* when activation occurs on a faster timescale, *e.g.* beam-type CID (within quadrupolar mass analysers), result in higher internal energies and are able to fragment *via* higher energy pathways.

For peptides and proteins, the lowest energy pathway tends to be cleavage of the amide N-C_O bond to produce *b* and *y* fragment ions [72], as shown in **Figure 1.6**. This fragmentation pathway observed following peptide CID is best explained by the 'mobile proton' model [73-75]. The mobile proton model proposes that following collisional activation of the peptide ion a proton from any basic site, *i.e.* N-terminus or amino acid residue, *e.g.*, arginine or lysine, is mobilised (with varying efficiencies), to a backbone heteroatom (either a carbonyl oxygen or amide nitrogen) leading to charge-directed fragmentation. In peptide CID the favourable fragmentation that occurs N-terminal to Pro amino acid residues can be explained by the mobile proton model. Specifically, the proline imide nitrogen has a greater gas-phase basicity than that of any other backbone nitrogen atoms in other amino acid residues, and hence the the proton is statistically more likely to be situated at this proline imide nitrogen, leading to favourable fragmentation [74, 76]. This fragmentation of CID is also a disadvantage when analysis of peptides with labile posttranslational modifications is completed, as CID of these species leads to the dominant fragmentation of the modifications, potentially decreasing the information which can be obtained from the sample. (This issue is explored in more detail in **Section 1.6**).

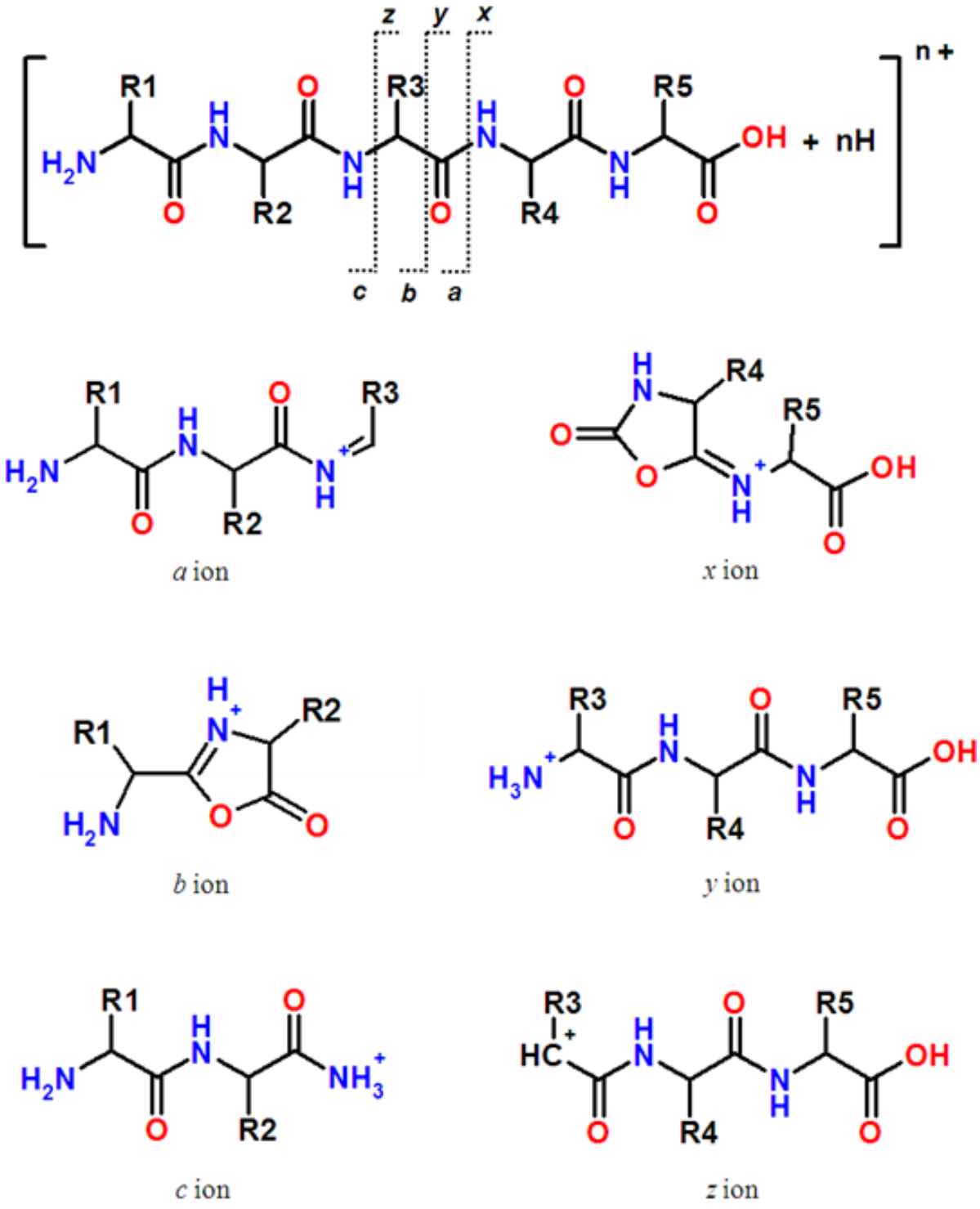

Figure 1.6: Peptide fragment ion structures

Structures of the peptide fragment ions observed following fragmentation of a standard peptide (**top row**). Fragment ions following fragmentation of C-C_O (*a* and *x* ions; **second row**), C_O-N (*b* and *y* ions; **third row**) and N-Cα (*c* and *z* ions; **bottom row**) bonds.

1.4.2 Electron capture dissociation

Electron capture dissociation (ECD) was first described by Zubarev *et al*. in 1998 [1] and has since proved an invaluable MS/MS technique for biomolecular analysis [77], particularly for peptides and proteins. In ECD, multiply charged ions of interest are irradiated with low energy electrons (<0.2 eV) producing charge-reduced species, which dissociate along radical-driven pathways and as such activation and fragmentation are temporally separated (~10^{-15} s) [68]. In the initial studies, electrons were generated through the use of a heated metal filament, *e.g.* tungsten or barium [1]; however, this was a very slow and inefficient process with sufficient irradiation for ECD taking up to 30 s. This problem was addressed by Tsybin *et al.* in 2001 with the introduction of the heated dispenser cathode [78]. By replacing the filament with this dispenser cathode, the number of electrons produced was increased thus increasing the efficiency and reducing the timescale required for peptide ECD to milliseconds.

Due to the radical mechanism of ECD, significant advantages for peptide and protein analysis were identified: firstly, cleavage is diverse (the only exception being N-terminal to proline, which fragments only very rarely [79]), therefore sequence coverage tends to be higher for ECD than for slow-heating techniques [6, 80], and secondly, labile posttranslational modifications are retained on peptide/protein backbone fragments [3]. ECD has been shown to be successful for localising sites of γ-carboxyglutamic acid [3], *N*- and *O*-glycosylation [81, 82], phosphorylation [83, 84], acetylation [85], oxidation [86], ubiquitination [87] and sumoylation [88]. Although ECD has been applied to the characterisation of a wide range of posttranslational modifications, the studies have not been exhaustive; indeed it has been recently been shown that interactions between phosphate groups and amino acid side-chains have an adverse effect on the ECD fragmentation of phosphopeptides [89].

A major disadvantage of ECD is the inability to successfully fragment large proteins. When ECD is undertaken of such a protein the backbone may fragment but any non-covalent bonds will likely not undergo fragmentation, thus preventing separation of the fragment ions. This was noted in a direct comparison of a range of proteins: ECD of cytochrome c (12.3 kDa) led to the identification of 75/103 backbone fragments, 30/152 for apomyoglobin (17 kDa), and 0/258 for carbonic anhydrase (29 kDa) [80]. To overcome this issue, Horn *et al*. introduced activated ion ECD (AI ECD), in which the precursor ions are heated using a slow-heating technique (*e.g.* infrared radiation) whilst simultaneously undergoing ECD, thus destroying any non-covalent bonds which may be present. AI ECD was applied for the fragmentation of carbonic anhydrase leading to observation of 116/258 backbone cleavages [90].

The major product of electron capture by peptide $[M + nH]^{n+}$ cations is typically the charge-reduced species $[M + nH]^{(n-1)+\bullet}$, *i.e.* the precursor ion which has captured an electron but not undergone dissociation. Often, this is accompanied by hydrogen radical loss, *i.e.* formation of $[M + (n-1)H]^{(n-1)+}$ [91]. The dominant peptide fragmentation pathways proceed *via* cleavage of the backbone N-Cα bond to give *c* and $z^{\bullet}$ fragment ions [92] (which may be accompanied by hydrogen atom transfer to give $c^{\bullet}$ and, more commonly, *z* fragment ions [93]) and disulfide bonds to give RSH and $^{\bullet}SR'$ [94]; however, the mechanism by which N-Cα and disulfide bond cleavage occurs following electron capture has been, and remains, the subject of intense debate with two proposed mechanisms holding precedence: the Cornell mechanism [1] and the Utah-Washington mechanism [95, 96].

1.4.2.1 Cornell mechanism

The mechanism for N-Cα bond cleavage following ECD was initially proposed by McLafferty in 1986 [97] with the suggestion that electron capture "should cause non-ergodic cleavage with relatively high efficiency at the sites of highest proton affinity" with the formation of odd- and even-electron ionic products. Once Zubarev *et al*. first described ECD in 1998 [1], fragmentation was proposed to follow a non-ergodic mechanism, *i.e.* cleavage occurs prior to energy dissipation. Since then these hypotheses have advanced into what is now known as the Cornell mechanism.

The Cornell mechanism (shown in **Figure 1.7**) postulates that electrons are initially captured to a high-*n* Rydberg state at a positively charged site (*e.g.* Arg/Lys side chain) to form a hypervalent radical centre, with computation studies showing that ~4 eV is gained for forming NH_3 from $[NH_3^+ + e^-]$ [80, 98]. This species then undergoes dissociative recombination with the hypervalent radical ejecting or releasing a H atom once the ground Rydberg level is reached, which is then proposed to attack either an S-S bond or a proximate amide carbonyl forming an aminoketyl intermediate [92]. Finally, the aminoketyl intermediate undergoes a β-fission, cleaving its N-Cα bond with the formation of *c* and $z^{\bullet}$ ions.

Following its proposal, the Cornell mechanism has received support from computational studies of N-Cα bond dissociations in model amide and peptide cation-radical systems containing ammonium groups [99, 100]; however, issues have arisen when attempting to explain the observation of *c* and *z* fragments for species that are remote from the charge site and for peptides which do not yield a mobile hydrogen atom, *e.g.* peptides catonized by metal

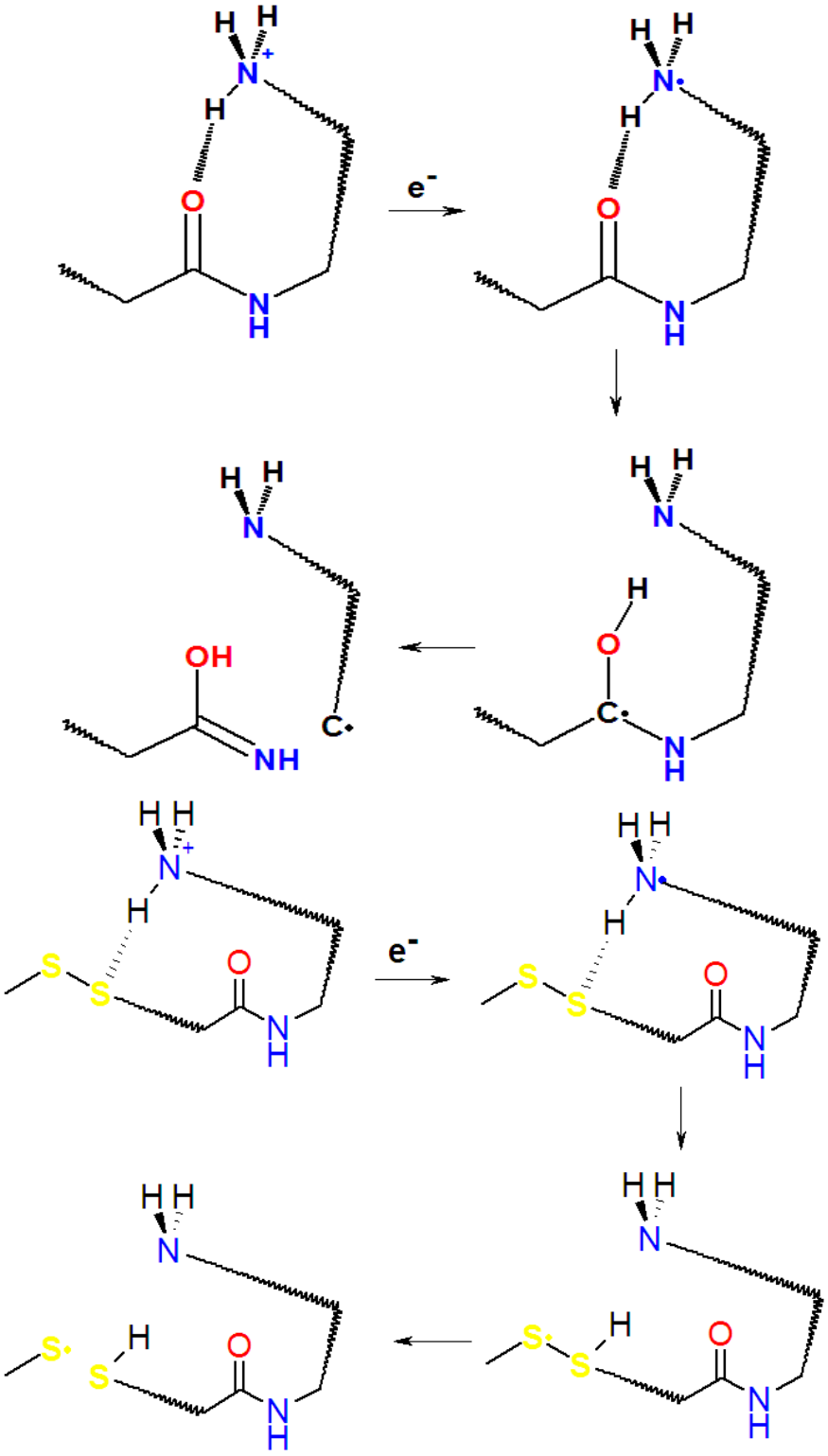

Figure 1.7: Cornell mechanism of peptide ECD

The Cornell mechanism of peptide ECD [92]. **Upper:** S-S cleavage resulting in RS˙ and HSR′ ions. **Lower:** N-Cα bond cleavage resulting in *c* and *z*˙ ions.

ion attachment [101] or fixed charge derivatives [102]. A further limitation is that hydrogen atom transfer from an arginine radical to an amide carbonyl is an endothermic process [95].

1.4.2.2 Utah-Washington mechanism

The Utah-Washington (UW) mechanism (shown in **Figure 1.8**) is focused on charge remote capture and was developed independently by Simons and co-workers [95] and Tureček and co-workers [96] in 2005. The UW mechanism differs from the Cornell mechanism by suggesting that electron capture takes place directly (Utah mechanism) into a Coulomb stabilised S-S σ* or amide π* orbital to cleave the disulfide bond or to form a delocalised $–C^{\bullet}(O^{-})NH–$ radical anion resulting in N-Cα bond cleavage, again forming *c* and $z^{\bullet}$ ions. The suggestion that the low-energy electrons are captured directly into these orbitals is counterintuitive, with work previously showing that these processes are endothermic with 1.04 eV (S-S σ*) [103] and 2.5 eV (amide π*) [104] required for attachment; however, it was proposed that these energies may be lowered by their Coulomb interactions with positively charge groups, rendering electron attachment exothermic. Indeed computational calculations show that electron attachment to Coulomb stabilised amide π* orbital makes the amide group an exceptionally strong base with a proton affinity in the range of 1100-1400 kJ mol^{-1} [95, 96]. The superbasic amide group is then able to undergo proton abstraction in an energetically favourable process *via* conformational change (Washington mechanism). This proton abstraction has been hypothesised to occur following N-Cα cleavage due to spectroscopic analysis on the structure of *c*-type fragments showing them to have an amide structure, not the enol-imine [105]; however, it should be noted that the energetically favoured amide structure may be a product of isomerisation of the initially-formed enol-imine.

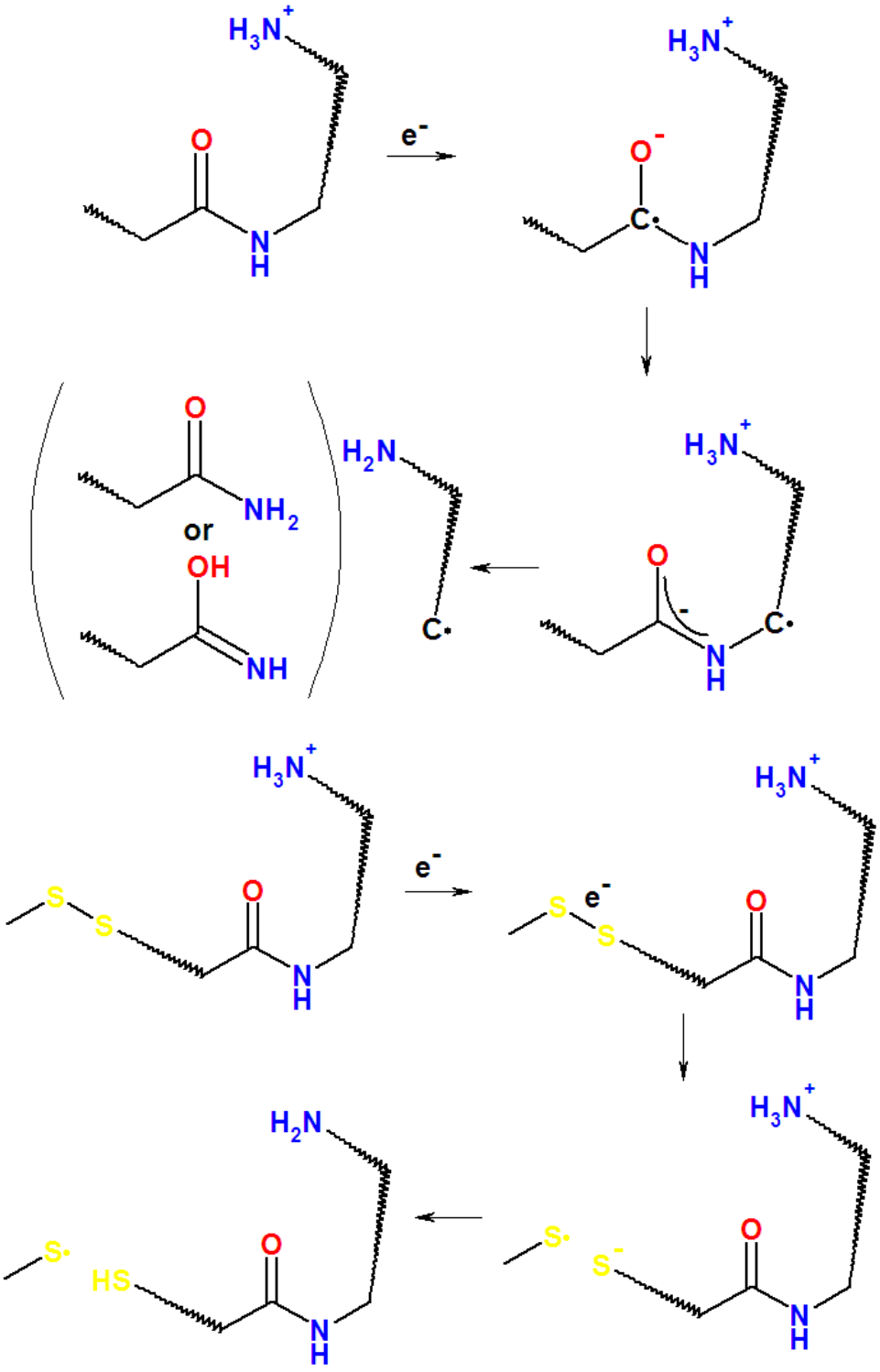

Figure 1.8: Utah-Washington mechanism of peptide ECD

Upper: S-S cleavage resulting in RS$^{\bullet}$ and HSR′ ions. **Lower:** N-Cα bond cleavage resulting in *c* and *z*$^{\bullet}$ ions. Note that the *c* ion formed may have either an enol-imine or an amide structure. [95, 96].

The Washington mechanism suggests that initial electron capture occurs at a charge site; however, unlike the Cornell mechanism, the Washington mechanism proposes that electron transfer occurs before the ground Rydberg level is reached and is transferred into a Coulomb stabilised S-S σ* or amide π* orbital. The Utah mechanism proposes that capture takes place directly into a Coulomb stabilised orbital leading to peptide fragmentation and in recent theoretical studies have shown that in 1-10 % of attachment events this occurs; however, this is a minor fraction when compared to electron capture at a protonation site (90-99 %) [98]. As such a high proportion of electron capture occurs at protonation sites, studies have been undertaken by Simons and co-workers investigating through-space and through-bond electron transfer [106, 107]. These findings have shown that electrons can undergo through-bond transfer up to ~15 Å (~5 intervening bonds) to a site of fragmentation, although transfer may occur to other protonation sites before further transfer. These show that gas-phase peptide conformation is very important when considering ECD fragmentation behaviour.

Unlike the Cornell mechanism, the UW mechanism does not require mobile hydrogen atoms or nonergodicity of dissociation, and allows explanation of ECD of multiply cationised ions where the charge carriers are metals ions or fixed charge peptides by ion-dipole interactions and the intramolecular electron transfer between the charge-stabilised π* orbital and the N-Cα σ* orbital [108]. Following its proposal, there have been many theoretical and experimental investigations supporting the UW mechanism [105, 109].

1.4.2.3 Other fragmentation pathways

These two mechanisms only cover the most common forms of peptide and protein ECD, *i.e.* S-S and N-Cα cleavage, and there have been many other minor fragmentation pathways and mechanisms proposed. One such fragmentation pathway was identified very early on after the development of ECD with $a^{\bullet}$ and *y* fragments being frequently identified in peptide ECD mass spectra [94]. It was speculated that $a^{\bullet}/y$ formation occurs *via* a variation of the Cornell mechanism, but rather than hydrogen atom transfer to an amide oxygen, hydrogen atom transfer to a backbone nitrogen occurs and is followed by heterolytic cleavage of the peptide bond with concomitant loss of CO [94]. Although the formation of $a^{\bullet}/y$ fragments following ECD tend to be minor, they have been shown to be the major fragments when analysing certain peptidic structures, *e.g.* ε-peptides [110] and β-peptides [111].

These ECD mechanisms focus primarily on peptide backbone cleavage although this is not always the case. In 2002, Cooper *et al*. [112] presented a report into neutral losses from amino acid side chains following ECD. Depending on the peptide being analysed, these neutral losses, *i.e.* small non-charged species, *e.g.* ammonia and water, may be very intense. The identification of neutral losses following ECD has proved to be of high interest in the field of radical-based chemistry as it has been shown to provide an insight into the similarities and differences between hydrogen abundant radical reactions (as with ECD) and hydrogen deficient radical reactions [113].

1.4.2.4 Oslo mechanism

The first major report of *b* ion formation following ECD was undertaken by Cooper in 2005 [114] – following earlier work where *b* ions were identified when looking at secondary fragmentation of linear peptides [79] – with the conclusion that the presence of *b* ions in ECD spectra is dependent on both the charge carrier and peptide structure. It was also shown that *b* ions are not formed as a secondary dissociation of *c* ions, and thus must be formed as a primary fragmentation pathway, with the postulation that following electron capture and eventual hydrogen atom loss the precursor peptide ion would result in a vibrationally-excited even-electron ion which could dissociate *via* a mobile proton pathway, as with CID [114]. A separate mechanism, termed the Oslo mechanism in a paper by the thesis author [115] and will be referred to as such, was first theorised in 2004 with the suggestion that $[CH_3\text{-}C(O)\text{-}^{+}NH_2\text{-}CH_3]^{\bullet}$, a nitrogen-protonated radical peptide, "breaks up to give *b* and *y* fragments rather than *c* and *z* fragments" [116]. These data suggest that it is the presence of a protonated backbone nitrogen which is necessary for *b* and *y* ion formation.

The Oslo mechanism has since been validated experimentally by Håkansson and co-workers with work focusing on ECD of peptides which did not contain basic amino acid residues [117]. These peptides, when protonated, must contain protonated amide nitrogens and it was indeed found that when ECD was completed, abundant *b* ions were observed; however, neither Cooper's [114] or Håkansson's [117] work identified any radical *b* ions, which the Olso mechanism has predicted. Although it could be postulated that following $b^{\bullet}$ formation, hydrogen atom transfer may occur similar to that of $c/z^{\bullet}$ ions which would explain the contradictions in these theoretical and experimental findings.

1.4.2.5 Electron predator and hydrogen trap mechanisms

Recently, it has been shown that the electron affinity (EA) of the species under investigation may also affect ECD behaviour, leading to a decrease in peptide backbone cleavage and the abundance of abundant neutral loss species [108]. None of the unmodified proteinogenic amino acids have a positive electron affinity and thus it was hypothesised that ECD of peptides containing modifications with high EAs may behave in an irregular way. Indeed it was shown that benzyl modifications of cysteine with an EA of ≥ 1.00 eV, specifically 3-nitrobenzylcysteine (EA of 1.00 eV [118]) and 3,5-dinitrobenzylcysteine (EA of 1.65 eV [119]), which were termed 'electron predators', inhibit peptide backbone cleavage by ECD and the related electron-transfer dissociation (see **section 1.4.3**) completely [108]. It was found that identical rates of electron capture were observed for doubly-charged peptides containing modifications with varying EA, thus suggesting that initial electron capture is governed by long-range interactions, *i.e.* the electron is captured to high-*n* Rydberg states, as proposed by Zubarev *et al*. [1]. If this was not the case then modifications with a large EA would be expected to have a greater rate of electron capture than others. Once captured, electron relaxation *via* through-space or through-bond transfer to the high EA modification occurs in competition with transfer to the amide π* orbital (UW mechanism). Like the superbasic amide group formed during the UW mechanism, the radical anions formed by the electron predator have high proton affinities thus enabling proton transfer from a site of protonation. The result of proton abstraction is a stable radical intermediate, which does not undergo N-Cα cleavage to produce $c/z^{\bullet}$ ions. This fragmentation pathway is now termed the electron predator mechanism.

Since these observations Tureček [120] completed a more extensive study investigating a wider range of modifications with EA ≥1.00 eV and noted that the electron affinity is not the only criterion for ECD backbone fragmentation sequestion to occur, but any modifications must also act as a hydrogen trap. The hydrogen trap mechanism proposes that following initial electron capture and transfer to the charge-stabilised N-C_O π* orbital (UW mechanism), whereas the electron predator mechanism suggests direct electron transfer to the electron withdrawing group (EWG), proton transfer to the amide group occurs resulting in an aminoketyl radical intermediate. Finally, hydrogen-atom transfer to the EWG takes place inhibiting typical N-Cα fragmentation. The hydrogen trap mechanism explains why pentafluorobenzyl, which has a sufficiently high EA, does not inhibit backbone fragmentation: The side-chain is bound by σ-bond substitution, thus lowering its H-atom trap efficiency.

1.4.3 Electron transfer dissociation

ECD is essentially limited to FT-ICR mass spectrometry, due to the requirement to trap electrons, with the attendant cost implications. ECD experiments have been performed on other mass analysers, but the data are characterised by lower ECD efficiency and poor quality mass spectra [121-123].

In response to this challenge an ion-ion analogue of ECD, electron transfer dissociation (ETD), was developed by Syka *et al*. in 2004 [2]. In ETD, the electron(s) are transferred to the analyte cation following collision with a radical anion, *e.g.* anthracene, fluoranthene [124]. The resultant fragmentation pathways are similar to that observed in ECD, *i.e.*, formation of *c*

and $z^{\bullet}$ ions. A comparison between the two ECD and ETD can be seen in **Figure 1.9**. ETD has been demonstrated on a range of mass analysers [125-127] but is most commonly performed on ion trap mass spectrometers. Consequently, ETD may be carried out on a shorter timescale and at higher sensitivity than ECD. ETD is now widely utilised in hybrid instruments in which fragmentation can take place in the ion trap followed by analysis in a high accuracy mass analyser. This configuration is shown in **Figure 1.5**, in which an ion source is situated in the rear of the instrument in which, for ETD, the reagent is heated to a vapour phase. Once vapourised the gaseous reagent undergoes electron ionisation resulting in a radical cation, which is transferred through the instrument to the ion trap for ETD to take place.

The efficiency of electron transfer is greater than electron capture [2]; however, the fragmentation efficiency is lower in ETD than for ECD. This lower fragmentation efficiency has been explored in theoretical studies in which is shown that free electrons, used in ECD, are able to be attached to the ground or any excited Rydberg state, whereas an ETD electron is unable to access as high Rydberg orbitals as the anion donor's electron binding energy must be overcome during the transfer process [98, 128]. This lower energy state following electron transfer results in the retention of noncovalent bonds and hence lower fragmentation efficiency is observed. To overcome this issue collisional activation of the non-dissociated products from electron transfer, *i.e.* ETnoD (electron transfer with no dissociation) products, has been developed, a technique termed supplemental activation ETD (saETD). It has been shown that a 26.4 % increase in median peptide sequence coverage is observed when applying saETD (88.9 %) in place of ETD (62.5 %) [129]. More recently, AI ETD has also been introduced, which, as with AI ECD, uses an infrared laser to activate the ion as ETD is

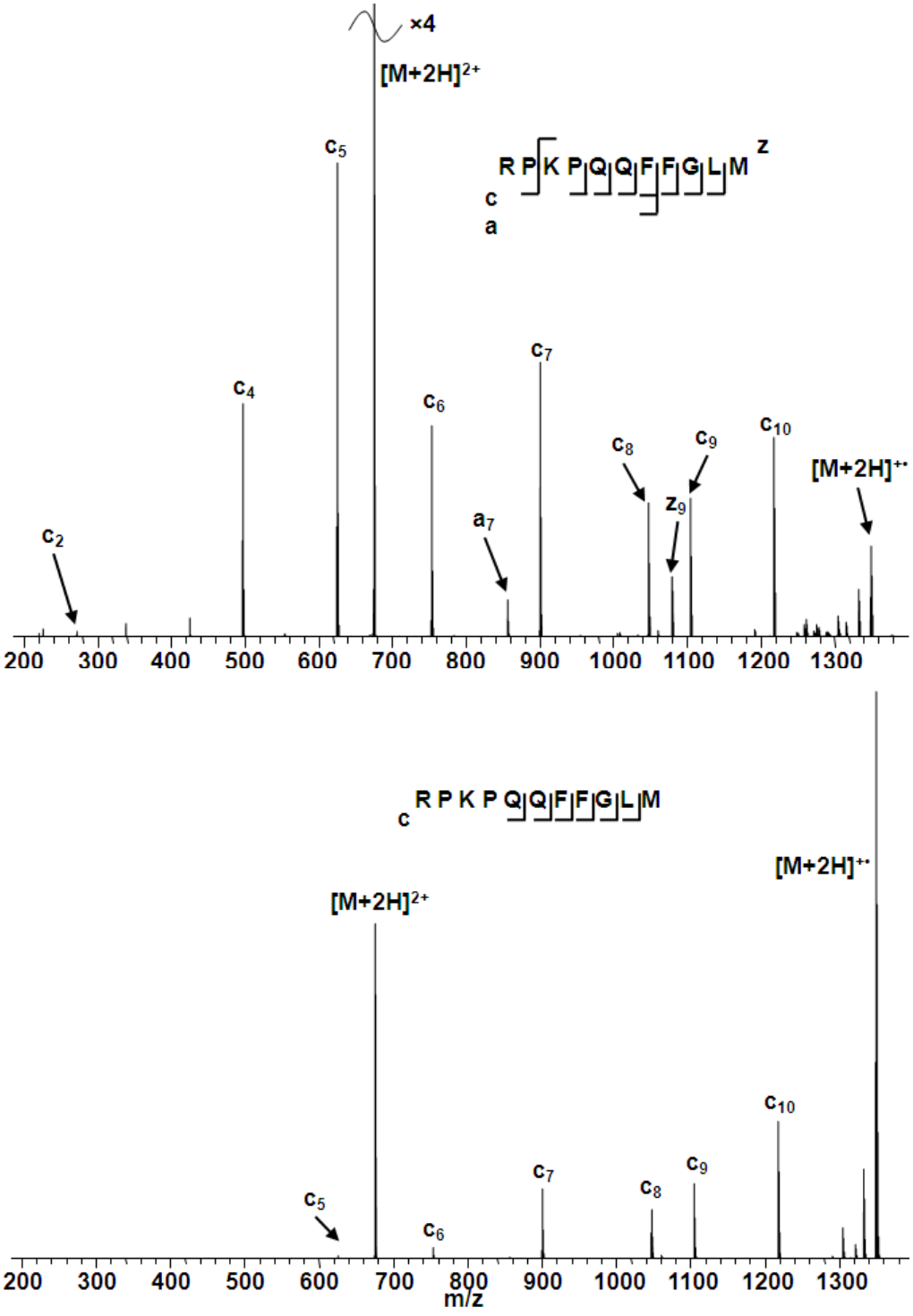

Figure 1.9: ECD and ETD mass spectra of a doubly-charged peptide

The ECD (**Upper**) and ETD (**Lower**) mass spectra of the doubly-charged peptide $[RPKPQQFFGLM + 2H]^{2+}$ (Substance P).

simultaneously taking place and has been used to reduce the presence, and inherent problem, of noncovalent bonds [130].

1.5 Proteomics by mass spectrometry

Mass spectrometry-based proteomics can be achieved *via* a 'bottom-up' or 'top-down' approach. The bottom-up approach typically involves proteolytic digestion, *e.g.* trypsin, of the protein(s) followed by MS/MS analysis of the resulting peptides. Rather than analysing all peptides together bottom-up analyses tend to include an initial separation stage, such as high-performance liquid chromatography (HPLC), prior to mass analysis. The peptide fragment ions following MS/MS provide sequence information which can be searched against protein databases thus enabling protein identification. To complete this identification algorithms are employed to match the measured peptide MS/MS spectrum with those calculated from *in silico* digests of known proteins contained in the database. The peptide assignment is scored according to the similarity between the experimental data and the theoretical mass spectrum. Commonly used search algorithms are Mascot [131] and OMSSA [132].

1.5.1 MS/MS technique complementarity

Several groups have undertaken comparisons of CID and ECD or ETD which have demonstrated their complementary nature. In one such comparison Creese and Cooper [133] showed that CID results in greater overall protein coverage while ECD gives greater peptide sequence coverage. These results suggested that CID is most appropriate for protein identification whereas ECD is best utilised for protein characterisation. These observations can be explained by the faster timescale of CID analysis (being completed in the ion trap)

leading to a greater number of identified peptides; whereas ECD fragments a specific peptide in a greater number of backbone sites, leading to more confident identifications.

In a 2007 study, Coon and co-workers compared CID with ETD and found a relatively small overlap (~12 %) in peptide identifications by the two techniques [134]. Regardless of peptide *m*/*z* CID outperformed ETD for 2+ ions, whereas for charge states of >2+, ETD outperformed CID at lower *m*/*z* with the reverse true at higher *m*/*z*. This *m*/*z* cut-off increased with charge state, *i.e.* an increase in charge state led to ETD identifying a greater number of peptides than CID. These observations led to the development of an automated method, termed the decision tree, which, depending on charge and *m*/*z* of the ion, initiates either CID or ETD fragmentation [135].

1.6 Protein post-translational modification

Any protein produced by ribosomes following protein translation is susceptible to covalent modifications, called post-translational modifications (PTMs). It is one of the later steps in protein biosynthesis for many proteins and any number of modifications may take place depending on the type and orientation of the amino acid within. Over 200 types of PTMs have been identified resulting in a wide range of different structures and functions of the proteins [136]. Examples of PTMs include tyrosine and tryptophan nitration, formation of disulfide bonds, nitrosylation of cysteine and tryptophan, and phosphorylation of serine, tyrosine and threonine. As PTMs typically result in a mass change following addition or removal, mass spectrometry and MS/MS has been shown to be highly successful in the identification and localisation of PTMs in both proteins and peptides [76].

Many PTMs undergo reversible binding to enable regulation of biological functions, and therefore tend to be fairly labile, and as discussed in **Section 1.4.1** CID typically leads to dominant loss of the modification. This provides easy detection of certain PTMs; however, it may also limit the successful localisation of the modification. This PTM loss is apparent in **Figure 1.10**, where CID of the phosphorylated peptide leads to dominant loss of H_3PO_4. ECD, as discussed in **Section 1.4.2**, has been highly successful in the identification and localisation of many PTMs, due to the radical mechanism leading to the retention of the modification on the peptide backbone; again shown in **Figure 1.10**. **Table 1.1** lists a range of common PTMs, along with their structures, and their fragmentation behaviour when analysed using CID and ECD. In this thesis, work is focused on the analysis of the PTMs 3-nitrotyrosine, *S*-nitrosylation and phosphoserine, phosphothreonine, and phosphotyrosine, (along with the synthetic modifications carbamidomethylation and carboxymethylation), all of which are discussed below.

1.6.1 Nitration

Nitration of a protein occurs at tyrosine and tryptophan residues. The first positive identification of 3-nitrotyrosine and thus interest in the topic, goes back to the 1960s [137, 138], whereas nitrotryptophan has been a much more recent discovery [139]. 3-nitrotyrosine is generated *in vivo* by the formation of the peroxynitrite anion ($ONOO^-$) in the reaction of the superoxide anion ($O_2^{-\bullet}$) with nitric oxide ($NO^\bullet$) [10-12]. Nitric oxide is produced by the action of nitric oxide synthases, and the superoxide anion is generated following many different types of biochemical reactions, *e.g.* respiration [140, 141]. 3-nitrotyrosine is a by-product of other cellular reactions and is not fundamental for protein function and structure and has been

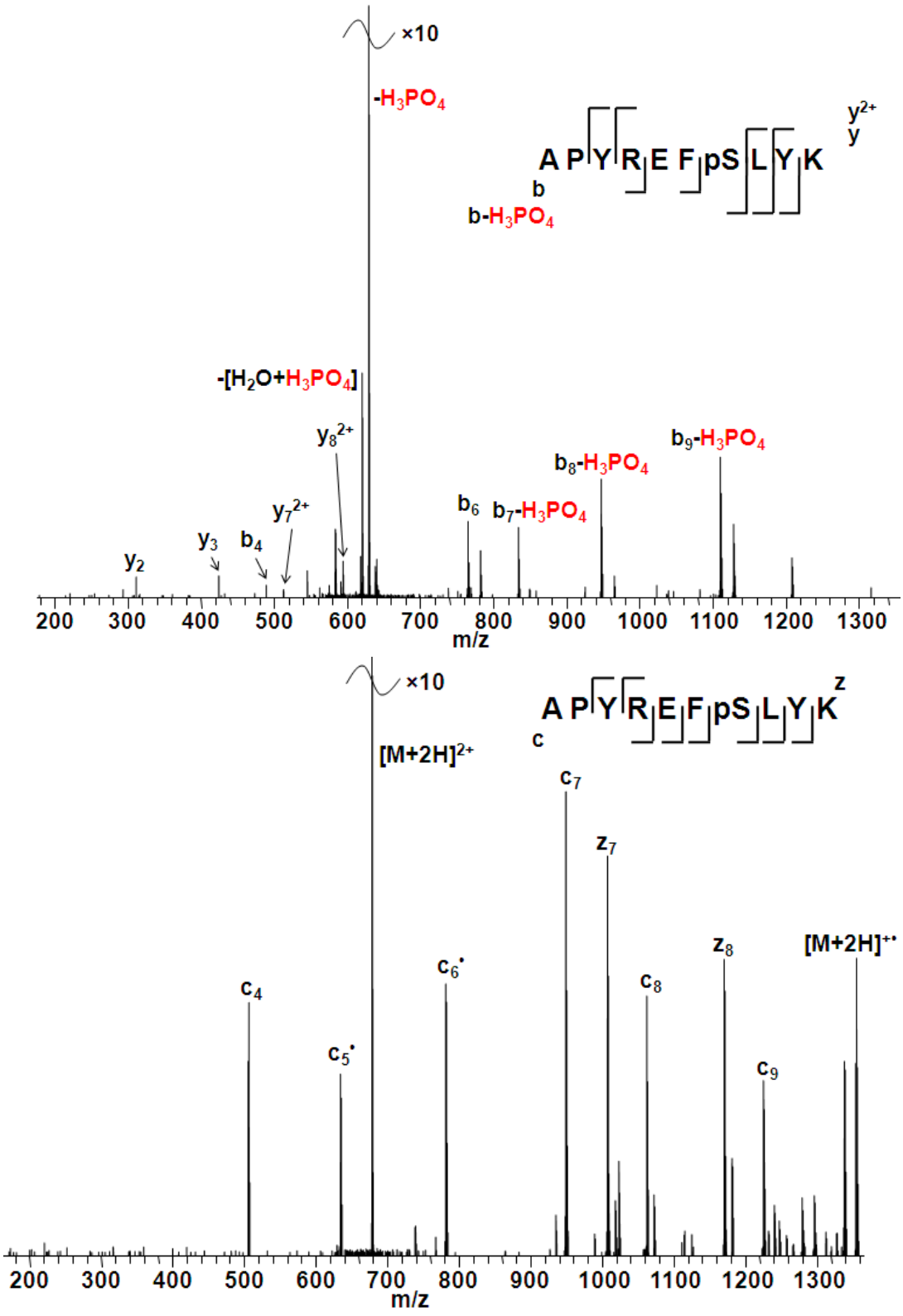

Figure 1.10: CID and ECD mass spectra of a phosphorylated peptide

The CID (**Upper**) and ECD (**Lower**) mass spectra of the doubly-charged phosphopeptide $[APYREFpSLYK + 2H]^{2+}$.

Name	Structure	Retained following CID	Retained following ECD
Acetylation (Lys)		✓	✓
Citrullination (Arg)		✗ (-43 Da)	✓
Cystine (disulfide bond) (Cys)		✓	✗ (Cleavage of S-S bond → Variable)
Glycosylation (N: Asn/Arg) (O: Ser/Thr/Tyr)		✗ (Various internal fragments)	✓
Oxidation (Met)		✗ (-64 Da)	✓
Phosphorylation (Ser/Thr/Tyr)		✗ (-80 Da) (-98 Da)	✓
Sulfonation (Tyr)		✗ (-80 Da)	✓

Table 1.1: Common PTMs and their CID and ECD fragmentation behaviour

Common *in vivo* PTM structures along with their fragmentation behaviour when fragmentation with CID or ECD. Cross represents fragmentation within or adjacent to the PTM limiting backbone sequence coverage, along with the corresponding mass loss, whereas a tick represents retention of the PTM on the peptide backbone fragment ions. A general schematic for N-linked glycosylation is shown although individual structures vary widely.

shown to result in a change in specific protein function [140]. 3-nitrotyrosine has been identified as a possible biomarker for diseases caused by radical species [12, 142, 143], *e.g.* Alzheimer's disease [144], cardiovascular disease [143] and atherothrombotic diseases [145].

The formation of 3-nitrotyrosine has been shown to interfere with tyrosine phosphorylation [146, 147], which itself is fundamental for protein function (as discussed in **Section 1.6.3**). The cause for this interference has been postulated to be due to either the change in pK_a of the phenolic hydroxyl group, due to the presence of the nitro group, or steric hindrance and hence protein structure distortion [142, 148]. Conversely, the presence of tyrosine phosphorylation has also been shown to prevent tyrosine nitration [149], therefore suggesting that nitration and phosphorylation are two competing chemical reactions. Interestingly, it was also identified that the presence of the 3-nitrotyrosine increased the susceptibility of proteolysis, thus being identified as a possible defence mechanism against the consequences of oxidative stress [146]. In addition, it has been shown that the presence of 3-nitrotyrosine can lead to an immune response, potentially leading to autoimmune disease [150].

A recent review by Abello *et al*. [140] discussed the current proteomic strategies utilised for the identification and localisation of 3-nitrotyrosine, with analysis typically completed through either separation and enrichment methods, *e.g.* immunoprecipitation followed by SDS-PAGE and western blot analysis, or mass spectrometric analysis, *e.g.* MALDI and ESI followed by MS/MS techniques. No one technique, however, has proven to be ideal, with one report in 2008 recommending a more stringent manual validation protocol should be followed due to the presence of common chemical artefacts leading to false positive results [151].

1.6.2 Cysteine modifications

Modifications of cysteine are highly variable in both structure and function. As a sulfur-containing amino acid, Cys contains a thiol (-SH) side chain, and due to the variable coordination states of sulfur, a much wider range of possible modifications than many others is available. It is therefore of great interest in finding an efficient and accurate analytical method for identification and comparison of the PTMs which occur. One modification is the formation of a disulfide bond between two cysteine residues. The thiol side chain of the cysteine amino acid is highly susceptible to oxidation from other cysteine residues and is favourable to form disulfide bonds; this serves a significant determinant role in the secondary and tertiary structure of many proteins.

S-nitrosylation is a ubiquitous PTM and is fundamental for protein function and modulation [152]. *S*-nitrosoproteins are formed by the addition of a nitrosyl (NO) group to the sulfur with the loss of a hydrogen atom. The production of NO from arginine, and thus formation of *S*-nitrosoproteins, is regulated by NO synthases. NO synthases are highly conserved enzymes in biology, with mammals containing only three types: NOS1 (or nNOS), NOS2 (or iNOS), and NOS3 (or eNOS) [152]. *S*-nitrosylation itself is an extremely highly labile PTM, with the S-N bond having approximately one-third the strength (20-28 kcal mol^{-1}), in bond dissociation energy, of a S-S bond (70-74 kcal mol^{-1}) [153, 154], and does not require enzymatic action for nitrosylation or denitrosylation to take place; however, recent reports have shown that the production of nitric oxide, and therefore nitrosylation itself is highly regulated within the cell [155].

Current proteomic analysis of *S*-nitrosylation has been recently reviewed by Torta *et al*. [156]. Comparisons between the methods show a great range of potentials to positively identify the PTM; however, all the analytical methods have disadvantages as well as advantages. The biotin switch [157] and SNOSID (SNO Site Identification) [158] methods (which both require the biotinylation of the nitroso group) have high sensitivity but require high amounts of starting material, due to low efficiency. Conversely, MS detection requires little starting material but the modification is easily lost on ionisation, due to the labile nature of the PTM. As such there is currently no one ideal analytical method for the identification and localisation of *S*-nitrosylation.

1.6.3 Phosphorylation

Phosphorylation is one of the most important reversible PTMs. Enzymes catalysed by phosphorylation and dephosphorylation of proteins are key regulatory events in prokaryotes and eukaryotes [9, 159]. Phosphorylation usually occurs on serine, threonine and tyrosine residues, with their prevalence being ~1800:200:1 in vertebrates, respectively [160]. Phosphoregulation in proteins is controlled by a group of enzymes called kinases (phosphorylation) and phosphatases (dephosphorylation).

Many complex processes such as cell cycle, cell growth and metabolism are controlled by reversible phosphorylation events. For example, reversible phosphorylation heavily regulates the p53 tumour suppressor protein, and activation can lead to cell cycle arrest or apoptotic cell death when the cell is damaged [161, 162]. Thus it is of great interest to garner structural

information to gain an insight into the functional role each phosphorylation site may play *in vivo*.

Monoclonal antibodies are commonly used for the detection of phosphorylation sites as they can be produced to be specific for an individual phosphorylated or dephosphorylated protein; however, these tend to be extremely expensive and tend to not be a suitable method for large scale analyses. Mass spectrometry has been shown to be very successful for specific and large scale analyses for the detection and localisation of phosphorylation sites. With the recent developments in ECD and ETD it is now possible to complete an LC-MS/MS analysis using neutral loss CID to identify the presence of the PTM followed by ECD/ETD for localisation [133, 163, 164]. Phosphorylation, being an acidic moiety, has been shown to play an important structural role by forming noncovalent bonds with basic amino acids [165]. These noncovalent bonds have also been shown to also be present in the gas-phase both as inter- [166] and intramolecular bonds [89], leading to issues for CID and ECD mass spectrometry analysis, respectively.

1.7 Quantum mechanical calculations

The current understanding of gas-phase structures and variable electronic states of radical ions is not possible in typical experimental studies, and as such are undertaken with the use of computational studies based on quantum chemistry. These computational studies vary widely in scope and method, with *ab initio* studies being common in the understanding of transition states and ground electronic states, and molecular dynamic simulations being developed for gas-phase structures.

1.7.1 *Ab initio* quantum chemistry methods

Ab initio, *i.e.* from the beginning, studies were first undertaken in 1950, along with the nomenclature, with the calculation of various excited states of benzene [167]. The technique has since developed into meaning "from first principles of quantum mechanics" with studies being completed later in the 1950s [168]. The *ab initio* approach can provide extremely accurate results due to being mathematically rigorous and hence can be completed on experimentally unknown systems, and utilised quantum physics; however, this process is extremely computationally expensive and therefore is only ideal for understanding small systems.

With respect to ECD, both the Utah [95] and Washington [96] mechanisms were proposed with the use of *ab initio* methods. The Utah mechanism utilised the Hartree-Fock (HF) and the Unrestricted Hartree-Fock (UHF) methods, methods of approximation, for the determination of the ground-state energy and electronic states of a variety of peptide bonds resulting in the identification of Coulombic stabilisation playing a pivotal role in radical systems. The Washington mechanism also incorporated density functional theory (DFT) methods to obtain their results. In comparison to the HF and UHF methods, density functional theory (DFT) is traditionally not as accurate as the properties of a system is determined by functions of spatially dependent electron density rather than a mathematical model, but is far less computationally expensive and hence is widely used.

1.7.2 Molecular dynamic simulations

The identification of gas-phase structures, as produced through ionisation methods, is not easily possible using experimental studies, although certain techniques *e.g.* ion-mobility spectrometry and infra-red spectroscopy, have shown great promise. To overcome this issue the use of quantum chemistry for the development of gas-phase ion molecular models has recently been used. Unlike *ab initio* studies, molecular mechanics requires previous experimentally derived data, typically from spectroscopy techniques or from *ab initio* calculations. These data are presented in the form of force-fields, and molecular dynamics can be undertaken of large systems; however, molecular mechanics utilises classical physics, unlike *ab initio* calculations and hence cannot accurately predict electronic states.

A report by Barran and co-workers in 2005 is one such study which used models generated from molecular dynamic simulations for the analysis of how peptide structure affects ECD fragmentation. In their study a range of gonadatropin releasing hormone (GnRH) variants were fragmented *via* ECD and compared to their predicted gas-phase structure. These gas-phase structures were obtained through the use of an AMBER force field, *i.e.* a set of parameters corresponding to the potential energy of a system calculated from the electron densities, bond length and tensional angle of each atom and bond. These structures then underwent simulated annealing and molecular dynamic simulations to ensure a final stable structure was obtained. These predicted structures provided a startling relationship to the ECD behaviour of the peptides with secondary structures which were present, *e.g.* the presence and intensity of $z^{\bullet}$ ions decreased significantly in areas of the peptide where β-turns were present.

Aims and Objectives

The overall aim of this work was to gain a greater insight into the fragmentation mechanism of electron capture dissociation (ECD) mass spectrometry of peptides and proteins. This was undertaken by focusing on the use of ECD for characterisation of a range of posttranslational modifications.

The specific aims of this work are:

- To investigate the effect that nitration has on ECD. 3-nitrotyrosine, a naturally occurring PTM, has a positive electron affinity and has been proposed to inhibit typical ECD peptide backbone fragmentation (see **Chapter 3**). This study was then expanded upon to investigate the abundant neutral losses identified, especially ammonia, following ECD of 3-nitrotyrosine-containing peptides (see **Chapter 4**).
- To investigate the effect that cysteine modifications have on ECD. As ECD predominantly cleaves at disulfide bonds, cysteine modifications were analysed to identify whether these too behave in similar ways. The PTMs investigated were both synthetic (*i.e.* carbamidomethylation and carboxymethylation) (see **Chapter 5**) and biological (*i.e.* nitrosylation) (see **Chapter 6**).
- To investigate the effect that intermolecular salt bridges between phosphorylation and basic amino acid residues have on ECD. ECD of phosphopeptides has previously been shown to be inhibited due to intramolecular salt bridges with protonated arginine residues, and it has been shown that these salt bridges can also occur between two separate peptides in the gas-phase (see **Chapter 7**).

Chapter 2: Materials and Methods

2.1 Materials

2.1.1 General laboratory reagents

4-(2-hydroxyethyl)-1-piperazineethanesulfonic acid (HEPES) (Sigma Aldrich, Dorset, UK)

Acetic anhydride (Sigma Aldrich)

Acetonitrile (J. T. Baker, Deventer, Netherlands)

Ammonium bicarbonate (Fisher Scientific, Leicestershire, UK)

β-glycerophosphate (Sigma Aldrich)

Complete Mini, Protease Inhibitor Cocktail Tablets (Roche Diagnostics, West Sussex, UK)

Coomassie protein assay kit (Fisher Scientific)

Dithiothreitol (DTT) (Sigma Aldrich)

Ethylenediaminetetraacetic acid (EDTA) (Fisher Scientific)

Formic acid (Fisher Scientific)

Iodoacetamide (Sigma Aldrich)

Iodoacetic acid (Sigma Aldrich)

Methanol (J. T. Baker)

Neocuproine (Sigma Aldrich)

Phosphate buffered saline (Oxoid, Cambridge, UK)

Phosphoric acid (Sigma Aldrich)

Potassium chloride (Sigma Aldrich)

Potassium dihydrogen phosphate (Fisons, now Sanofi)

S-nitrosoglutathione (GSNO) (Sigma Aldrich)

Sodium fluoride (Sigma Aldrich)

Sodium orthovanadate (Sigma Aldrich)

Trifluoroacetic acid (TFA) (Sigma Aldrich)

Trizma® hydrochloride (Sigma Aldrich)

Urea (VWR International, Leicestershire, UK)

Water (J. T. Baker)

2.1.2 Peptides

3-nitrotyrosine (indicated by nY) containing synthetic peptides GPLEnYGFAK, GPLEnYGFAR, GPLEnYGFAL, GPLEnYGFAKGPLAK, GPLEnYGFARGPLAR, NYCGLPGEnYWLGNDK, their unmodified counterparts (*i.e.* GPLEYGFAK, GPLEYGFAR, GPLEYGFAL, GPLEYGFAKGPLAK, GPLEYGFARGPLAR, and NYCGLPGEYWLGNDK), AAAAAAAK and an A_xnY_yAK series (where x, y = 0-6, and x + y = 6; *e.g.* AAnYAAAAK), were synthesised by Alta Bioscience (Birmingham, UK). The peptides GPLEnYGFAK-NH_2, GPLEnYGFAR-NH_2 and AAAnYAAAK-NH_2 were synthesised by Bachem (Weil am Rhein, Germany). All peptides were synthesised to >80 % purity with free N-termini.

NYCGLPGEYWLGNDR, NACGAPGEKWAGNDK, NYGLPGCEKWYGNDK, and NYGLPGEKWYGCNDK were synthesised by Alta Bioscience. NYCGLPGEKYLGNDK and NYCGLPGERWLGNDR were synthesised by Bachem.

The peptide VLRRRAVN and the phosphotyrosine (indicated by pY) containing peptide AAApYAAA-NH_2 were synthesised by Alta Bioscience. The phosphoserine (indicated by pS) and phosphothreonine (indicated by pT) containing peptides AAApSAAA-NH_2 and AAApTAAA-NH_2 were synthesised by peptides&elephants GmbH (Nuthetal, Germany).

2.1.3 Proteases

The protease Trypsin Gold, Mass Spectrometry Grade (Promega, Madison, Wisconsin, USA) was used.

2.1.4 Mass spectrometry instrumentation

Analyses were completed on a LTQ FT™, LTQ FT Ultra™ (Thermo Fisher Scientific, Bremen, Germany), a LTQ Orbitrap Velos™ (Thermo Fisher Scientific) and a 12 T Apex Qe Ultra (Bruker, Billerica, Massachusetts, USA) mass spectrometers. In all cases samples were injected by use of a TriVersa NanoMate® electrospray source (Advion Biosciences, Ithaca, New York, USA).

2.2 Methods

2.2.1 Whole cell preparation and lysis

Mouse fibroblast NIH 3T3 cells were cultured at 37 °C, 5 % CO_2 in Dulbecco's modified Eagle's medium (Invitrogen, Renfrewshire, UK) supplemented with 2 mM L-glutamine (Invitrogen), 0.1 mg/mL streptomycin, 0.2 units/mL penicillin (Sigma-Aldrich), and 10 % (v/v) donor bovine serum (Invitrogen). Following serum starvation in medium containing 0.1 % serum for 18 h, cells were treated with 2 mM sodium pervanadate for 20 min prior to lysis. Cells were pelleted by centrifugation at 3300 rpm using a benchtop centrifuge for 5 min at 4 °C. (Above performed by Dr. D. L. Cunningham).

The pellet was washed with phosphate buffered saline prior to addition of 1 ml of ice-cold lysis buffer (17 mM HEPES, pH 8, 7.65 M urea, 1mM sodium orthovanadate, 50 mM sodium fluoride, 25 mM β-glycerophosphate, and one tablet of Complete Mini for every 10 mL of buffer). The cells were lysed by sonication on ice. Lysates were subsequently cleared by centrifugation at 14000 × *g* for 10 min at 4 °C. Total protein concentrations of the cleared lysates were then determined by Coomassie (Bradford) protein assay kit according to the manufacturer's instructions.

2.2.2 Manual nitration of myoglobin (performed by Dr. J. Iniesta)

Equine skeletal myoglobin (Sigma Aldrich) was electrochemically nitrated in a water-cooled cell at 284 ± 2 K, with the potential fixed at 1.05 V versus Ag/AgCl/Cl^- (3 M) using a 2053 potentiostat (Amel Instruments, Milan, Italy). The cathodic compartment was a 5 mm

diameter cylindrical chamber separated from the anodic compartment by a nonselective sintered glass membrane. A 0.5 mm diameter, ≥99.995 % purity platinum wire (Goodfellow, Cambridgeshire, UK) was used as the counter electrode. The cathodic compartment was filled with 1 mL of buffer solution comprising 50 mM $Na_2B_4O_7.10H_2O$ and 50 mM $NaNO_2$ adjusted to pH 9.0 with H_3BO_3. A 0.1 × 2.5 × 5.0 cm bipolar boron-doped diamond working electrode was pretreated by cycling the electrode between 0 and 4 V versus Ag/AgCl, 0.1 V/s, 10 cycles, in 1 M nitric acid, and thereafter electrodes were thoroughly rinsed with ultrapure water. Buffer solution (50 mL) contained 1 mg/mL of protein. Sodium nitrite concentration was 50 mM. Electrosynthetic nitration was monitored with an electronic A.h coulometer (Digatron, Aachen, Germany) by measuring the charge passed through the circuit. The nitration was expected to take place at Tyr103 [169]. The reaction mixture was extensively dialyzed against 10 mM ammonium acetate, pH 6.0, using Spectra/Por® (Spectrum Laboratories, Rancho Dominguez, California, USA) molecular porous membrane tubing with 3500 Da cut-off. Samples were subsequently freeze-dried and stored at -20 °C.

^{15}N-isotopic 3-nitrotyrosine labelling was completed by the above procedure with the exception that >98 % ^{15}N labelled sodium nitrate was used.

2.2.3 Reduction and carbamidomethylation/carboxymethylation

Samples were suspended in 50 mM ammonium bicarbonate and reduced for 30 min at 50 °C in the presence of 8 mM dithiothreitol and alkylated with 20 mM iodoacetamide (carbamidomethylation) or iodoacetic acid (caboxymethylation) for 30 min at room temperature in the dark.

2.2.4 Enzymatic digestion

Reduced and alkylated samples were suspended in 50 mM ammonium bicarbonate and 10 % acetonitrile, and digested by the addition of 1:50 (enzyme:protein) (w/w) trypsin and incubated overnight at 37 °C. The digestion was quenched by adding 0.5 % (v/v) formic acid. Acetonitrile was removed by vacuum centrifugation in a Concentrator plus (Eppendorf, Hamburg, Germany).

2.2.5 Desalting of samples

Digested proteins were desalted by the use of a C_8 MacroTrap^{TM} cartridge (Michrom, Auburn, California, USA). The trap cartridge was prepared by washing with 200 µl acetonitrile and water (50:50), and 200 µl formic acid (0.1 %). The sample (200 µg) was loaded, washed with 500 µl formic acid (0.1 %), and eluted in 200 µl acetonitrile, water and formic acid (70:29.9:0.1).

2.2.6 Strong cation exchange (SCX) chromatography

1 mg desalted trypsinised peptides was resuspended in 100 µl of mobile phase A (5 mM potassium dihydrogen phosphate, 25 % (v/v) acetonitrile, pH 3 with phosphoric acid) and loaded onto a 100 × 2.1 mm polysulfoethyl aspartamide column (5 µm particle size, 20 nm pore size) (PolyLC, Columbia, Maryland, USA) at a flow rate of 200 µl min^{-1}. Separation used a gradient elution profile that started with 100 % mobile phase A, increased from 0 to 30 % mobile phase B (5 mM potassium dihydrogen phosphate, 25 % (v/v) acetonitrile, 250 mM potassium chloride, pH 3 with phosphoric acid) over 30 min, increased to 50 % mobile phase

B over 5 min, and then returned to 100 % mobile phase A. 750 µl fractions were collected throughout the run.

2.2.7 Selective N-terminus acetylation

Selective N-terminus acetylation was completed by incubating 1:1 acetic anhydride:peptide in 100 mM ammonium bicarbonate overnight at 37 °C. Modified peptides were then desalted.

2.2.8 Nitrosylation of cysteine

Cysteine containing peptides were dissolved in 20 mM Trizma® hydrochloride (pH 7.6), 1 mM EDTA and 0.1 mM neocuproine for a final concentration of 1 mg/ml. 10 µl *S*-nitrosoglutathione (GSNO) was added to 90 µl of this peptide/protein buffer solution (concentration of GSNO was dependent on cysteine concentration of peptide/protein, *e.g.* for 1:10 (cysteine:total number of amino acids) 1 mM GSNO would be used, for 1:5 2 mM GSNO would be used), and stored for 30 min at 37 °C.

2.2.9 Synthetic peptide preparation

All synthetic peptides were used without further purification and diluted to 2 pmol/µl in 49.5:49.5 % methanol:water, and 1 % formic acid for analysis.

2.2.10 Direct infusion electrospray ionisation

Samples were resuspended in methanol, water and formic acid (49.5:49.5:1) for a final concentration of ~2 pmol/µl. The TriVersa NanoMate® was set to collect 10 µl of sample and spray with a gas pressure of 0.3 psi and an applied voltage of 1.7 kV at a flow rate of ~200 nl/min. All MS/MS spectra were acquired at a resolution of 100 000 (unless stated) and comprise of 30 scans each comprising of 4 co-added microscans.

2.2.10.1 Collision induced dissociation mass spectrometry

CID experiments were performed in the linear ion trap and the fragments were transferred to the ICR cell (LTQ FT Ultra™) or orbitrap (LTQ Orbitrap Velos™) for detection. Automatic gain control (AGC) target was 2×10^5, maximum fill time 1 s. Isolation width was *m*/*z* 5. Unless stated, CID experiments were performed with helium gas at normalised collision energy 35 %. The normalised collision energy is a measure of the voltage applied to the endcaps which itself is scaled depending on the parent mass prior to fragmentation.

2.2.10.2 Electron capture dissociation mass spectrometry

ECD was completed on a LTQ FT Ultra™. Precursor ions were isolated in the linear ion trap and transferred to the ICR cell for ECD. AGC target was 2×10^5 with maximum fill time 1 s. Isolation width was *m*/*z* 5. Electrons for ECD were produced by an indirectly heated barium-tungsten cylindrical dispenser cathode (5.1 mm diameter, 154 mm from the cell, 1 mm off axis) (HeatWave Labs, Watsonville, California, USA). The current across the electrode was ~0.9 A. Ions were irradiated with electrons for 70 ms at 5 % energy (corresponding to a cathode potential of between -2.225 V and -3.238 V). Hot ECD was undertaken by increasing

the cathode potential to -32 V. This cathode potential is the value set by the instrument for the optimal fragmentation of Substance P and changes when the ECD is calibrated, hence the variation seen throughout this work.

2.2.10.3 Activated ion electron capture dissociation mass spectrometry

Photons for infrared irradiation were provided by a 75 W in-built CO_2 laser (Synrad, Milkilteco, Washington, USA) for 100 ms and measured as a percent of the maximum (*i.e.*, 75 W). The exact laser power used was varied according to the analyte and its associated infra-red multiphoton dissociation (IRMPD) threshold (*i.e.*, the energy at which *b* and *y* fragment ions form). Infrared irradiation was followed by ECD with a delay. This delay initially was 85 ms, as this was found by Mikhailov and Cooper to be the period of magnetron motion [170]; however, following an instrument upgrade resulting in an increase in ICR cell volume and a later change in trapping voltages the magnetron motion varied.

2.2.10.4 Electron transfer dissociation mass spectrometry

ETD was completed on a LTQ Orbitrap Velos^{TM}. Precursor ions were isolated in the linear ion trap and subjected to ETD before being transferred to the orbitrap for analysis. AGC target was 2×10^5 with maximum fill time of 1 s. Isolation width was *m*/*z* 5. Fluoranthene was heated to 180 °C and transferred to the ion trap for ETD and exposed to the ions for 100 ms. Supplemental activation ETD (saETD) was completed with helium gas at normalised collision energy 25 %.

2.2.10.5 MS^3 (IRMPD of ECD fragments)

Analyses were performed on a Bruker 12 T Apex Qe Ultra. Precursor ions were isolated by use of the mass resolving quadrupole. For ECD, 1.8 A was applied to the dispenser cathode filament (HeatWave Technologies), 20 V to the lens, 0.8 V to the bias, and a pulse of 70 ms was applied. For MS^3, ions were isolated in the ICR cell via correlated sweep excitation (COSE) and exposed to a 25 W CO_2 laser (Synrad, Mukilteo, Washington, USA) at 70 % power for 100 ms. Mass spectra are the sum of 300 acquisitions.

2.2.11 Reversed phase liquid chromatography

Peptides were loaded onto a 75 μm (internal diameter) IntegraFrit™ (New Objective, Woburn, Massachusetts, USA) C_8 resolving column (10 cm length) and separated over a 40 min gradient from 0 to 40 % acetonitrile. Peptides eluted directly (~350 nl/min) via a TriVersa NanoMate® source into a LTQ FT where they were subjected to data-dependent CID and ECD.

The mass spectrometer alternated between a full FT-MS scan (*m*/*z* 400-1600) and subsequent CID and ECD MS/MS scans of the most abundant ion above a threshold of 40000. Survey scans were acquired in the ICR cell with a resolution of 100000 at *m*/*z* 400. Precursor ions were isolated and subjected to CID in the linear ion trap with the completion of the full FT-MS scan. The width of the precursor isolation window was *m*/*z* 6. Only multiply charged precursor ions were selected for MS/MS. CID was performed with helium gas at a normalized collision energy of 35 %. Automated gain control was used to accumulate sufficient precursor ions (target value was 5×10^4, maximum fill time 0.2 s). Precursor ions were activated for 30

ms. For ECD precursor ions were isolated in the ion trap and transferred to the ICR cell. Isolation width was *m*/*z* 6. Automated gain control was used (target value was 1×10^6, maximum fill time 1 s). Each ECD scan comprised four co-added microscans acquired with a resolution of 25000 at *m*/*z* 400.

2.2.12 Data analysis

2.2.12.1 Direct infusion

Spectra collected from the LTQ FT Ultra™ or LTQ Orbitrap Velos™ mass spectrometers were analysed using Xcalibur® software (Thermo Fisher Scientific). Spectra collected from the 12 T Apex Qe Ultra were analysed using DataAnalysis 4.0 software (Bruker Daltonics). All mass spectra were manually searched for all theoretical fragment ions using ProteinProspector software (UCSF, San Francisco, California, USA). All positive peak assignments were identified with less than ±10 ppm mass error.

2.2.12.2 Liquid chromatography

DTA files were created from the raw data using Bioworks 3.3.1 (Thermo Fisher Scientific). The OMSSA Browser 2.1.1 and Mascot 2.2 (Matrix Science, London, UK) were used to search the DTA files against a concatenated database consisting of the mouse International Protein Index (IPI) database (version 3.40) supplemented with common contaminants (including keratins, trypsin and bovine serum albumin). CID and ECD were searched separately, resulting in two database searches per experiment. Pre-search prefiltering was completed using adapted perl scripts (Appendix 1) taken from Sweet *et al* [171], in which three regions of each CID and ECD mass spectrum was removed: a prominent noise peak (*m*/*z*

101.7-102.1), the isolation window around the precursor ion (*m*/*z* ±3), and any fragments which may constitute a neutral loss from the charge reduced precursor up to 57, 60 or 91 Da (with the exceptions of any peak which may be a real fragmentation, *e.g.* loss of Gly (58.03 Da)).

OMSSA searches were completed for CID using the following parameters: peptide *m*/*z* tolerance ±0.02; MS/MS *m*/*z* tolerance ±0.8; 2 miscleavages allowed; maximum number of variable modifications per peptide, 32; fixed modification, Cys-carbamidomethylation; variable modifications, protein N-terminus-acetylation, Met-oxidation; product ion types to search, *b* and *y*; precursor search type, monoisotopic; product search type, monoisotopic; E-value cutoff, 50; lower bound of precursor charge, 2; upper bound of precursor charge 6; charge at which to start considering multiply charged products, 3. For ECD, the parameters remained the same with the following exceptions: peptide *m*/*z* tolerance, ±1.1; MS/MS *m*/*z* tolerance, ±0.02; product ion types to search, *c*, *y* and *z*. The variation in peptide tolerance for CID and ECD has been optimised to ensure that a low false positive rate is encountered and this is necessitated by the variation in product ion tolerance, which itself is due to the difference in mass analyser [163].

Mascot searches were completed for CID using the following parameters: peptide *m*/*z* tolerance, ±1.1 Da; MS/MS *m*/*z* tolerance ±0.5 Da; 2 miscleavages allowed; instrument, ESI-TRAP; fixed modification, Cys-carbamidomethylation; variable modifications, protein N-terminus-acetylation, Met-oxidation. For ECD, the parameters remained the same the following exceptions: MS/MS *m*/*z* tolerance, ±0.02; instrument, FTMS-ECD.

Output from the Mascot and OMSSA searches were further scrutinised by manual post-search filtering to ensure that each DTA resulted in only the top peptide, with respect to the Peptide Score (Mascot) or E-value (OMSSA), followed by removing all identifications with a ppm error of >8.79 or <-0.44 (Mascot) and >8.37 or <-1.99 (OMSSA) to ensure that, within this ppm window, all remaining peptides have a false discovery (FD) rate of ≤1 %. This FD rate was confirmed by the presence of the concatenated database sequence, thus if any search resulted in a positive identification of a concatenated peptide sequence it is believed to be a false positive (this ppm window ensured that, at most, 1 % of all identified peptides were a concatenated peptide).

2.2.13 Molecular modelling

All simulations were performed using AMBER 10 and the ff99SB-ILDN forcefield. The 3-nitrotyrosine and *S*-nitrosylation amino acid residues were added manually using previously calculated parameters [172, 173]. Peptides underwent 500 cycles of steepest descent and conjugated gradient minimisation followed by heating in a stepwise from 0 K to 325 K. Each heating step consisted of 10 000 steps of 0.5 fs each (nstlim=10 000, dt=0.0005) using a Langevin thermostat (ntt=3, gamma ln=1.0) with no interacting solvent (igb=0). The production simulation was at 325 K for a total of 500 ns (100 stages of 5 ns containing 2 500 000 steps of 2 fs each), again using a Langevin thermostat with no interacting solvent.

Clustering of the peptide structures obtained in 100 ns windows was completed using kclust (a k-means algorithm implemented in the MMTSB tool set [174]), with clusters being centred upon a 3 Å radii of the heavy atoms. The most representative structure, *i.e.* that with the

lowest rmsd from the average structure for the cluster, found within the top, *i.e.* most abundant, cluster was then identified. The most representative structures from each 100 ns window were then compared with each other using the RMSD calculator extension in visual molecular dynamics (VMD) to ensure that the final structure at 500 ns was fully converged. The surface accessibility of atoms and residues was calculated using a spherical probe of radius of 1.4 Å using naccess and atom-to-atom distances were calculated using VMD.

Chapter 3: Electron Capture Dissociation Mass Spectrometry of Nitrated Peptides*

3.1 Introduction

Protein tyrosine nitration is a marker of nitrative stress [140], and is of great interest because it may be used as a diagnostic biomarker for diseases caused by radical species [12, 142, 175]. Examples include cardiovascular disease [143], Alzheimer's disease [144] and atherothrombotic diseases [145]. Peroxynitrite anions ($ONOO^-$), formed in the reaction of superoxide radical anions and nitric oxide radicals, or other nitrating agents, *e.g.* $^{\bullet}NO_2$ radicals, react with tyrosine to produce the 3-nitrotyrosine modification [10-12]. Mass spectrometry approaches for the study of protein tyrosine nitration have been reviewed recently [140] with most studies utilising MALDI-TOF-MS and a few utilising ESI-MS/MS approaches, specifically employing CID.

ECD offers some advantages over other MS/MS techniques, such as CID, for the analysis of peptides and proteins. One benefit is the tendency of backbone fragments to retain labile PTMs [3]; however, studies have not been exhaustive and it has been shown that the analysis of modifications with high electron affinities result in atypical ECD behaviour. In work undertaken by Sohn *et al*. [108] ECD of peptides with nitro-containing benzyl modifications which have an electron affinity (EA) of ≥1.00 eV were considered. Examples included 3-nitrobenzylcysteine (EA=1.00 eV [118]) and 3,5-dinitrobenzylcysteine (EA=1.65 eV [119]), termed 'electron predators'. ECD and ETD of these species resulted in a complete inhibition

*Work presented in this chapter has been published as:
Jones, A.W., Mikhailov, V.A., Iniesta, J. and Cooper, H.J., *Electron capture dissociation mass spectrometry of tyrosine nitrated peptides*. J. Am. Soc. Mass Spectrom., 2010. **21**: p. 268-277

of peptide backbone cleavage and observation of abundant neutral losses [108]. Identical rates of electron capture were observed for doubly-charged peptides containing modifications with disparate EA suggesting electron capture is governed by long range interactions, *i.e.*, the electron is captured to high-*n* Rydberg states, as proposed by McLafferty and co-workers [1], rather than initial capture taking place at the electron predator itself. Once captured, electron relaxation *via* through-space or through-bond transfer to the high-EA modification occurs in competition with transfer to the amide π* orbital (UW mechanism). The radical anions formed by the electron predator have high proton affinities thus enabling proton transfer from a site of protonation. The result is a stable radical intermediate, which does not undergo N-Cα cleavage to produce *c*/*z* ions. None of the unmodified proteinogenic amino acids have a positive electron affinity; however, it was suggested that 3-nitrotyrosine-containing peptides may behave as an electron predator as the PTM has a similar structure and electron affinity to nitrobenzylcysteine [108].

Since these initial observations, and in parallel with the work contained in this thesis, Tureček [120] has completed a more extensive study investigating a wider range of modifications with EA ≥1.00 eV and noted that the electron affinity is not the only criterion for ECD backbone fragmentation inhibition to occur, but any modifications must also act as a hydrogen trap. The hydrogen trap mechanism proposes that following initial electron capture and transfer to the charge-stabilised N-C_O π* orbital (UW mechanism), proton transfer to the amide group occurs resulting in an aminoketyl radical intermediate. Finally, hydrogen-atom transfer to the electron withdrawing group takes place inhibiting typical N-Cα fragmentation. The hydrogen trap mechanism explains why pentafluorobenzyl, which has a sufficiently high EA, does not inhibit backbone fragmentation due to the side-chain being bound by σ-bonds lowering its H-

atom trap efficiency. The nitro-group on 3-nitrotyrosine contains π-bonds, and therefore is likely to have a sufficiently high H-atom trap efficiency for electron predation to occur.

In this chapter, the ECD of peptides containing 3-nitrotyrosine is discussed. The ECD and CID of 3-nitrotyrosine containing peptides were compared with the aim of determining the analytical utility of ECD for localisation of PTMs and sequencing nitrated peptides.

3.2 Results

3.2.1 CID and ECD of doubly-charged 3-nitrotyrosine containing peptides

Peptides were synthesised as described in **Section 2.1.2**: GPLEYGFAK, GPLEYGFAKGPLAK and NYCGLPGEYWLGNDK (*Homo sapiens* fibrinogen β-chain amino acids 314-328, previously identified to undergo nitration *in vivo* at Tyr322 [145]), as well as YLEFISDAIIHVLHSK (from equine myoglobin which was manually nitrated, digested and desalted as described in **Section 2.2.2**, **2.2.4** and **2.2.5**). These synthetic peptides and the desalted digested myoglobin were then resuspended as detailed in **Section 2.2.9**, directly infused into the FT-ICR mass spectrometer, and analysed by CID and ECD (described in **Section 2.2.10.1** and **2.2.10.2** respectively).

As shown in **Figure 3.1,** CID of the peptides appears to be unaffected by the presence of a nitro group on the tyrosine amino acid residue. In all cases, abundant peptide backbone fragments (*b* and *y* ions) were identified for both unmodified and nitrated peptides. In all cases there is no significant decrease (or increase) in the peptide sequence coverage on nitration: *i.e.* CID of GPLEYGFAK resulted in 7/8 backbone cleavages, and nitrated GPLEnYGFAK resulted in 6/8, CID of GPLEYGFAKGPLAK resulted in 11/13, and nitrated

GPLEnYGFAKGPLAK resulted in 12/13, CID of GPLEYGFAKGPLAK resulted in 11/13, and nitrated GPLEnYGFAKGPLAK resulted in 12/13, CID of NYCGLPGEYWLGNDK resulted in 13/14, and nitrated NYCGLPGEnYWLGNDK resulted in 13/14, and CID of YLEFISDAIIHVLHSK resulted in 9/15, and nitrated nYLEFISDAIIHVLHSK resulted in 10/15.

In some cases there does appear to be a change in fragment ion abundance, *e.g.* CID of GPLEYGFAK resulted in y_5 being the most abundant ion, whereas y_7 was the most abundant ion formed following CID of GPLEnYGFAK. For GPLEnYGFAKGPLAK and NYCGLPGEnYWLGNDK, the change appears to be less pronounced; however, it can be seen that the abundance of the y_9 and y_{10} (GPLEnYGFAKGPLAK), and y_6 and y_7 ions (NYCGLPGEnYWLGNDK) appear decreased with all other *y* ions increasing in intensity. This observation indicates that fragmentation at sites adjacent to nTyr is less favoured, which can be explained by the mobile proton model if it is predicted that the backbone amide nitrogen basicity of the Tyr residue is decreased by the addition of the nitro-group. These results therefore suggest that the addition of the 3-nitrotyrosine residue does not affect, in a significant manner, the mobile proton model proposed for CID fragmentation with abundant *b* and *y* ions identified throughout, and that localisation of this PTM can be easily achieved with CID. This is explainable by the PTM having a high bond strength [172] and thus will be not undergo favourable fragmentation at this site.

The ECD mass spectra can be seen in **Figure 3.2**. As discussed in **Section 1.4.2** the predominant fragmentation pathway in peptide ECD is the formation of *c* and $z^{\bullet}$ ions, with minor hydrogen transfer leading to the formation of $c^{\bullet}$ (*i.e.* [*c*-H$^{\bullet}$]) and *z* (termed *z′*) ions. In

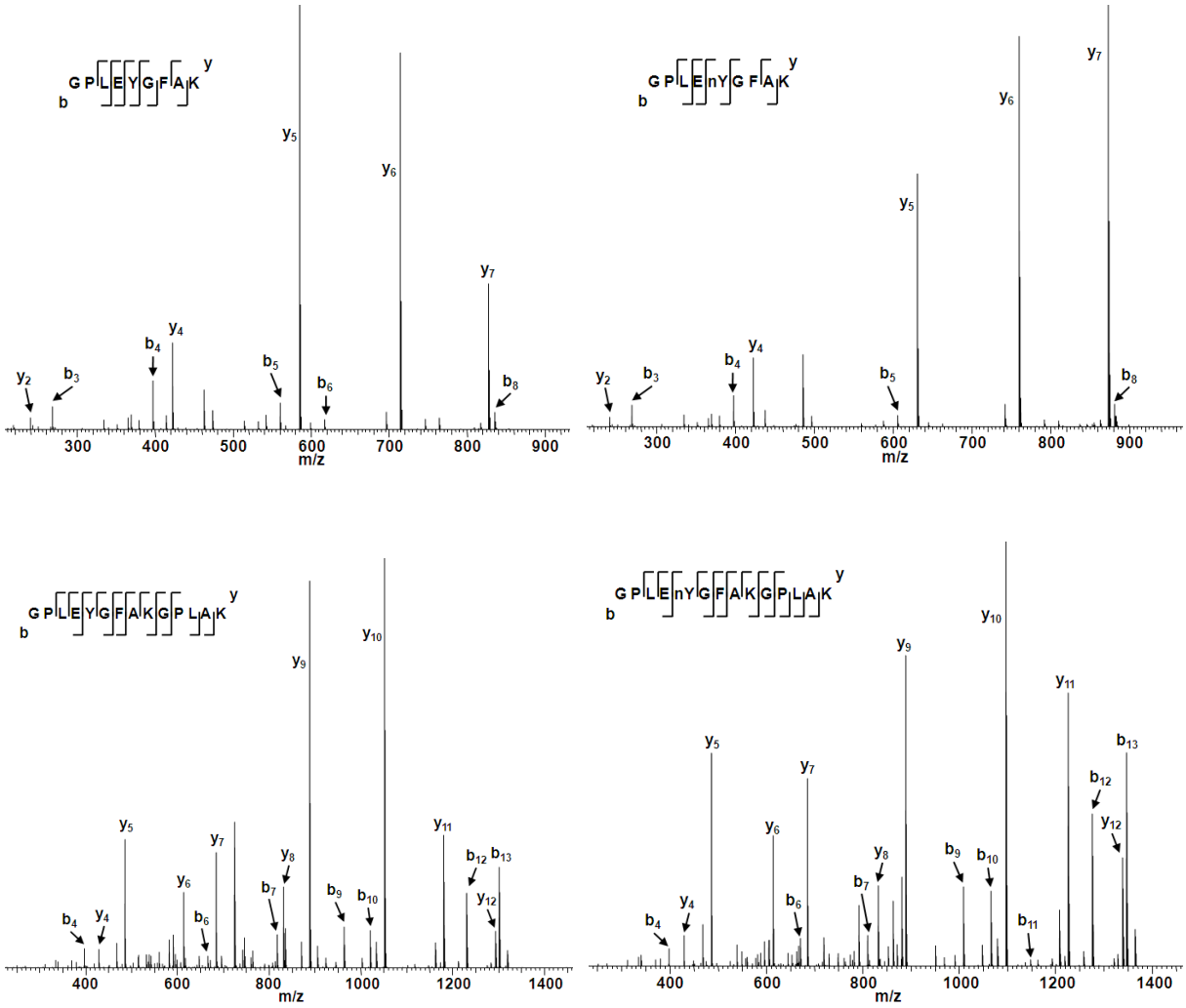

Figure 3.1.1: CID mass spectra of unmodified and nitrated doubly-charged peptides

CID mass spectra of doubly-charged unmodified (**Left**) and nitrated (**Right**) [GPLEYGFAK + 2H]$^{2+}$ ions and [GPLEYGFAKGPLAK + 2H]$^{2+}$ ions. nY denotes 3-nitrotyrosine. The presence of the 3-nitrotyrosine modification results in very little change in CID peptide sequence coverage.

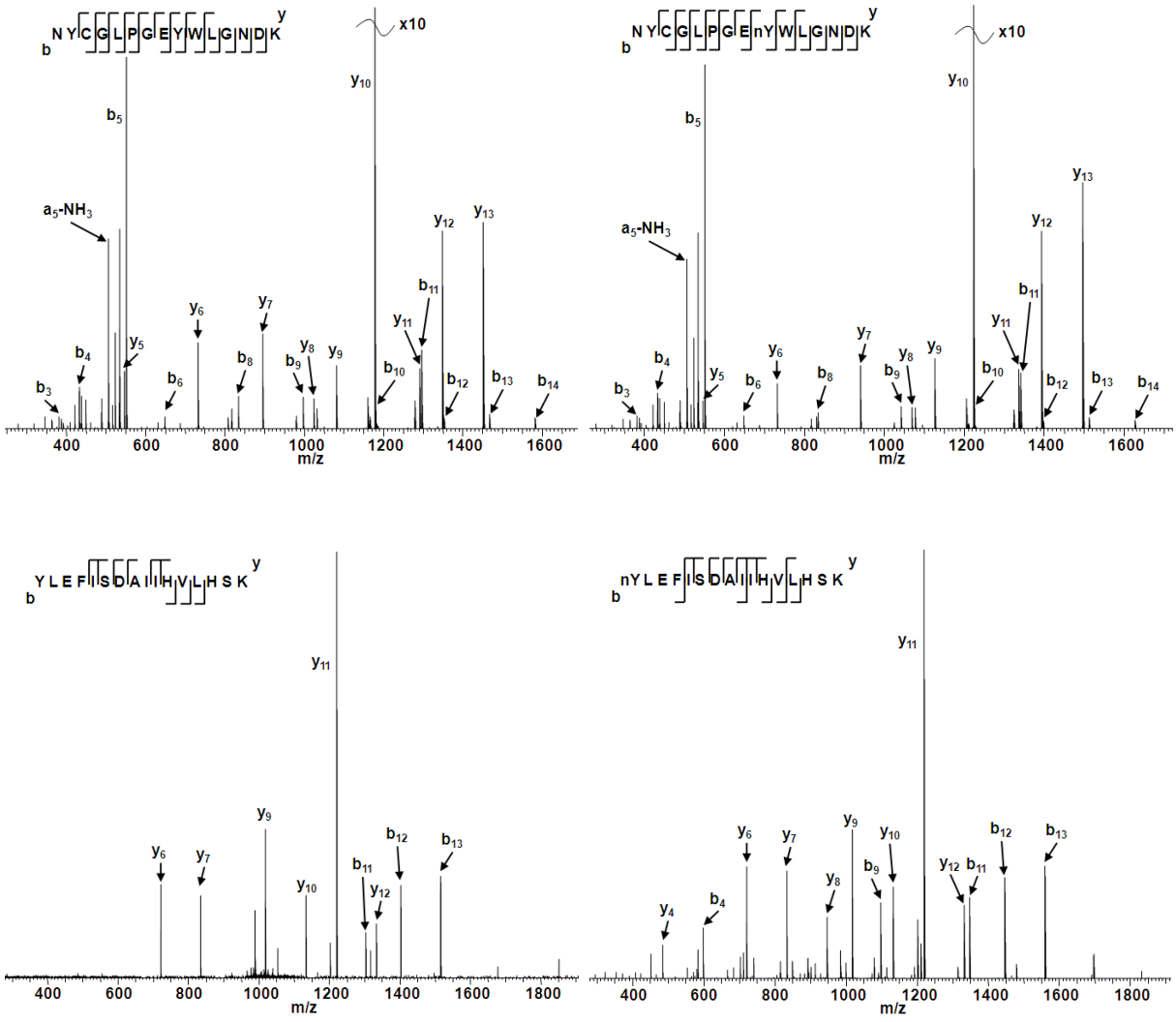

Figure 3.1.2: CID mass spectra of unmodified and nitrated doubly-charged peptides

CID mass spectra of doubly-charged unmodified (**Left**) and nitrated (**Right**) $[NYCGLPGEYWLGNDK + 2H]^{2+}$ ions and $[YLEFISDAIIHVLHSK + 2H]^{2+}$ ions. nY denotes 3-nitrotyrosine. The presence of the 3-nitrotyrosine modification results in very little change in CID peptide sequence coverage.

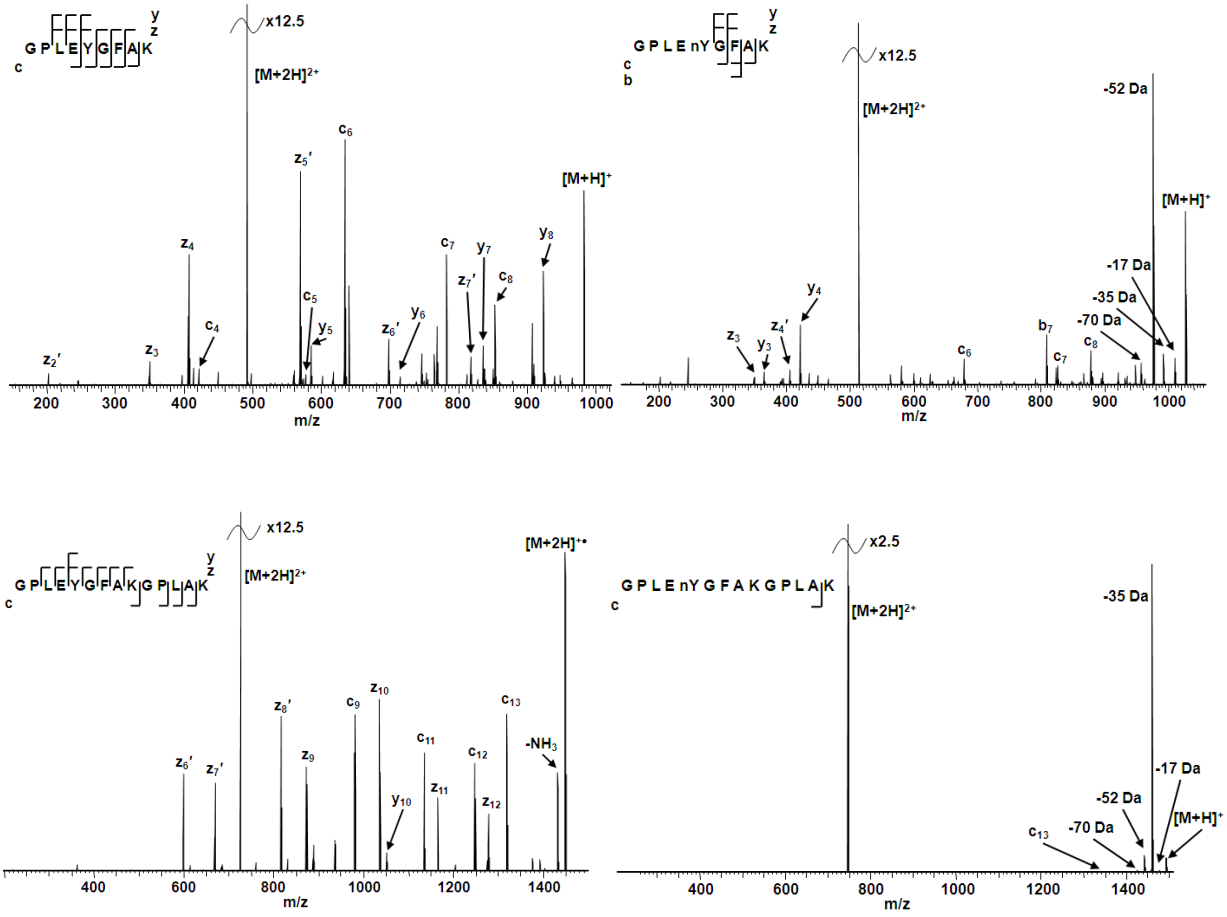

Figure 3.2.1: ECD mass spectra of unmodified and nitrated doubly-charged peptides

ECD mass spectra of doubly-charged unmodified (**Left**) and nitrated (**Right**) [GPLEYGFAK + 2H]$^{2+}$ ions and [GPLEYGFAKGPLAK + 2H]$^{2+}$ ions. nY denotes 3-nitrotyrosine. The presence of the 3-nitrotyrosine modification results in a dramatic change in ECD behaviour, especially in the presence of backbone fragment ions and neutral losses.

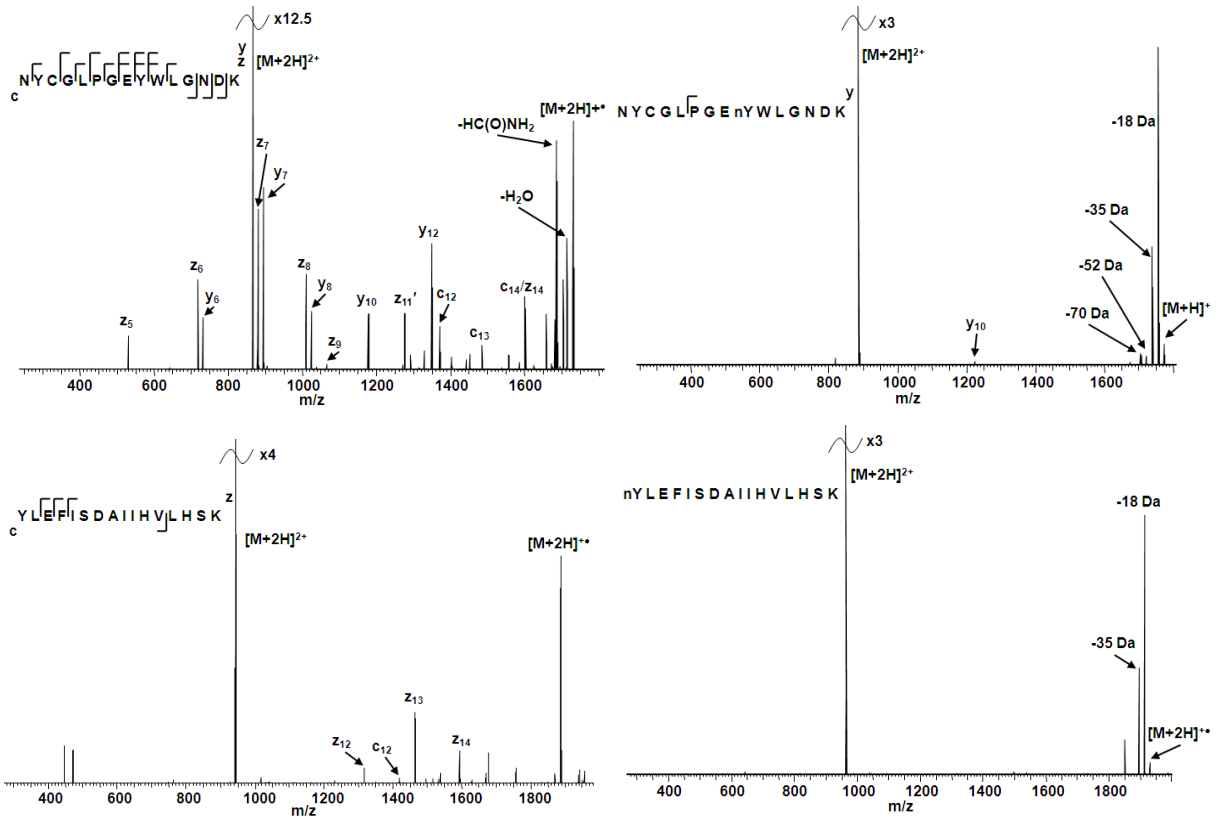

Figure 3.2.2: ECD mass spectra of unmodified and nitrated doubly-charged peptides

ECD mass spectra of doubly-charged unmodified (**Left**) and nitrated (**Right**) [NYCGLPGEYWLGNDK + 2H]$^{2+}$ ions and [YLEFISDAIIHVLHSK + 2H]$^{2+}$ ions. nY denotes 3-nitrotyrosine. The presence of the 3-nitrotyrosine modification results in a dramatic change in ECD behaviour, especially in the presence of backbone fragment ions and neutral losses.

this thesis, as is common practice, $z^{\bullet}$ ions will be referred to as *z*, whereas the other related ions will be referred to as *c*, $c^{\bullet}$ and z'. This allows more simple identification of when hydrogen transfer has taken place. The addition of the nitro-group results in a significant alteration in ECD behaviour. Consider the ECD of the unmodified peptides: In three of four cases, near complete sequence coverage is obtained. Seven out of eight N-Cα bonds fragmented following ECD of GPLEYGFAK. The only site which did not fragment was N-terminal to proline. Such fragments are rarely seen due to the cyclic structure of the Pro side-chain, *i.e.* two bonds are required to break for *c*/*z* fragments to be observed. 11/13 N-Cα bonds were cleaved for GPLEYGFAKGPLAK (only fragments not observed were N-terminal to Pro) and 10/14 for NYCGLPGEYWLGNDK (additional sequence coverage is obtained when *y* ions are included). ECD of YLEFISDAIIHVLHSK resulted in only four N-Cα bond fragment ions out of a possible fifteen. As fragment ions are only noted C-terminal to Ile5 this may suggest that intermolecular bonds are present between the adjacent acidic Ser and the C-terminus preventing fragmentation or separation of fragment ions in this region.

The addition of the nitration on the tyrosine of the peptides drastically decreases the ECD sequence coverage in all cases. ECD of GPLEnYGFAK led to the fragmentation of only 4/8 N-Cα bonds, a decrease in sequence coverage of 42.9 %. A decrease of 90.9 % sequence coverage with ECD of GPLEnYGFAKGPLAK was seen, as only one fragment ion was observed. Nitration of NYCGLPGEYWLGNDK led to a decrease in N-Cα bond fragmentation of 100 %, as only one *y* fragment ion was observed. Finally, ECD of nYLEFISDAIIHVLHSK led to the identification of zero N-Cα bond fragment ions.

These data show that nitration of tyrosine severely inhibits N-Cα backbone cleavage following electron capture of doubly-charged peptide ions. This result can be explained by the electron predator or hydrogen trap mechanisms proposed previously [108, 120]: following initial electron capture to high-*n* Rydberg states, through-space or through-bond electron transfer to the 3-nitrotyrosine (electron predator) or hydrogen transfer following aminoketyl radical formation (hydrogen trap) takes place over typical *c*/*z* type cleavage (Cornell or UW). An alternative explanation is that *c*/*z* type cleavage does occur but there is insufficient charge repulsion to overcome any intramolecular hydrogen bonds between the resulting fragments due to the presence of the 3-nitrotyrosine. To interrogate this suggestion activated ion ECD (AI ECD), as discussed in **Section 1.4.2**, was employed. The AI ECD mass spectra at near-IRMPD threshold using both pre- and post-activation were collected. The IRMPD threshold is the laser power at which the peptides favourably fragment *via* IRMPD rather than ECD, and hence a 'near IRMPD threshold' is used for optimum AI ECD. Pre-activation, *i.e.* laser activation prior to ECD, cleaves any pre-existing intramolecular bonds and the peptide is unfolded, whereas post-activation ensures that any ECD fragments are separated after formation. The mass spectra for AI ECD at near IRMPD threshold are shown in **Figure 3.3** (pre-activation) and **Figure 3.4** (post-activation). There is no increase in *c*/*z* fragment ion abundance following AI ECD, showing that N-Cα bond fragmentation is not taking place. There is, however, an increase in the relative abundance of *y* ions. This observation can be explained by an increase in internal energy of the peptide ions leading to minor IRMPD. These data therefore show that the N-Cα bond fragmentation typically observed in peptide ECD is inhibited by the addition of 3- nitrotyrosine, hence suggesting that the Cornell or UW mechanisms are unfavoured with the electron predator or hydrogen trap mechanisms taking precedence. It is concluded that the use of ECD mass spectrometry for the localisation of

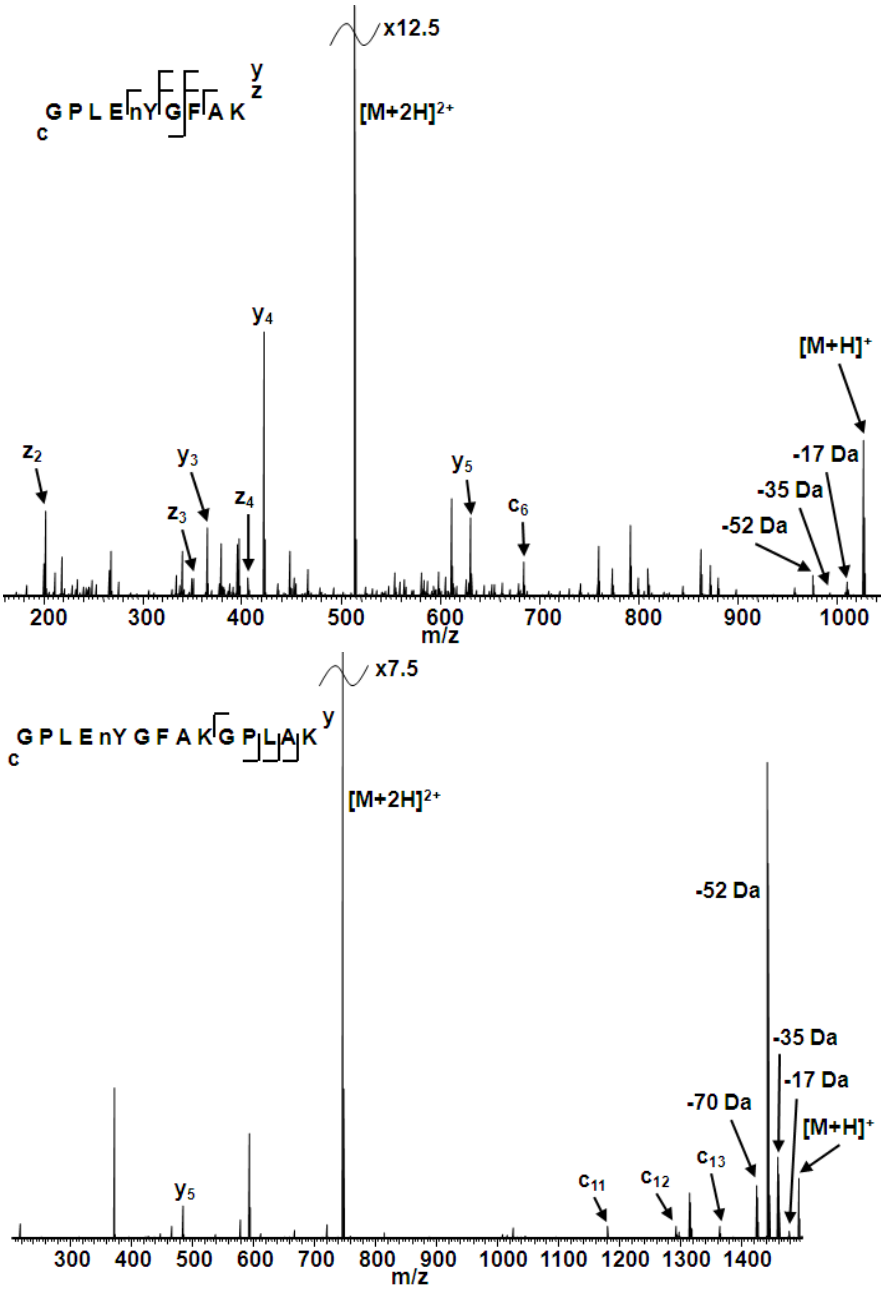

Figure 3.3: Pre-ECD AI ECD mass spectra of nitrated peptides

Pre-ECD infrared laser activation AI ECD mass spectra of doubly-charged nitrated peptides $[GPLEnYGFAK + 2H]^{2+}$ and $[GPLEnYGFAKGPLAK + 2H]^{2+}$ ions. As an increase in *c*/*z* backbone fragment ions is not identified, pre-existing intramolecular bonds are not inhibiting ECD backbone fragmentation.

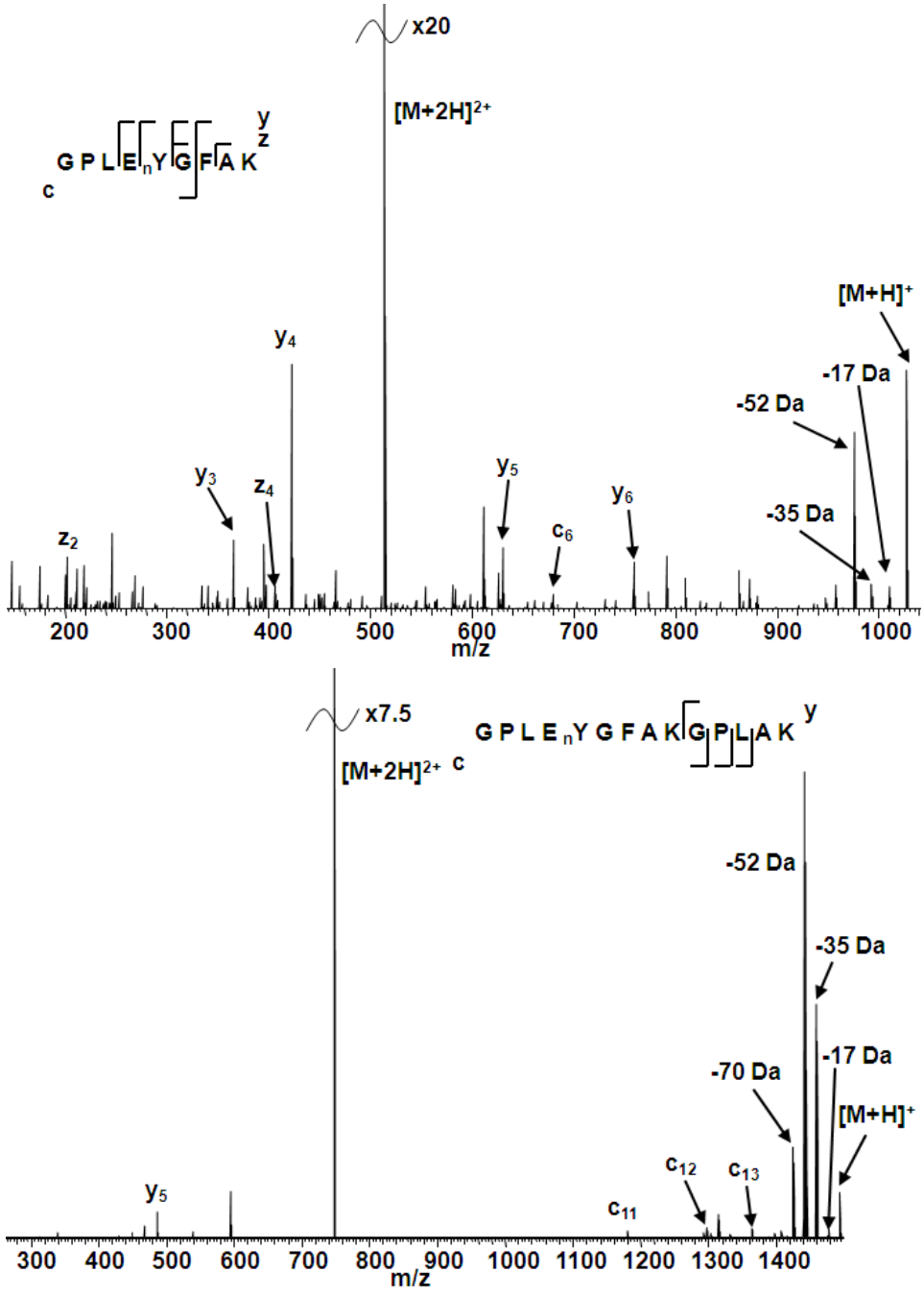

Figure 3.4: Post-ECD AI ECD mass spectra of nitrated peptides

Post-ECD infrared laser activation AI ECD mass spectra of doubly-charged nitrated peptides $[GPLEnYGFAK + 2H]^{2+}$ and $[GPLEnYGFAKGPLAK + 2H]^{2+}$ ions. As an increase in *c*/*z* backbone fragment ions is not identified ECD fragment ions are not being held together inhibiting detection.

nitration sites within doubly-charged peptides is not recommended, and that CID is the optimum approach.

3.2.2 ECD of triply-charged nitrated peptides

Two of the peptides, GPLEnYGFAKGPLAK and nYLEFISDAIIHVLHSK, were also observed in the 3+ charge state following ESI. ECD mass spectra are shown in **Figure 3.5**. As discussed in **Section 1.5.1**, the efficiency of ECD increases with charge state, and this was also observed for these samples. Addition of a third proton led to a significant increase in peptide sequence coverage: A further four *c* and *z* ions were observed following ECD of $[GPLEnYGFAKGPLAK + 3H]^{3+}$, and eight extra *c* and *z* fragment ions were identified for $[nYLEFISDAIIHVLHSK + 3H]^{3+}$ in comparison to their doubly-charged ion counterparts. Of these fragment ions, none were observed close to the nTyr.

The probable protonation sites for $[GPLEnYFAKGPLAK + 3H]^{3+}$ are the N-terminus and the two lysine side-chains, and for $[nYLEFISDAIIHVLHSK + 3H]^{3+}$ are the N-terminus, the lysine side-chain and one of the histidine side chains (likely His11 due to charge repulsion between His14 and Lys16). The fact that no fragments are observed in the vicinity of the nTyr residue for either triply-charged peptide suggests that the peptide ion structure is important for fragmentation. It is predicted that the triply-charged peptides have more extended conformations than their doubly-charged counterparts due to charge-repulsion within the peptides. Conformation is critical when discussing radical fragmentation as through-bond electron-transfer rates have been shown to be dependent on distance [106, 107], and hence

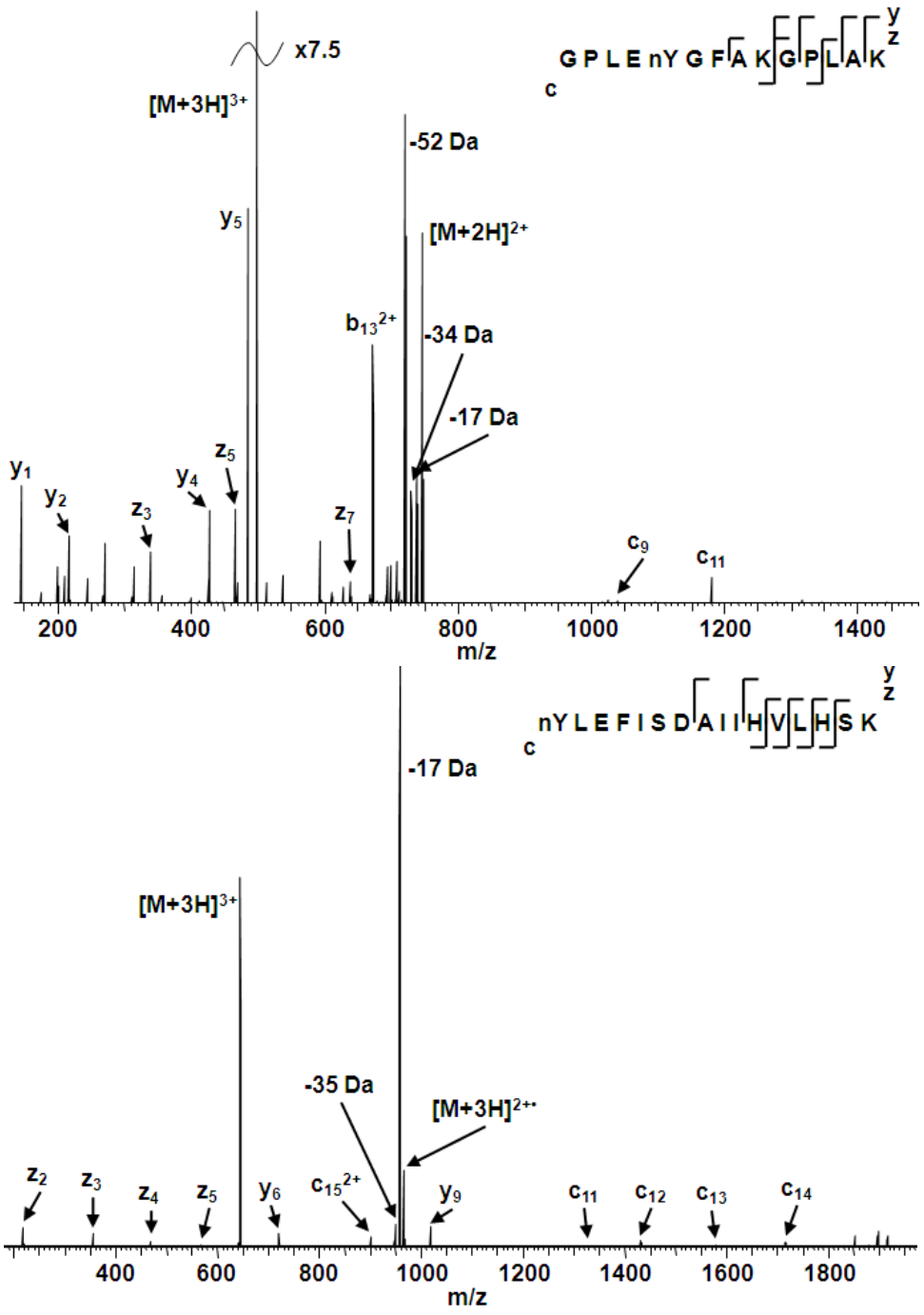

Figure 3.5: ECD mass spectra of triply-charged nitrated peptides

ECD mass spectra of triply-charged nitrated $[GPLEnYGFAKGPLAK + 3H]^{3+}$ ions and $[nYLEFISDAIIHVLHSK + 3H]^{3+}$ ions. Peptide sequence coverage is increased in comparison to their doubly-charged counterparts (Figures 3.2.1 and 3.2.2), although these fragment ions are always at sites distant from the PTM.

this extended conformation would prevent electron transfer between, for example, Lys16 and nTyr1 within [nYLEFISDAIIHVLHSK + 3H]$^{3+}$, whereas for its doubly-charged counterpart its structure is likely more folded allowing electron transfer between these sites. Therefore, these observations may suggest that if electron capture to a high-*n* Rydberg state of the central lysine (GPLEnYGFAKGPLAK) or histidine (nYLEFISDAIIHVLHSK) occurs, the 3-nitrotyrosine intercepts and traps the electron, whereas if the electron is captured to a high-*n* Rydberg state of the C-terminal lysine (both peptides), relaxation to the amide π* orbital proceeds with subsequent N-Cα cleavage. This hypothesis, therefore, explains why peptide backbone fragment ions are observed near the C-terminus but not near the nTyr amino acid residue.

These results show that the use of ECD mass spectrometry for the localisation of nitration sites within triply-charged peptides allow some minor localisation and an increase in sequence coverage in comparison to their doubly-charged peptide counterparts. It also suggests that, as confirmed by Mikhailov *et al*. [176], completed in consequence to this study, higher charge states of 3-nitrotyrosine containing peptides and proteins allow PTM site localisation.

3.2.3 Analysis of small neutral losses

In all peptides and charge states studied thus far, the ECD mass spectra of nitrated peptides show intense peaks corresponding to small neutral losses from the charge-reduced $[M+2H]^{+\bullet}$ species following electron capture. In all cases, at least one of these peaks was more abundant than that of the charge-reduced species, *e.g*., the most abundant peak following ECD of GPLEnYGFAK corresponded to $[M+2H]^{+\bullet}$-[52 Da]. These neutral losses appear to be very

similar for all peptides and charge states, with losses of 17 Da, 18 Da, 35 Da, 52 Da and 70 Da from the charge-reduced species being identified in the majority of cases. These neutral losses are explored in **Figure 3.6**, where the *m*/*z* regions of the ECD mass spectra are expanded, and **Table 3.1**, in which all the neutral losses and their measured masses are listed. As well as these losses, the loss of a hydrogen atom from the charge-reduced species was observed for all nitrated peptides, *i.e.* peaks corresponding to $[M+H]^+$. The formation of $[M+H]^+$ is commonly observed in ECD mass spectra of peptides [91], and is indeed noted for unmodified GPLEYGFAK (**Figure 3.1**). Given that events following electron capture appear to be different to those for unmodified peptides, it cannot be concluded that hydrogen atom loss observed here proceeds as previously proposed in the literature.

These neutral losses have been confidently assigned with errors all being less than 10 ppm. Importantly, ammonia has a theoretical mass of 17.0265 Da, whereas hydroxyl radical has a theoretical mass of 17.0027 Da. The resolution afforded by FT-ICR allows differentiation of the two species, even when both are present. For example, see **Figure 3.7** in which an expanded region of the AI ECD mass spectrum (laser power of 20 %) of $[GPLEnYGFAKGPLAK + 2H]^{2+}$ shows the peak splitting of $[H_2O + NH_3]$ (*m*/*z* 1458.7598) and $[^{\bullet}OH + H_2O]$ (*m*/*z* 1458.7926) loss from the charge-reduced precursor ion. These identifications have a ppm error of 1.44 ppm and 4.73 ppm, respectively.

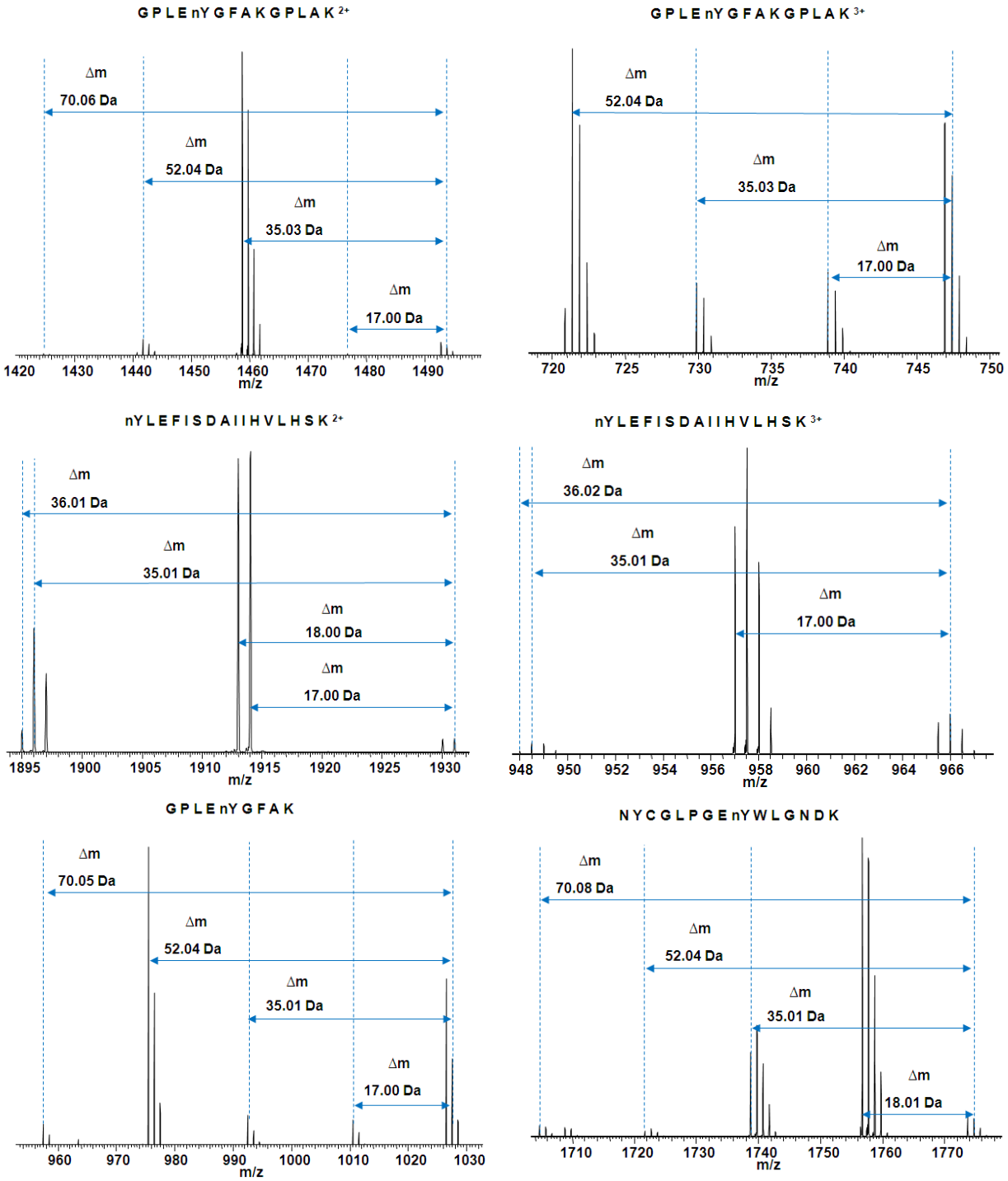

Figure 3.6: Expanded ECD mass spectra for neutral loss identification

Expanded *m*/*z* regions of ECD mass spectra showing peaks corresponding to neutral losses from the charge-reduced cation radical for precursor ions. Mass shifts (Δm) from the mass of the charge-reduced $[M+2H]^{+\bullet}$ and $[M+3H]^{2+\bullet}$ ions for doubly- and triply-charged precursor ions, respectively, are indicated.

Peptide precursor ion	Assignment m/z_{meas} Δm (Da)	Assignment m/z_{meas} Δm (Da)	Assignment m/z_{meas} Δm (Da)	Assignment m/z_{meas} Δm (Da)
[GPLEnYGFAK + 2H]$^{2+}$	$^{\bullet}$OH 1010.4988 16.9984	$^{\bullet}$OH + H_2O 992.4878 35.0094	$^{\bullet}$OH + H_2O + NH_3 975.4618 52.0354	$^{\bullet}$OH + 2H_2O + NH_3 957.4507 70.0465
[GPLEnYGFAKGPLAK + 2H]$^{2+}$	$^{\bullet}$OH 1476.7963 16.9971	H_2O + NH_3 1458.7590 35.0344	$^{\bullet}$OH + H_2O + NH_3 1441.7562 52.0372	$^{\bullet}$OH + 2H_2O + NH_3 1423.7293 70.0641
[GPLEnYGFAKGPLAK + 3H]$^{3+}$	$^{\bullet}$OH 738.8972 16.9986	H_2O + NH_3 729.8806 35.0318	$^{\bullet}$OH + H_2O + NH_3 721.3785 52.0360	
[NYCGLPGEnYWLGNDK + 2H]$^{2+}$	H_2O 1756.7663 18.0063	$^{\bullet}$OH + H_2O 1739.7595 35.0131	$^{\bullet}$OH + H_2O + NH_3 1772.7254 52.0361	$^{\bullet}$OH + 2H_2O + NH_3 1704.7013 70.0713
[nYLEFISDAIIHVLHSK + 2H]$^{2+}$	$^{\bullet}$OH 1914.0190 17.0042	H_2O 1913.0167 17.9980	$^{\bullet}$OH + H_2O 1896.0096 35.0051	2H_2O 1895.0059 36.0088
[nYLEFISDAIIHVLHSK + 3H]$^{3+}$	$^{\bullet}$OH 957.5086 17.0030	$^{\bullet}$OH + H_2O 948.5045 35.0135	2H_2O 948.0017 36.0191	

Table 3.1: Measured mass shifts for neutral loss identifications

Summary of neutral losses observed for each peptide and charge state. Assignments are given together with experimental *m/z* values (m/z_{meas}) of the peaks and mass shifts (Δm) from the charge-reduced $[M+2H]^{+\bullet}$ or $[M+3H]^{2+\bullet}$ ions. Calculated mass shifts for $^{\bullet}$OH, H_2O and NH_3 are 17.0027 Da, 18.0106 Da, and 17.0265 Da, respectively. Similar losses are identified in all cases in variable combinations. The most abundant neutral loss peak for each peptide and charge state is shown in red.

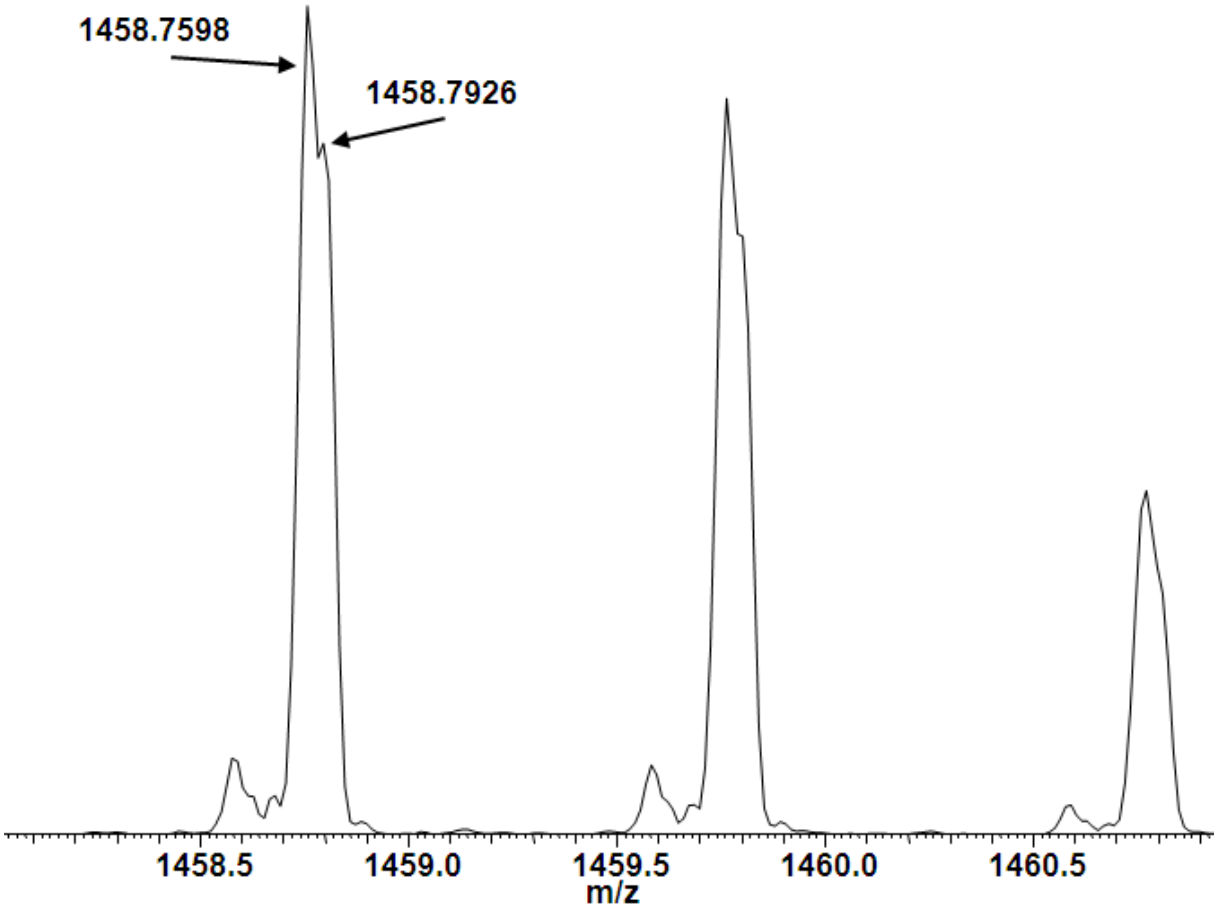

Figure 3.7: Expanded neutral loss peaks suggesting peak splitting

Expanded AI ECD mass spectrum of $[GPLEnYGFAKGPLAK + 2H]^{2+}$ showing peak splitting between *m/z* 1458.7598 and *m/z* 1458.7926 allowing the positive identification between NH_3 and $^{\bullet}OH$, despite having similar masses (17.0265 Da and 17.0027 Da, respectively). The peak at *m/z* 1458.7598 is identified as the neutral loss of $[H_2O + NH_3]$ from the charge-reduced precursor, $[M+2H]^{+\bullet}$ (*m/z* 1493.7989) and *m/z* 1458.7926 is identified to be the neutral loss of $[^{\bullet}OH + H_2O]$.

The *sole* loss of ˙OH, which was observed following ECD of $[GPLEnYGFAK + 2H]^{2+}$, $[GPLEnYGFAKGPLAK + 2H]^{2+}$, $[GPLEnYGFAKGPLAK + 3H]^{3+}$, $[nYLEFISDAIIHVLHSK + 2H]^{2+}$ and $[nYLEFISDAIIHVLHSK + 3H]^{3+}$, is never seen to be the most abundant neutral loss (with the exception of $[nYLEFISDAIIHVLHSK + 3H]^{3+}$). This therefore suggests that the sole loss of a single hydroxyl radical is not the major dominant pathway following electron capture.

Polášek and Tureček, have shown that the phenylnitronic radical is stable on the microsecond time scale and undergoes unimolecular dissociation *via* hydroxyl loss [177]. The loss of hydroxyl radicals was noted in the work of Sohn *et al*. [108] on the ECD of doubly-charged peptides containing the electron predators 3-nitrobenzylcysteine and 3,5-dinitrobenzylcysteine. It was concluded that formation of the nitrobenzyl radical anion was followed by intramolecular proton transfer and subsequent homolytic cleavage of the N-OH bond. With respect to the hydrogen trap mechanism, the phenylnitronic radical is formed directly following hydrogen atom transfer from the aminoketyl radical intermediate. It is postulated that a similar process occurs here (shown in **Figure 3.8**), *i.e.* the nitrotyrosine radical anion is formed on electron capture and is followed by intramolecular proton transfer (electron predator) or formation of the aminoketyl radical followed by hydrogen atom transfer to the nitrotyrosine (hydrogen trap).

Similar to the sole loss of hydroxyl radical, the loss of *one* water molecule is not observed for all peptides but, when present, does appear to be more abundant than ˙OH loss. ECD of two of the peptides analysed, *i.e.* $[NYCGLPGEnYWLGNDK + 2H]^{2+}$ and $[nYLEFISDAIIHVLHSK + 2H]^{2+}$, led to the identification of a peak with a mass 18 Da less than the charge-reduced

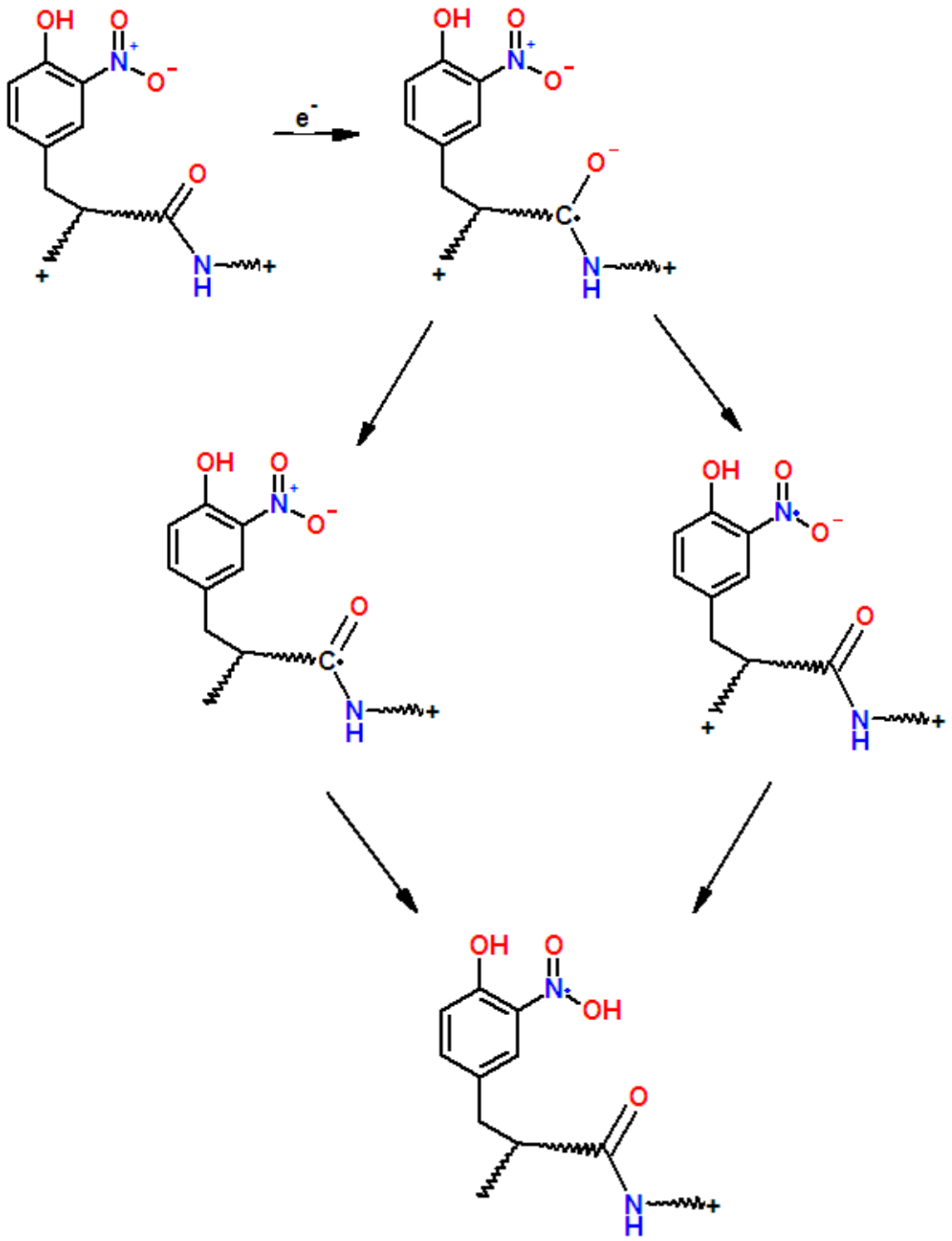

Figure 3.8: Mechanistic formation of the stable phenylnitronic radical

Following initial electron capture and transfer to the charge-stabilised π* orbital, either electron transfer to the nitro group takes place (**right-hand** intermediate) followed by proton transfer (electron predator mechanism) or proton transfer forms the aminoketyl radical (**left-hand** intermediate) followed by H-atom transfer (hydrogen trap mechanism).

species and tentatively assigned as water loss; however, it cannot be certain that these peaks do not correspond to the combined loss of $^{\bullet}OH$ and $^{\bullet}H$. Indeed, the ECD mass spectrum of $[nYLEFISDAIIHVLHSK + 2H]^{2+}$ shows the presence of both $[M + H]^{+}$ and $[M + 2H]^{+\bullet}$ ions and peaks corresponding to the loss of 17.004 Da from both, and these neutral loss peaks have the same ratio of abundances as the charge-reduced peaks, suggesting that the loss of $^{\bullet}OH$ occurs both from $[M + H]^{+}$ and $[M + 2H]^{+\bullet}$. Unlike with the sole loss of a hydroxyl radical, for these two peptides the sole loss of water, or $[^{\bullet}OH + {}^{\bullet}H]$, is the most intense fragment peak in the mass spectrum. This suggests that the loss of one water molecule results in a more stable product than the loss of one hydroxyl radical.

With the exception of GPLEnYGFAKGPLAK, ECD of the nitrated peptides led to the observation of the combined loss of $[^{\bullet}OH + H_2O]$. Possibly, the water loss is related to hydrogen bonding of the phenol group to the nitro-group. The loss of water molecules was not noted by Sohn *et al*. [108] for any modification or peptide; however, the loss of water was observed when they undertook AI ECD of the nitrobenzylcysteine-containing peptides, suggesting that the loss of water is associated with higher vibrational excitation.

In addition to losses of $^{\bullet}OH$ and water, ammonia losses from the charge-reduced precursors were observed; however, unlike that of hydroxyl radicals and water, the loss of ammonia was never observed in isolation. Ammonia loss following ECD of peptides is not uncommon and indeed is identified in the ECD of $[GPLEYGFAKGPLAK + 2H]^{2+}$ (**Figure 3.2.1**); however, the intensity of the neutral losses involving ammonia of the nitrated peptides are strikingly high. In the cases of $[GPLEnYGFAK + 2H]^{2+}$, and $[GPLEnYGFAKGPLAK + 3H]^{3+}$ the most abundant peak within the ECD mass spectra corresponds to the loss of $[^{\bullet}OH + H_2O + NH_3]$,

whereas the most intense peak in the ECD mass spectra of $[GPLEnYGFAKGPLAK + 2H]^{2+}$ corresponds to the loss of $[H_2O + NH_3]$. ECD of $[NYCGLPGEnYWLGNDK + 2H]^{2+}$ resulted in the loss of $[^{\bullet}OH + H_2O + NH_3]$, and, despite being the second most intense peak within the mass spectrum, is still far more intense than the charge-reduced precursor ion. The loss of ammonia, in any combination, was not observed following ECD of nYLEFISDAIIHVLHSK in either charge state. The combined losses suggest that NH_3 loss is intrinsically linked to the nitrotyrosine radical anion formed following ECD. From the ECD mass spectra shown here this ammonia loss does appear to be dependent on the position of the 3-nitrotyrosine with respect to the basic amino acid residue (BAAR), as ECD of nYLEFISDAIIHVLHSK, in which the modification is a significant distance from the BAAR, did not lead to ammonia loss, and the ammonia loss peak within the ECD mass spectrum of NYCGLPGEnYWLGNDK was not the most intense. Investigation into the loss of ammonia following ECD of 3-nitrotyrosine containing peptides is the focus of **Chapter 4**.

The observed reaction pathways can be expressed as such:

1. $[M+nH]^{n+} + e^- \rightarrow [M+nH]^{(n-1)+\bullet}$
2. $[M+nH]^{n+} + e^- \rightarrow [M+(n-1)H]^{(n-1)+} + H^{\bullet}$
3. $[M+nH]^{n+} + e^- \rightarrow [M+nH-{}^{\bullet}OH]^{(n-1)+} + {}^{\bullet}OH$
4. $[M+nH]^{n+} + e^- \rightarrow [M+nH-H_2O]^{(n-1)+\bullet} + H_2O$
5. $[M+nH]^{n+} + e^- \rightarrow [M+nH-({}^{\bullet}OH + H_2O)]^{(n-1)+} + {}^{\bullet}OH + H_2O$
6. $[M+nH]^{n+} + e^- \rightarrow [M+nH-(H_2O + NH_3)]^{(n-1)+\bullet} + H_2O + NH_3$
7. $[M+nH]^{n+} + e^- \rightarrow [M+nH-({}^{\bullet}OH + H_2O + NH_3)]^{(n-1)+} + {}^{\bullet}OH + H_2O + NH_3$

The frequency of these reaction pathways, and hence loss channels being open or closed, vary considerably depending on the peptide sequence and charge state, as shown in **Table 3.1**. For

example $[GPLEnYGFAK + 2H]^{2+}$ favourably fragments through the reaction pathway 7, along with $[GPLEnYGFAKGPLAK + 3H]^{3+}$, whereas $[GPLEnYGFAKGPLAK + 2H]^{2+}$ follows pathway 6, and the loss channel for pathway 7 is completely closed for ECD of $[nYLEFISDAIIHVLHSK + 2H]^{2+}$ and $[nYLEFISDAIIHVLHSK + 3H]^{3+}$.

3.2.4 ETD of nitrated peptides

Figures 3.9 and **3.10** show the ETD and saETD mass spectra, respectively, of doubly-charged peptides GPLEnYGFAK and GPLEnYGFAKGPLAK. Initially, these data appear very similar to the mass spectra collected following ECD of the peptides, with little or no peptide backbone fragmentation, and abundant neutral losses; however, variations in intensities and type of the neutral losses are noted. In all cases, following ECD of the peptides, the most abundant neutral loss ion contains the loss of ammonia, be it with only water ($[H_2O + NH_3]$) or water and a hydroxyl radical ($[^{\bullet}OH + H_2O + NH_3]$), whereas following ETD the most abundant neutral loss ion is the sole loss of water. In the case of saETD the 'neutral loss profile' shifts, and the loss of $[NH_3 + H_2O]$ is the most abundant peak within the mass spectrum. Interestingly, ETD or saETD of any of the peptides does not result in the loss of a hydroxyl radical. Thus ETD and saETD must close down the loss channel of pathways 3, 5 and 7, as described above.

These data suggest that the internal energy of the peptides is critical to the neutral loss profile following ECD or ETD. ETD and saETD takes place through lower energy regimes than following ECD as the electron transferred through ETD and saETD cannot access as high-

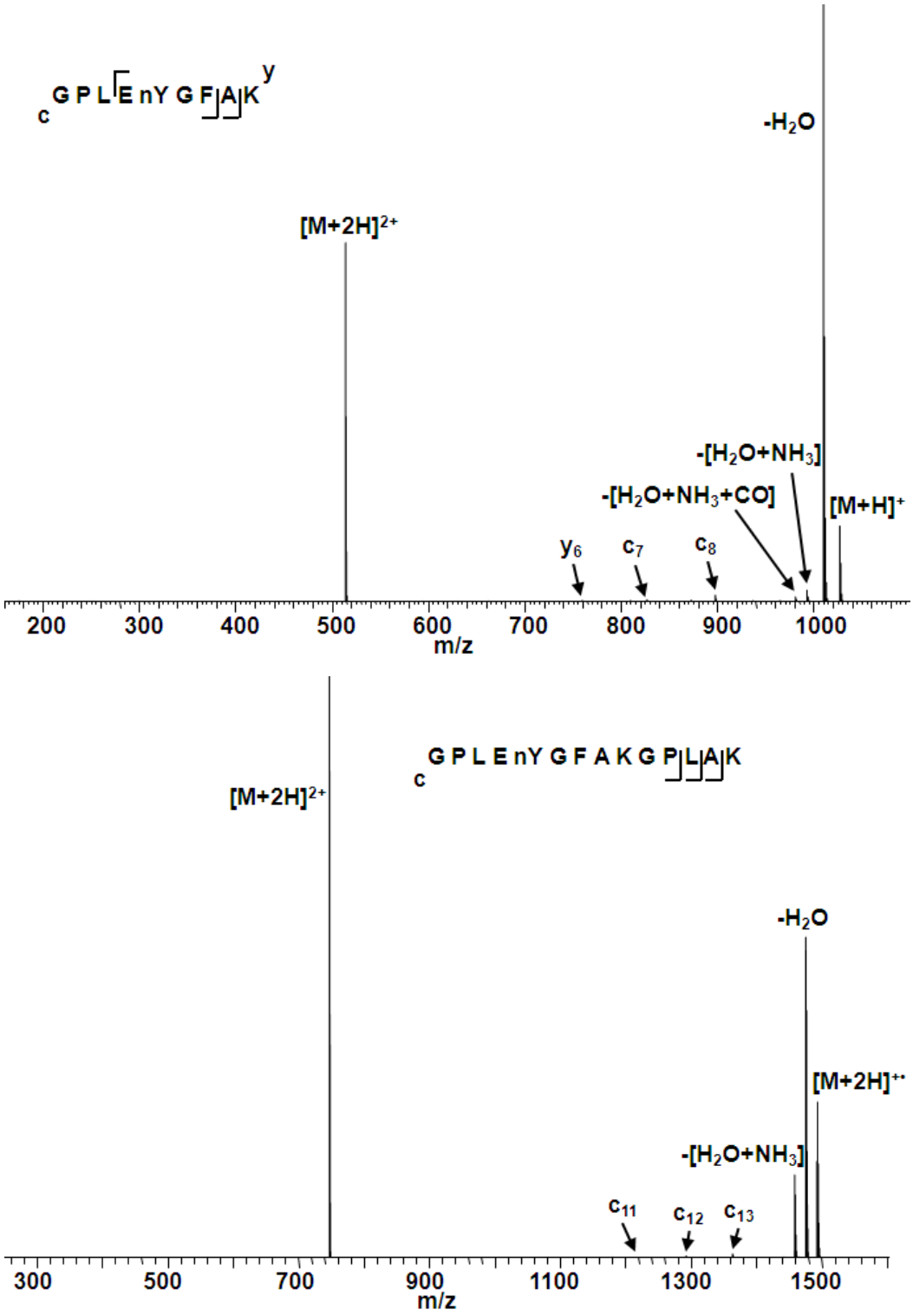

Figure 3.9: ETD mass spectra of doubly-charged nitrated peptides

ETD mass spectra of doubly-charged nitrated [GPLEnYGFAK + 2H]$^{2+}$ ions and [GPLEnYGFAKGPLAK + 2H]$^{2+}$ ions. ETD results in similar peptide sequence coverage as with ECD, but a variation in neutral loss profiles is observed.

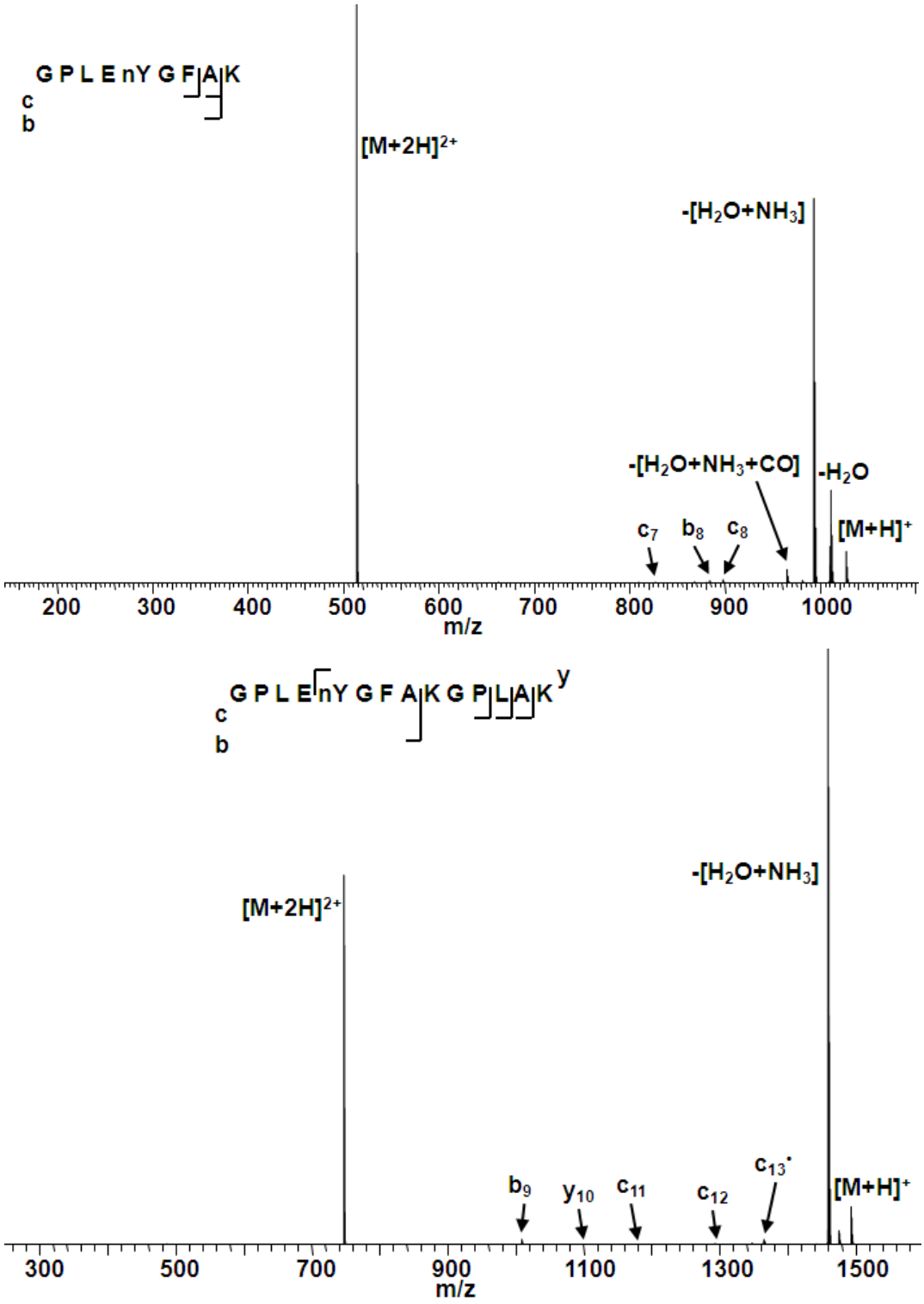

Figure 3.10: saETD mass spectra of doubly-charged nitrated peptides

saETD mass spectra of doubly-charged nitrated $[GPLEnYGFAK + 2H]^{2+}$ ions and $[GPLEnYGFAKGPLAK + 2H]^{2+}$ ions. The increase in internal energy associated with supplemental activation (compared to ETD) leads to the promotion of ammonia loss.

energy Rydberg orbitals [98, 128]. It therefore can be extrapolated that the neutral losses following ECD or ETD of a 3-nitrotyrosine-containing peptide are dependent on the energy levels with the loss of H_2O being the lowest (being identified following ECD, ETD and saETD), followed by NH_3 (following ECD and saETD), and $^{\bullet}OH$ (following ECD) being lost only at sufficiently high energy states.

3.3 Discussion

In terms of sequencing and characterising sites of modification, these results conclusively show that ECD is not the favoured method of choice for localising the modification site in doubly-charged 3-nitrotyrosine-containing peptides ions, although the modifications can be easily attributed to that peptide due to the abundant neutral losses which result. Some sequence information can be gleaned from triply-charged precursor ions, although again does not allow localisation of the modification site was not achieved. Due to the non-labile nature of 3-nitrotyrosine, CID is shown to be highly successful, with little, if any, decrease in sequence coverage being identified. ECD of nitrated peptides is characterised by the loss of small neutrals including hydroxyl radicals, water and ammonia. These neutral losses are highly abundant, with at least one being more intense than the charge-reduced precursor and may be utilised as a possible marker for tyrosine nitration. The neutral losses formed following the electron predator or hydrogen trap mechanism appear to be dependent on the internal energy of the peptide, as shown by comparisons between ECD, ETD and saETD experiments, with H_2O loss having the lowest activation energy, followed by NH_3 and $^{\bullet}OH$. Due to the appearance of ammonia loss, which had not been previously identified in the literature, further investigations were undertaken into the mechanistic formation and origin of the species, and the outcome of which is discussed in **Chapter 4**.

Chapter 4 – Origin of Ammonia Loss Following ECD of Nitrated Peptides*

4.1 Introduction

In **Chapter 3**, it was shown that the presence of 3-nitrotyrosine within a peptide sequence has a deleterious effect on ECD backbone cleavage of the *c*/*z* type, and this effect can be explained by either the electron predator [108] or hydrogen trap [120] mechanisms. In addition, it was shown that the ECD mass spectra were dominated by peaks corresponding to the loss of small neutrals ($^{\bullet}OH$, H_2O, and NH_3) from the charge-reduced precursor. Within the mass spectra the peaks corresponding to the neutral loss of ammonia, [$^{\bullet}OH + H_2O + NH_3$], or [$H_2O + NH_3$] (depending on the peptide) were particularly intense.

In this chapter, the origin of the ammonia loss is investigated. To elucidate the origin of ammonia the effect of the 3-nitrotyrosine site within the peptide was identified. As well as comparisons between lysine, arginine, and non-BAAR-containing peptides, and isotopic-labelling, AI ECD experiments, N-terminal acetylation, MS^3 (ECD of the precursor peptide followed by IRMPD of the neutral loss ECD fragments) experiments, and molecular dynamic simulations of the peptides were all undertaken. These results show how the hierarchy of ECD mechanisms can be deduced by considering the fragmentation behaviour of nitrated peptides.

---

*Work presented in this chapter has been published as:
Jones, A.W., and Cooper, H.J., *Probing the mechanisms of electron capture dissociation mass spectrometry with nitrated peptides*. Phys. Chem. Chem. Phys., 2010. **12**(41): p. 13394-13399
Jones, A.W., Mikhailov, V.A., Iniesta, J. and Cooper, H.J., *Electron capture dissociation mass spectrometry of tyrosine nitrated peptides*. J. Am. Soc. Mass Spectrom., 2010. **21**: p. 268-277

4.2 Results

4.2.1 ECD of isotopically labelled nitrated peptides

As the water and hydroxyl radical losses originate from the 3- nitrotyrosine, it was initially speculated that ammonia may also arise from this site. Also, ammonia loss is only observed in combination with other neutral species, suggesting it is intrinsically linked to the 3-nitrotyrosine radical anion formed following ECD. To investigate these proposals, ECD mass spectra of ^{15}N-labelled GPLEnYGFAKGPLAK were recorded, as shown in **Figure 4.1**. The neutral loss profiles of the ECD mass spectra of the light GPLEnYGFAKGPLAK (see **Figures 3.2.1** and **3.5**) and heavy GPLEnYGFAKGPLAK, for both double- and triple-charge states, are identical, with the dominant losses being 35 and 52 Da, for +2 and +3 charge states, respectively, in both cases. Thus these data show that ammonia does not arise from the 3-nitrotyrosine itself and therefore must arise from elsewhere.

4.2.2 AI ECD analysis of nitrated peptides

It was then hypothesised that ammonia originates from the BAAR side chain, which would indicate that the proximity between the 3-nitrotyrosine side chain and the BAAR side chain is critical for ammonia loss. To identify whether this was the case, pre-activation AI ECD of the peptides was completed. If the proximity between the 3-nitrotyrosine and BAAR side chain is important, then an increase in vibrational energy, induced by an infra-red irradiation, would lead to unfolding of the peptides, and hence neutral losses would not be observed.

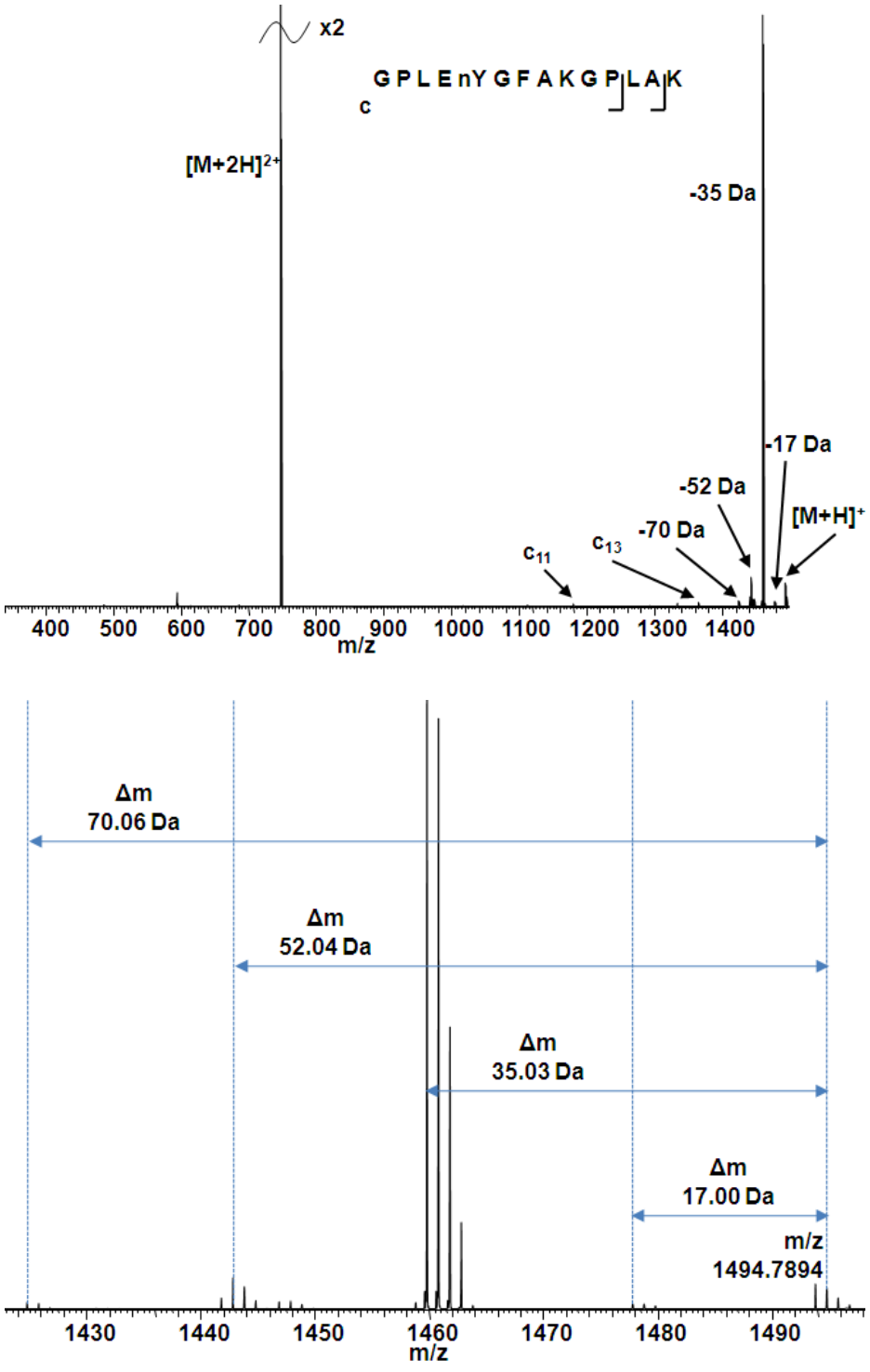

Figure 4.1.1: ECD mass spectra of ^{15}N-isotopically-labelled nitrated peptides

ECD mass spectrum of doubly-charged ^{15}N labelled [GPLEnYGFAKGPLAK + 2H]$^{2+}$. Note that the 35 Da ([H_2O + NH_3]) and 52 Da ([$^{\bullet}OH$ + H_2O + NH_3]) neutral losses have not increased in mass (when compared to the unlabelled peptide shown in **Figure 3.2.1**), showing that ammonia does not originate from the 3-nitrotyrosine.

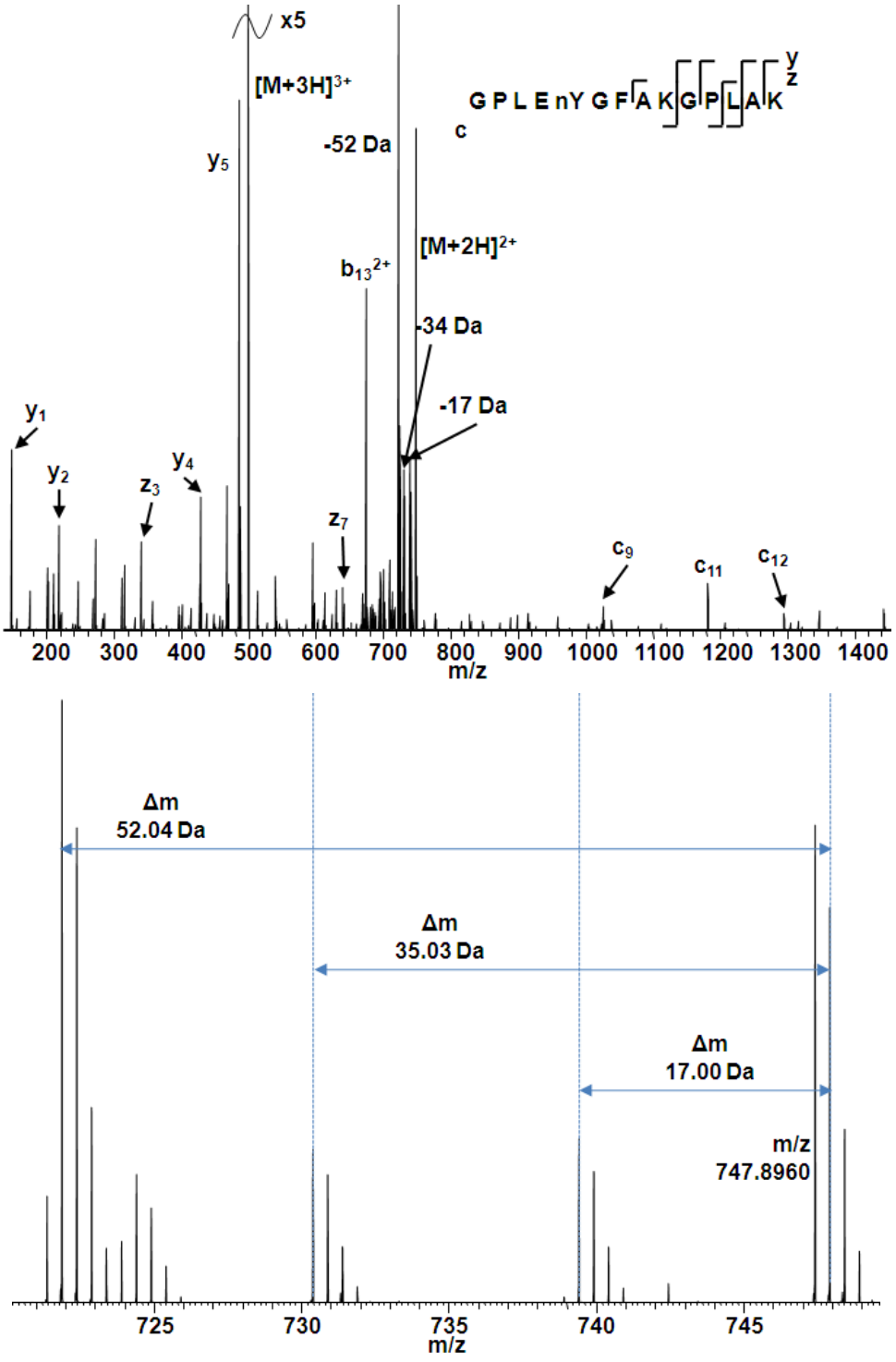

Figure 4.1.2: ECD mass spectra of ^{15}N-isotopically-labelled nitrated peptides

ECD mass spectrum of triply-charged ^{15}N labelled [GPLEnYGFAKGPLAK + 3H]$^{3+}$. Note that the 35 Da ([H_2O + NH_3]) and 52 Da ([$^{\bullet}OH$ + H_2O + NH_3]) neutral losses have not increased in mass (when compared to the unlabelled peptide shown in **Figure 3.6**), showing that ammonia does not originate from the 3-nitrotyrosine.

Graphs showing the normalised intensities of the neutral loss peaks, *i.e.* [$^{\bullet}$OH], [$^{\bullet}$OH + H_2O], [H_2O + NH_3], [$^{\bullet}$OH + H_2O + NH_3], and [H_2O + NH_3 + CO], following AI ECD at increasing laser power of the peptides are shown in **Figure 4.2**. Pre ECD activation of [GPLEnYGFAK + 2H]$^{2+}$ has a dramatic effect on the combined loss of [$^{\bullet}$OH + H_2O + NH_3], whereas the neutral losses which do not contain ammonia, *e.g.* [$^{\bullet}$OH], appear to have a much less pronounced decrease in relative abundance. A similar pattern is observed with AI ECD of [GPLEnYGFAKGPLAK + 3H]$^{3+}$. As well as the dramatic decrease in intensity of [$^{\bullet}$OH + H_2O + NH_3], the combined losses of [$^{\bullet}$OH + H_2O + NH_3 + CO] (observed in ECD of [GPLEnYGFAK + 2H]$^{2+}$) and [H_2O + NH_3] (observed in ECD of [GPLEnYGFAKGPLAK + 3H]$^{3+}$) (both of which contain ammonia) also decrease in intensity far more sharply than for the losses which do not contain ammonia. These data appear to corroborate the suggestion that ammonia loss requires interaction between the BAAR and the 3-nitrotyrosine.

The AI ECD results for doubly-charged GPLEnYGFAKGPLAK are less straightforward to interpret, with a rapid decrease in [H_2O + NH_3], not noted in any of the other peptides or charge states, and a general increase of [$^{\bullet}$OH + H_2O + NH_3] loss up to ~30 % laser power followed by a general decrease at higher energies. This would suggest that an increase in infrared activation promotes $^{\bullet}$OH formation hence resulting in [$^{\bullet}$OH + H_2O + NH_3] formation Although it cannot be disproved that water or ammonia are also promoted, $^{\bullet}$OH loss is suggested due to the increase in [$^{\bullet}$OH + H_2O + NH_3] mirroring the decrease in [H_2O + NH_3] intensity. A similar observation was made by Sohn *et al*. [108]: they showed that $^{\bullet}$OH loss was promoted following occupation of higher vibrational energy levels. As reported in **Chapter 3**, ETD and saETD analysis did not result in $^{\bullet}$OH loss; however, this can also be concluded to be due to the vibrational energy of the peptide being insufficient, whereas ECD

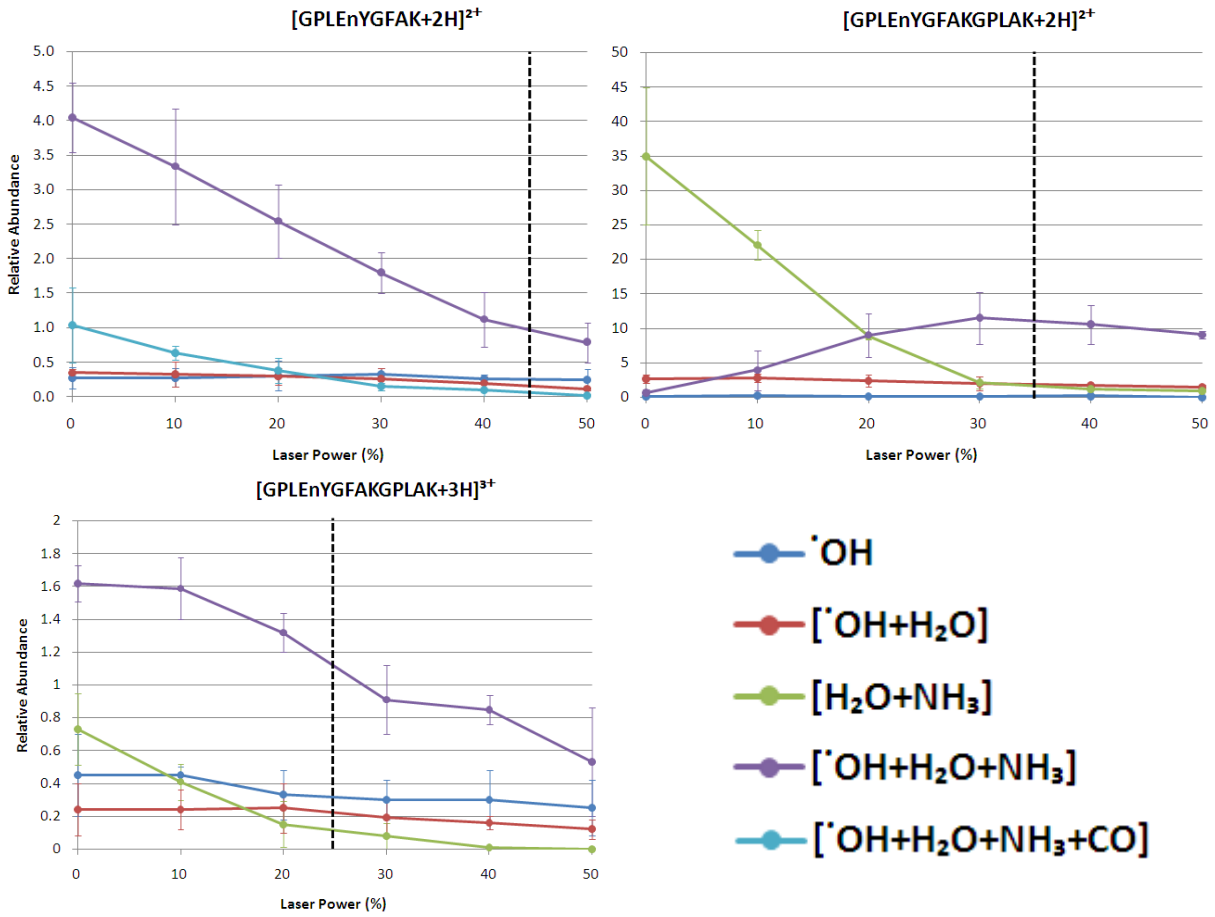

Figure 4.2: Effect of pre-ECD infrared activation of neutral loss formation

Effect of increasing pre-ECD infrared irradiation on the intensities of neutral loss peaks (normalised to the charge-reduced species) for $[GPLEnYGFAK + 2H]^{2+}$ (**Upper Left**), $[GPLEnYGFAKGPLAK + 2H]^{2+}$ (**Upper Right**), and $[GPLEnYGFAKGPLAK + 3H]^{3+}$ (**Lower Left**). The dashed vertical line shows the IRMPD threshold of the peptide, *i.e.* the laser power at which IRMPD is observed. The loss of ammonia, in combination with other neutral species, is highly sensitive to interactions within the peptides, induced by infrared activation. Errors bars constitute standard deviation of n=3.

results in sufficient vibrational energy for •OH loss. Nevertheless, these results conclusively show that interactions between sites within each peptide are crucial for ammonia loss.

4.2.3 Effect of 3-nitrotyrosine site on ammonia loss

The AI ECD data shown above suggest that intramolecular interactions within the peptide are extremely important for ammonia loss following ECD. This conclusion also suggests that the site of 3-nitrotyrosine within the peptide would likely be important to allow (or prevent) intramolecular interactions (and hence ammonia loss). To investigate whether the site of the 3-nitrotyrosine residue affects the abundance and/or presence of ammonia loss a range of synthetic peptides (nYAAAAAAK, AnYAAAAAK, AAnYAAAAK, AAAnYAAAK, AAAAnYAAK, AAAAAnYAK, and AAAAAAAnYK) were analysed by ECD.

ECD mass spectra of these nitrated peptides along with their unmodified counterpart with the same total number of amino acid residues, *i.e.* AAAAAAAK, are shown in **Figure 4.3**. These peptides do not appear to fragment *via* typical Cornell or UW mechanisms, *i.e.* N-Cα bond cleavage. The favoured fragmentation pathway appears to be at the N-C_O bond resulting in *b* and *y* fragment ions. This behaviour has been identified previously by Tsybin and co-workers [178], and is likely due to the formation of secondary structures within the gas phase [179]; however, this observation does not prevent conclusions being made about the effect of the site of a 3-nitrotyrosine amino acid residue within a peptide on ECD generated neutral losses.

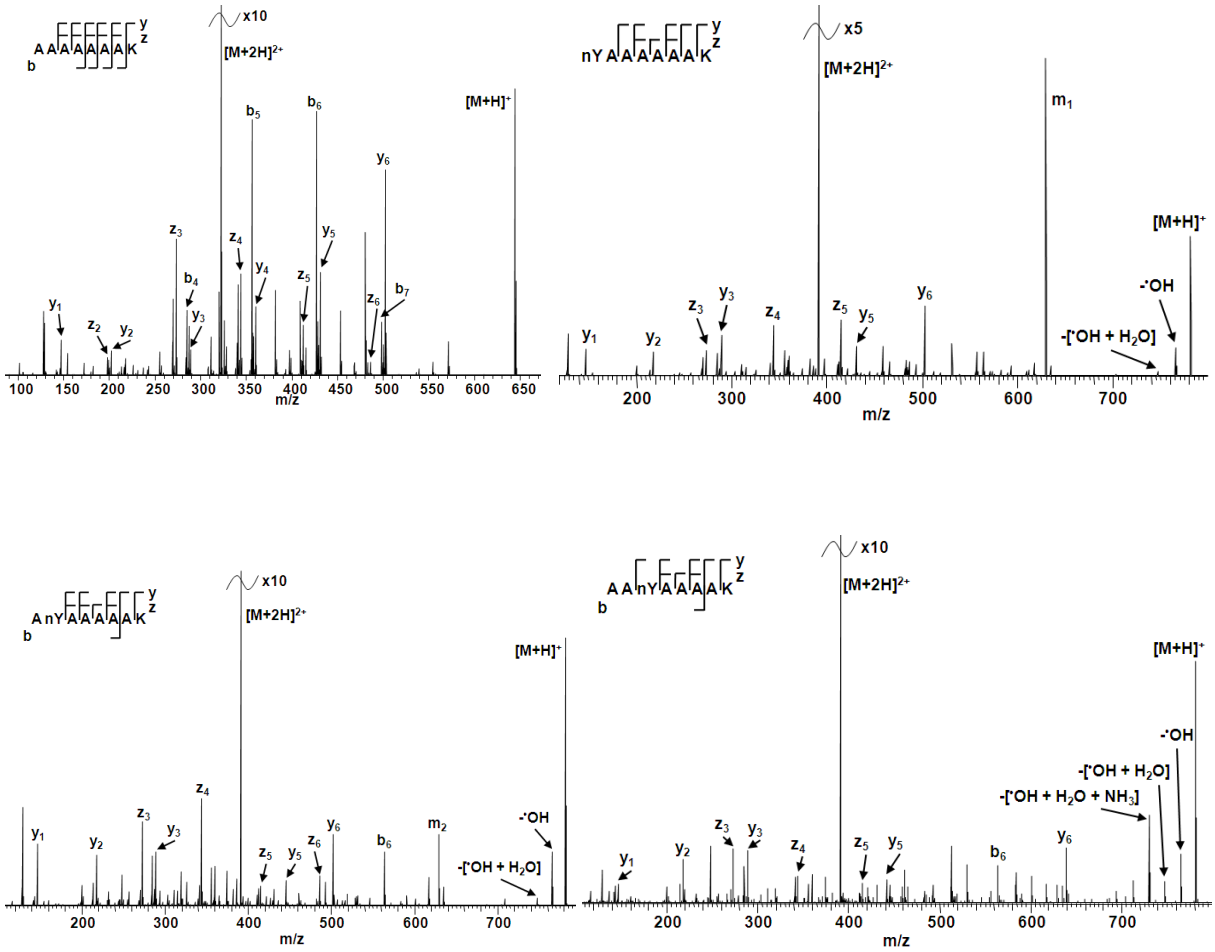

Figure 4.3.1: ECD mass spectra of polyAla 3-nitrotyrosine-containing peptides

ECD mass spectra of doubly-charged unmodified $[AAAAAAAK + 2H]^{2+}$ (**Upper Left**) peptide ions, and the doubly-charged nitrated $[nYAAAAAAK + 2H]^{2+}$ (**Upper Right**), $[AnYAAAAAK + 2H]^{2+}$ (**Lower Left**), and $[AAnYAAAAK + 2H]^{2+}$ (**Lower Right**) peptide ions. Ammonia loss, as $[^{\bullet}OH + H_2O + NH_3]$, is only present following ECD of $[AAnYAAAAK + 2H]^{2+}$.

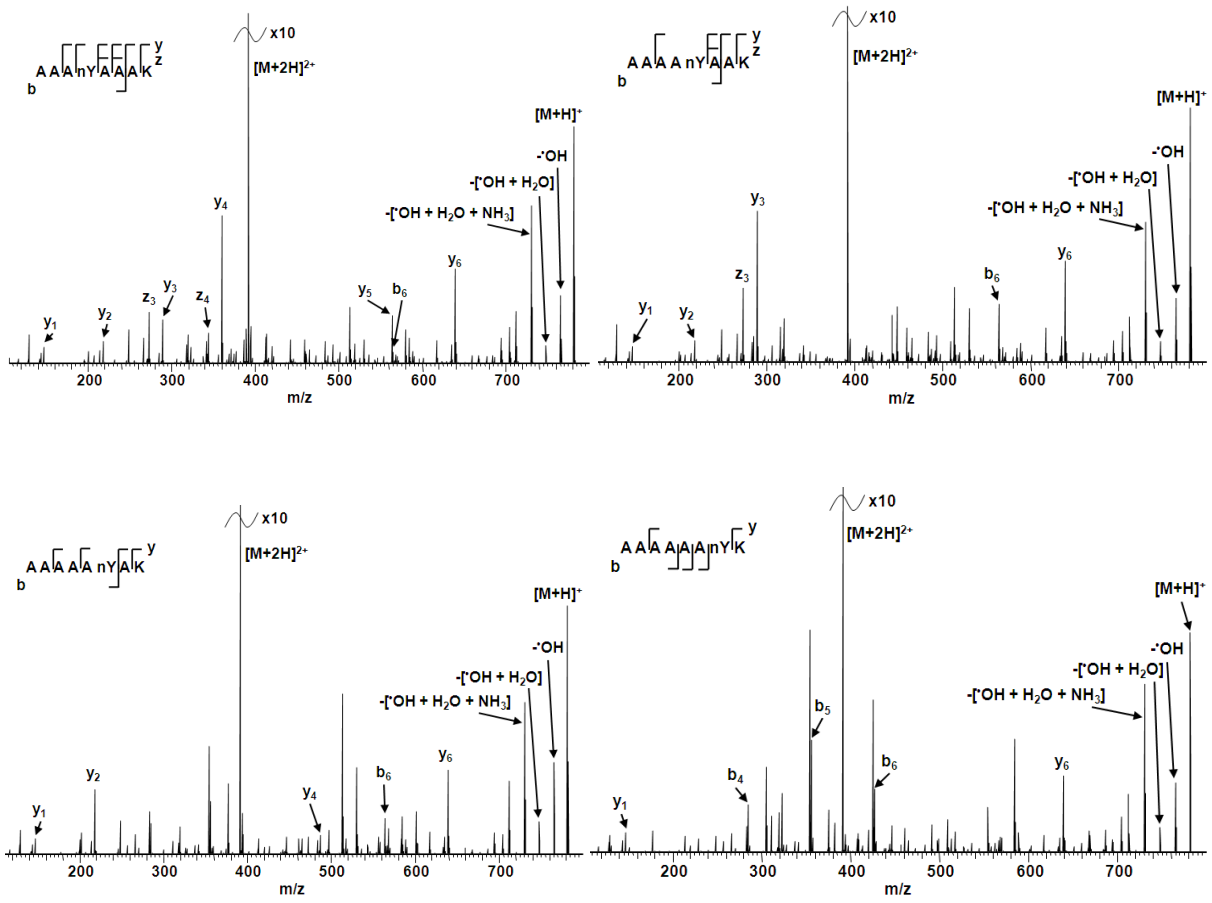

Figure 4.3.2: ECD mass spectra of polyAla 3-nitrotyrosine-containing peptides

ECD mass spectra of the doubly-charged nitrated $[AAAnYAAAK + 2H]^{2+}$ (**Upper Left**), $[AAAAnYAAK + 2H]^{2+}$ (**Upper Right**), $[AAAAAnYAK + 2H]^{2+}$ (**Lower Left**), $[AAAAAAnYK + 2H]^{2+}$ (**Lower Right**) peptide ions. Ammonia loss, as $[^{\bullet}OH + H_2O + NH_3]$, is present following ECD of all peptides in high intensities.

Interestingly, ECD of both [nYAAAAAAK + 2H]2+ and [AnYAAAAAK + 2H]2+ results in intense peaks identified as m1 and m2 ions, respectively. m ions, which are not seen in any other mass spectra in this work, are the notation used for the ion formed following cleavage of the Cα-Cβ bond, resulting in the total loss of the amino acid residue side chain.

In these ECD mass spectra, peaks corresponding to loss of $^{\bullet}OH$, and [$^{\bullet}OH + H_2O$] are seen in all cases; however, the loss of [$^{\bullet}OH + H_2O + NH_3$] is only observed for peptides AAnYAAAAK, AAAnYAAAK, AAAAnYAAK, AAAAAnYAK, and AAAAAAnYK, supporting the hypothesis that ammonia loss is dependent on the site of the 3-nitrotyrosine within the peptide. This relationship is more easily seen in **Figure 4.4**. Neither $^{\bullet}OH$ or [$^{\bullet}OH + H_2O$] losses are affected by the site of the nTyr amino acid residue within the peptide; however, the position of nitration is critical for the loss of [$^{\bullet}OH + H_2O + NH_3$]. It can be seen that when the nTyr residue is greater than five amino acids away from the Lys, no ammonia loss is observed; however, once this distance is reduced it appears as though there is a direct correlation between the proximity of the nTyr to the Lys and the intensity of the neutral loss (the shorter the distance the greater the intensity of [$^{\bullet}OH + H_2O + NH_3$] loss) except AAAnYAAAK. Alternatively, the loss of ammonia may require a specific distance between the nTyr residue and the protonated N-terminus to allow sufficient peptide folding.

4.2.4 ECD of Arg-containing nitrated peptides

Data above suggest that ammonia arises from the Lys side chain, and that an interaction between the nitro group and the Lys side chain is required for ammonia loss. To investigate

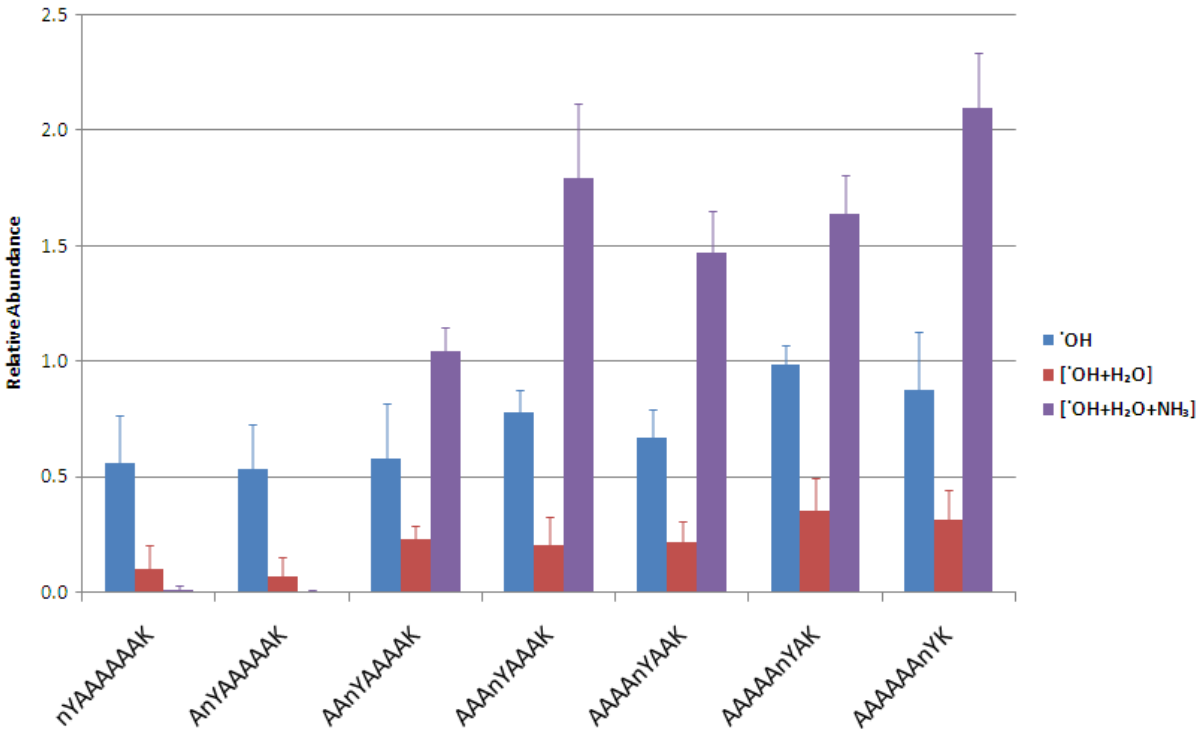

Figure 4.4: Effect of 3-nitrotyrosine position within a peptide on neutral losses observed following ECD

Effect of the site of the 3-nitrotyrosine within a peptide on the presence and intensity (normalised to the charge-reduced species) of certain neutral losses attributed to be formed from either the electron predator or hydrogen trap mechanism. The site of 3-nitrotyrosine does not largely affect the intensity of either $^{\bullet}OH$ or [$^{\bullet}OH + H_2O$] loss, whereas the formation and intensity of [$^{\bullet}OH + H_2O + NH_3$] is dramatically affected. Errors bars constitute standard deviation of n=3.

this hypothesis, the ECD of Arg-containing peptides, *i.e.* GPLEYGFAR and GPLEYGFARGPLAR, were undertaken to ascertain whether a change in basic amino acid residue (BAAR) would affect the outcome of peptide ECD of these nitrated peptides. The ECD mass spectra of these nitrated peptides are shown in **Figure 4.5**. As for the Lys-containing peptides, ECD results in very minor peptide sequence coverage (3/8 N-Cα bonds cleaved for GPLEnYGFAR and 3/13 N-Cα bonds cleaved for GPLEnYGFARGPLAR). This result shows that either the electron predator or hydrogen trap mechanism is dominant independent of the nature of the BAAR.

Abundant peaks corresponding to neutral losses from the charge-reduced species were also observed for the Arg-containing nitrated peptides. As for the Lys-containing analogue, the most abundant loss observed on ECD of $[GPLEnYGFAR + 2H]^{2+}$ is $[^{\bullet}OH + H_2O + NH_3]$; however, the neutral loss profiles do vary between the peptides with the relative abundance of $[^{\bullet}OH + H_2O]$ loss being much greater for the Arg peptide than for the Lys peptide. In addition, neutral losses involving CO were observed for the Arg peptide, as were fragments resulting from cleavages within the Arg side chain. For the longer peptides ($[GPLEnYGFA(R/K)GPLA(R/K) + 2H]^{2+}$), variation in the neutral loss profiles is again observed. For the Lys-containing peptide, the most abundant loss was $[H_2O + NH_3]$ whereas for the Arg-containing peptide the most abundant losses are $[^{\bullet}OH + H_2O + NH_3]$ and H_2O. Losses involving CO were again observed for the Arg-containing peptide. These data do not disprove the hypothesis that ammonia loss derives from the BAAR side chain. To identify whether intramolecular interactions within Arg-containing peptides are necessary for ammonia loss, as noted with Lys peptides, AI ECD experiments were undertaken.

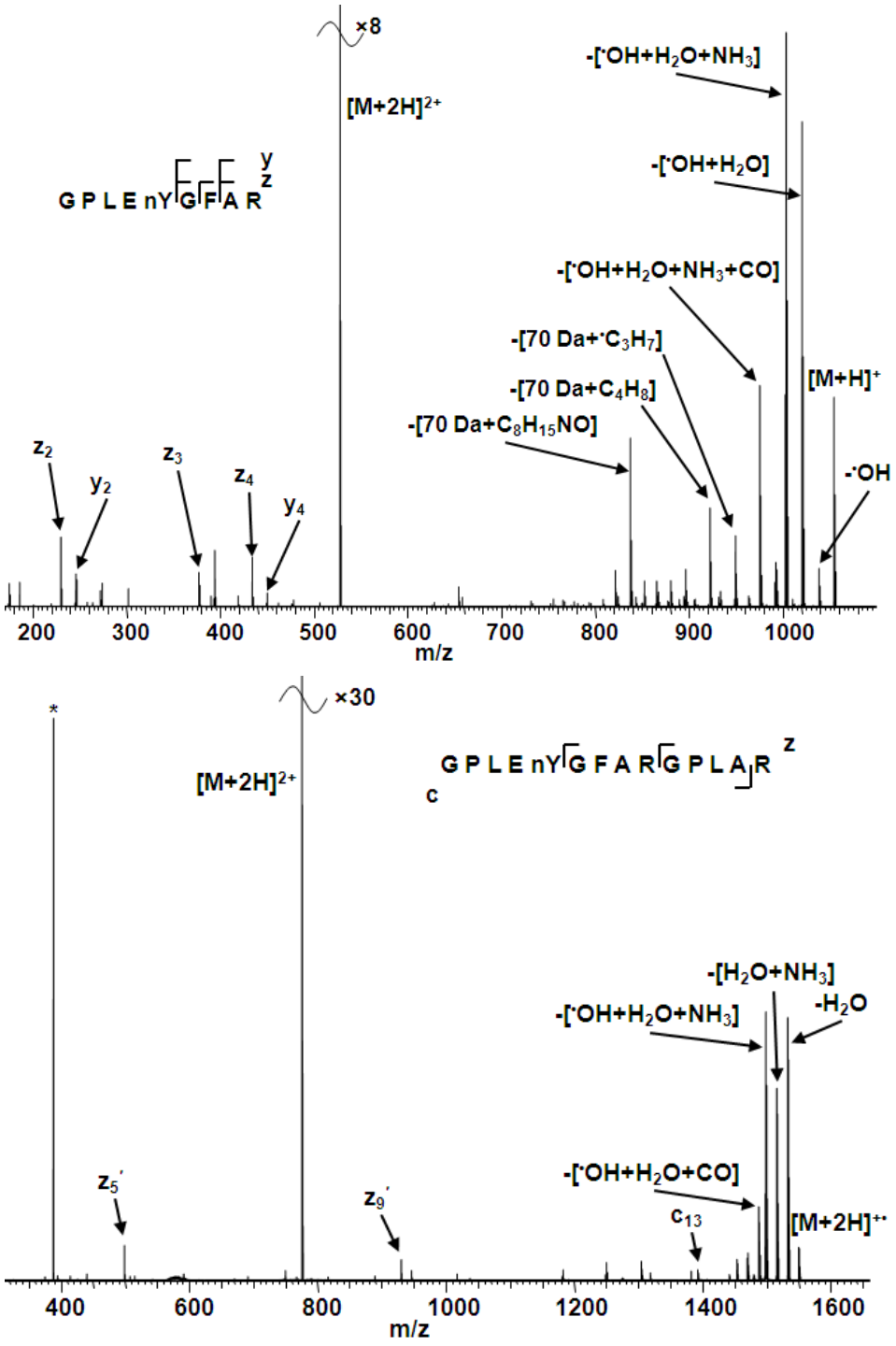

Figure 4.5: ECD mass spectra of nitrated doubly-charged Arg-containing peptides

ECD mass spectra of doubly-charged and nitrated $[GPLEnYGFAR + 2H]^{2+}$ and $[GPLEnYGFARGPLAR + 2H]^{2+}$ peptide ions. The second harmonic peak, present within the ECD mass spectrum of $[GPLEnYGFARGPLAR + 2H]^{2+}$ is identified by *. Loss of 70 Da is used for the combined loss of $[^{\bullet}OH + H_2O + NH_3 + CO]$. The substitution of Lys for Arg makes little difference to ECD behaviour, with the electron predator or hydrogen atom mechanism dominating, and neutral losses from the charge-reduced precursor ion.

Data collected from AI ECD (pre-ECD activation) experiments of doubly-charged GPLEnYGFAR and doubly- and triply-charged GPLEnYGFARGPLAR are shown in **Figure 4.6**. The neutral losses formed following AI ECD all follow a similar trend irrelevant of peptide sequence or charge state, unlike that seen for Lys-containing peptides, with the exception of $[GPLEnYGFAKGPLAK + 2H]^{2+}$. Here, in all cases the dominant neutral loss corresponds to the combined loss of [$^{\bullet}OH + H_2O + NH_3$], and when increasing infrared irradiation results in an increase in abundance. This increase in [$^{\bullet}OH + H_2O + NH_3$] loss is noted up to a laser power of ~30 % before a gradual decrease in peak intensity. As with the Lys-peptides, the other neutral losses do not appear to be largely affected by infrared activation.

The behaviour observed may be due to the nature of the BAARs. Arginine has a higher proton affinity than lysine. It can be proposed that in a protonated state the corresponding peptides will have differing energies, with the Arg-containing peptide having a lower energy than its Lys-containing counterpart. In **Chapter 3** it was shown that the neutral losses depend largely on the energy following ECD, ETD and saETD. Therefore it is suggested that [$^{\bullet}OH + H_2O + NH_3$] loss is promoted once sufficient energy is available, hence an increase in intensity is observed following laser activation of these peptides. In the Arg-peptides the maximum intensity is reached at ~30 % laser power. The subsequence decrease can be explained by disruption of intramolecular bonds and prevention of ammonia loss.

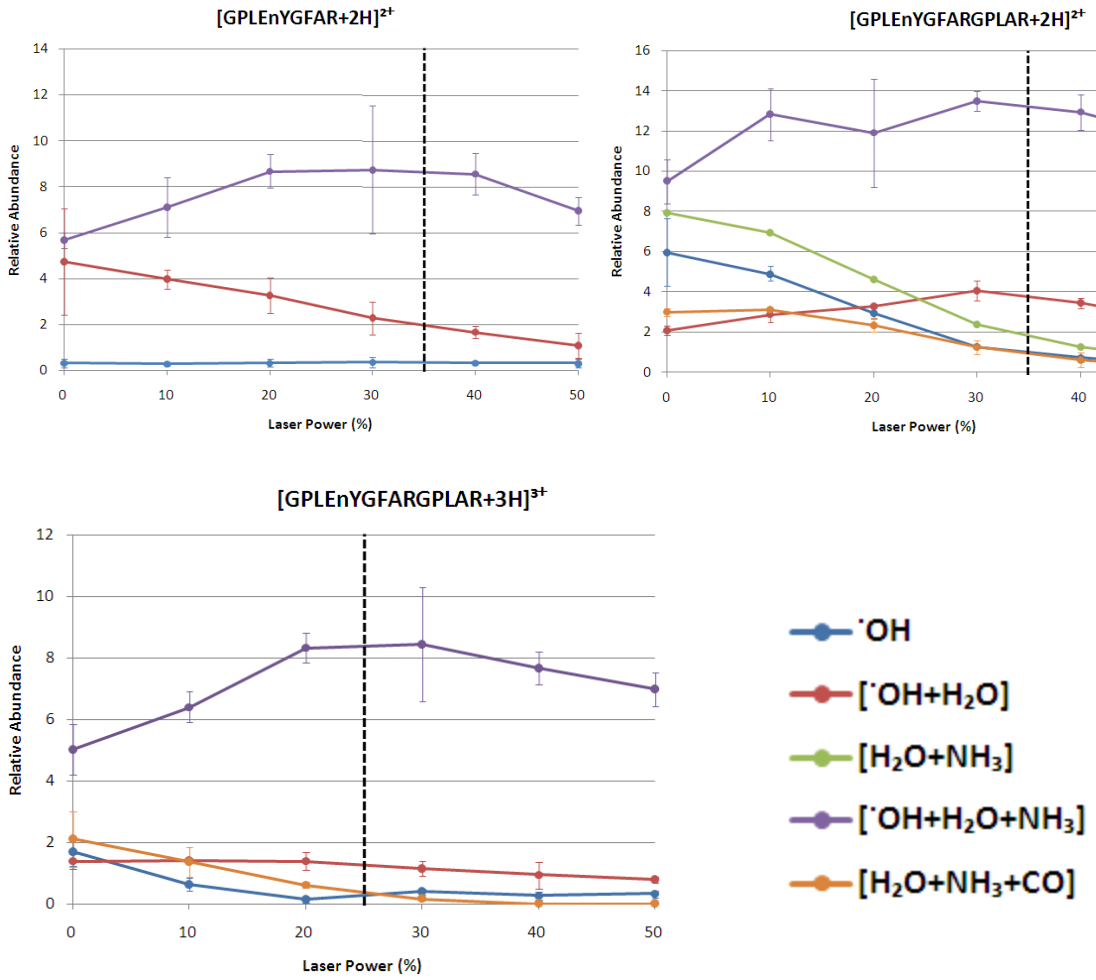

Figure 4.6: Effect of AI ECD of Arg-containing peptides on neutral loss formation

Effect of increasing pre-ECD infrared irradiation on the intensities of neutral loss peaks (normalised to the charge-reduced species) for $[GPLEnYGFAR + 2H]^{2+}$ (**Upper Left**), $[GPLEnYGFARGPLAR + 2H]^{2+}$ (**Upper Right**), and $[GPLEnYGFARGPLAR + 3H]^{3+}$ (**Lower Left**). The dashed vertical line shows the IRMPD threshold of the peptide. The combined loss of $[^{\bullet}OH + H_2O + NH_3]$ increases up to ~30 % for all peptides, suggesting a mechanistic optimal vibrational energy, followed by a decrease, suggesting removal of intramolecular bonds which are otherwise required for ammonia loss. Errors bars constitute standard deviation of n=3.

4.2.5 ECD of non-BAAR-containing nitrated peptides

It has been previously shown that ammonia loss following ECD of unmodified peptides originates from the N-terminus [180]; however, the data shown so far in this chapter appear to suggest that the loss of ammonia is arising from the BAAR side chain. To investigate this hypothesis, analysis of peptides without Arg or Lys, *i.e.* non-BAAR-containing peptides, was undertaken. Specifically, these peptides were GPLEYGFAL and GPLEnYGFAL, synthesised and analysed as described in **Section 2.1.2** and **2.2.10.2**.

The ECD mass spectra of the unmodified and the nitrated non-BAAR-containing peptide are shown in **Figure 4.7**. ECD of the nitrated peptide results in the neutral loss of both $^{\bullet}$OH and H_2O (although in relatively low abundances). Neither loss is identified following ECD of the unmodified non-BAAR-containing peptide suggesting that $^{\bullet}$OH and H_2O loss result from the presence of 3-nitrotyrosine. Importantly, no neutral losses containing ammonia are observed. Therefore these data appear to corroborate the initial hypothesis that the ammonia loss is originating from the BAAR side chain, be it Arg or Lys. Interestingly, both ECD mass spectra appear very similar with abundant backbone fragments including *b* ions being identified, suggesting that ECD does not simply follow the electron predator or hydrogen trap mechanism, and this issue is discussed in more detail in **Section 4.3**.

4.2.6 ECD of N-terminal acetylated nitrated peptides

To further investigate the origin of ammonia loss, ECD of selectively N-terminal acetylated GPLEnYGFAK and GPLEnYGFAR were undertaken. Along with the ECD mass spectra of the N-acetylated nitrated peptides, shown in **Figure 4.8**, CID mass spectra are also shown to

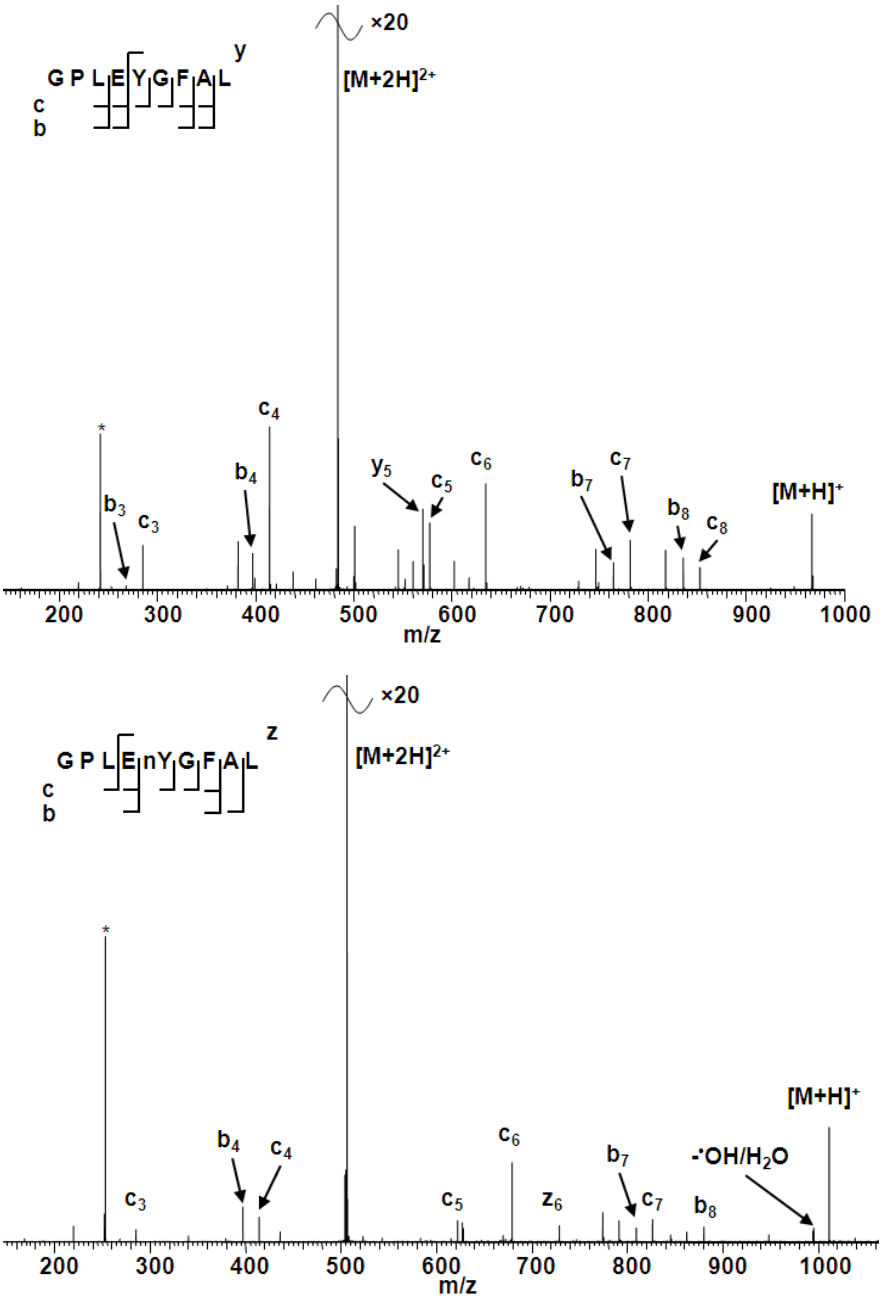

Figure 4.7: ECD mass spectra of non-BAAR-containing peptides

ECD mass spectra of unmodified [GPLEYGFAL + 2H]$^{2+}$ peptide ions, and nitrated [GPLEnYGFAL + 2H]$^{2+}$ peptide ions. The second harmonic peak, present within both ECD mass spectra is identified by *. Addition of the nitro group appears to make very little difference to the ECD behaviour of non-BAAR-containing peptides, with the observation of backbone fragment ions in both cases. Loss of ammonia is not observed.

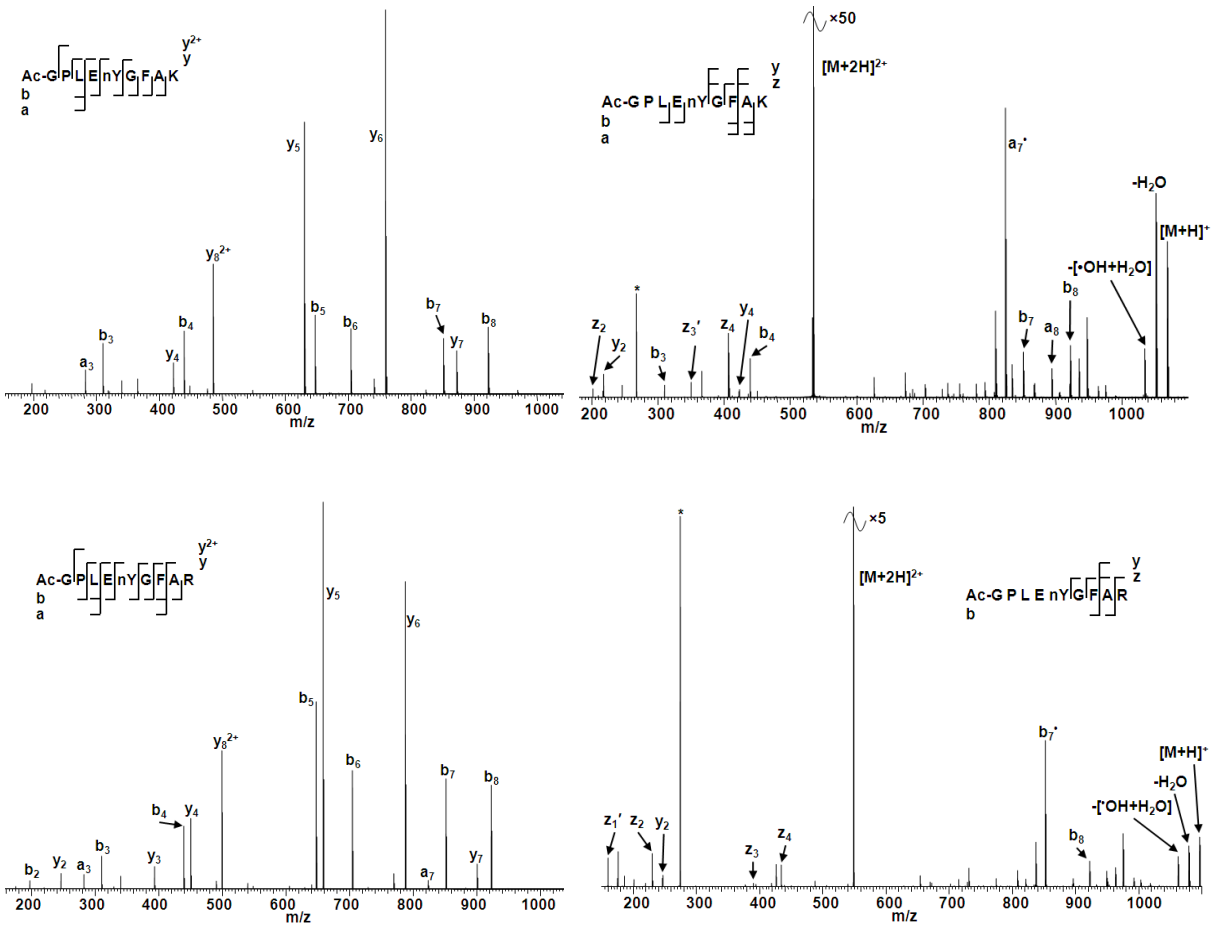

Figure 4.8: MS/MS mass spectra of selectively N-terminal acetylated nitrated peptides

CID (**Left**) and ECD (**Right**) mass spectra of selectively N-terminal acetylated doubly-charged nitrated [Ac-GPLEnYGFAK + 2H]$^{2+}$ (**Upper**) and [Ac-GPLEnYGFAR + 2H]$^{2+}$ (**Lower**). CID confirms that acetylation has taken place selectively on the N-terminus of the peptides only (see text for masses of identified fragment ions).ECD results in abundant losses of H_2O and [$^{\bullet}OH$ + H_2O] from the charge-reduced precursor ion. No ammonia loss was observed. An increase in peptide sequence coverage is noted following ECD, especially with the formation of *a*, *b* and *y* ions.

confirm that the acetylation was selectively attached to the N-terminus of the peptides. Indeed all *b* ions identified within the CID mass spectra for both peptides have a mass larger than the unmodified theoretical value for the addition of an acetyl-group, whereas all *y* ions all correlate to their unmodified theoretical value. For example, b_7 of [Ac-GPLEnYGFAK + 2H]$^{2+}$ had an observed *m*/*z* of 851.3564, a theoretical unmodified value of *m*/*z* 809.3464 and a theoretical N-terminal acetylated *m*/*z* of 851.3570; whereas the y_6 ion was observed to be *m*/*z* 759.3302, a theoretical unmodified value of *m*/*z* 759.3308, and a theoretical Lys-acetylated *m*/*z* of 801.3414.

From the ECD mass spectra, three points of note can be identified. Firstly, neutral losses containing ammonia were not observed, contradicting the non-BAAR-containing data, and suggesting that the ammonia does originate from the N-terminus. Secondly, abundant losses of H_2O and [$^{\bullet}OH + H_2O$] are identified, suggesting that the electron predator or hydrogen trap mechanism is taking place. Finally, the backbone cleavage observed differs from that observed in the absence of the N-acetylation, with the observation of abundant *a*, *b* and *y* ions. This latter observation is discussed in more detail in **Section 4.3**.

4.2.7 MS^3 (ECD-IRMPD) analysis of nitrated peptides

The ECD data from the non-BAAR-containing peptide and the N-acetylated nitrated peptides appear to give conflicting results with regard to the origin of ammonia loss. To unambiguously determine the origin of ammonia loss, MS^3 experiments were performed. As in-cell isolation is not possible on the LTQ-FT instrument, these experiments were performed on the Bruker 12 T Apex Qe Ultra at the University of Edinburgh in collaboration with Dr.

Logan Mackay, as detailed in **Section 2.2.10.5**. Data were collected and analysed by the author.

MS^3 (IRMPD of ECD fragments) experiments were completed of the most abundant neutral loss peak following ECD of GPLEnYGFAK, GPLEnYGFAR, and AAAnYAAAK, *i.e.* $[[M + 2H]-[^{\bullet}OH + H_2O + NH_3]]^+$ in all cases. These peptides were chosen to allow analysis of various BAARs, and because the most abundant ECD fragment of all these peptides is the same. This fragment ion was first formed with ECD, isolated within the ICR cell using correlated sweep excitation [181], and fragmented with IRMPD. The ECD mass spectra obtained on the Bruker reflect the ECD mass spectra of the same peptides obtained on the LTQ-FT as shown in **Figure 4.9**.

The MS^3 mass spectra are shown in **Figure 4.10**. In the MS^3 mass spectrum of GPLEnYGFAK, two peaks corresponding to singly-charged y_3 and y_4 fragments of the precursor peptide are observed, suggesting that none of the neutral losses originate C-terminal to the 3-nitrotyrosine residue. There is no peak corresponding to a y_5 ion; however, there is a peak corresponding to a y_5 ion with a mass loss equivalent to two oxygen atoms. This result suggests that the 3-nitrotyrosine residue is the site from which both hydroxyl radical and water derive, as postulated earlier in this thesis. The presence of these *y*-ion fragments also show that ammonia does not derive from the Lys residue.

No peaks corresponding to *b* ions are observed. A peak corresponding to $[b_3\text{-}NH_3\text{-}2H]^+$ is

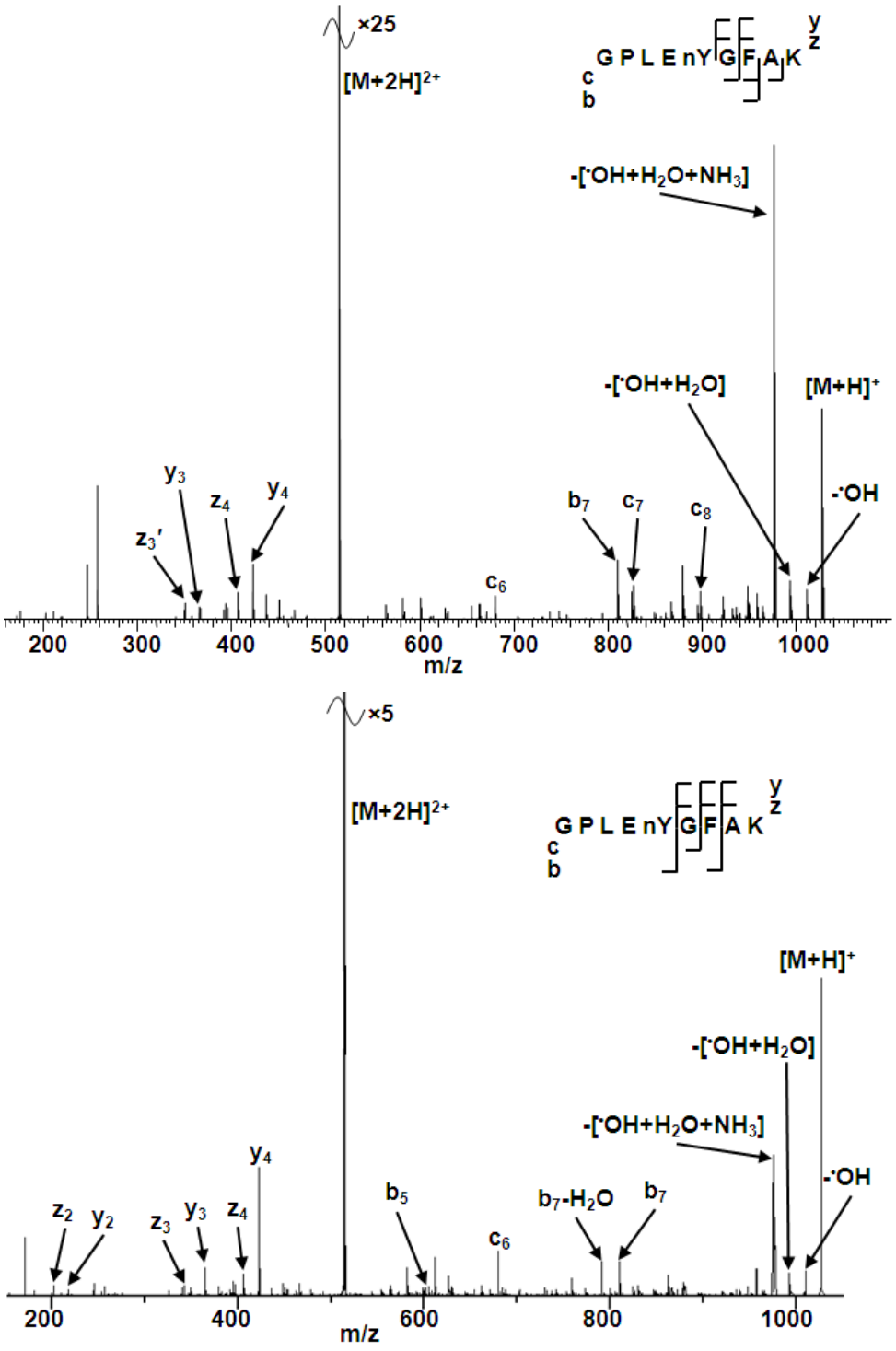

Figure 4.9: Comparison of ECD mass spectra from Thermo and Bruker MS

ECD mass spectra of doubly-charged nitrated [GPLEnYGFAK + 2H]$^{2+}$ analysed with the Thermo LTQ FT-Ultra (**Upper**) and Bruker 12 T Apex Qe Ultra (**Lower**). Both instruments resulted in similar ECD behaviour with abundant neutral losses, especially the combined loss of [$^{\bullet}$OH + H_2O + NH_3].

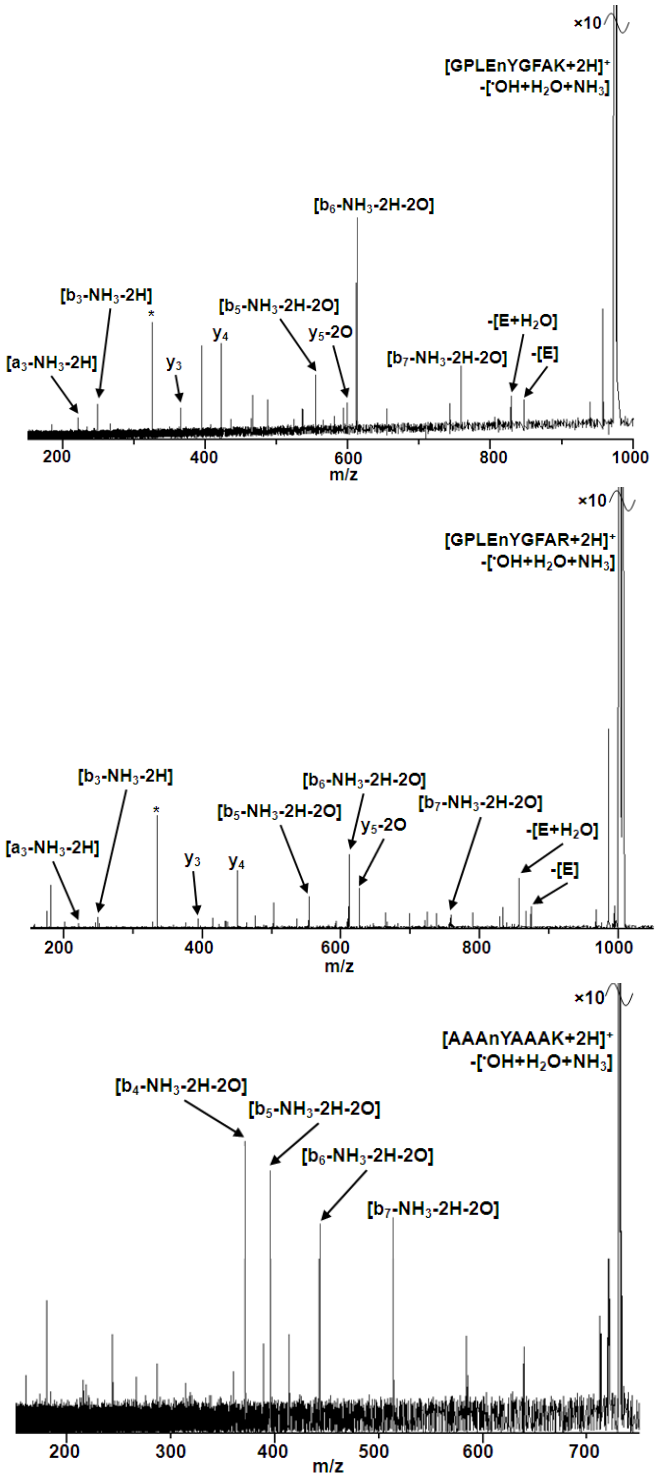

Figure 4.10: MS^3 mass spectra of 3-nitrotyrosine-containing peptides

MS^3 (ECD-IRMPD) mass spectra of doubly-charged nitrated $[GPLEnYGFAK + 2H]^{2+}$, $[GPLEnYGFAR + 2H]^{2+}$, and $[AAAnYAAAK + 2H]^{2+}$ peptide ions. For all peptides ECD resulted in the most dominant peak corresponding to $[M+2H]^{2+}$-$[^{\bullet}OH+H_2O+NH_3]$ which was further analysed with IRMPD to identify sites of neutral loss.

observed, as is $[a_3\text{-}NH_3\text{-}2H]^+$. The presence of these two ions suggests that ammonia is lost from the N-terminus. Further peaks within the mass spectrum, corresponding to sequence ions from the N-terminus, are also noted, specifically b_5, b_6 and b_7 all of which have a mass less than their theoretical value corresponding to ammonia, two oxygen atoms and two hydrogen atoms. These ions corroborate with the *y*-ion sequence suggesting that water and hydroxyl radical originate from the 3-nitrotyrosine and the ammonia from the N-terminus.

Curiously, there is a peak corresponding to the loss of a glutamic acid residue, as well as the loss of glutamic acid and water. This fragment could only arise following cyclisation of the N-terminal region of the peptide. It is hypothesised that this cyclisation forms following a reaction between the N-terminus and the 3-nitrotyrosine during ECD, likely resulting in the formation of ammonia, with concomitant cleavage of either the Glu-nTyr or Leu-Glu bonds. MS^3 results in the further fragmentation of the other bond, *e.g.* if Leu-Glu was the initial broken bond following ECD, then IRMPD resulted in the fragmentation of Glu-nTyr.

MS^3 of GPLEnYGFAR results in very similar data with the same backbone fragment ions being identified in both mass spectra. Once again, the C-terminal fragment ions suggest that water and hydroxyl radicals originate from the 3-nitrotyrosine, whereas the N-terminal fragment ions suggest that ammonia originates from the N-terminus. Again, loss of a glutamic acid residue is noted. These data also show that the BAAR does not affect the how ammonia loss, with the mechanism appearing to be consistent for both peptides.

Few fragments are identified in the MS^3 mass spectrum for AAAnYAAAK. These ions correspond to $[b_4\text{-}NH_3\text{-}2H\text{-}2O]^+$, $[b_5\text{-}NH_3\text{-}2H\text{-}2O]^+$, $[b_6\text{-}NH_3\text{-}2H\text{-}2O]^+$ and $[b_7\text{-}NH_3\text{-}2H\text{-}2O]^+$.

This result suggests that the hydroxyl radical, water, and ammonia losses all originate N-terminal of Ala4.

The results from the MS^3 analysis suggests the previous data from the poly-Ala peptides did not reflect the dependence of the position of the 3-nitrotyrosine with respect to the BAAR, but, in fact, the position of the 3-nitrotyrosine with respect to the N-terminus. This proximity between the N-terminus and 3-nitrotyrosine and ammonia loss appears inversely proportional, with ammonia loss occurring when the modification is at least three amino acid residues away from the N-terminus.

4.2.7 Molecular models of nitrated peptides

To fully investigate how the structure of the peptides and the interaction between the 3-nitrotyrosine, BAAR and N-terminus affects the ECD behaviour, molecular models of the polyAla peptides were generated, as described in **Section 2.2.13**, by the use of AMBER 10 and the ff99SB-ILDN forcefield. The molecular dynamic (MD) simulations were completed in 0.5 fs steps for a total of 500 ns at 325 K using a Langevin thermostat, to ensure that the gas-phase structures of the peptides would fully converge at a stable temperature. Once generated, the models were grouped together into five 100 ns windows, *i.e.* 0-100 ns, 100-200 ns, etc., prior to clustering analysis of the peptide structures depending on the root mean square deviation (RMSD) of their heavy atoms, *i.e.* C, O, and N, to ensure similar structures are clustered together. These clusters were then analysed against each other, again using RMSD of the heavy atoms, to identify whether a single stable converged structure, or several, had been obtained during the MD simulations.

The molecular models acquired for $[nYAAAAAAK + 2H]^{2+}$, shown in **Figure 4.11**, initially show a largely linear, unfolded structure. Although this was the most common structure within 1-100 ns of the MD simulations, it is likely to be relatively unstable as only 41.36 % of the total structures within this timeframe were grouped within this cluster and a further seven clusters were identified (with populations ranging from 1.22 % to 19.05 %). This linear structure remained the most dominant cluster for a further 100 ns of simulations with 38.47 % being identified as similar structures, and a direct comparison between these two dominant structures having a RMSD of the heavy atoms of only 0.978 Å, indicating large confidence of high similarity between cluster structure.

After 200 ns of MD simulations, the dominant structure changed significantly becoming far more folded than previously observed. The dominant structure, now with the two termini and 3-nitrotyrosine and lysine close-in-space, is significantly different to the dominant structure observed following 101-200 ns of MD with a RMSD of 5.507 Å, suggesting only small levels of spatial overlap between the peptidic structures; however, this dominant cluster is populated by only 30.7 % of the structures within 201-300 ns of simulations and a further 10 clusters calculated (with 0.83 % to 21.56 % populations).

After 300 ns, the peptide structure becomes far more stable, with a rotation of the C- and N-termini, such that the positively-charged N-terminus is directed at the C-terminal, and remains this way between 301-400 ns and 401-500 ns, with a RMSD of these two structures being 0.724 Å. These structures appear to be very stable with 100 % of the structures observed within the 301-400 ns timeframe being clustered together and 97.3 % within the 401-500 ns

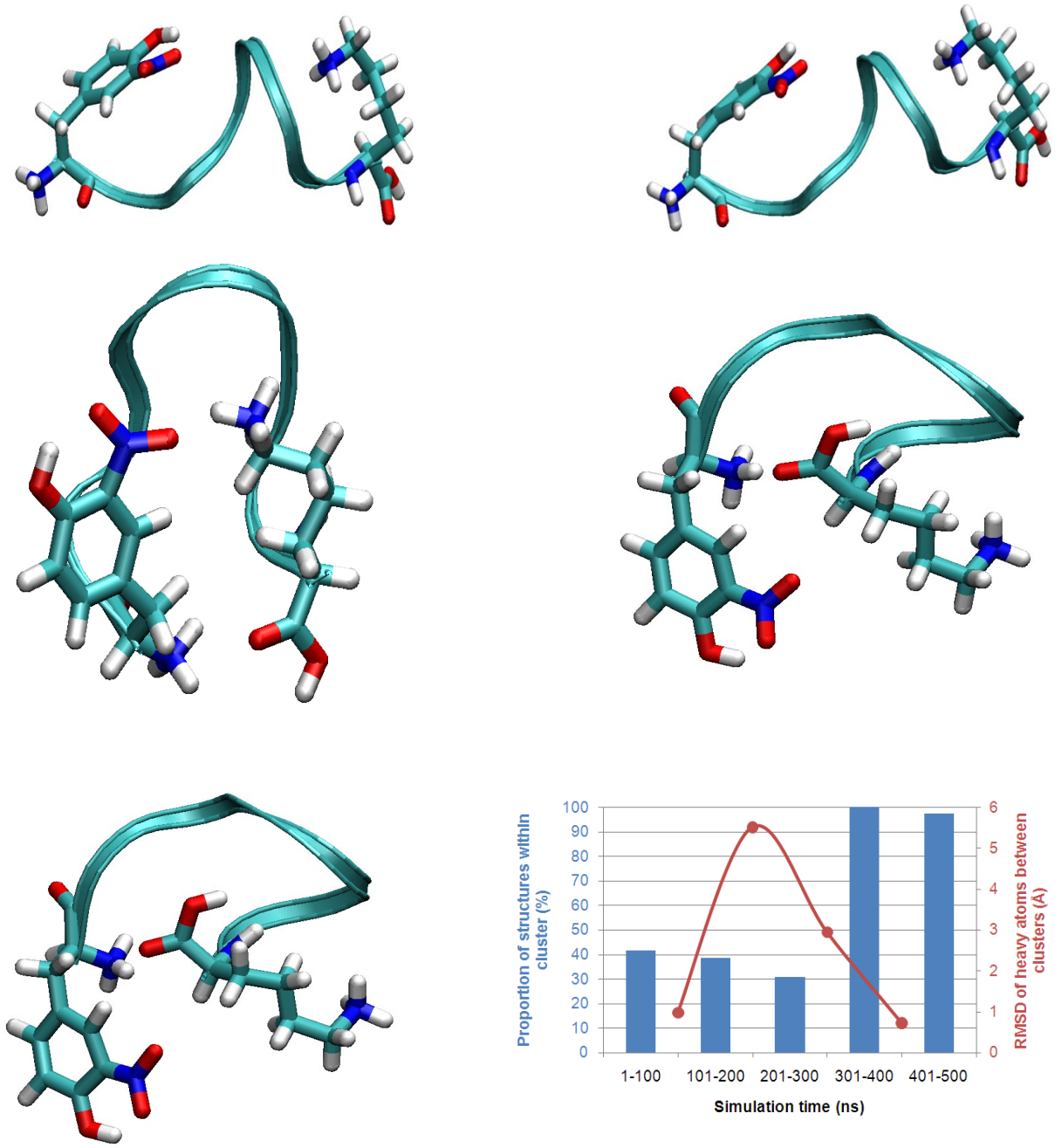

Figure 4.11: Molecular models of [nYAAAAAAK + 2H]$^{2+}$

Figures shown represent the most common structure between 0-100 ns (**Upper Left**), 101-200 ns (**Upper Right**), 201-300 ns (**Middle Left**), 301-400 ns (**Middle Right**) and 401-500 ns (**Lower Left**). (**Lower Right**) Graph shows the percentage proportion of the dominant structure within this simulation time window, and the RMSD in angstroms of heavy atoms between the structure and the most common structure from the previous time window.

timeframe. The very low RMSD value also indicates with high confidence that structural convergence of the peptides has taken place, and hence analysis of this structure can be undertaken.

Previously in this work it was observed that ECD of $[nYAAAAAAK + 2H]^{2+}$ does not result in the loss of ammonia. It was hypothesised that following initial electron capture at a protonated site, the electron must transfer to the 3-nitrotyrosine *via* the electron predator mechanism; when compared to the final dominant MD simulated structure it is likely that such a process is possible. Despite there not being any direct non-covalent interaction between the positive lysine and the 3-nitrotyrosine, the peptidic structure appears relatively strong especially with the interaction between the N- and C-termini. It is proposed that the electron would ultimately transfer to the 3-nitrotyrosine leading to hydroxyl and water neutral losses, but transfer to the N-terminus is inhibited. Similarly, if electron capture were to take place at the N-terminus it is predicted that the electron would be unable to transfer directly to the 3-nitrotyrosine. Thus it is proposed that the electron must transfer to other sites within the peptide prior to electron or hydrogen atom transfer to the nitro group.

To investigate the hypothesis that ammonia loss originates from the N-terminus, MD structures of the other peptides was undertaken. As shown previously ECD of $[AAAnYAAAK + 2H]^{2+}$ leads to abundant neutral loss of ammonia, in the form of $[^{\bullet}OH + H_2O + NH_3]$, which was concluded to originate from the N-terminus following MS^3 experiments. The molecular models of this peptide are shown in **Figure 4.12**. Immediately, it can be seen that the structures appear drastically different to those for [nYAAAAAAK +

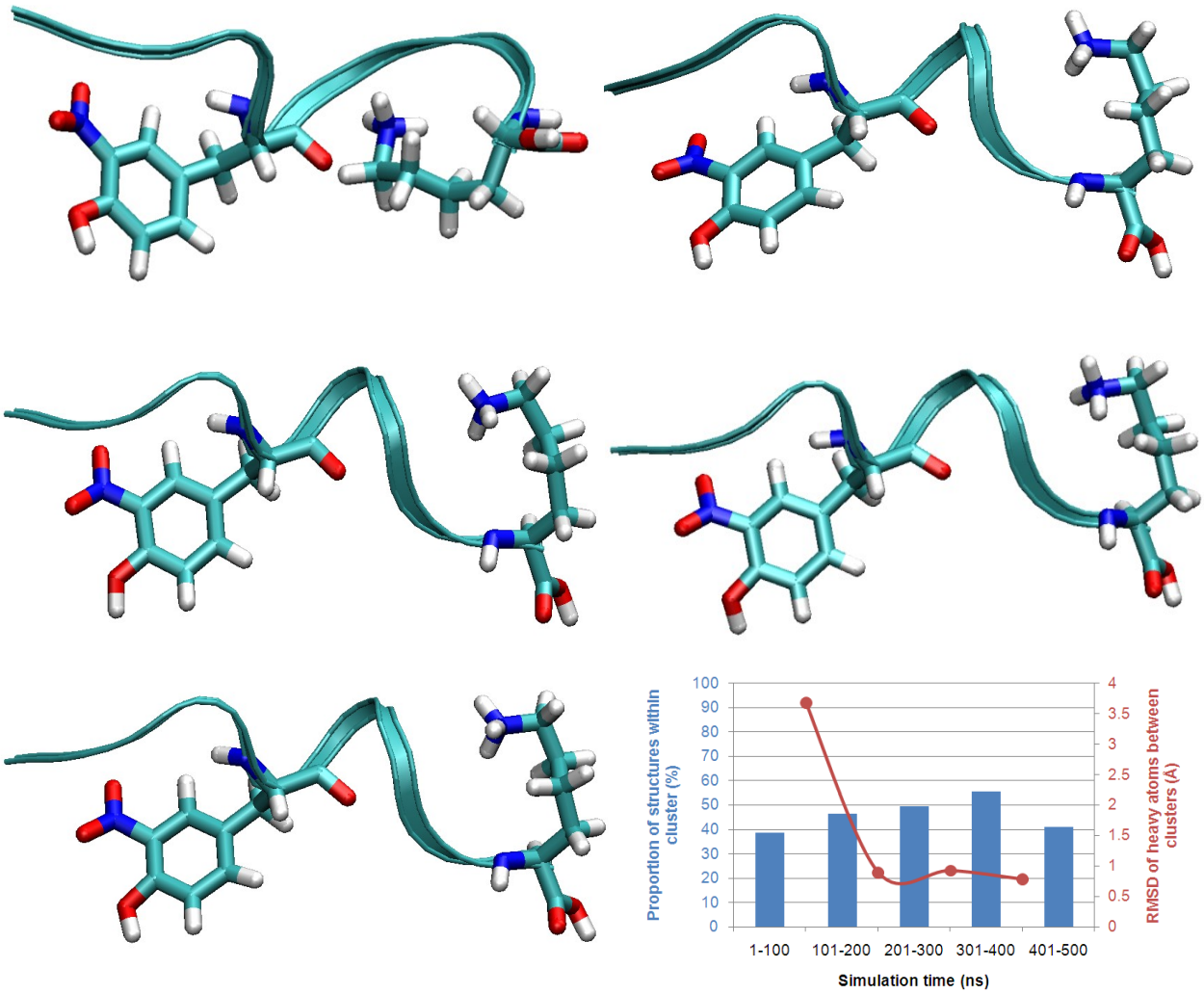

Figure 4.12: Molecular models of [AAAnYAAAK + 2H]$^{2+}$

Figures shown represent the most common structure between 0-100 ns (**Upper Left**), 101-200 ns (**Upper Right**), 201-300 ns (**Middle Left**), 301-400 ns (**Middle Right**) and 401-500 ns (**Lower Left**). (**Lower Right**) Graph shows the percentage proportion of the dominant structure within this simulation time window, and the RMSD in angstroms of heavy atoms between the structure and the most common structure from the previous time window.

$2H]^{2+}$, as there appears to be little, if any, alteration in structure from the initial extemded, unfolded, dominant structure identified in the initial 100 ns of MD simulations. Despite this apparent similarity, RMSD analysis does show some changes between the dominant structures formed between 1-100 ns and 101-200 ns, with a variation of 3.678 Å, which is due to rotation about the Ala residues at the C-terminus, resulting in the lysine side chain being directed into the peptide backbone. The peptide structure observed from 200 ns appears to be highly conserved up to the upper limit performed in these experiments with RMSD values of only 0.891 Å, 0.921 Å and 0.778 Å; however, in all these cases the cluster population is startling low with the only cluster being larger than 50 % at 301-400 ns, suggesting that a separate stable structure is also present.

Indeed, when analysing the second most abundant clusters throughout the simulations, a converged structure of maximum abundance of 45 % was also present. These are shown in **Figure 4.13**. In stark comparison to the dominant structure, this secondary structure appears to be far more compact and folded due to a further rotation about the C-terminal Ala residues, again with the lysine side chain appearing to be directed into the peptide backbone. RMSD analysis of the peptide structures between the timescales corroborates the hypothesis that a second stable converged structure is formed for this peptide, with values between the four structures identified between 101-500 ns of simulations being 0.790 Å, 0.960 Å and 0.900 Å.

A third converged structure is not present, at least in significant quantities, as the sum of the first and second most abundant clusters accounts for 80.94 % of the total population for 101-200 ns, 94.14 % for 201-300 ns, 96.33 % for 301-400 ns, and 66.97 % for 401-500 ns. A

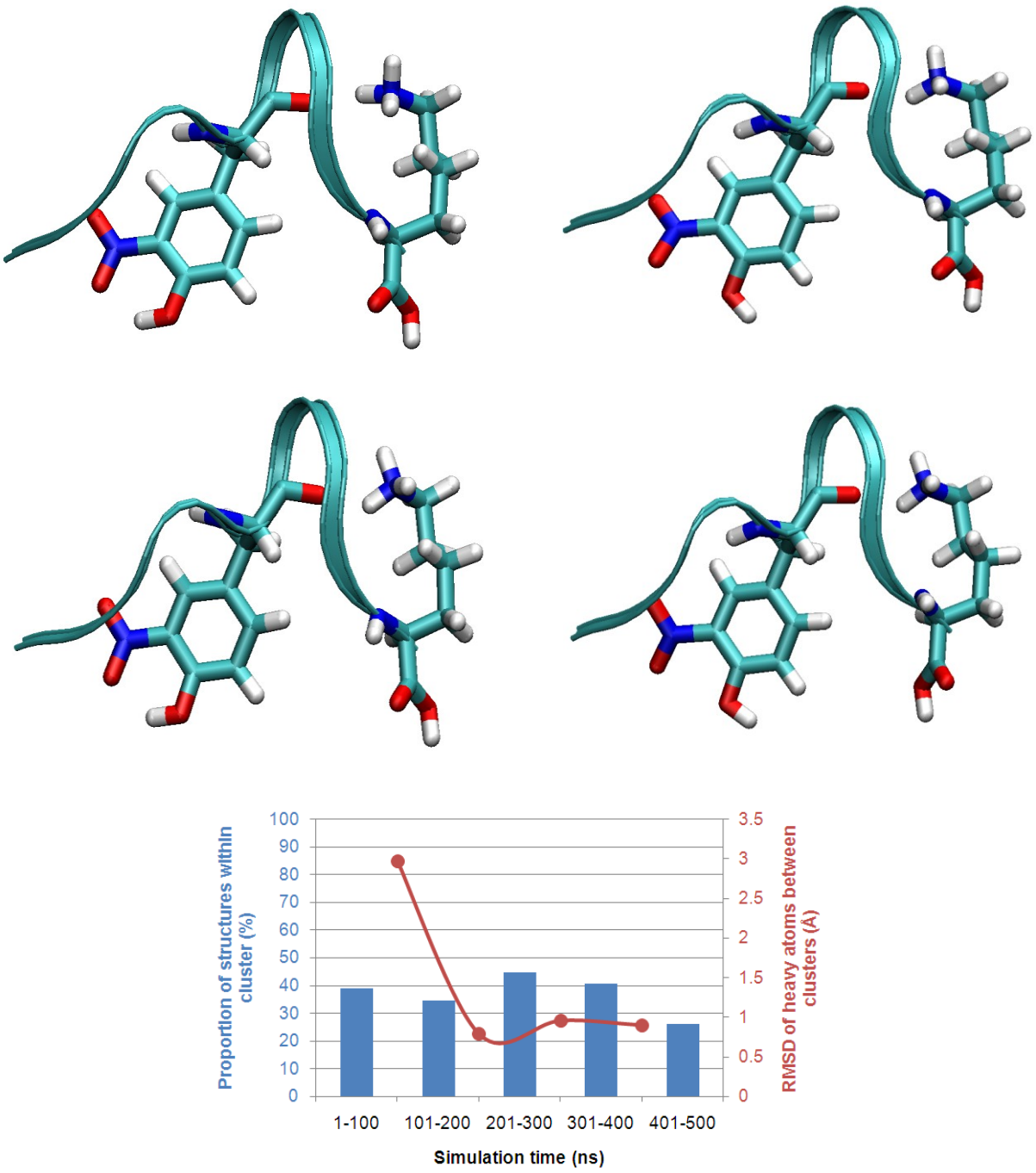

Figure 4.13: Second most abundant molecular models of [AAAnYAAAK + 2H]$^{2+}$

Figures shown represent the second most common structure between 101-200 ns (**Upper Left**), 201-300 ns (**Upper Right**), 301-400 ns (**Middle Left**) and 401-500 ns (**Middle Right**). (**Lower**) Graph shows the percentage proportion of the second most dominant structure within this simulation time window, and the RMSD in angstroms of heavy atoms between the structure and the second common structure from the previous time window (except for 101-200 ns which is compared to the most common structure at 1-100 ns).

direct comparison between the final, *i.e.* 401-500 ns timeframe, dominant and second most abundant structures corresponds to a RMSD of 2.585 Å, again confidently assigning two separate structures. It may be suggested that these MD simulations were not performed to allow total structural convergence, which only being completed for 500 ns is far lower than any experimental data collected; however, it has been reported, in parallel with this work, that field asymmetric ion mobility spectrometry (FAIMS) data for $[AAAnYAAAK + 2H]^{2+}$ also suggests it is formed of at least two stable structures [182].

For both converged structures the lysine side chain appears directed into the region of the peptide containing Ala5 and Ala6, which itself is adjacent to the 3-nitrotyrosine residue, thus it is likely that following initial electron capture at the lysine side chain, electron transfer would occur either directly to the 3-nitrotyrosine or into the peptide backbone at Ala5 or Ala6 prior to electron predation to the 3-nitrotyrosine.

In both the dominant and second most abundant peptide structures generated, it can be seen that the C-terminal of the peptide appears highly conserved. In fact RMSD of the heavy atoms between the two structures from Ala1 to Ala5 is 0.897 Å, but rises dramatically when adding further amino acid residues. This suggests that once electron transfer to the 3-nitrotyrosine has taken place, it is likely that both structures would follow the same mechanistic pathways for neutral losses. The experiments performed previously strongly suggest that ammonia loss originates from the N-terminus of the peptide with hydroxyl radicals and water originating from the 3-nitrotyrosine and these structures further strengthen these hypotheses, with the NO_2 group of the 3-nitrotyrosine directly interacting with the N-terminus.

The MD simulations for the other polyAla nitrated doubly-charged peptides were also completed. The dominant structures for $[AnYAAAAAK + 2H]^{2+}$, $[AAnYAAAAK + 2H]^{2+}$, $[AAAAnYAAK + 2H]^{2+}$, and $[AAAAAnYAK + 2H]^{2+}$ identified between 401-500 ns are shown in **Figure 4.14**. As with $[nYAAAAAAK + 2H]^{2+}$, these peptides had one dominant converged structure after 500 ns of MD, with at least 71 % of the population within 401-500 ns timeframe being clustered together (in two of the four cases, the entire population were grouped as a single cluster up to 3 Å of heavy atoms). With respect to the hypotheses developed in this work, these four structures support the finding that ammonia loss following ECD originates from the N-terminus. In can be seen in the representative model for $[AnYAAAAAK + 2H]^{2+}$, which does not result in ammonia loss in any form following ECD, that the NO_2 group of the 3-nitrotyrosine is directed away from the N-terminus toward the backbone and lysine side chain; however, for the other three peptides, which result in the neutral loss of ammonia following ECD, all have the 3-nitrotyrosine residue directed toward the N-terminus.

The molecular models generated for $[AAAAAAnYK + 2H]^{2+}$ are shown in **Figure 4.15**. ECD of this peptide resulted in the most abundant loss of ammonia, in the form of [$^{\bullet}OH + H_2O + NH_3$], for all of the polyAla nitrated peptides, and thus it would be expected that there would be a very strong interaction present between the 3-nitrotyrosine and the N-terminus; whereas, in fact, the 3-nitrotyrosine appears close-in-space to the lysine side chain (3.44 Å in comparison to 9.00 Å between 3-nitrotyrosine and N-terminus). These molecular models therefore suggest that in the case of $[AAAAAAnYK + 2H]^{2+}$ the ammonia originates from the lysine side chain rather than the N-terminus, indicating that perhaps there are two separate mechanisms for the neutral loss of ammonia following the electron predator mechanism. It should be noted, however, that further structural change such that the 3-nitrotyrosine becomes

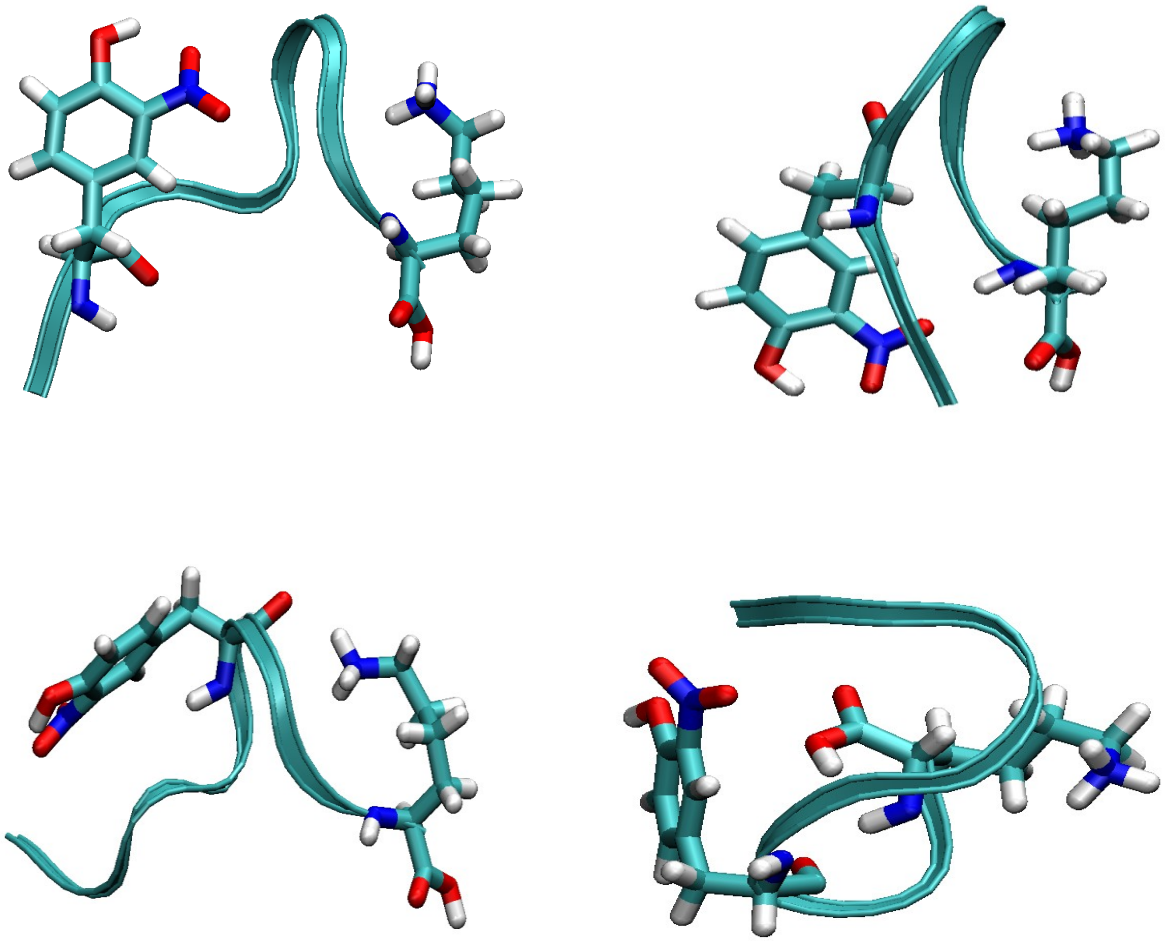

Figure 4.14: Molecular models of other polyAla nitrated peptides

Figures shown represent the most common molecular model structure between 401-500 ns of molecular dynamic simulations of $[AnYAAAAAK + 2H]^{2+}$ (71.9 % of the structures within this time window had this structure within 3 Å of heavy atoms) (**Upper Left**), $[AAnYAAAA + 2H]^{2+}$ (100 %) (**Upper Right**), $[AAAAnYAAK + 2H]^{2+}$ (78.6 %) (**Lower Left**), and $[AAAAAnYAK + 2H]^{2+}$ (100 %) (**Lower Right**).

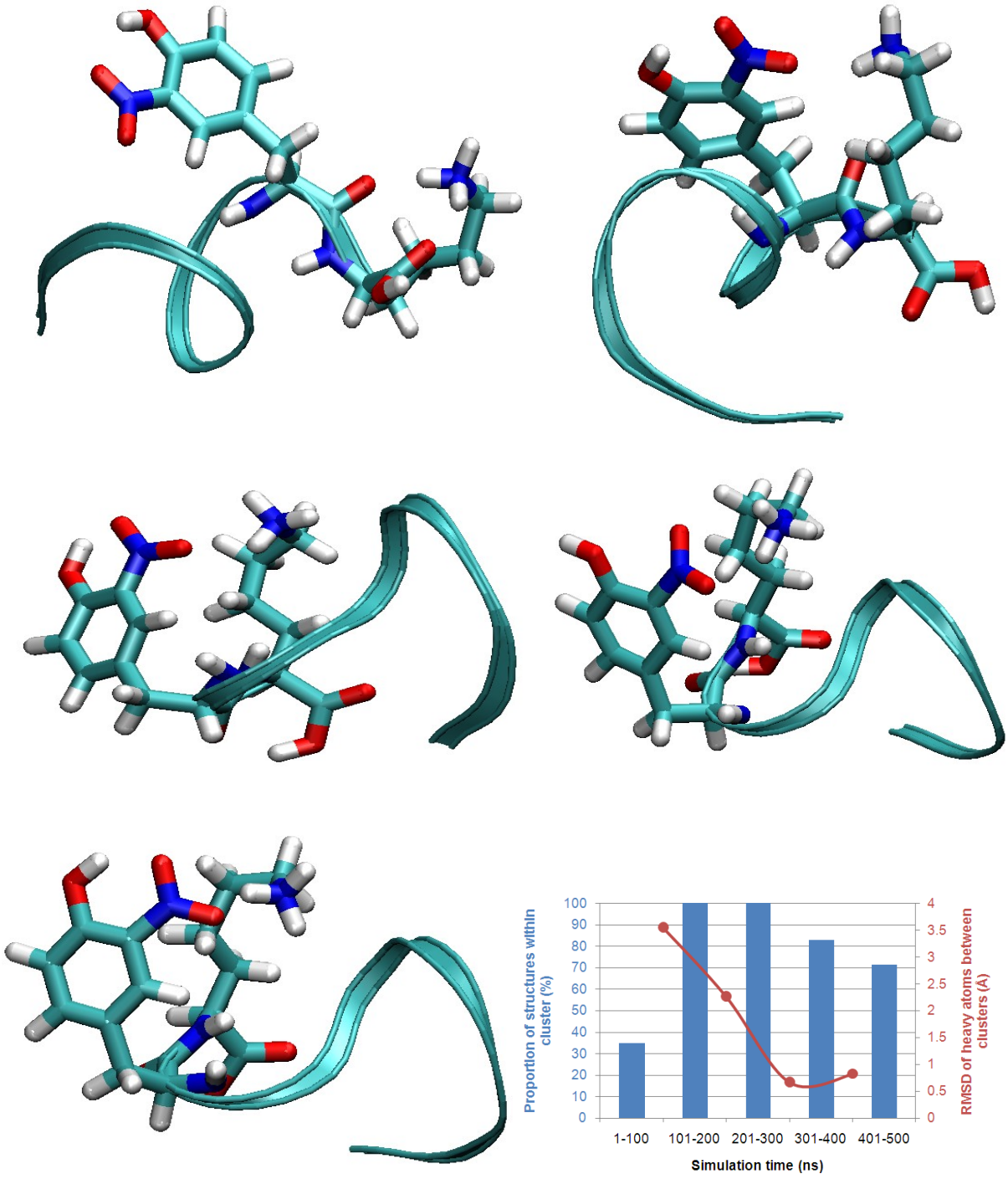

Figure 4.15: Molecular models of $[AAAAAAnYK + 2H]^{2+}$

Figures shown represent the most common structure between 0-100 ns (**Upper Left**), 101-200 ns (**Upper Right**), 201-300 ns (**Middle Left**), 301-400 ns (**Middle Right**) and 401-500 ns (**Lower Left**). (**Lower Right**) Graph shows the percentage proportion of the dominant structure within this simulation time window, and the RMSD in angstroms of heavy atoms between the structure and the most common structure from the previous time window

close in space to the N-terminus, either prior to or following electron transfer to the 3-nitrotyrosine side chain cannot be precluded. Also, it should be noted that MS^3 of this peptide was not performed, and therefore it is plausible that ammonia does originate from the BAAR side chain for this peptide.

Despite the anomalous result identified for $[AAAAAAnYK + 2H]^{2+}$ it can be seen that the use of these molecular models developed through MD simulations offer significant potential for understanding mechanistic pathways and corroborating experiments.

4.3 Discussion

In this chapter it is shown that ammonia loss following ECD of 3-nitrotyrosine containing peptides originates from the peptide N-terminus. Initially, isotopic-labelling of the 3-nitrotyrosine was completed which showed that ammonia did not arise from this site. AI ECD of the peptides provided insight into the interactions within the peptide associated with ammonia loss, and analysis of polyAla peptides show that these interactions are site-sensitive. ECD of non-BAAR-containing and N-terminal acetylated peptides resulted in contradictory data with neither resulting in ammonia loss; however, the site was conclusively identified using MS^3 analysis. Finally, molecular dynamic simulations of the polyAla peptides were generated to identify how these peptides would fold in the gas-phase and to identify the non-covalent interactions within. These molecular models largely agree with the conclusion that ammonia originates from the N-terminus. One peptide model appears to suggest that ammonia arises from the BAAR side chain, although this peptide was not analysed using MS^3 and it is plausible that for this peptide ammonia does arise from this site.

As shown in **Figure 4.7**, ECD of $[GPLEnYGFAL + 2H]^{2+}$ resulted in the identification of six out of eight possible sites of backbone fragmentation, with a total of nine backbone fragment ions; whereas ECD of the unmodified $[GPLEYGFAL + 2H]^{2+}$ fragmented 6/8 backbone bonds with 11 backbone ions identified. Similarly, in **Figure 4.8** ECD of $[Ac\text{-}GPLEnYGFAK + 2H]^{2+}$ and $[Ac\text{-}GPLEnYGFAR + 2H]^{2+}$ resulted in the fragmentation of 6/8 and 5/8 bonds, respectively.

To explain these observations, the site of protonation within these peptides needs to be considered. For the non-BAAR-containing peptide, due to the addition of Leu in place of Arg/Lys, it is predicted that the second proton (following initial protonation of the N-terminus) will likely reside on a backbone amide nitrogen atom. This will therefore facilitate the Oslo mechanism [116], as described in **Section 1.4.2**, in which electron capture will result in the formation of $b^{\bullet}$ and *y* backbone fragment ion formation. Håkansson and co-workers have shown experimentally that *b*-type fragmentation is favoured in the ECD of non-BAAR-containing peptides [117]. Here, three *b* ions are observed following ECD of GPLEnYGFAL, *i.e.* b_4, b_7, and b_8, (as well as b_3 for GPLEYGFAL) suggesting that the Oslo mechanism takes precedence over the electron predator/hydrogen trap mechanism.

Likewise, the addition of the N-terminal acetylation results in the appearance of numerous *a*- and *b*-type fragments. ECD of Ac-GPLEnYGFAK, led to the observation of b_3, b_4, $a_7^{\bullet}$, b_7, a_8, and b_8 ions, whereas ECD of GPLEnYGFAK resulted in the observation of b_7 only. The most abundant fragment from the N-acetylated peptide corresponded to the $a_7^{\bullet}$ fragment ion. N-acetylation of GPLEnYGFAR also resulted in similar ECD behaviour with the appearance of $b_7^{\bullet}$ and b_8 fragments, with $b_7^{\bullet}$ being the most abundant product ion. ECD of GPLEnYGFAR resulted in the formation of no *b* ions. These observations for N-terminal acetylated peptides can, again, be explained in terms of the protonation sites of the precursor ions. For the non-acetylated nitrated peptides, the sites of protonation are presumed to be the BAAR side-chain, *i.e.* Lys or Arg, and the N-terminus; however, acetylation prevents protonation at the N-terminus and therefore the second proton is likely to reside, as with the non-BAAR-containing peptides, on a backbone amide nitrogen atom. The presence of this protonated backbone nitrogen atom promotes the Oslo mechanism of ECD, as shown by the presence of *b*-type

fragment ions in these mass spectra, which takes precedence over the electron predator/hydrogen trap mechanism.

The results shown in this chapter show 3-nitrotyrosine-containing peptides provide insight into the hierarchy of the mechanisms of ECD, see schematic in **Figure 4.17**. Regardless of whether a peptide contains 3-nitrotyrosine or not, if the peptide does not contain a BAAR (*i.e.* a protonated amide nitrogen), ECD of doubly-charged ions will proceed *via* the Oslo mechanism to produce *b*- and *y*-type fragment ions. If a peptide contains a BAAR and 3-nitrotyrosine (or another modification with positive electron affinity and sufficiently high H-atom trap efficiency), the electron predator or hydrogen trap mechanism will take precedence, resulting in no, or few, backbone fragments, and abundant losses of small neutral species. Losses involving ammonia will only be observed if the N-terminus of the peptide is able to interact with the nitro-group. Only in the absence of 3-nitrotyrosine (or other similar modification) and presence of a BAAR will ECD proceed *via* the UW or Cornell mechanism.

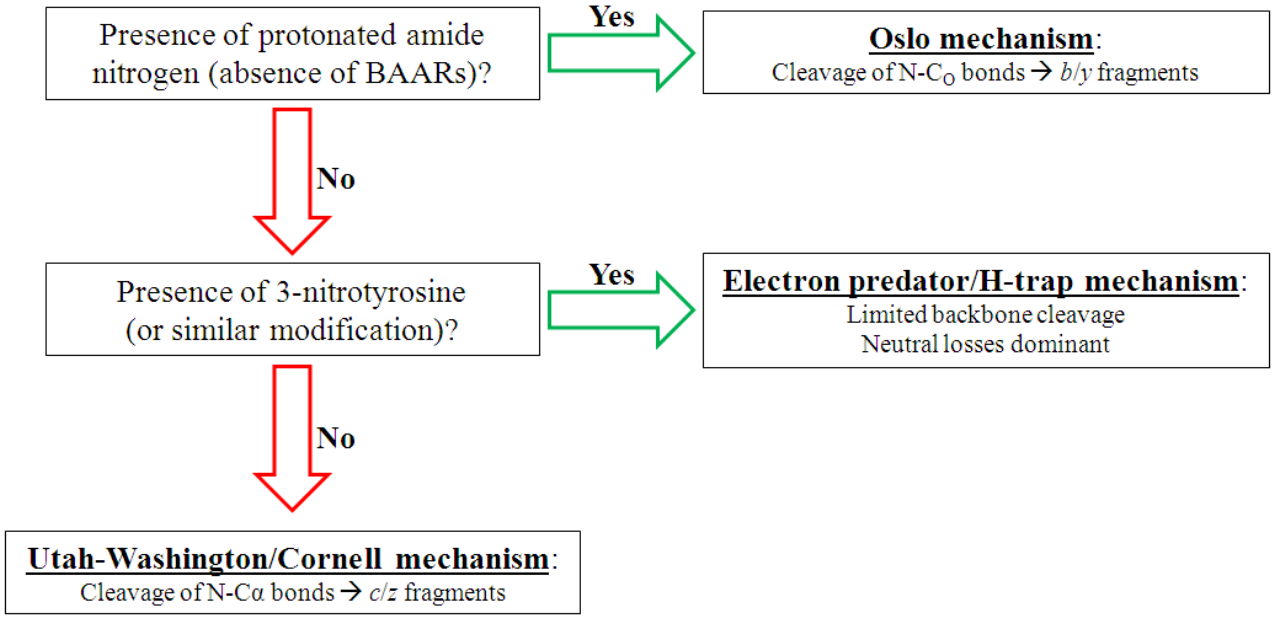

Figure 4.16: Hierarchy of ECD mechanisms

Flowchart describing which ECD fragmentation mechanism will dominate and associated fragmentation patterns which will be observed when ECD is completed on a specified peptide.

Chapter 5: Electron Capture Dissociation Mass Spectrometry of *S*-Alkylated Peptides

5.1 Introduction

Modifications of cysteine are highly variable in both structure and function. The thiol-containing side chain is not present in any other amino acid and allows a wide range of possible modifications. The thiol side chain is susceptible to oxidation from other cysteine amino acids to form a disulfide bond, which serves an important structural role in many proteins. Unfortunately the formation of disulfide bonds can cause analytical issues. For example, one of the two major ECD pathways is the cleavage of S-S bonds, and CID does not fragment the S-S bonds, resulting in limited sequence coverage and complicated mass spectra, respectively. Therefore, it is now commonplace to reduce, using dithiothreitol, and alkylate, using iodoacetamide (carbamidomethylation) or iodoacetic acid (carboxymethylation), the proteins or peptides to prevent the formation of disulfide bonds. Despite the frequent use of these techniques, there has been, to date, no major investigation to how these modifications affect CID and ECD.

In this chapter, the effect of carbamidomethylation and carboxymethylation on the CID and ECD behaviour of three synthetic peptides is considered. The effect of alkylation on protein database search results is investigated by analysis of a whole cell lysate digest.

5.2 Results

5.2.1 CID and ECD mass spectrometry of *S*-alkylated peptides

The synthetic peptide NACGAPGEKWAGNDK was reduced and alkylated as described in **Section 2.2.3**, and desalted as described in **Section 2.2.5**. The three peptide samples (one unmodified, one carbamidomethylated, and one carboxymethylated), were resuspended and analysed by CID and ECD mass spectrometry.

The CID mass spectra of the unmodified and alkylated doubly-charged peptides of $[NACGAPGEKWAGNDK + 2H]^{2+}$, shown in **Figure 5.1** (carbamidomethylation is shown by a green cysteine residue, and carboxymethylation is shown in red), appear to show very little, if any, alteration in CID behaviour following modification. CID of the unmodified peptide resulted in a peptide backbone sequence coverage of 92.9 %, with 13 of the 14 peptide bonds being cleaved, and a total of 16 *b*/*y* fragment ions. Addition of the carbamidomethyl group on the cysteine resulted in a sequence coverage of 85.7 % (12/14 N-C_O bonds cleaved), but an increase in total *b*/*y* fragment ions observed to 17. CID of the carboxymethylated peptide also resulted in an 85.7 % peptide backbone sequence coverage with a total of 18 *b*/*y* fragment ions being observed. These data suggest that alkylation of the cysteine amino acid residue does not affect CID in any significant manner. The only cleavage not observed following alkylation was between Gly12-Asn13, a site distant from the modified cysteine.

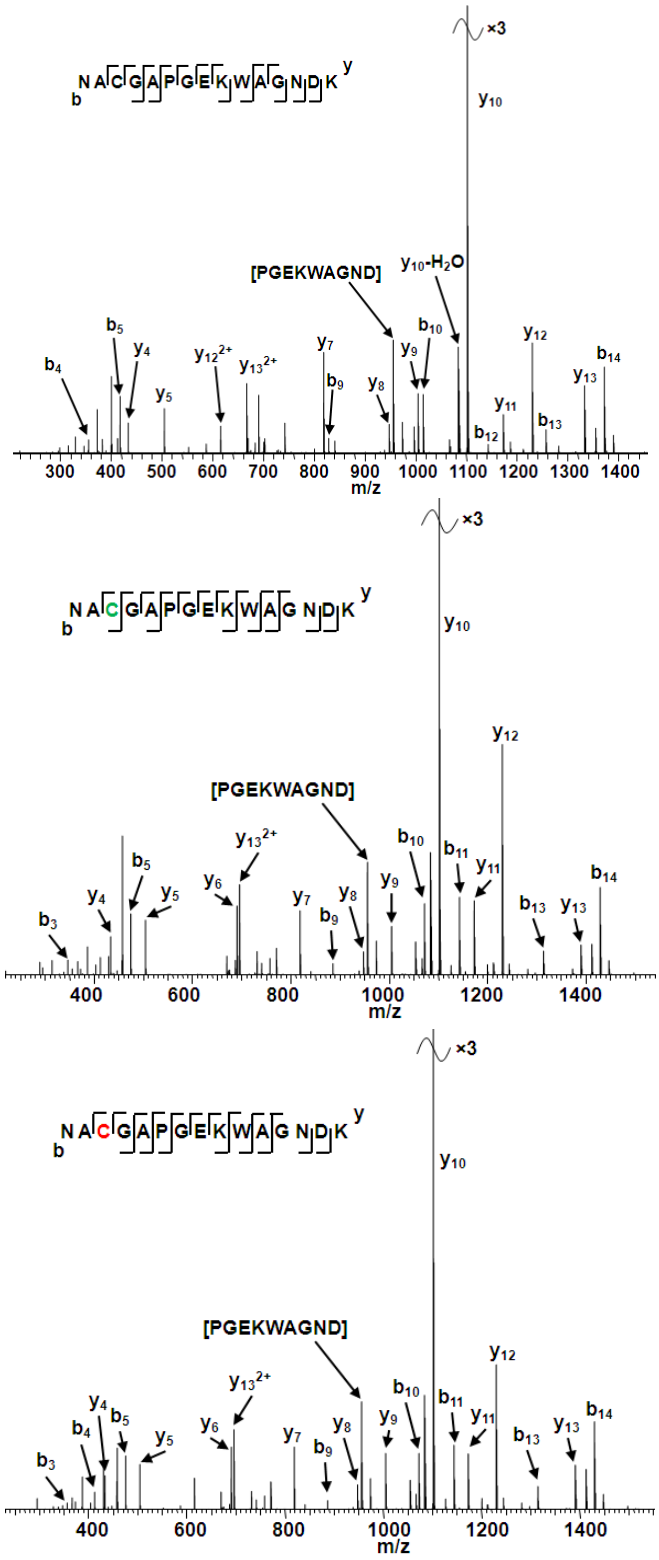

Figure 5.1: CID mass spectra of unmodified and alkylated doubly-charged peptides

CID mass spectra of doubly-charged unmodified (**Upper**), carbamidomethylated (**Middle**), and carboxymethylated (**Lower**) [NACGAPGEKWAGNDK + 2H]$^{2+}$ peptide ions. The modifications do not appear to change the CID behaviour.

A similar conclusion can be made regarding the ECD of the doubly-charged peptides, shown in **Figure 5.2**. Peptide sequence coverage is only marginally affected. ECD of the unmodified $[NACGAPGEKWAGNDK + 2H]^{2+}$ resulted in a peptide sequence coverage of 64.3 % (9/14 N-Cα bonds cleaved), with a total of 11 *c*/*z* ions, whereas ECD of the carbamidomethylated peptide resulted in a coverage of 71.4 % (10/14 N-Cα bonds cleaved) with nine *c*/*z* ions, and ECD of the carboxymethylated peptide led to a peptide sequence coverage of 71.4 % (10/14 N-Cα bonds cleaved) with nine *c*/*z* backbone ions. Although alkylation of cysteine residues does not appear to have a dramatic effect on the peptide sequence coverage following ECD, a change in the observed neutral losses from the charge-reduced precursor is observed.

ECD of the unmodified doubly-charged peptide ion resulted in losses of NH_3, CO, $[H_2O + NH_3]$, and $[H_2O + CO]$ from the charge-reduced precursor peptide ion. As well as these neutral losses, the ECD mass spectra for the two alkylated peptides contain abundant peaks corresponding to the loss of CH_2CONH_2 (carbamidomethylated peptide), and CH_2COOH (carboxymethylated peptide) from the charge-reduced precursor ion. These two neutral species correspond to the alkyl group bound to the cysteine sulfur atom in each respective modification, indicating that the RS-C bond is broken. Both of these neutral loss peaks are the most abundant neutral loss peak within the mass spectrum and are of similar intensity to the most intense backbone fragment peaks.

Losses of CH_2CONH_2 and CH_2COOH are proposed to occur *via* a similar mechanism to the Cornell [92] and UW [95, 96] mechanisms for the fragmentation of disulfide bonds, see **Figure 5.3**. Here, it is proposed that following electron capture at a site of protonation either hydrogen transfer to the sulfur atom (Cornell) or electron transfer to the S-C σ* orbital (UW)

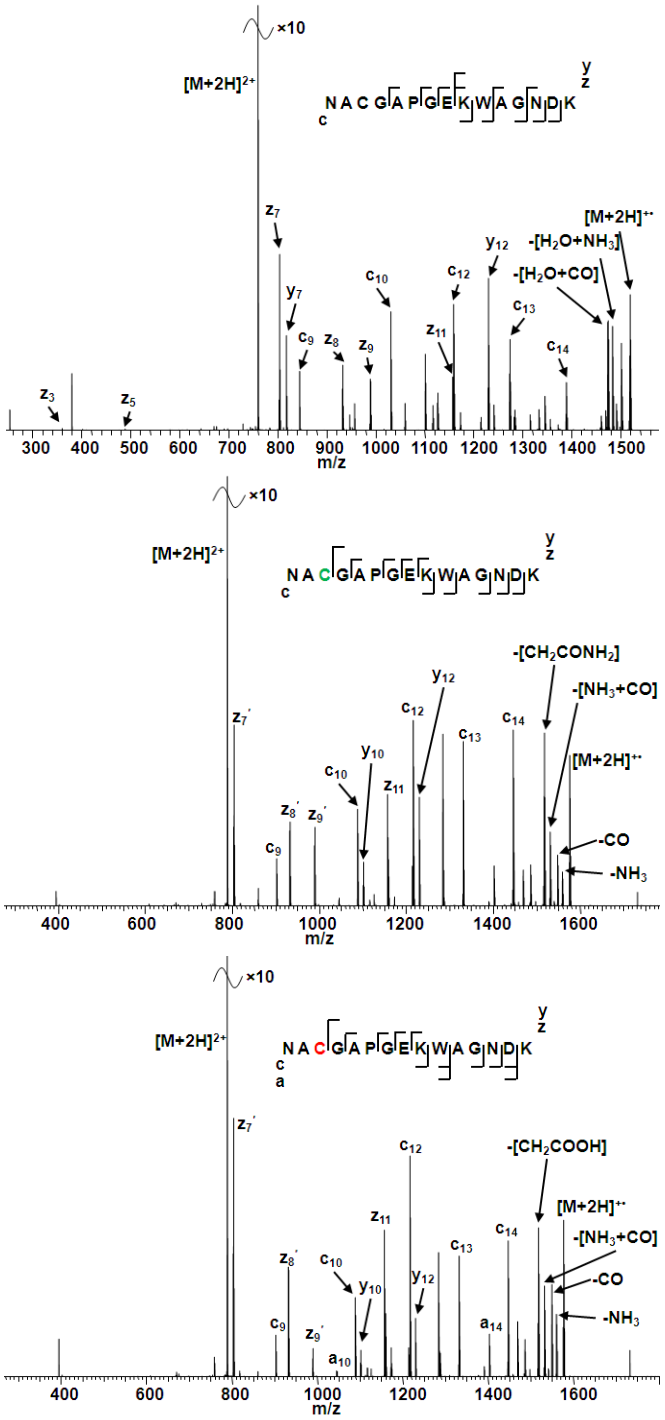

Figure 5.2: ECD mass spectra of unmodified, and alkylated doubly-charged peptides

ECD mass spectra of doubly-charged unmodified (**Upper**), carbamidomethylated (**Middle**), and carboxymethylated (**Lower**) $[NACGAPGEKWAGNDK + 2H]^{2+}$ peptide ions. The modifications do not appear to decrease the peptide sequence coverage, although a dominant neutral loss of the alkyl group is identified for both alkylated peptides.

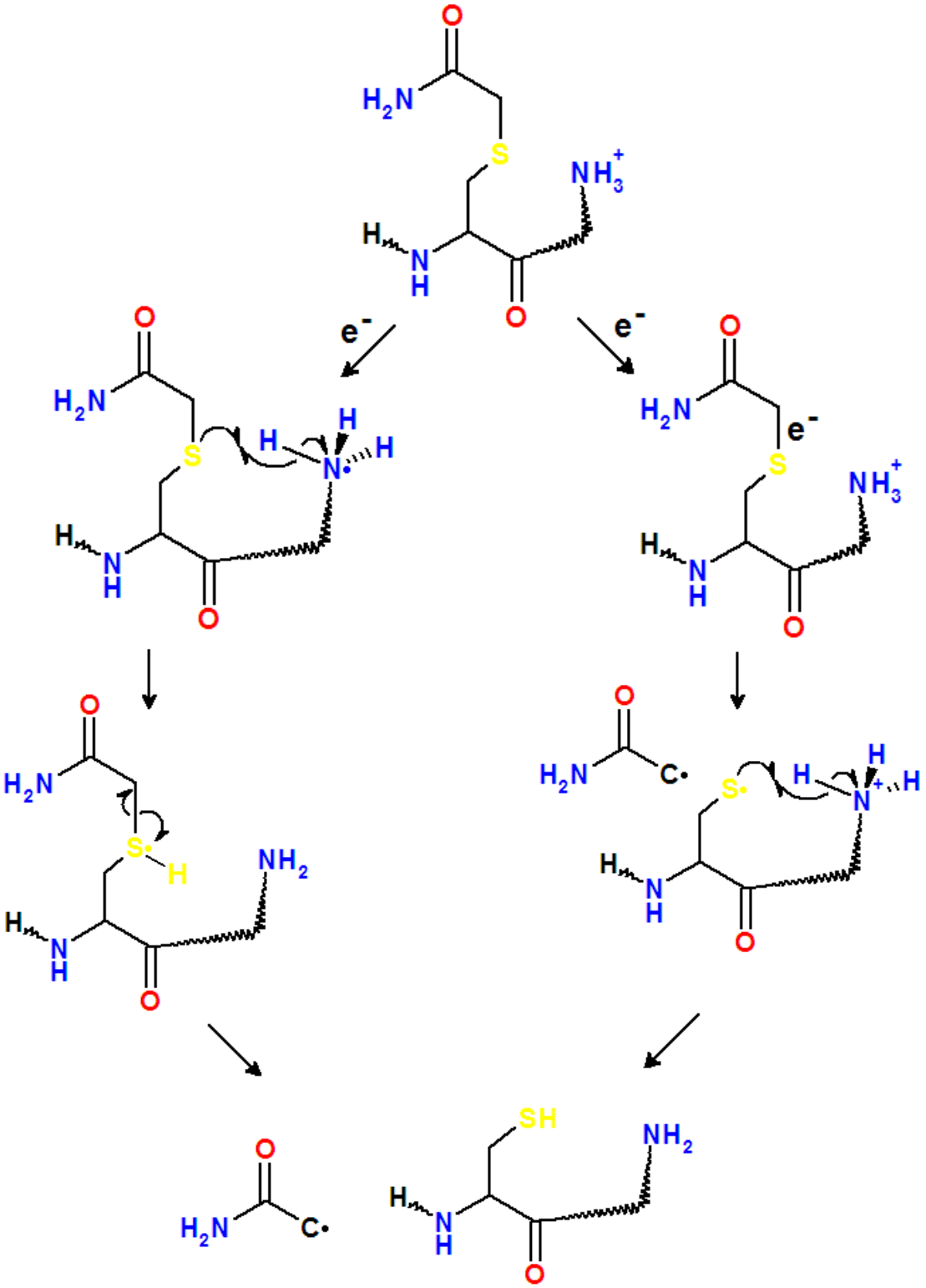

Figure 5.3: Proposed mechanism of alkyl neutral loss following ECD

Following initial electron capture at a site of protonation fragmentation takes place *via* an adapted Cornell or UW mechanism. Hydrogen transfer to the sulfur atom prior to S-C bond cleavage (**Left**) or electron transfer to the S-C σ* orbital initiates homolysis followed by hydrogen transfer (**Right**). This schematic shows carbamidomethylation (CH_2CONH_2), although carboxymethylation (CH_2COOH) would follow the same process.

takes place resulting in S-C bond homolysis, and the formation of CH_2CONH_2 or CH_2COOH and the intact peptide.

These peptides were chosen as they contained two basic amino acids residues (BAARs), and thus were also observed in the 3+ charge state. The CID mass spectra of the 3+ precursor ions are shown in **Figure 5.4**. The first noticeable point is the large decrease in peptide sequence coverage as compared to their doubly-charged counterparts; however, this is also observed for the unmodified peptide, and is due to the efficiency of CID decreasing with an increase in charge state [134]. CID of the unmodified $[NACGAPGEKWAGNDK + 3H]^{3+}$ resulted in the peptide backbone sequence coverage of 50 % (7/14 N-C_O bonds cleaved) and 10 *b*/*y* ions. CID of the carbamidomethylated peptide resulted in 57.1 % sequence coverage (8/14 N-C_O bonds cleaved) and 11 *b*/*y* ions. CID of the carboxymethylated peptide resulted in 50 % (7/14 N-C_O bonds cleaved) sequence coverage and 10 *b*/*y* ions. These data suggest that neither carbamidomethylation nor carboxymethylation have an effect on the efficiency of peptide sequence coverage following CID.

A similar conclusion can be made with respect to ECD of the triply-charged peptides. Little change in peptide sequence coverage was observed between the unmodified and alkylated peptides. As predicted, these results (**Figure 5.5**) show an increase in peptide sequence coverage in comparison to ECD of the doubly-charged peptides. An increase of ~100 % in observed *c*/*z* fragments in all cases: 21 *c*/*z* ions observed for the unmodified peptide (an increase of 10 fragments), 20 for the carbamidomethylated peptide (increase of 10 fragments),

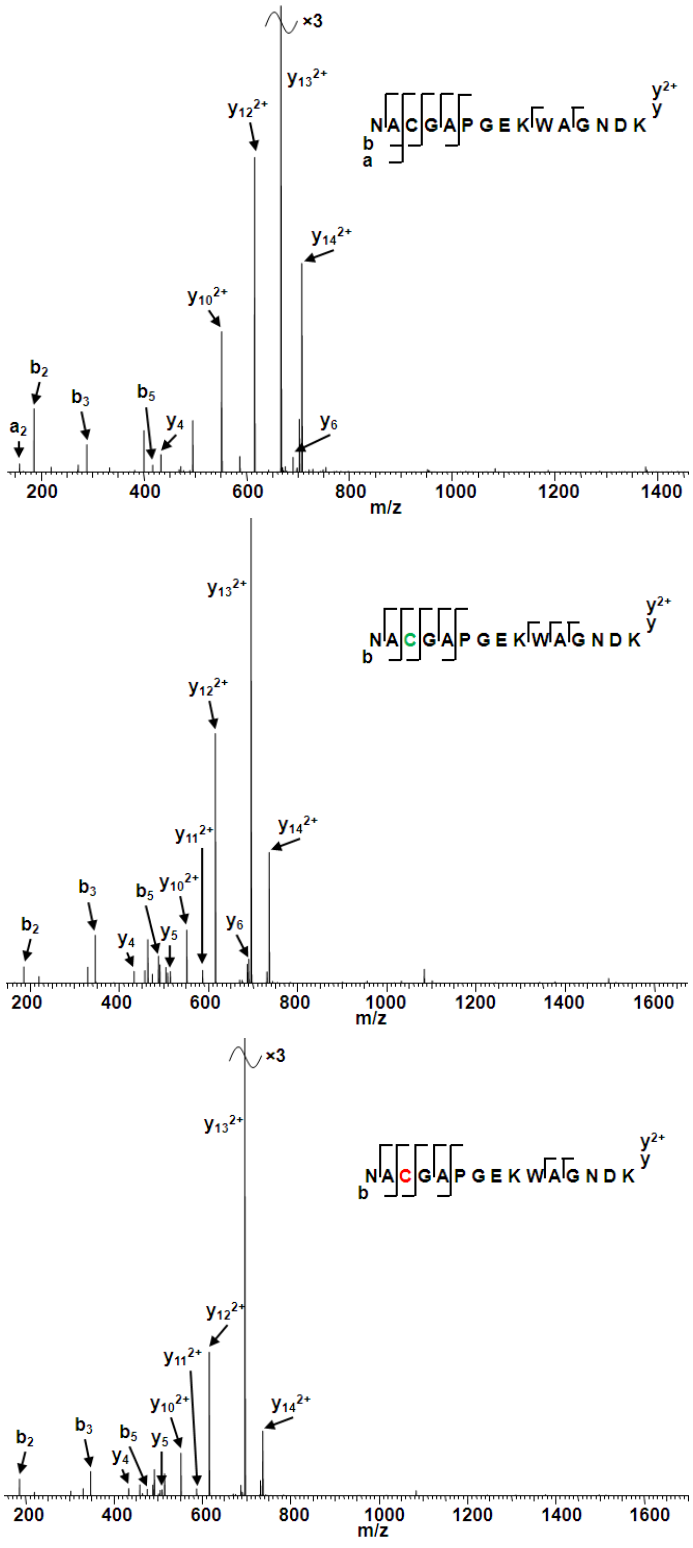

Figure 5.4: CID mass spectra of unmodified, and alkylated triply-charged peptides

CID mass spectra of triply-charged unmodified (**Upper**), carbamidomethylated (**Middle**), and carboxymethylated (**Lower**) $[NACGAPGEKWAGNDK + 3H]^{3+}$ peptide ions. CID of triply-charged peptides results in lower sequence coverage in comparison to their doubly-charged counterparts (**Figure 4.1**), although the modifications do not appear to be affecting CID behaviour.

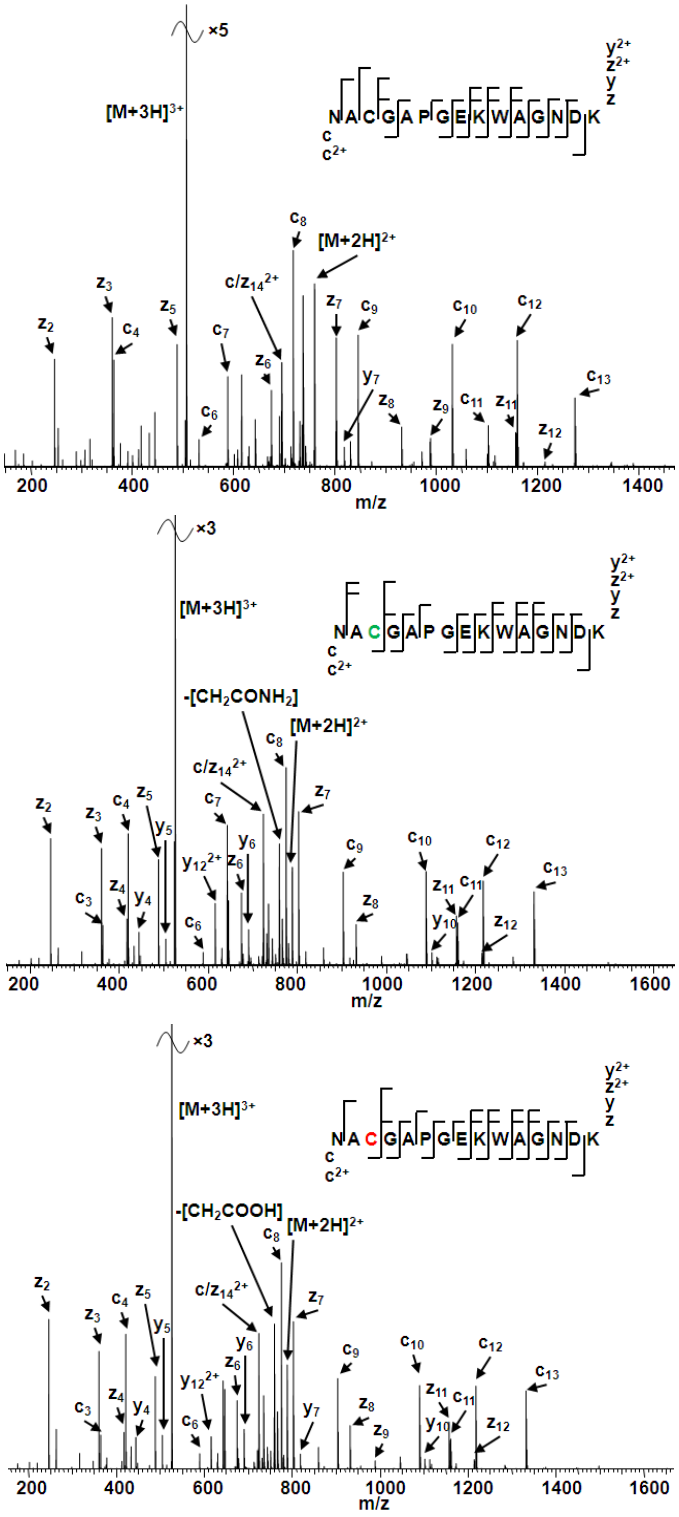

Figure 5.5: ECD mass spectra of unmodified, and alkylated triply-charged peptides

ECD mass spectra of triply-charged unmodified (**Upper**), carbamidomethylated (**Middle**), and carboxymethylated (**Lower**) [NACGAPGEKWAGNDK + 3H]$^{3+}$ peptide ions. As with their doubly-charged counterparts (**Figure 5.2**) ECD of the alkylated peptides results in fragmentation of the RS-C bond and loss of the alkyl group.

and 21 for the carbamidomethylated peptide (an increase of 11 fragments). As with ECD of the doubly-charged alkylated peptides, ECD of the triply-charged alkylated peptides resulted in peaks corresponding to the neutral loss of CH_2CONH_2, for the carbamidomethylated peptide, and CH_2COOH, for the carboxymethylated peptide. This neutral loss peak is, again, more intense than the charge-reduced precursor peak. There is no peak in either ECD mass spectra corresponding to a *c*/*z* fragment ion with further loss of an alkyl neutral. If present, such a peak would indicate secondary electron capture has taken place, *i.e*. initial electron capture resulting in RS-C bond cleavage followed by secondary electron capture resulting in N-Cα bond cleavage.

It could be speculated that the site of alkylation would have a deleterious effect on peptide backbone fragment following ECD when the modification is close to the BAARs. That is, following initial electron capture at the BAAR, electron transfer to the RS-C σ* orbital might be favoured over electron transfer to the N-Cα π* orbitals if the alkylation is adjacent to the site of electron capture. It can be seen in **Figure 5.6** that the site of carbamidomethylation or carboxymethylation within the peptide does not appear to influence ECD behaviour.

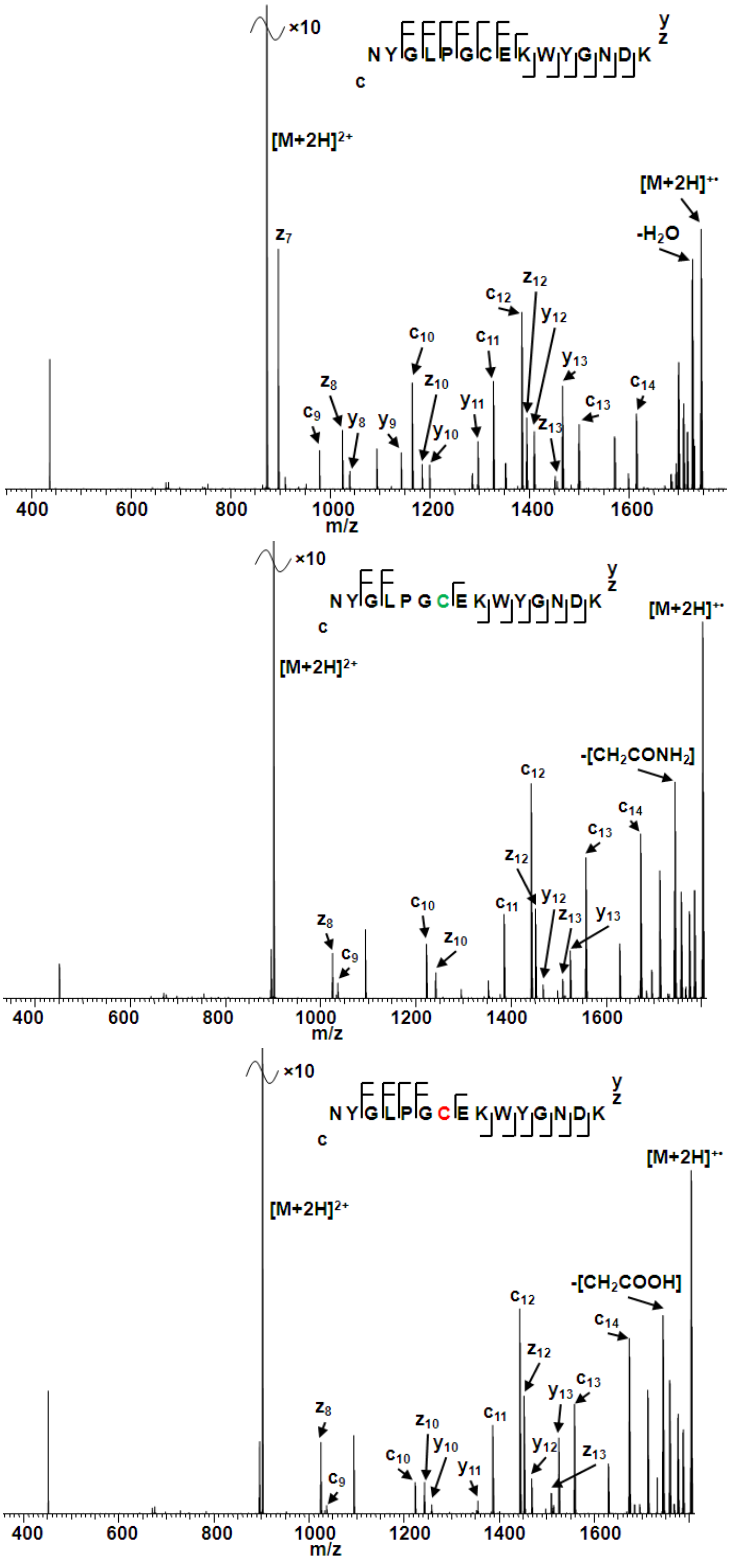

Figure 5.6.1: Effect of *S*-alkylation site on ECD

ECD mass spectra of doubly-charged unmodified (**Upper**), carbamidomethylated (**Middle**), and carboxymethylated (**Lower**) $[NYGLPGCEKWYGNDK + 2H]^{2+}$ peptide ions.

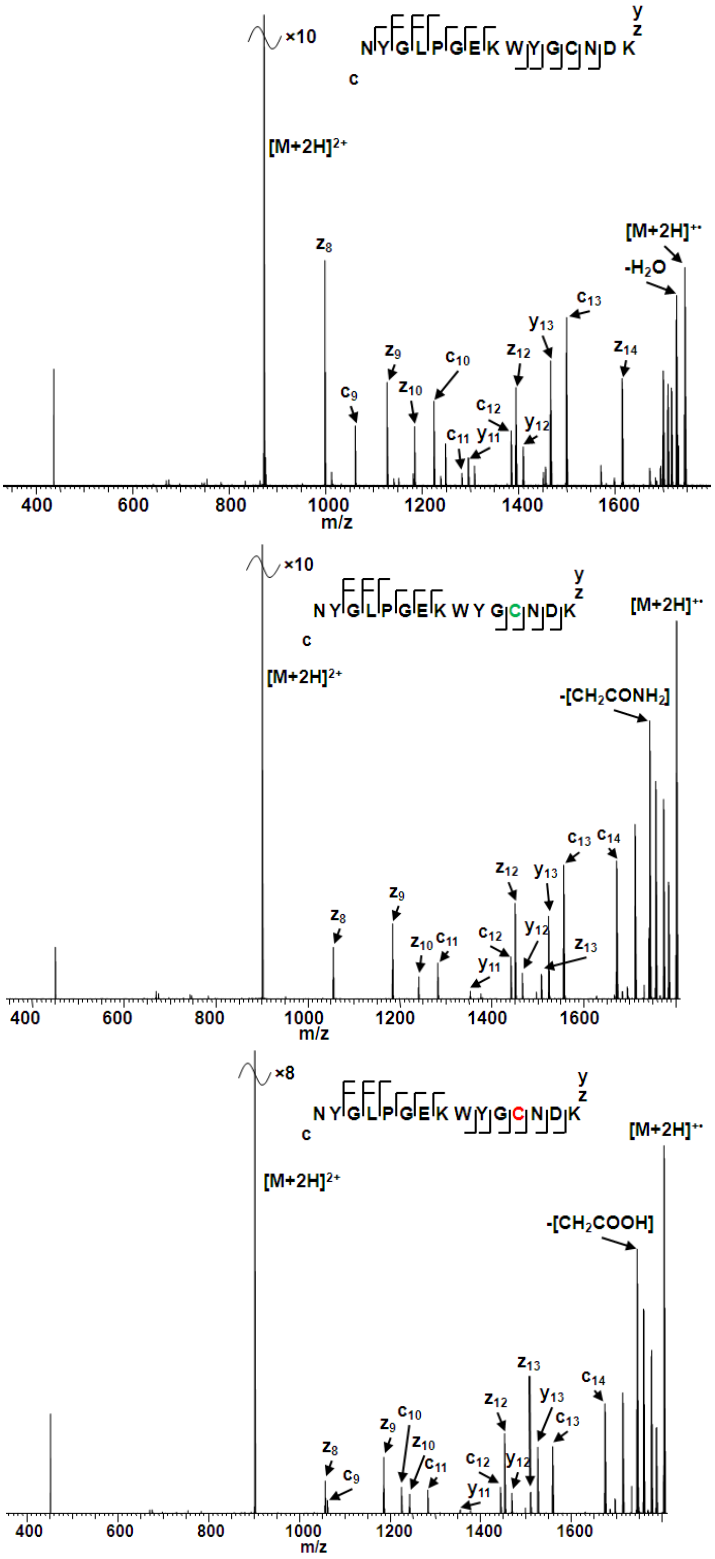

Figure 5.6.2: Effect of *S*-alkylation site on ECD

ECD mass spectra of doubly-charged unmodified (**Upper**), carbamidomethylated (**Middle**), and carboxymethylated (**Lower**) [NYGLPGEKWYGCNDK + 2H]$^{2+}$ peptide ions.

5.2.2 Large scale analysis of *S*-carbamidomethylated peptides

Search algorithms function by comparing *in silico* digestion and fragmentation of protein databases with experimentally derived mass spectra; however, problems can arise when using ECD mass spectra due to the frequent presence of neutral loss peaks. The presence of these neutral loss peaks lead to an increase in false positive results as the search algorithms will identify these peaks as backbone fragment ions or give lower peptide scores because not all the peaks within the mass spectrum can be assigned. Therefore, despite the fact that the presence of carbamidomethyl or carboxymethyl groups on cysteine residues does not appear to affect the efficiency of CID or ECD on a small scale with manual validation, the presence of extra peaks within ECD mass spectra may change the efficiency of analysing large amounts of data when using automated search algorithms.

To investigate this issue, mouse fibroblast 3T3 cells were grown and lysed by Dr. Debbie Cunningham as detailed in **Section 2.2.1**. Whole cell lysates were reduced and carbamidomethylated (**Section 2.2.3**), trypsin digested (**Section 2.2.5**), and desalted (**Section 2.2.5**). The digested sample was then separated offline using strong cation exchange chromatography (**Section 2.2.6**) resulting in a total of 11 fractions, before being desalted again, and finally undergoing online LC-MS/MS analysis (CID and ECD) (**Section 2.2.11**).

LC-MS/MS analysis of the 11 samples resulted in a total of 6682 MS/MS events: 3341 CID and 3341 ECD mass spectra. The data were analysed with the use of search algorithms, Mascot and OMSSA. In parallel to this study, these data were also used by Sweet *et al*. to identify how best to optimise LC-ECD-MS/MS generated data for Mascot and OMSSA. We

showed that a series of pre- and post-search filtering techniques gave the maximum number of assignments [171]. These included removal of specific areas of the ECD mass spectra, *i.e.* a noise peak at *m*/*z* 101.83 (peculiar to our LTQ-FT), the precursor window (charge-reduced precursor(s)), and a neutral-loss window. This neutral-loss window removed all peaks <57 Da from the charge-reduced precursor and peaks ≥57 Da up to 140 Da from the charge-reduced precursor which do not correspond to a calculated *c*, *y*, *z* or $z^{\cdot}$ ion, *e.g.* any peaks with a mass 58.0293 Da less than the charge-reduced precursor are retained.

A similar approach was undertaken in this work; however, as the focus was on *S*-carbamidomethylated peptides, the perl script was changed to remove specific regions of the ECD mass spectra corresponding to 57 Da, 60 Da and 91 Da from the charge-reduced precursor ion. (Modified perl scripts used are included in **Appendix 1**). All peaks in these regions were removed with the exception of any peaks which correspond to any theoretical fragment ions. The mass of CH_2CONH_2 (the loss of which is observed following ECD of carbamidomethylated peptides) is 58.0292 Da, thus by comparing the results obtained following the removal of 57 Da and 60 Da it is possible to determine the effect of these fragments on peptide scoring. The use of 91 Da was chosen because, although not previously noted, the theoretical neutral loss of the alkyl group with the attached sulfur atom (*i.e.* C_β-S bond cleavage) would be 90.9853 Da and 90.0013 Da, for carboxymethylation and carbamidomethylation, respectively.

The results collected from the Mascot searches of the LC-ECD-MS/MS data are shown in **Figure 5.7**. The results presented are as follows: all identified peptides following pre-search filtering, and all peptides which contain at least one carbamidomethylated cysteine residue.

Pre-search	ID rate	+2 rate	+3 rate	+4 rate	FD rate
ECD search (3341 DTAs) Mascot					
None	43.94%	26.04%	16.76%	1.17%	0.48%
-57 Da	49.33%	30.26%	17.69%	1.38%	1.15%
-60 Da	49.33%	30.26%	17.69%	1.38%	1.15%
-91 Da	49.30%	30.23%	17.69%	1.38%	1.15%

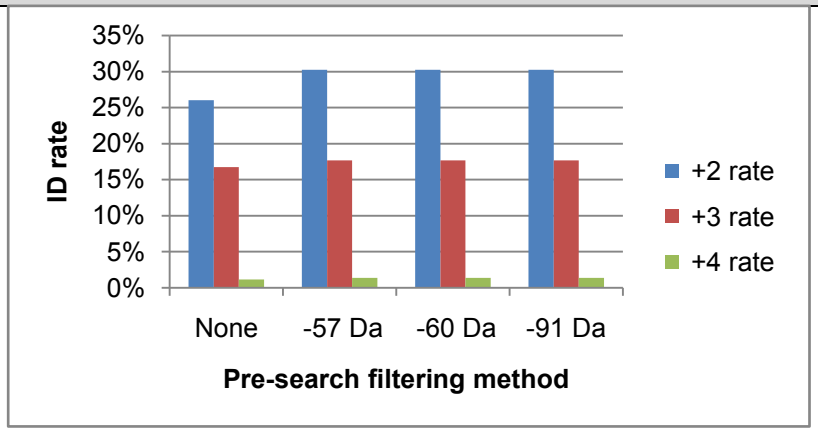

Pre-search	ID rate	+2 rate	+3 rate	+4 rate	FD rate
ECD search (3341 DTAs) Mascot – *S*-Carbamidomethyl					
None	5.48%	2.36%	2.39%	0.72%	1.09%
-57 Da	6.79%	3.38%	2.60%	0.81%	0.88%
-60 Da	6.79%	3.38%	2.60%	0.81%	0.88%
-91 Da	6.82%	3.41%	2.60%	0.81%	0.88%

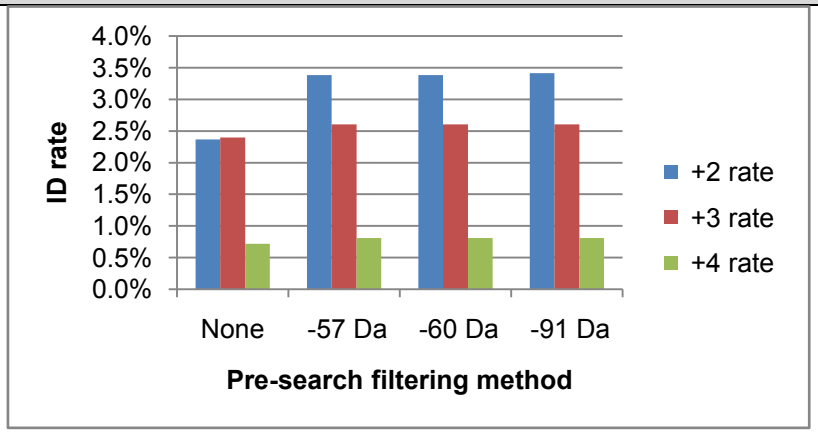

Figure 5.7: Effect of pre-search filtering of ECD data on Mascot identification

Number of peptides retained through LC-MS/MS (ECD) analysis following pre-search filtering (none, removal of $[M+nH]^{(n-1)+\bullet}$-57 Da, $[M+nH]^{(n-1)+\bullet}$-60 Da, and $[M+nH]^{(n-1)+\bullet}$-91 Da), Mascot search, and post-search filtering (removal of all peptides with a ppm error ≥8.79 or ≤-0.44). **Upper**: All identified peptides. **Lower**: All peptides with at least one carbamidomethylated cysteine residue.

The ID rate is the percentage of peptides which were retained following the database search and are shown according to their charge state. The FD rate refers to the total number of reverse peptides which were retained following the pre-search filtering.

As expected, the use of pre-search removal of the neutral loss windows within the ECD mass spectra improves the ID rate for carbamidomethylated peptides. The use of a neutral loss cut off of 57 Da and 60 Da led to an increase in positive IDs of nearly 6 % (180 peptides) in comparison to the unfiltered data.

Similar results were obtained for the OMSSA search algorithm, see **Figure 5.8**. As identified for the Mascot searches, the OMSSA algorithm showed an increase in carbamidomethylated peptide identification when pre-search filtering was completed. The use of pre-search filtering of all ranges led to an increase in ID rate in comparison to the unfiltered data; however, the appearance of a CH_2CONH_2 or SCH_2CONH_2 peak within an ECD mass spectrum does not affect the efficiency of the search algorithm.

Pre-search	ID rate	+2 rate	+3 rate	+4 rate	FD rate
ECD search (3341 DTAs) OMSSA					
None	42.47%	22.39%	18.47%	1.50%	0.78%
-57 Da	45.67%	24.84%	18.74%	1.59%	0.79%
-60 Da	45.67%	24.84%	18.74%	1.59%	0.79%
-91 Da	45.41%	24.57%	18.74%	1.59%	0.79%

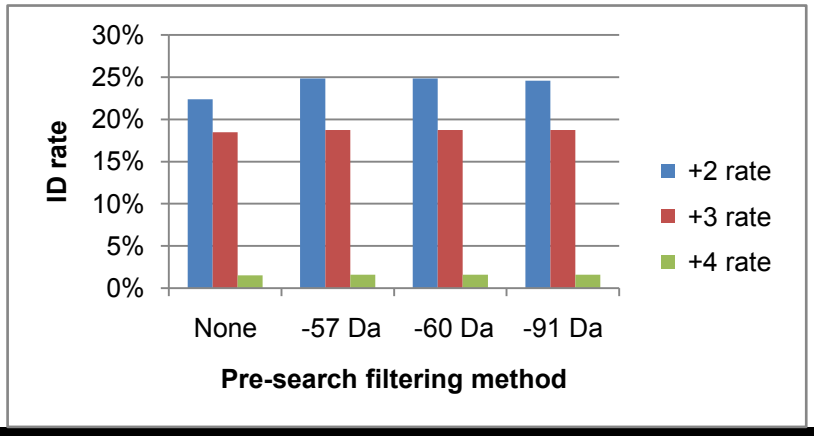

Pre-search	ID rate	+2 rate	+3 rate	+4 rate	FD rate
ECD search (3341 DTAs) OMSSA – *S*-Carbamidomethyl					
None	5.84%	2.13%	2.87%	0.81%	0.51%
-57 Da	6.29%	2.48%	2.93%	0.84%	0.95%
-60 Da	6.29%	2.48%	2.93%	0.84%	0.95%
-91 Da	6.29%	2.48%	2.93%	0.84%	0.95%

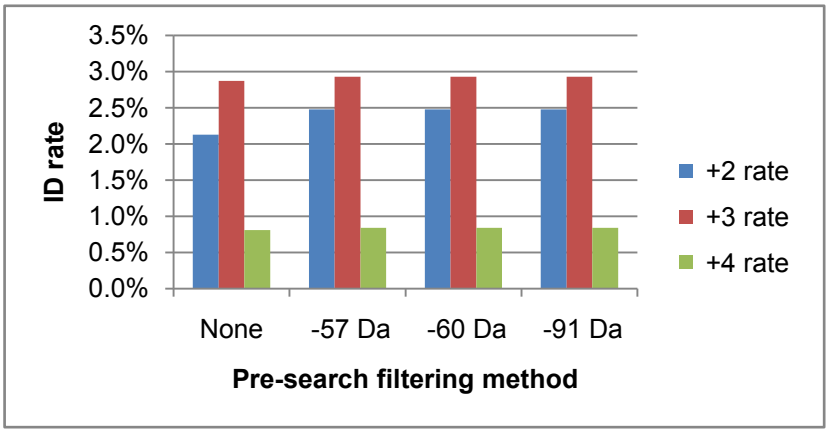

Figure 5.8: Effect of pre-search filtering of ECD data on OMSSA identification

Number of peptides retained through LC-MS/MS (ECD) analysis following pre-search filtering (none, removal of $[M+nH]^{(n-1)+\bullet}$-57 Da, $[M+nH]^{(n-1)+\bullet}$-60 Da, and $[M+nH]^{(n-1)+\bullet}$-91 Da), OMSSA search, and post-search filtering (removal of all peptides with a ppm error ≥8.37 or ≤-1.99). **Upper**: All identified peptides. **Lower**: All peptides with at least one carbamidomethylated cysteine residue.

5.3 Discussion

The results described in this chapter show that ECD of cysteine-bound modifications, specifically carbamidomethylation and carboxymethylation, results in the cleavage of the S-C bond in a dominant fashion, with these peaks typically being among the most intense within each ECD mass spectrum. This cleavage is proposed to follow an adapted Cornell or UW mechanism, in which the S-C rather than the S-S bond is broken. Nevertheless, these modifications do not appear to result in a decrease in ECD peptide sequence coverage. When analysing large datasets, search algorithms can be optimised by the removal of specific areas of ECD mass spectra. Despite the appearance of extra non-backbone peaks within ECD mass spectra, however, when analysing carbamidomethylated peptides these peaks do not appear to affect the identification of false positives or decrease peptide identification scores when using Mascot or OMSSA.

Chapter 6: Radical Ion Chemistry of *S*-Nitrosylated Peptides

6.1 Introduction

Unlike the synthetic modifications discussed in Chapter 5, *S*-nitrosylation, the addition of nitric oxide to the sulfur side chain of cysteine, is a ubiquitous PTM in nature and is fundamental for protein function and modulation [152]. The use of CID for the identification and localisation of this PTM has been shown to be highly problematic: CID of *S*-nitrosopeptides, as with phosphorylation, leads to facile loss of the modification [183] – although identification of the PTM can be successful when a biotin-switch method (*i.e.* conversion of the *S*-nitrosylation into a biotinylation site) [158] or specific buffers and instrument parameters are utilised [184].

The first study into the CID behaviour of *S*-nitrosopeptides was undertaken by Hao *et al*. [183] in which they showed that as well as facile loss of $^{\bullet}$NO following CID of a *S*-nitrosopeptide the resultant radical peptide ion leads to the formation of radical fragment ions, *i.e. c* and *z* ions, following a further stage of CID, *i.e.* MS^3 (CID-CID). That study focused on just two very similar peptides, one of which was a truncated version (13 amino acids) of the other (22 aa). Likewise, ETD of a single *S*-nitrosopeptide (30 aa) has also been performed with the dominant neutral loss of $^{\bullet}$NO being observed [185]. This radical peptide ion, following the loss of the $^{\bullet}$NO radical, has been identified to be a long-lived sulfur radical [186]. Recently, examinations using infrared spectroscopy, ion-molecule reactions and theoretical calculations have focused on this cysteine radical species [187-189]. Despite most of these reports showing that the distonic structure remains, it has been calculated that radical migration to the cysteine α-carbon is favourable (-2.5 kJ mol^{-1}) and was shown that when formed *via* in-source CID a much greater proportion of radical α-carbon was noted when

reacted with dimethyl sulfide than *via* ion-trap CID [189], thus suggesting that this radical rearrangement occurs in a time-dependent manner.

The overall aim of the work presented in this chapter was a comprehensive study of the gas-phase fragmentation chemistry of a suite of *S*-nitrosopeptides. The following issues are addressed: PTM localisation, ECD and CID behaviour, and ECD and CID of the hydrogen-deficient radical with comparison to ECD of the hydrogen-abundant precursor.

6.2 Results

6.2.1 ECD of doubly-charged *S*-nitrosopeptides

The cysteine-containing fibrinogen β-chain peptide NYCGLPGEYWLGNDK, selected following the nitration work, along with the similar NACGAPGEKWAGNDK, NYGLPGCEKWYGNDK, NYGLPGEKWYGNCDK, NYCGLPGEYWLGNDR, NYCGLPGEKYLGNDK and NYCGLPGERWLGNDR, were nitrosylated on the cysteine amino acid residue, see **Section 2.2.8**.

ECD of $[NYCGLPGEYWLGNDK + 2H]^{2+}$, $[NACGAPGEKWAGNDK + 2H]^{2+}$, $[NACGAPGEKWAGNDK + 3H]^{3+}$ (see **Figure 3.2.2**, **5.2**, and **5.5**, respectively), and the other unmodified peptides (mass spectra shown in **Figure 6.1**) resulted in significant backbone fragmentation; however, *S*-nitrosylation resulted in a decrease in peptide sequence coverage in nearly all cases, see **Figure 6.2**. For the doubly-charged peptides, with the exception of $[NYC_{NO}GLPGERWLGNDR + 2H]^{2+}$ and $[NYC_{NO}GLPGEKYLGNDK + 2H]^{2+}$,

there is a striking lack of backbone fragmentation when compared to their unmodified counterparts. With the exception of $[NYC_{NO}GLPGEKYLGNDK + 2H]^{2+}$, no backbone fragment ions observed following ECD of the doubly-charged peptide ions retain the PTM, thus preventing the localisation of the site of modification. In the case of $[NYC_{NO}GLPGEKYLGNDK + 2H]^{2+}$, three *c* ions, *i.e.* c_{12}, c_{13} and c_{14}, were observed which retain the nitrosyl group; however, these are all distant from the modification site, and would only aid partially in site localisation.

For all peptides $^{\bullet}$NO loss is the dominant process following ECD, with the $[M + 2H]^{2+}$ -$^{\bullet}$NO ion being the most abundant fragment peak in the mass spectra. Dominant $^{\bullet}$NO neutral loss is also observed following CID of *S*-nitrosopeptides [183] which might suggest a thermal process is occurring here, *e.g.* concomitant thermal $^{\bullet}$NO loss following ECnoD. As shown in **Figure 6.3**, it can be seen that no loss of $^{\bullet}$NO from the doubly-charged or charge-reduced precursor was observed and the presence of the $[M+2H-NO]^{+}$ ions were noted when the energy of the electrons was reduced.

The loss of $^{\bullet}$NO following ECD can be explained by a modified Cornell and UW mechanism, see **Figure 6.4**. The modified UW mechanism presented here proposes that initial electron capture to a high-*n* Rydberg state of the protonated basic amino acid residue (BAAR) or protonated N-terminus occurs followed by electron transfer to the RS-NO σ* orbital, with cleavage of the S-NO bond being followed by proton abstraction from an accessible site. Theoretical studies have suggested that in 1-10 % of cases, electron capture takes place directly into the S-S σ* orbital [98], and this may also be true for the S-NO σ* orbital. Once the $^{\bullet}$NO has been lost, the remaining species is even-electron and would not dissociate further.

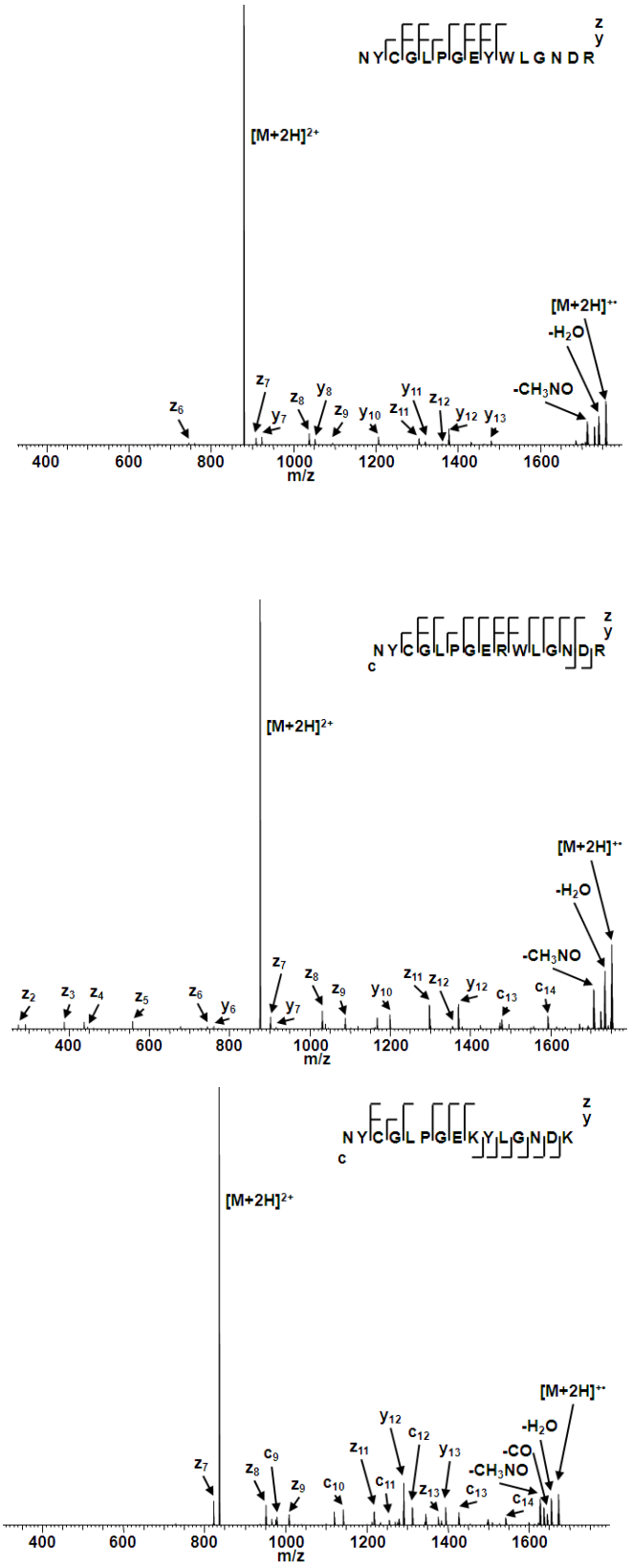

Figure 6.1.1: ECD of unmodified cysteine-containing peptides

ECD mass spectra of the doubly-charged [NYCGLPGEWYLGNDR + 2H]$^{2+}$, [NYCGLPGERWLGNDR + 2H]$^{2+}$, and [NYCGLPGEKYLGNDK + 2H]$^{2+}$ peptide ions.

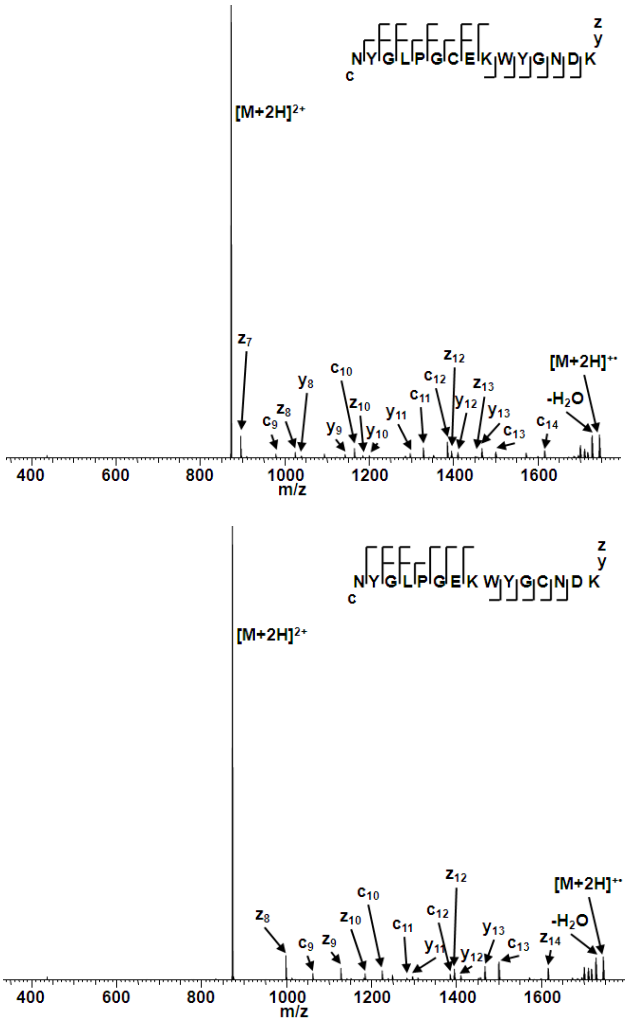

Figure 6.1.2: ECD of unmodified cysteine-containing peptides

ECD mass spectra of the doubly-charged $[NYGLPGCEKWYGNDK + 2H]^{2+}$, and $[NYGLPGEKWYGCNDK + 2H]^{2+}$ peptide ions.

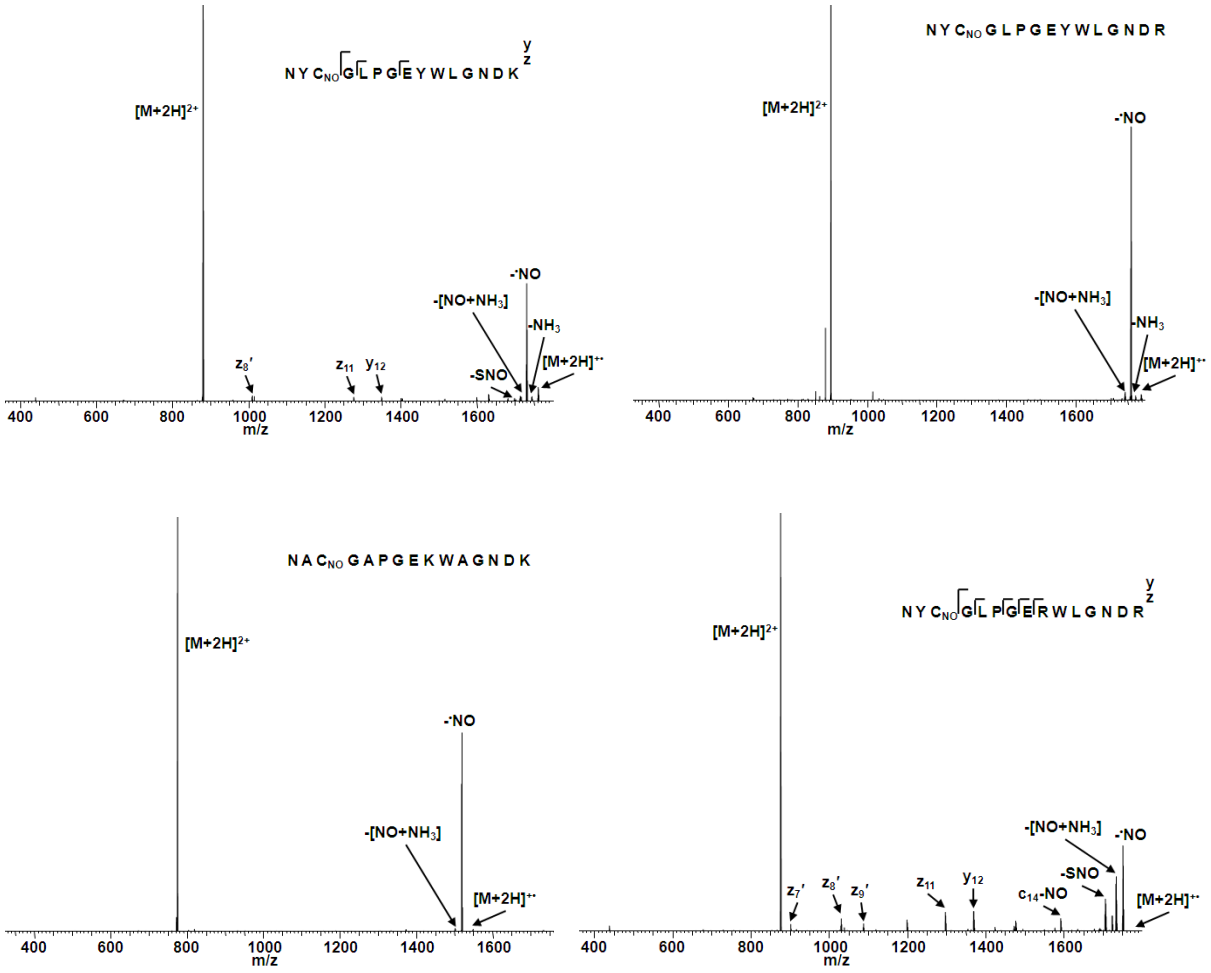

Figure 6.2.1: ECD of doubly-charged *S*-nitrosopeptides

ECD mass spectra of nitrosylated doubly-charged $[NYC_{NO}GLPGEYWLGNDK + 2H]^{2+}$, $[NYC_{NO}GLPGEYWLGNDR + 2H]^{2+}$, $[NAC_{NO}GAPGEKWAGNDK + 2H]^{2+}$, and $[NYC_{NO}GLPGERWLGNDR + 2H]^{2+}$ peptide ions. C_{NO} denotes *S*-nitrosylation. ECD results in the dominant loss of $^{\bullet}NO$ following electron capture, *i.e.* $[M+2H]^{+}$-$^{\bullet}NO$. Peptide sequence coverage is extremely low in most cases. ECD of $[NYC_{NO}GLPGERWLGNDR + 2H]^{2+}$ results in the identification of five backbone fragment ions, although modification localisation is not possible.

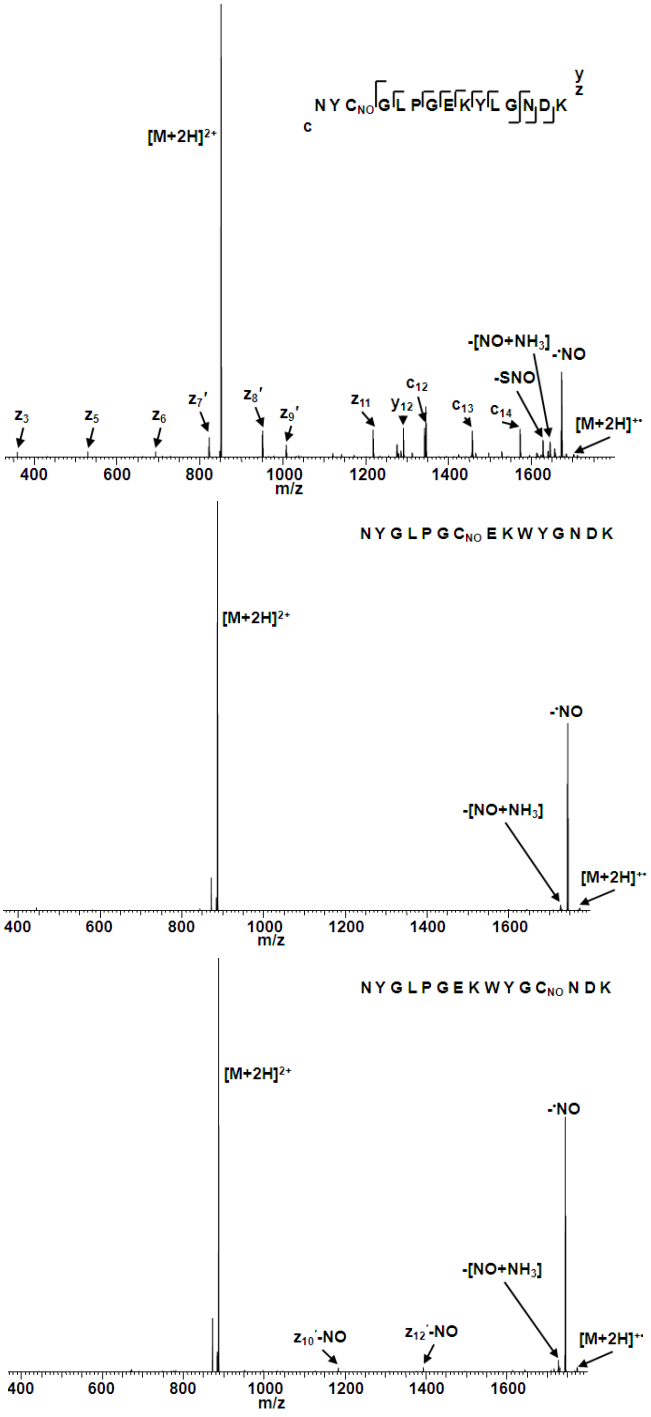

Figure 6.2.2: ECD of doubly-charged S-nitrosopeptides

ECD mass spectra of nitrosylated doubly-charged $[NYC_{NO}GLPGEKYLGNDK + 2H]^{2+}$, $[NYGLPGC_{NO}EKWYGNDK + 2H]^{2+}$, and $[NYGLPGEKWYGC_{NO}NDK + 2H]^{2+}$, peptide ions. C_{NO} denotes *S*-nitrosylation. ECD results in the dominant loss of $^{\bullet}NO$ following electron capture, *i.e.* $[M+2H]^{+}$-$^{\bullet}NO$. Peptide sequence coverage is extremely low for the doubly-charged peptides with the exception of $[NYC_{NO}GLPGEKYLGNDK + 2H]^{2+}$ which also allows some modification localisation possible.

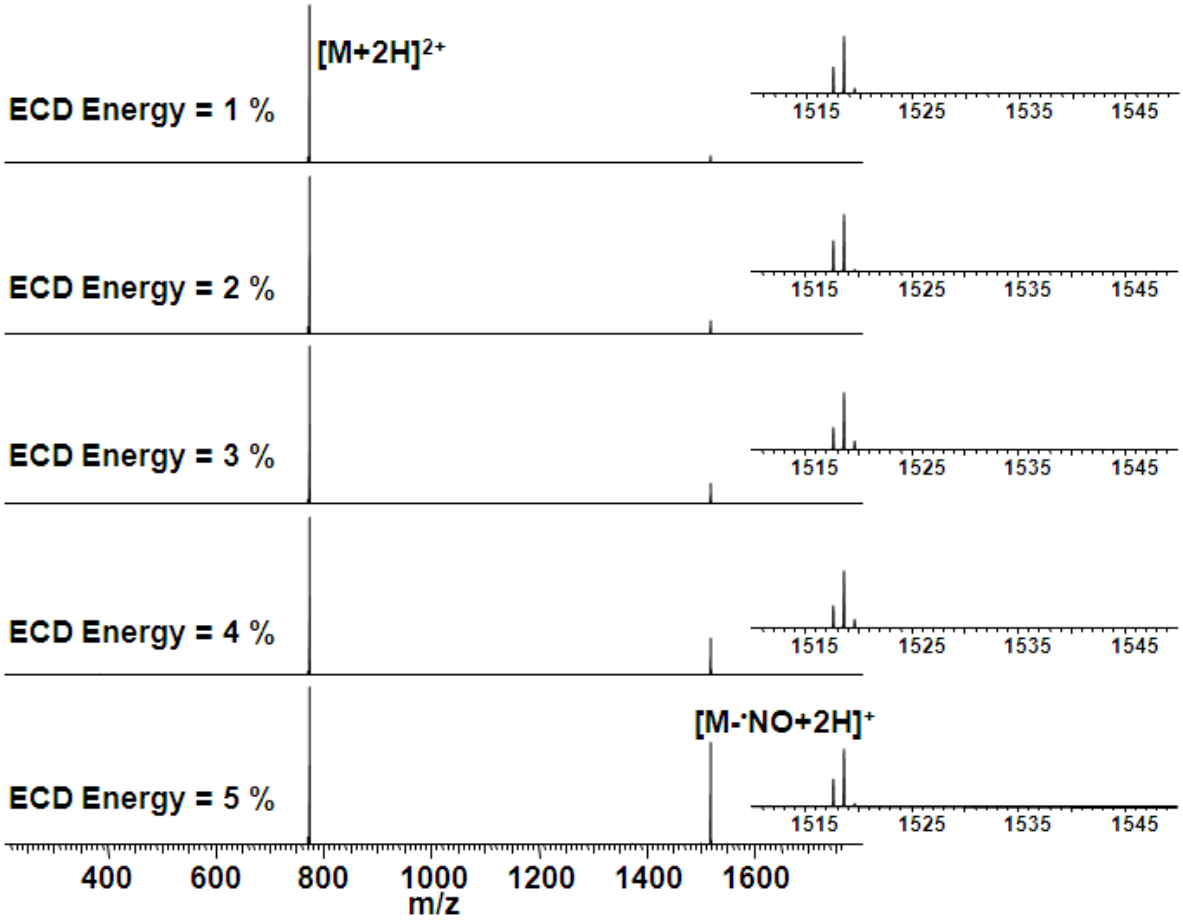

Figure 6.3: Effect of ECD energy on radical •NO loss from *S*-nitrosopeptides

ECD mass spectra of doubly-charged nitrosylated $[NAC_{NO}GAPGEKWAGNDK + 2H]^{2+}$ with varying levels of energy corresponding to cathode potentials of +1.6625 V (1 %) to -2.79 V (5 %). Insets are zoomed in regions of the full ECD mass spectra where $[M+2H]^{+\bullet}$ (calculated *m*/*z* = 1546.6703) and $[M+2H]^{+}$-•NO (calculated *m*/*z* = 1516.6723) are identified. Neutral loss of •NO from the precursor ion are not identified. Neutral loss of •NO following ECD is a radical process due to bond cleavage taking place without the need of a specific energy threshold.

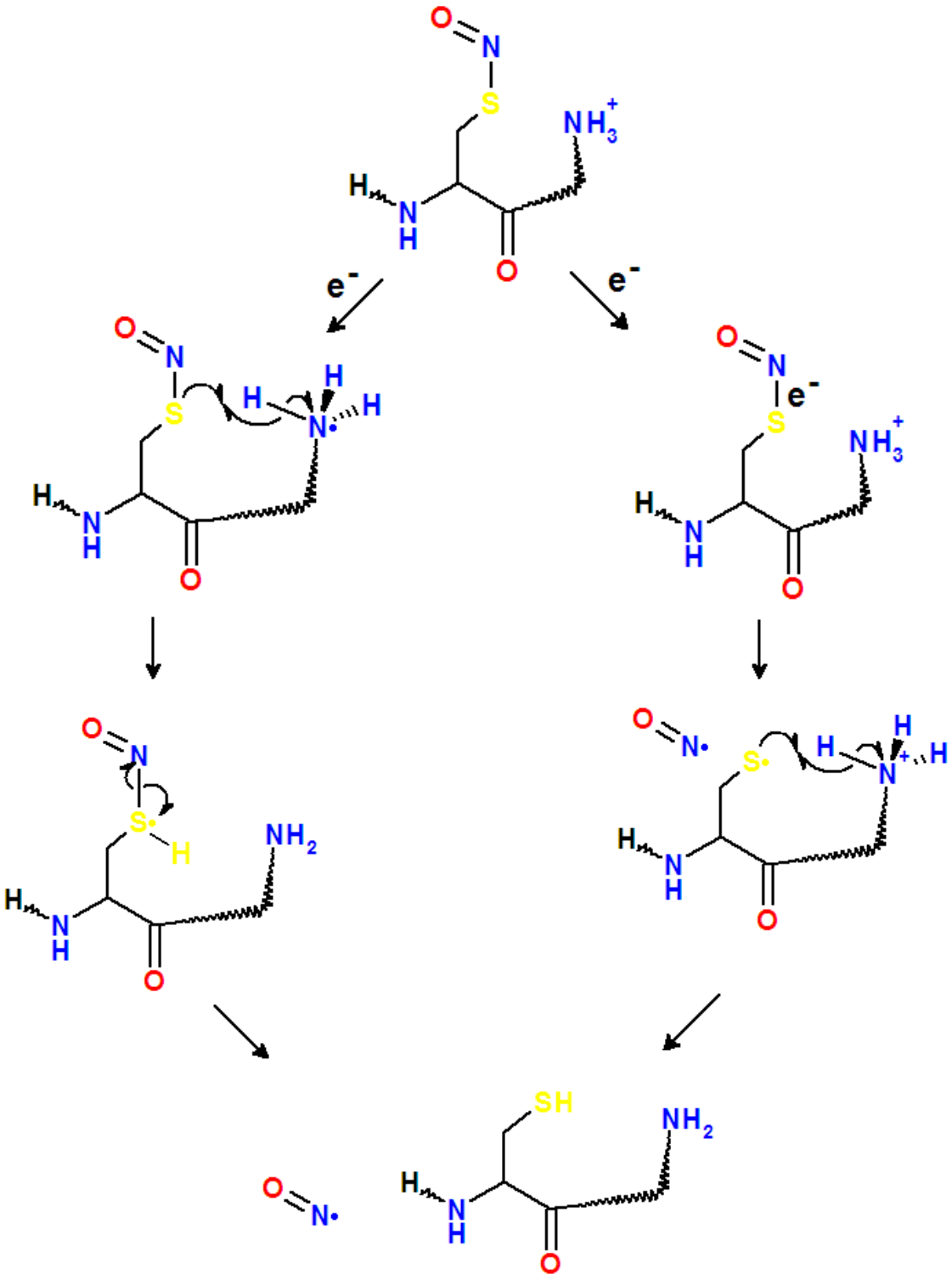

Figure 6.4: Proposed mechanism of NO neutral loss following ECD of S-nitrosopeptides

Following initial electron capture at a site of protonation fragmentation takes place *via* a modified Cornell or UW mechanism. Hydrogen transfer to the sulfur atom prior to RS-NO bond cleavage (**Left**) or electron transfer to the RS-NO σ* orbital initiates homolysis followed by hydrogen transfer (**Right**).

electron transfer to the S-N σ* orbital is therefore in competition with transfer to a Coulomb-stabilised amide π* orbital.

Recent quantum calculations have shown the weakness of the S-N bond in *S*-nitrothiols is due to delocalisation from the oxygen lone pair into the S-N σ* orbital [190], *i.e.* the S-N σ* orbital is stabilised. Thus electron capture or transfer to the S-N σ* orbital occurs at a much lower energetic cost than would be expected for the S-C σ* orbitals of carbamidomethylated and carbamidomethylated peptides. This favourable electron transfer explains $^{\bullet}$NO loss being far greater than that of CH_2CONH_2 and CH_2COOH loss following ECD of the alkylated peptides as showed in **Chapter 5**.

As mentioned previously, ECD of the doubly-charged peptides led to a greatly diminished peptide sequence coverage in nearly all cases. For three of the peptides, no backbone fragments were observed, and ECD of $[NYC_{NO}GLPGEYWLGNDK + 2H]^{2+}$ resulted in only two *c*/*z* ions (and one *y* ion), whereas ECD of its unmodified counterpart led to 11 *c*/*z* ions (and eight *y* ions). Addition of the nitrosyl group led to a decrease in sequence coverage following ECD of $[NYC_{NO}GLPGERWLGNDR + 2H]^{2+}$ (from 13/14 N-Cα bonds cleaved to 6/14 N-Cα bonds cleaved). All fragment ions had comparable abundance to those from its unmodified counterpart. ECD of $[NYC_{NO}GLPGEKYLGNDK + 2H]^{2+}$ gave the highest sequence coverage (10/14 N-Cα bonds cleaved), a decrease of only two fragmentation sites from its unmodified counterpart. None of the fragments show loss of $^{\bullet}$NO; however, the neutral loss of $^{\bullet}$NO from the charged reduced precursor is still the most abundant peak within the ECD mass spectrum. These data suggest that there is a competition between electron capture/transfer into either the RS-NO σ* orbital or the N-Cα π* orbital, and appears to be

most competitive for $[NYC_{NO}GLPGEKYLGNDK + 2H]^{2+}$ peptide ions in which both $^{\bullet}NO$ and abundant *c*/*z* ions are identified.

The major product of ECD of *S*-nitrosopeptides is even-electron and hence does not dissociate further. The observation that ECD of $[NYC_{NO}GLPGERWLGNDR + 2H]^{2+}$ and $[NYGLPGEKWYGC_{NO}DK + 2H]^{2+}$ led to the formation of a total of three *c*/*z* ions with the loss of $^{\bullet}NO$ is presumably derived from radically-driven backbone fragmentation with concomitant thermally-driven loss of $^{\bullet}NO$.

In three cases in which backbone fragments are observed following ECD, ($[NYC_{NO}GLPGEYWLGNDK + 2H]^{2+}$, $[NYC_{NO}GLPGERWLGNDR + 2H]^{2+}$ and $[NYC_{NO}GLPGEKYLGNDK + 2H]^{2+}$), a peak corresponding to the loss of $^{\bullet}SNO$ from the charge reduced species is observed. This C_{β}-S bond cleavage can be explained by a mobile radical [113]: α-hydrogen abstraction from a distant radical site results in the formation of a stable radical at the α-carbon of the nitrosocysteine residue (stabilised by the captodative effect), ultimately leading to homolysis of the C_{β}-S bond (see **Figure 6.5**).

The ECD mass spectra of $[NYC_{NO}GLPGEYWLGNDK + 2H]^{2+}$ and $[NYC_{NO}GLPGEYWLGNDR + 2H]^{2+}$ contain peaks corresponding to the neutral loss of NH_3. The sites of protonation are likely to be on the BAAR (Lys or Arg) and the N-terminus, and therefore, from previous work [180] and from the data collected from 3-nitrotyrosine-containing peptides shown previously in this thesis, ammonia loss appears to originate from the protonated N-terminus when electron capture occurs at this site. This is supported by the

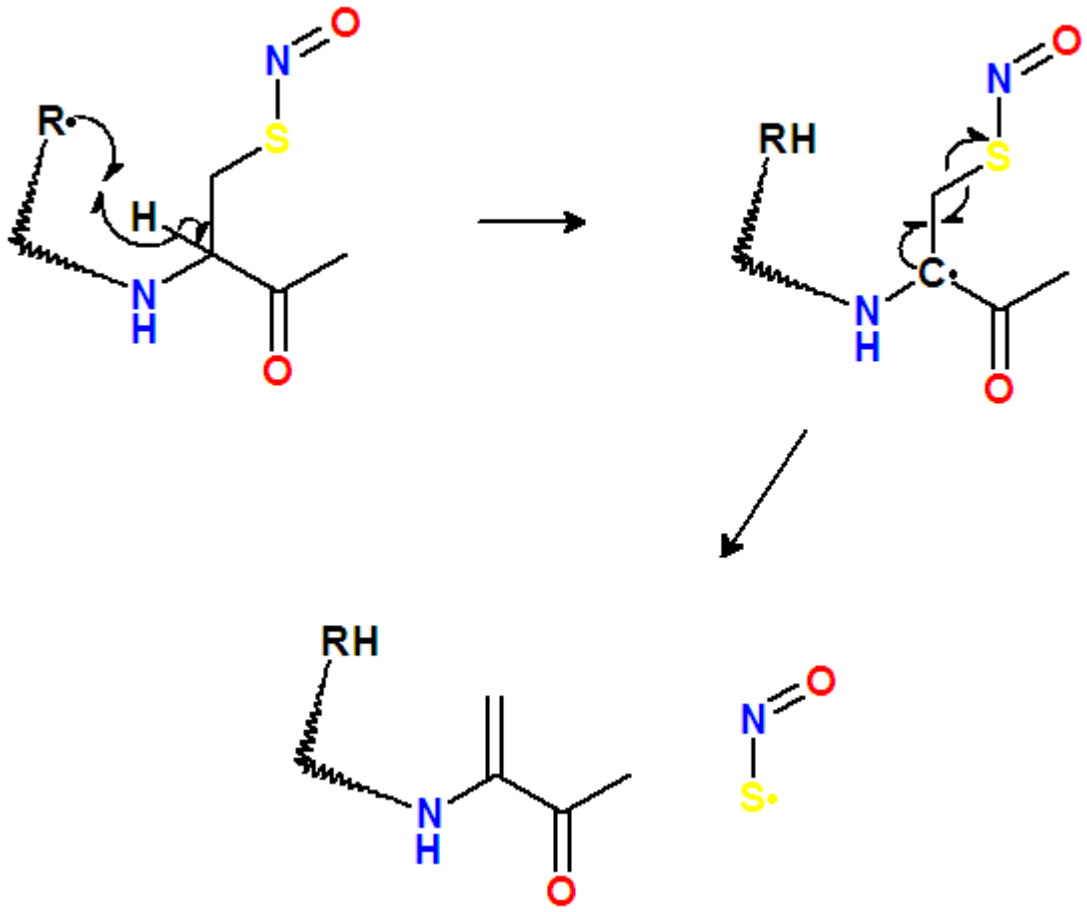

Figure 6.5: Proposed mechanism of ˙SNO neutral loss following ECD of *S*-nitrosopeptides

Following initial electron capture at a site of protonation fragmentation takes place *via* α-hydrogen abstraction followed by homolysis of the C_β-S bond.

exclusively C-terminal fragment ions identified. ECD of all of the doubly-charged peptides resulted in the combined neutral loss of [$^{\bullet}$NO + NH_3] from the charge reduced precursor ion. In these cases, it can be speculated that following initial ammonia loss from the N-terminal or the BAAR, the α- or ε-radical (product of ammonia loss from N-terminal and BAAR, respectively) must interact, directly or indirectly, with the sulfur atom to lead to subsequent $^{\bullet}$NO loss. This transfer may be from a direct or indirect interaction. Alternatively, in this case, only $^{\bullet}$NO or NH_3 loss is generated through the radical-driven mechanism and the other loss is thermally driven.

6.2.2 ECD of triply-charged *S*-nitrosopeptides

The ECD mass spectra of the triply-charged *S*-nitrosylated peptide ions contrast with their doubly-charged counterparts, see **Figure 6.6**. In all cases a sequence coverage of >50 % is noted, and in the case of $[NYGLPGEKWYGC_{NO}NDK + 3H]^{3+}$, 10 *c*/*z* ions were identified, resulting in a sequence coverage of 71.4 %, in comparison to zero ions for its doubly-charged counterpart. It should be noted that, despite the much increased sequence coverage, the ECD mass spectrum is still dominated by a single peak corresponding to the neutral loss of $^{\bullet}$NO following initial electron capture. The exception is $[NYC_{NO}GLPGEKYLGNDK + 3H]^{3+}$ in which this peak is the second most abundant within the ECD mass spectrum (the most intense being the triply-charged precursor ion). ECD of $[NYC_{NO}GLPGERWLGNDR + 3H]^{3+}$ and $[NYC_{NO}GLPGEKYLGNDK + 3H]^{3+}$ led to the identification of five and eight *c* ions, respectively, which retained the modification. As with the doubly-charged peptides, these data suggest that $NYC_{NO}GLPGERWLGNDR$ and $NYC_{NO}GLPGEKYLGNDK$ behave differently to the other peptides analysed in this work.

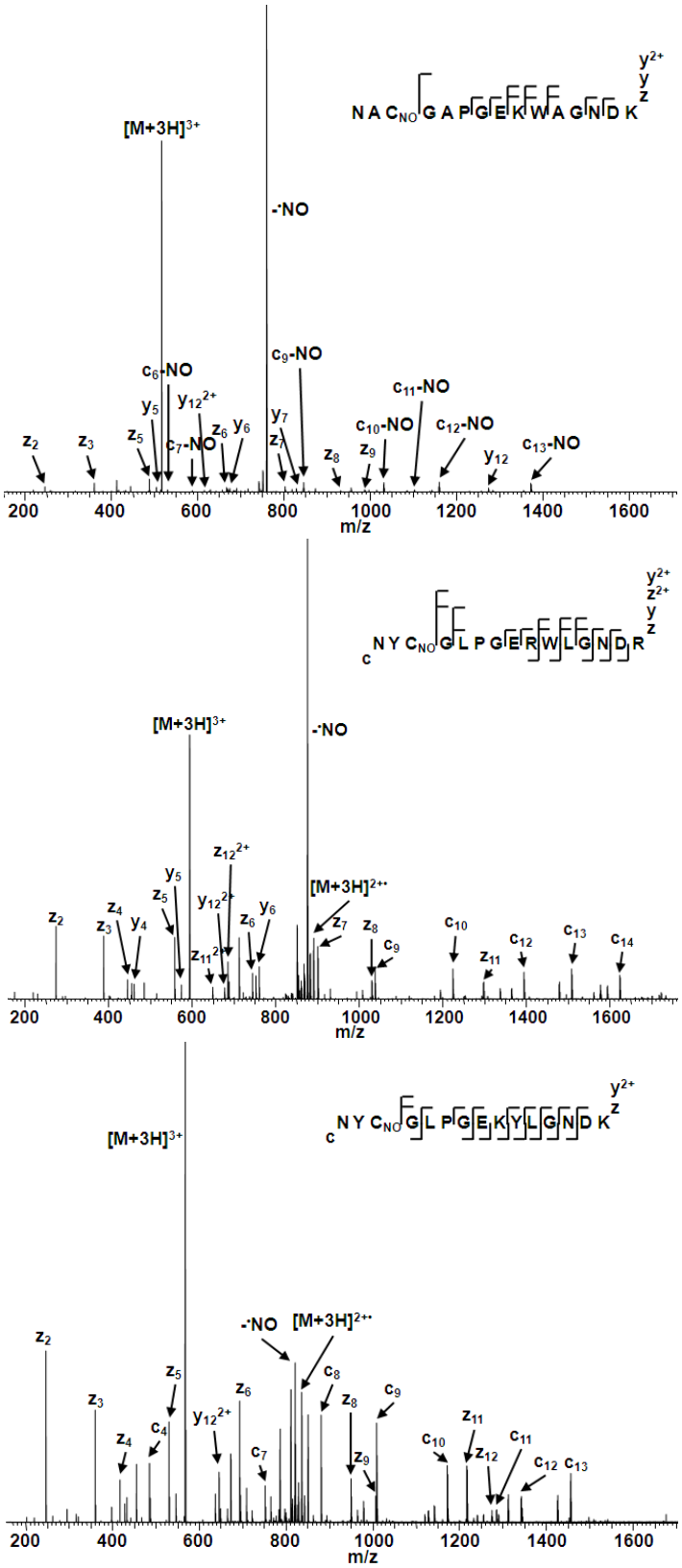

Figure 6.6.1: ECD of triply-charged *S*-nitrosopeptides

ECD mass spectra of nitrosylated triply-charged [NAC$_{NO}$GAPGEKWAGNDK + 3H]3+, [NYC$_{NO}$GLPGERWLGNDR + 3H]$^{3+}$, and [NYC$_{NO}$GLPGEKYLGNDK + 3H]$^{3+}$ peptide ions. C$_{NO}$ denotes *S*-nitrosylation. ECD of triply-charged peptides leads to a much greater peptide sequence coverage compared to their doubly-charged peptide counterparts.

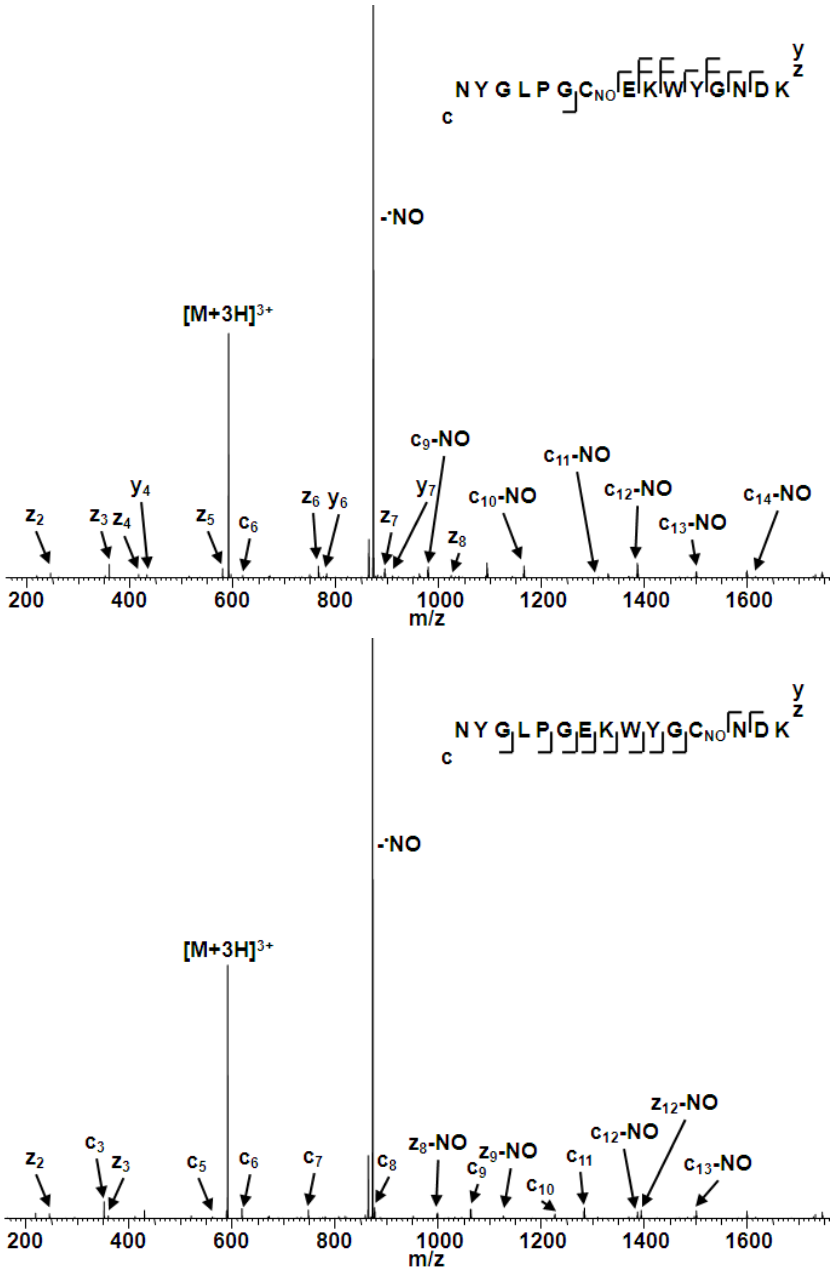

Figure 6.6.2: ECD of triply-charged *S*-nitrosopeptides

ECD mass spectra of nitrosylated triply-charged $[NYGLPGC_{NO}EKWYGNDK + 3H]^{3+}$, and $[NYGLPGEKWYGC_{NO}NDK + 3H]^{3+}$ peptide ions. C_{NO} denotes *S*-nitrosylation. ECD of triply-charged peptides leads to a much greater peptide sequence coverage compared to their doubly-charged peptide counterparts.

The abundant neutral loss of $^{\bullet}$NO can be explained by the modified Cornell/UW mechanism proposed above, *i.e.* electron capture/transfer to the S-N σ* orbital is in direct competition with capture/transfer to an N-Cα π* orbital. The results for triply-charged $NAC_{NO}GAPGEKWAGNDK$, $NYGLPGC_{NO}GEKWYGNDK$ and $NYGLPGEKWYGC_{NO}NDK$ suggest that initial electron capture results in $^{\bullet}$NO loss, forming $[M-^{\bullet}NO+3H]^{2+}$, followed by secondary electron capture at a site of protonation resulting in *c*/*z* fragments, thus producing no doubly-charged backbone fragments and singly-charged fragments which exhibit $^{\bullet}$NO loss. The results for triply-charged $NYC_{NO}GLPGERWLGNDR$ and $NYC_{NO}GLPGEKYLGNDK$, in which backbone fragment ions retain the nitrosyl group are identified, suggest a more even competition between transfer to the S-N σ* orbital and an amide π* orbital.

6.2.3 Molecular models of *S*-nitrosopeptides

The ECD behaviour of these nitrosylated peptides appears to have a broad range, from dominant electron transfer to the S-N σ* orbital (in most cases) to a relatively even competition between transfer to the S-N σ* orbital and an N-Cα π* orbital. In order to explain these behaviours, molecular structures of the peptides were generated by molecular dynamic (MD) simulations. Representative molecular models for $[NAC_{NO}GAPGEKWAGNDK + 2H]^{2+}$ (chosen to represent those peptides where no backbone fragmentation is observed), $[NYC_{NO}GLPGERWLGNDR + 2H]^{2+}$ (which exhibited intermediate sequence coverage), and $[NYC_{NO}GLPGEKYLGNDK + 2H]^{2+}$ (which exhibited extensive sequence coverage) following 500 ns of MD simulations are shown in **Figure 6.7**. (The remaining structures are shown in **Appendix 2**). In all cases a stable structure has converged after 500 ns of MD

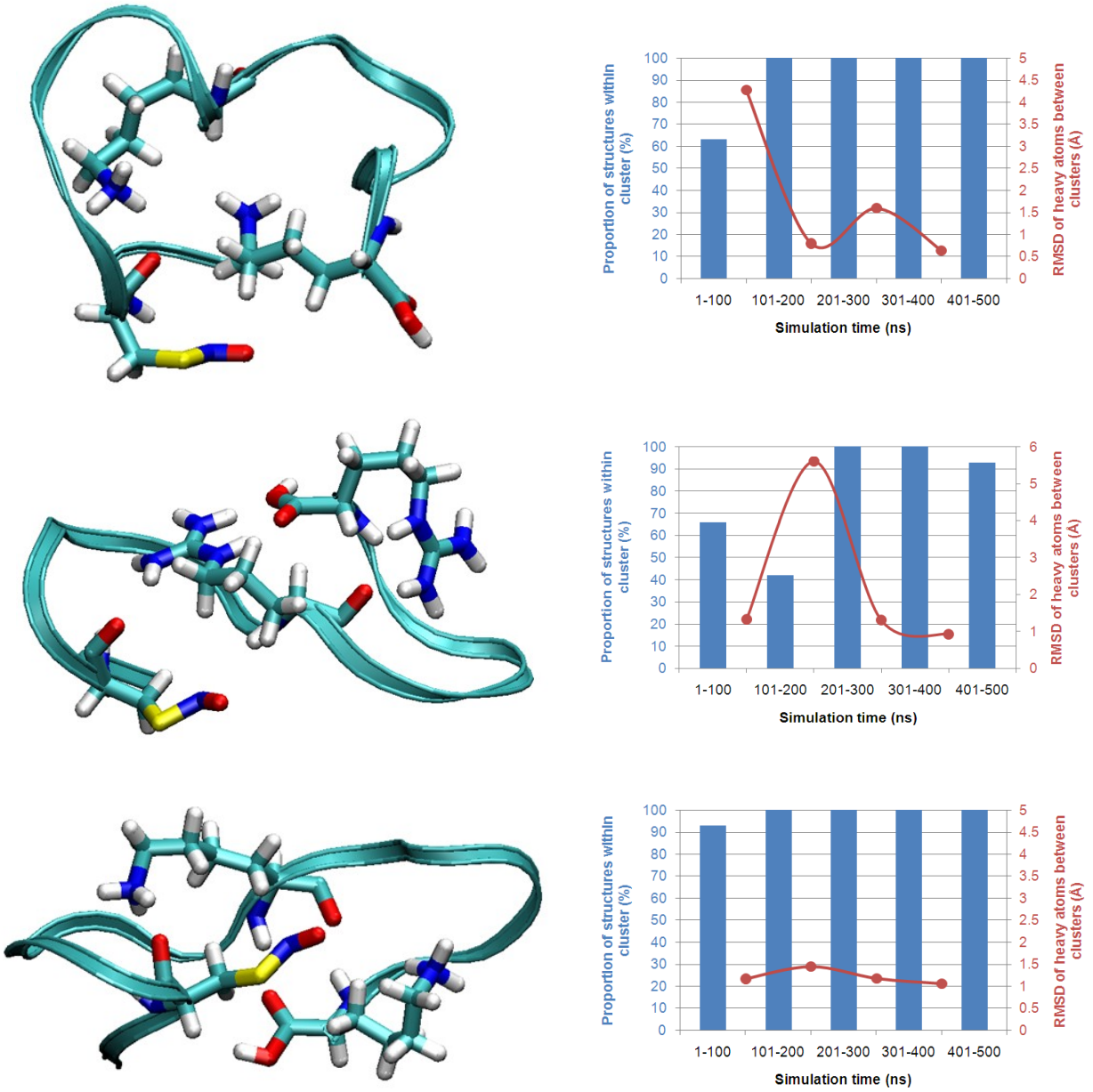

Figure 6.7: Molecular models of doubly-charged *S*-nitrosopeptides

Structures shown are the most common following 401-500 ns of molecular dynamic simulations for doubly-charged $[NAC_{NO}GAPGEKWAGNDK + 2H]^{2+}$ (**Upper**), $[NYC_{NO}GLPGERWLGNDR + 2H]^{2+}$ (**Middle**), and $[NYC_{NO}GLPGEKYLGNDK + 2H]^{2+}$ (**Lower**) peptide ions. Graphs show the percentage proportion of the most populated cluster between each simulation time window, and the RMSD in angstroms of heavy atoms between the most common structures between time windows.

simulations (six of the seven peptides had only one structure after this time period), and RMSD analysis between the representative models of the 300-400 ns and 400-500 ns windows being ≤1 Å.

For $[NAC_{NO}GAPGEKWAGNDK + 2H]^{2+}$, which displayed no backbone fragmentation following ECD, the protonated central Lys is close in space to the carbonyl of the nitrosocysteine residue (4.32 Å), and the protonated C-terminal Lys has a fairly open structure and is not embedded within any region of the peptide backbone (solvent accessibility of the polar atoms in the side chain was 68.05 $Å^2$, *cf*. 112.79 $Å^2$ for the total residue). ECD of $[NYC_{NO}GERWLGNDR + 2H]^{2+}$ resulted in intermediate backbone fragmentation, with ions identified between Cys3 and Arg9, and no fragment ions C-terminal of Arg9. The molecular structure shows the central protonated Arg residue is buried (solvent accessibility of the polar atoms in the side chain was 20.84 $Å^2$ *cf*. 88.95 $Å^2$ for the total residue) within the Cys3-Arg9 region of the peptide, whereas the C-terminal protonated Arg is not interacting closely with the peptide backbone (solvent accessibility of the polar atoms in the side chain was 45.64 $Å^2$ *cf*. 144.57 $Å^2$ for the total residue). This observation suggests that the embedded central Arg encourages N-Cα fragmentation in this region rather than electron transfer to the S-N σ* orbital, which dominates when electron capture takes place at the C-terminal Arg. Finally, the structure of $[NYC_{NO}GLPGEKYLGNDK + 2H]^{2+}$ reveals the central protonated lysine to be buried in the N-terminal region of the peptide (solvent accessibility of the polar atoms in the side chain was 0.00 $Å^2$ *cf*. 82.13 $Å^2$ for the total residue) and the C-terminal protonated lysine to be buried (solvent accessibility of the polar atoms in the side chain was 21.64 $Å^2$ *cf*. 110.25 $Å^2$ for the total residue) in the C-terminal region of the peptide. For this species, backbone fragments were observed between Cys3 and Lys14.

These data therefore suggest that the observed backbone fragmentation is the result of the proximity and interaction of the protonation site with the backbone cleavage site. Either these interactions increase the Coulomb stabilisation of the amide π* orbital thus encouraging electron transfer into that orbital or electron transfer is directed to the amide π* orbital following electron capture at the protonation site.

All of the other doubly-charged peptides resulted in no, or very minor, fragmentation following ECD and the molecular models generated for these also appear to agree with the observations above. The one exception is $[NYC_{NO}GLPGEYWLGNDK + 2H]^{2+}$ in which the protonated Lys14 residue is buried (solvent accessibility of the polar atoms in the side chain was 18.15 $Å^2$ *cf.* 109.25 $Å^2$ for the total residue) in the C-terminal region of the peptide, an area of the peptide which did not fragment. As discussed above, ECD of this peptide led to the neutral loss of ammonia from the N-terminus, suggesting that electron capture occurs at the N-terminus, which is not buried (solvent accessibility was 73.44 $Å^2$ *cf.* 98.62 $Å^2$ for the total residue) within the peptide backbone, rather than the C-terminal Lys.

The predicted molecular structures for the three peptides discussed in detail above are shown as their triply-charged counterparts along with the clustering and RMSD data in **Figure 6.8**. (The remaining triply-charged peptides are shown in **Appendix 2**). In these cases the MD simulations do not appear to have resulted in a converged structure for all peptides. It is worth noting that, as expected, (due to charge-repulsion) the triply-charged peptide ions have more extended structures that their doubly-charged counterparts, and therefore it is probable that, as through bond electron transfer rates are dependent on distance [106, 107], electron transfer to the S-N σ* orbital may be prevented in some instances.

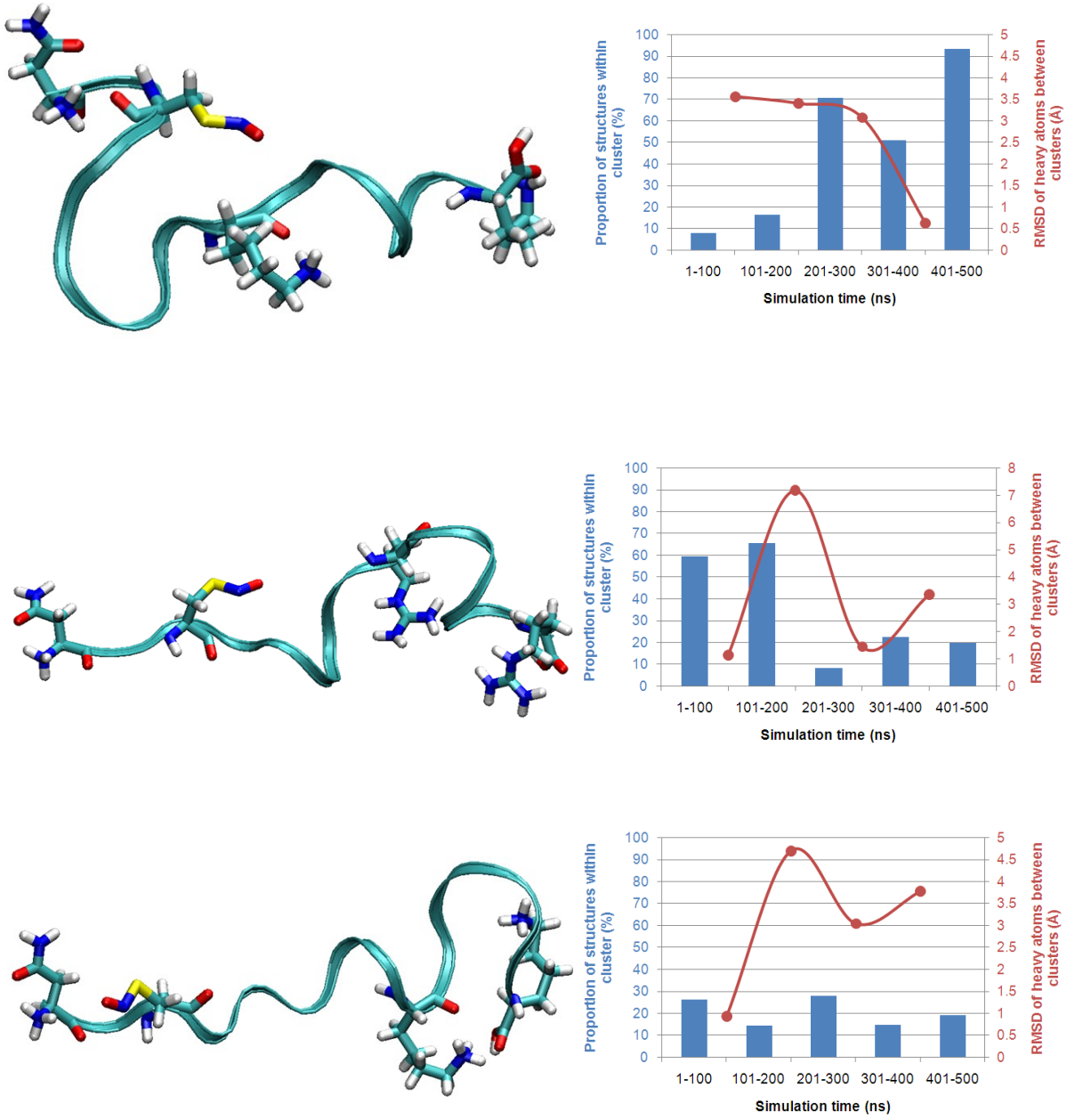

Figure 6.8: Molecular models of triply-charged *S*-nitrosopeptides

Structures shown are the most common following 401-500 ns of molecular dynamic simulations for triply-charged $[NAC_{NO}GAPGEKWAGNDK + 3H]^{3+}$ (**Upper**), $[NYC_{NO}GLPGERWLGNDR + 3H]^{3+}$ (**Middle**), and $[NYC_{NO}GLPGEKYLGNDK + 3H]^{3+}$ (**Lower**) peptide ions. Graphs show the percentage proportion of the most populated cluster between each simulation time window, and the RMSD in angstroms of heavy atoms between the most common structures between time windows.

6.2.4 CID of *S*-nitrosopeptides

The CID mass spectra of the unmodified peptides $[NYCGLPGEYWLGNDK + 2H]^{2+}$ and the doubly- and triply-charged NACGAPGEKWAGNDK are shown in **Figure 3.1**, **5.1** and **5.4**, respectively. CID mass spectra of the other unmodified peptides are shown in **Figure 6.9**. All show extensive N-C_O bond fragmentation with numerous *b*/*y* ions being observed. For the doubly-charged precursors, as observed by Gross and co-workers [183], *S*-nitrosylation leads to extremely diminished peptide backbone fragmentation, with the neutral loss of the $^{\bullet}$NO group dominating the CID mass spectrum, see **Figure 6.10**.

The most abundant peaks in the CID mass spectra of all the doubly-charged *S*-nitrosopeptides correspond to neutral loss of $^{\bullet}$NO. This behaviour would be expected due to the extremely low average bond dissociation energy of the S-N bond (20-28 kcal mol^{-1}) [153] (*cf.* RS-SR 70-74 kcal mol^{-1} [154]). In some cases additional losses, corresponding to amino acid side chains are observed, and these are discussed in more detail in **Section 6.2.6.1**. Five of the eight doubly-charged peptides dissociated to give the y_{10} ion, which corresponds to cleavage N-terminal to the Pro residue – a highly favourably fragmentation site following CID [74]. CID of $[NYC_{NO}GLPGERWLGNDR + 2H]^{2+}$ also resulted in y_7 and b_{14} fragments, both of which derive from cleavage at the arginine residues and can be explained by the basicity of arginine in relation to the mobile proton model [73-75].

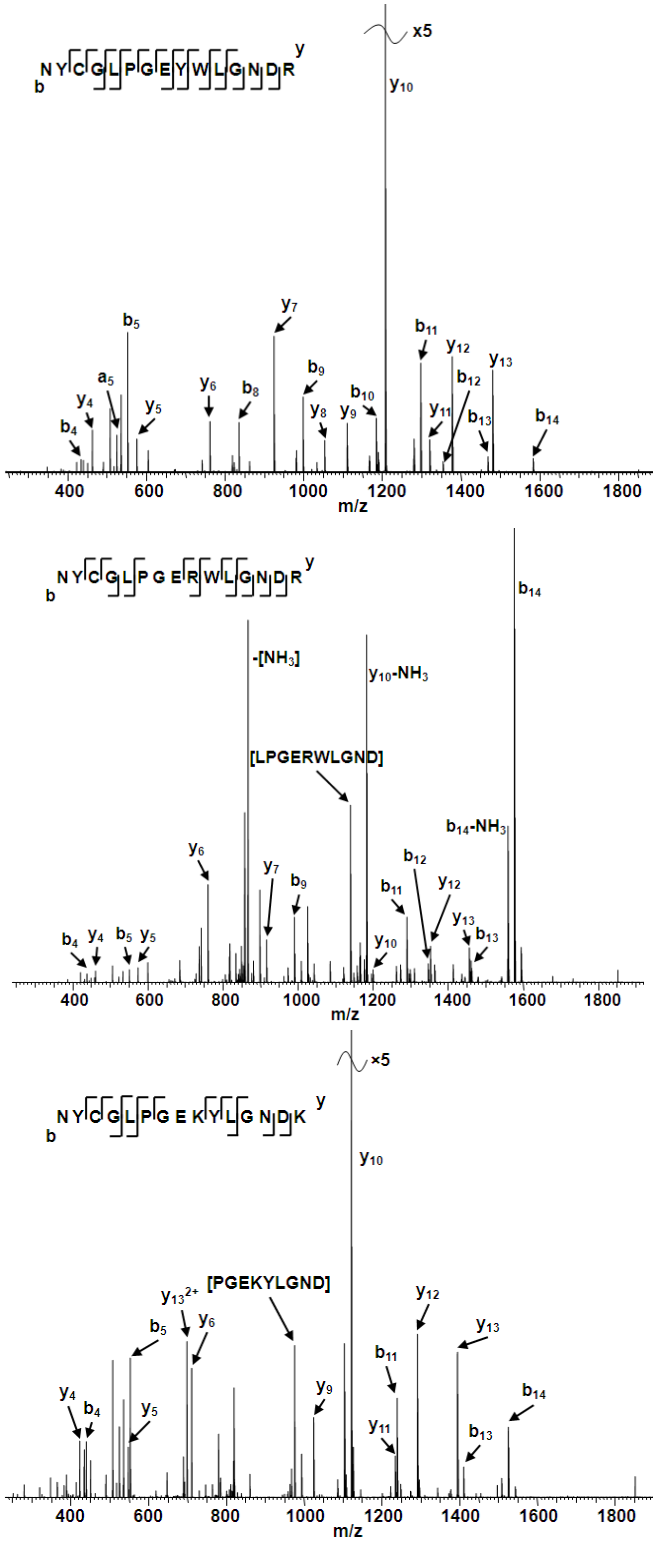

Figure 6.9.1: CID of unmodified doubly- and triply-charged cysteine-containing peptides

CID mass spectra of the doubly-charged [NYCGLPGEYWLGNDR + 2H]$^{2+}$, [NYCGLPGERWLGNDR + 2H]$^{2+}$, and [NYCGLPGEKYLGNDK + 2H]$^{2+}$ peptide ions.

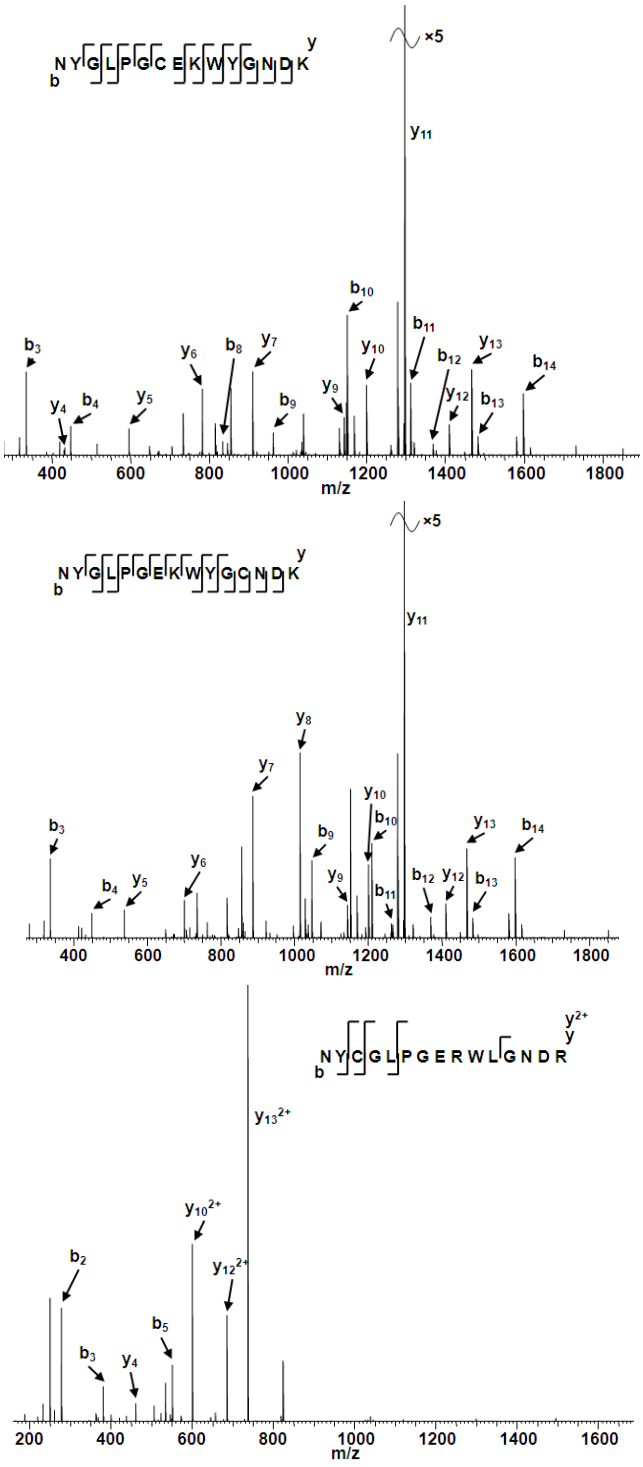

Figure 6.9.2: CID of unmodified doubly- and triply-charged cysteine-containing peptides

CID mass spectra of the doubly-charged [NYGLPGCEKWYGNDK + 2H]$^{2+}$, and [NYGLPGEKWYGCNDK + 2H]$^{2+}$, and triply-charged [NYCGLPGERWLGNDR + 3H]$^{3+}$ peptide ions.

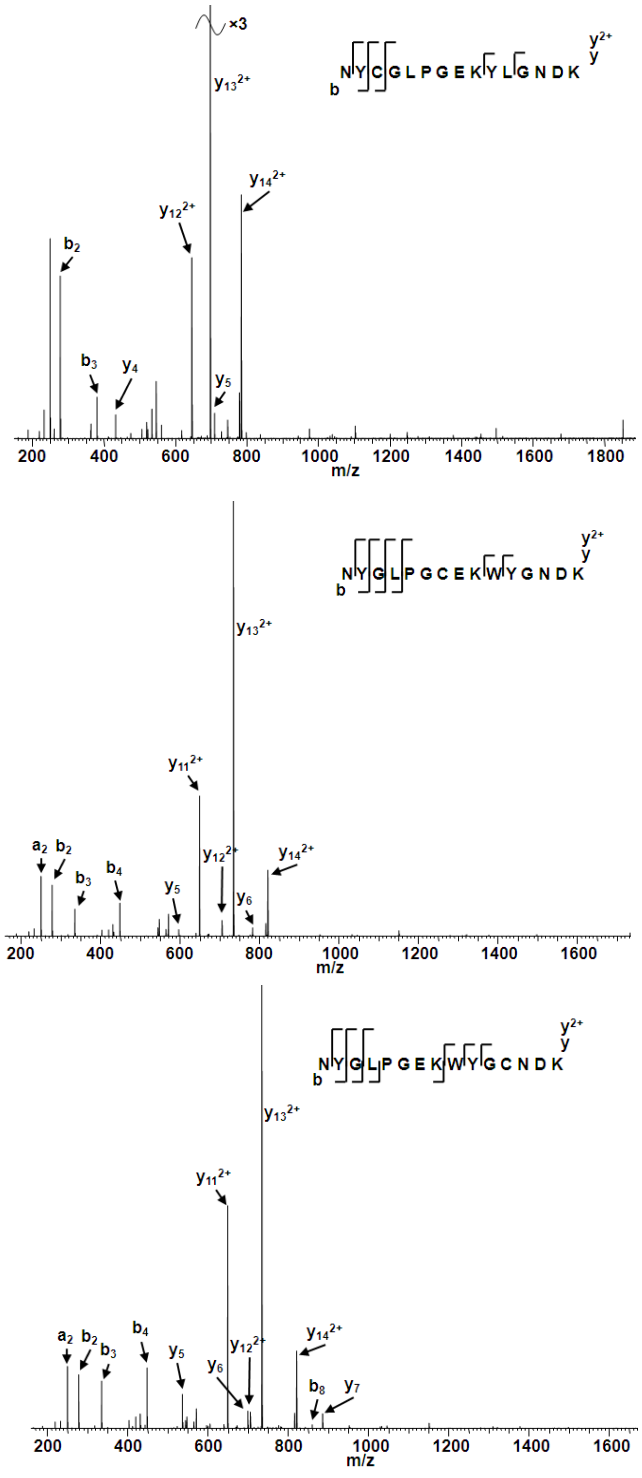

Figure 6.9.3: CID of unmodified doubly- and triply-charged cysteine-containing peptides

CID mass spectra of the triply-charged [NYCGLPGEKYLGNDK + 3H]$^{3+}$, [NYGLPGCEKWYGNDK + 3H]$^{3+}$, and [NYGLPGEKWYGCNDK + 3H]$^{3+}$ peptide ions.

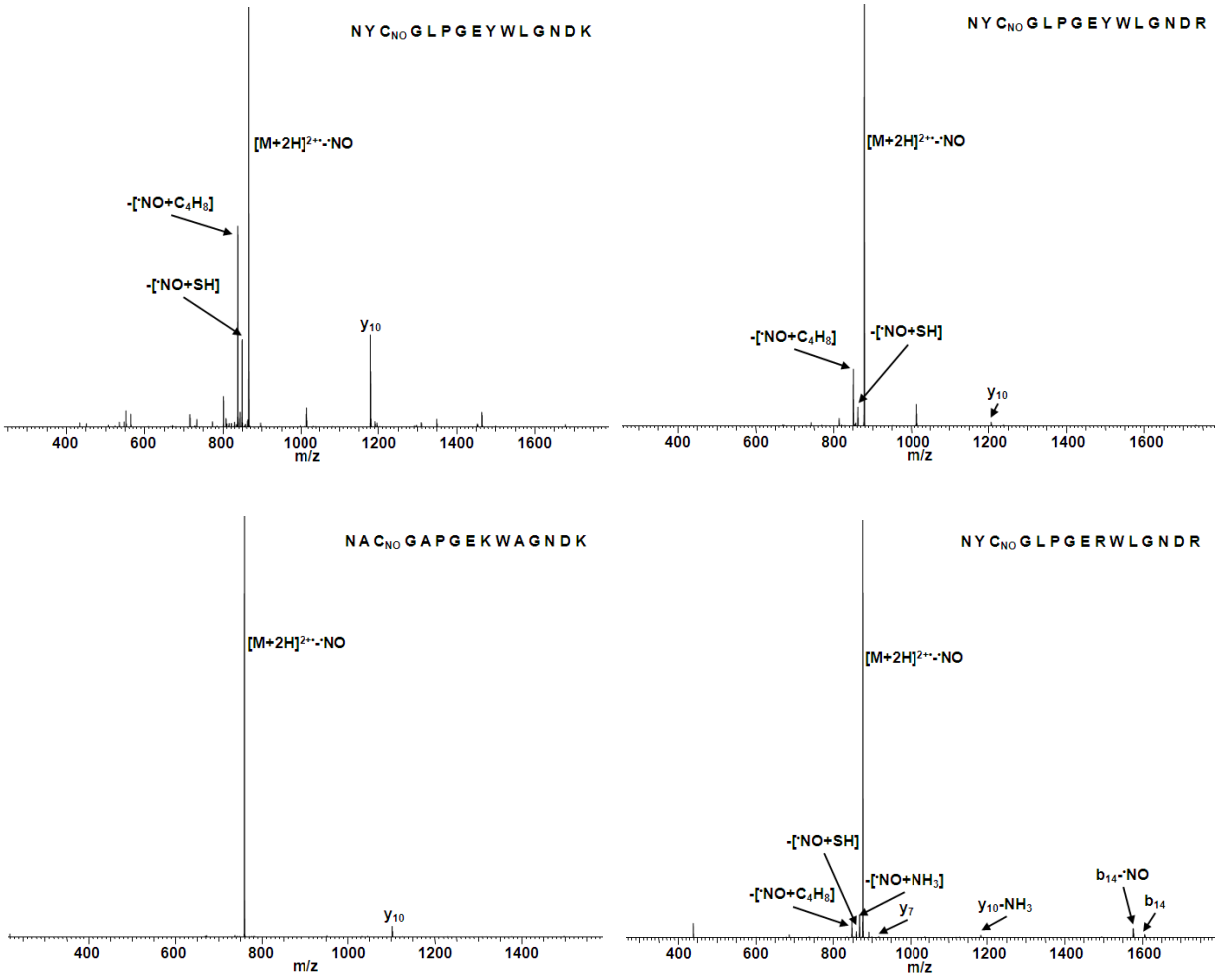

Figure 6.10.1: CID of *S*-nitrosopeptides

CID mass spectra of nitrosylated doubly-charged $[NYC_{NO}GLPGEYWLGNDK + 2H]^{2+}$, $[NYC_{NO}GLPGEYWLGNDR + 2H]^{2+}$, $[NAC_{NO}GAPGEKWAGNDK + 2H]^{2+}$, and $[NYC_{NO}GLPGERWLGNDR + 2H]^{2+}$ peptide ions. C_{NO} denotes *S*-nitrosylation. CID results in the dominant neutral loss of $^{\bullet}$NO, resulting in the hydrogen-deficient radical $[M+2H]^{2+\bullet}$-$^{\bullet}$NO ion. Peptide sequence coverage is limited, with the identification of only one or two backbone fragment ions.

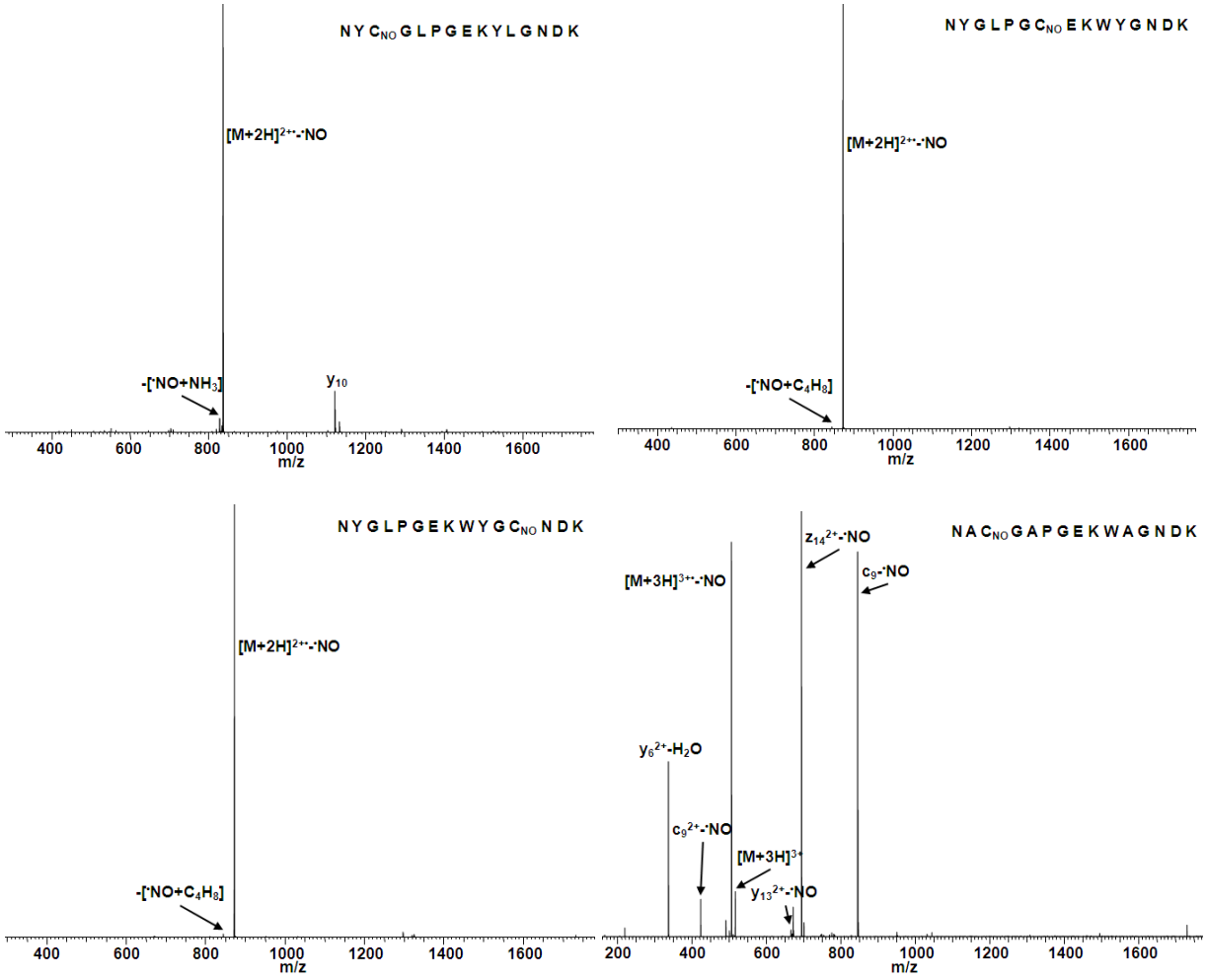

Figure 6.10.2: CID of *S*-nitrosopeptides

CID mass spectra of nitrosylated doubly-charged $[NYC_{NO}GLPGEKYLGNDK + 2H]^{2+}$, $[NYGLPGC_{NO}EKWYGNDK + 2H]^{2+}$, $[NYGLPGEKWYGC_{NO}NDK + 2H]^{2+}$, and triply-charged $[NAC_{NO}GAPGEKWAGNDK + 3H]^{3+}$ peptide ions. C_{NO} denotes *S*-nitrosylation. CID results in the dominant neutral loss of $^{\bullet}NO$, resulting in the hydrogen-deficient radical $[M+2H]^{2+\bullet}$-$^{\bullet}NO$ ion ($[M+3H]^{3+\bullet}$-$^{\bullet}NO$ for $[NAC_{NO}GAPGEKWAGNDK + 3H]^{3+}$). Peptide sequence coverage is limited, with the identification of only one or two backbone fragment ions. *c*/*z* ions are observed in the CID mass spectrum of $[NAC_{NO}GAPGEKWAGNDK + 3H]^{3+}$.

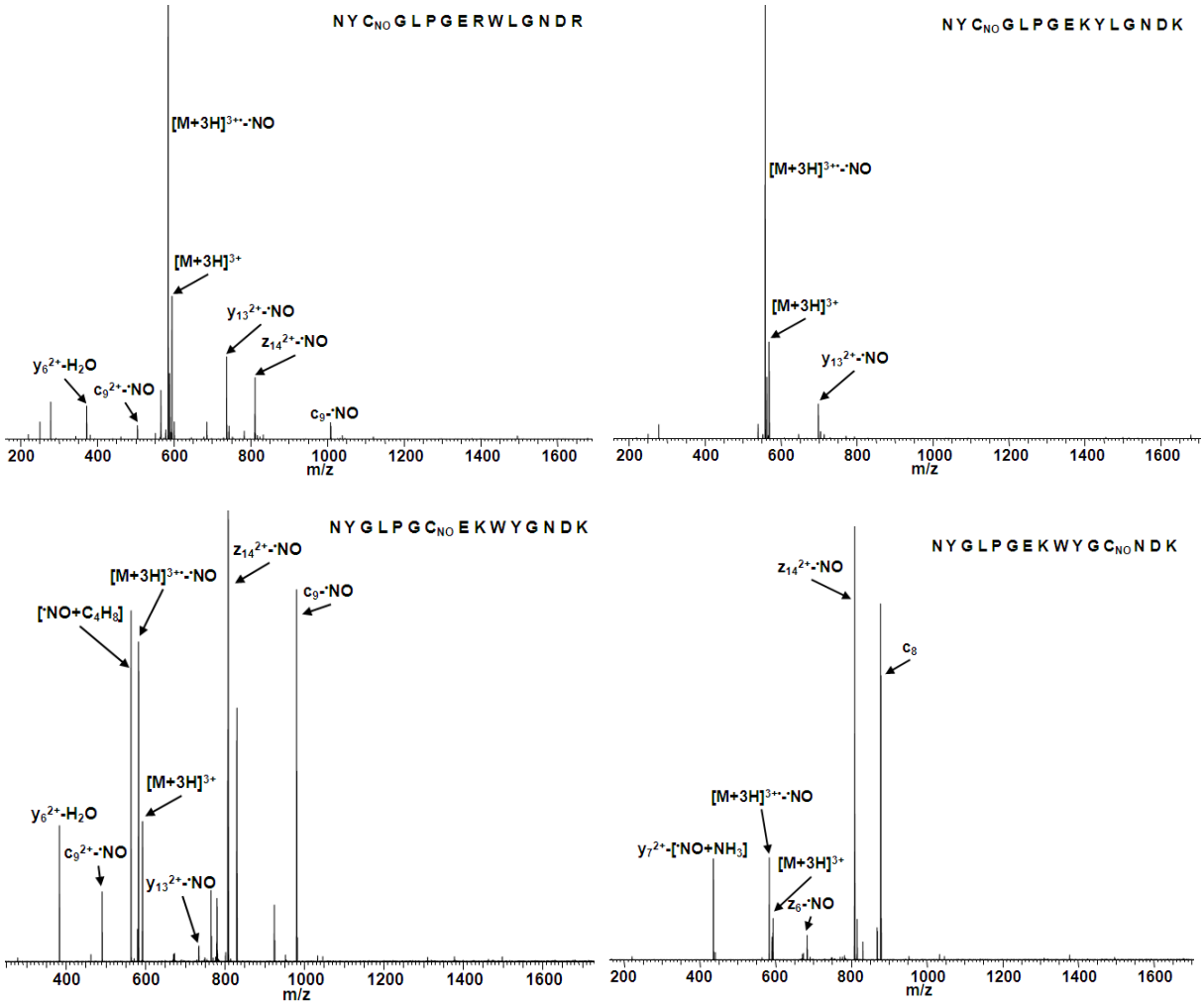

Figure 6.10.3: CID of *S*-nitrosopeptides

CID mass spectra of nitrosylated triply-charged $[NYC_{NO}GLPGERWLGNDR + 3H]^{3+}$, $[NYC_{NO}GLPGEKYLGNDR + 3H]^{3+}$, $[NYGLPGC_{NO}EKWYGNDK + 3H]^{3+}$, and $[NYGLPGEKWYGC_{NO}NDK + 3H]^{3+}$ peptide ions. C_{NO} denotes *S*-nitrosylation. CID results in the dominant neutral loss of $^{\bullet}NO$, resulting in the hydrogen-deficient radical $[M+3H]^{3+\bullet}$-$^{\bullet}NO$. Peptide sequence coverage is limited, with the identification of only one or two backbone fragment ions. With the exception of the $[NYC_{NO}GLPGEKYLGNDK + 3H]^{3+}$ CID mass spectrum *c*/*z* ions are observed in all cases.

In the case of the triply-charged *S*-nitrosopeptides, only two of the peptides, *i.e.* $[NYC_{NO}GLPGERWLGNDR + 3H]^{3+}$ and $[NYC_{NO}GLPGEKYLGNDK + 3H]^{3+}$, resulted in the neutral loss of $^{\bullet}NO$ as the most intense peak within the CID mass spectrum. For the other three peptides, the most intense peaks all correspond to backbone fragment ions with the additional loss of $^{\bullet}NO$. This may come about following initial loss of the $^{\bullet}NO$, due to the extremely low bond strength, followed by secondary backbone fragmentation. Of these backbone fragment ions, all peptides which contained tryptophan fragmented at that residue to give *c* and *y* ions, and with the exception of $[NYC_{NO}GLPGERWLGNDR + 3H]^{3+}$ these *c* ions were particularly intense. Four of the five peptides fragmented to give abundant $[z_{14}–^{\bullet}NO]^{2+}$ ions, *i.e.* cleavage adjacent to the N-terminal asparagine residue. Backbone fragmentation is discussed in more detail in **Section 6.4.6.2** and **6.4.6.3**.

6.2.5 ECD of *S*-radicals

As discussed above, CID of *S*-nitrosopeptides results in the abundant neutral loss of $^{\bullet}NO$ and a long-lived radical cation species *via* homolysis of the RS-NO bond. This stable radical species has one less hydrogen atom than a peptide in a given charge state would typically have, *i.e.* $[(M-H) + nH]^{n+\bullet}$, and is termed a 'hydrogen deficient' radical ion. These species have been recently shown to play a pivotal role in the dissociations of ECD, in which hydrogen-abundant species, *i.e.* $[(M+H) + nH]^{n+\bullet}$, are quickly converted into hydrogen-deficient radicals [113]. The cysteine sulfur-based radical species has been the subject of a number of studies and has been shown to be the distonic structure, despite the most stable structure being shown to undergo favourable electron transfer from the initial site of the sulfur atom to the cysteine α-carbon stabilised by the captodative effect, with calculations showing that radical migration between these sites results in a decrease in energy of 2.5 kJ mol^{-1} [189].

This stabilisation derives from the electron-withdrawing carbonyl oxygen and electron-donating amino nitrogen atoms, both neighbouring the radical α-carbon centre [191]. Work by O'Connor and co-workers [192] has also shown that α-carbon radical species can undergo multiple radical rearrangements within peptides, thus peptide fragmentation can take place in sites distant from the initial site of the radical. The migration of the cysteine sulfur radical has been shown to occur in a time-dependent manner: The radical formed through CID in an ion trap was more reactive to dimethyl sulfide when exposed than those formed *via* in-source CID, and then reacted within an ion trap [189]. Therefore, it is likely that in these experiments, in which the radical species is formed *via* ion trap CID, the radical is situated on the sulfur atom in the majority of the radical peptide ions formed (~70:30 $^{\bullet}$S:$^{\bullet}$Cα [189]), *i.e.* has the distonic structure.

The ECD mass spectra of the hydrogen deficient radical peptide ions following $^{\bullet}$NO loss of *S*-nitrosopeptides generated by CID are shown in **Figure 6.11**. ECD of both [NYC$^{\bullet}$GLPGEYWLGNDK + 2H]$^{2+\bullet}$ and [NYC$^{\bullet}$GLPGEYWLGNDR + 2H]$^{2+\bullet}$ leads to only one peptide backbone fragment, a y_{10} ion which is adjacent to Pro and hence may be thermally driven. These data show a dramatic decrease in sequence coverage in comparison to their unmodified counterparts which obtained a 92.9 % and 57.1 % coverage, respectively. It might be predicted that if the radical underwent transfer to the backbone α-carbons (likely the Cys residue [189]) then we would expect to observe some radical migration throughout the peptide backbone leading to *c*/*z* ion formation [192]. As this is not noted in these mass spectra, it is assumed that the radical site remains on the sulfur atom for these peptides. Thus in the case of these two peptides it is likely that initial electron capture occurs at the N-terminus, as proposed earlier in this work due to the observation of NH_3 loss, and will then undergo through-bond or through-space transfer to the radical present on the sulfur atom. This will

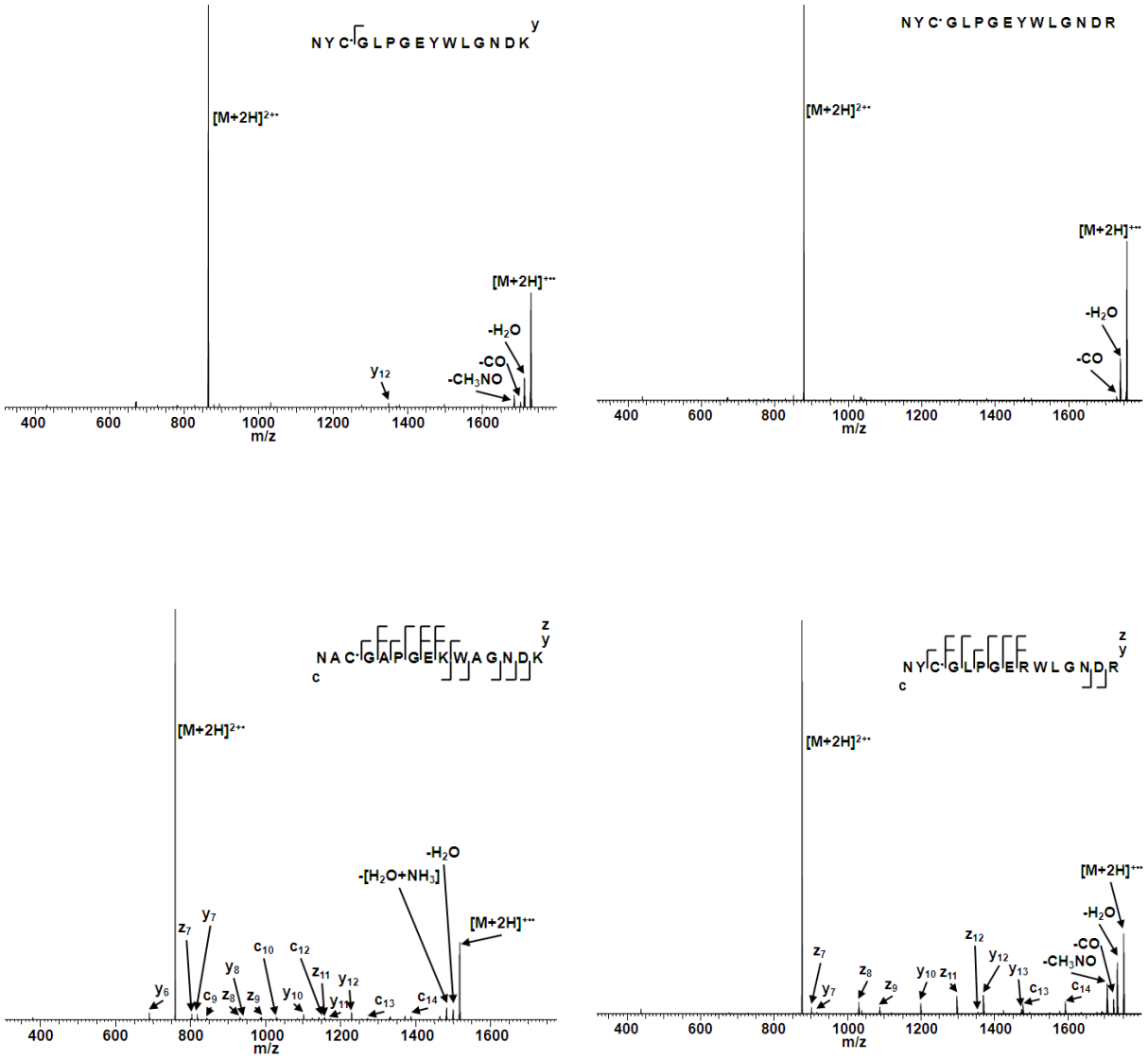

Figure 6.11.1: ECD mass spectra of hydrogen-deficient peptide ions

ECD mass spectra of doubly-charged hydrogen-deficient [NYC$^{\bullet}$GLPGEYWLGNDK + 2H]$^{2+\bullet}$, [NYC$^{\bullet}$GLPGEYWLGNDR + 2H]$^{2+\bullet}$, [NAC$^{\bullet}$GAPGEKWAGNDK + 2H]$^{2+\bullet}$, and [NYC$^{\bullet}$GLPGERWLGNDR + 2H]$^{2+\bullet}$ radical peptide ions. C$^{\bullet}$ was formed from CID of corresponding *S*-nitrosopeptide.

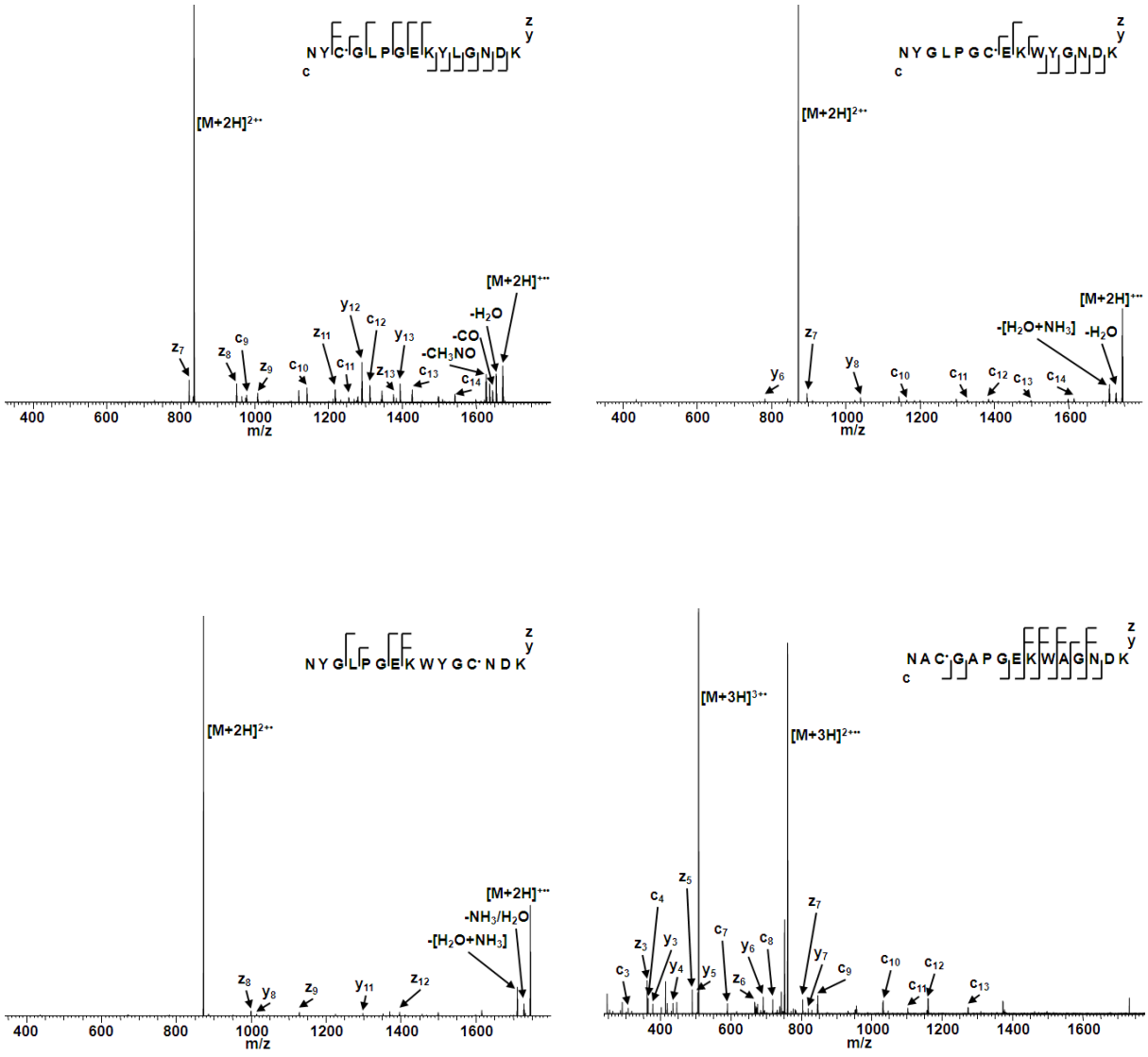

Figure 6.11.2: ECD mass spectra of hydrogen-deficient peptide ions

ECD mass spectra of doubly-charged hydrogen-deficient $[NYC^{\bullet}GLPGEKYLGNDK + 2H]^{2+\bullet}$, $[NYGLPGC^{\bullet}EKWLGNDK + 2H]^{2+\bullet}$, $[NYGLPGEKWYGC^{\bullet}NDK + 2H]^{2+\bullet}$, and $[NAC^{\bullet}GAPGEKWAGNDK + 3H]^{3+\bullet}$ radical peptide ions. $C^{\bullet}$ was formed from CID of corresponding *S*-nitrosopeptide.

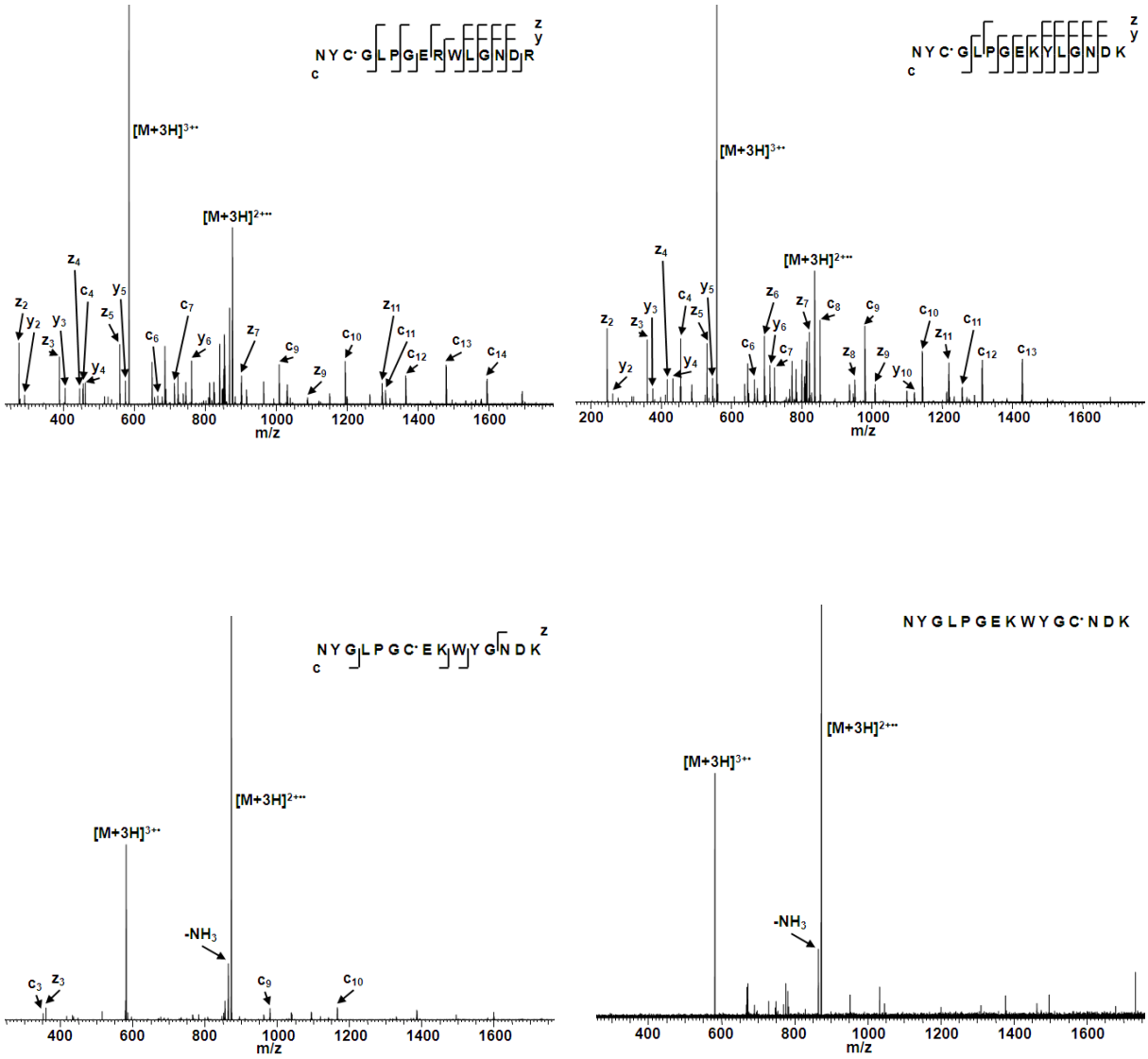

Figure 6.11.3: ECD mass spectra of hydrogen-deficient peptide ions

ECD mass spectra of doubly-charged hydrogen-deficient [NYC$^{\bullet}$GLPGERWLGNDR + 3H]$^{3+\bullet}$, [NYC$^{\bullet}$GLPGEKYLGNDK + 3H]$^{3+\bullet}$, [NYGLPGC$^{\bullet}$EKWYGNDK + 3H]$^{3+\bullet}$, and [NYGLPGEKWYGC$^{\bullet}$NDK + 3H]$^{3+\bullet}$ radical peptide ions. C$^{\bullet}$ was formed from CID of corresponding *S*-nitrosopeptide.

result in a fully occupied electron orbital on the sulfur, precluding any radical migration and fragmentation.

In the case of the ECD mass spectra of $[NAC^{\bullet}GAPGEKWAGNDK + 2H]^{2+\bullet}$, $[NYC^{\bullet}GLPGERWLGNDR + 2H]^{2+\bullet}$, and $[NYC^{\bullet}GLPGEKYLGNDK + 2H]^{2+\bullet}$, there is a much higher peptide sequence coverage (78.6 %, 64.3 %, and 85.7 %, respectively) than those discussed above, which is comparable to that achieved for their unmodified counterparts (85.7 %, 92.9 %, and 85.7 %, respectively). In these cases there can be two possible hypotheses: either radical transfer to the Cys α-carbon is favoured in these peptides leading to backbone fragmentation, or the captured electron does not (or cannot) undergo through-bond or through-space transfer to the sulfur radical and there is a greater competition with transfer to a Coulomb-stabilised amide π* orbital.

This hypothesis becomes more clear when the ECD of $[NYGLPGC^{\bullet}EKWYGNDK + 2H]^{2+\bullet}$, and $[NYGLPGEKWYGC^{\bullet}NDK + 2H]^{2+\bullet}$ are also considered. In these examples there is a significant decrease in peptide sequence backbone coverage (57.1 %, and 28.6 %, respectively) in comparison to their unmodified counterparts (100 %, and 85.7 %, respectively). Again, if consideration is taken for the two hypotheses mentioned above, it can be assumed that the decrease in backbone fragmentation can be attributed to the distance of the sulfur radical to a protonation site (in these cases the two Lys).

Therefore this decrease in peptide backbone fragmentation can be explained by the protonation site interacting with the sulfur radical, and upon electron capture is immediately transferred to form a fully occupied electron orbital. It is therefore hypothesised that the large

peptide backbone fragmentation as noted with ECD of $[NAC^{\bullet}GAPGEKWAGNDK + 2H]^{2+\bullet}$, $[NYC^{\bullet}GLPGERWLGNDR + 2H]^{2+\bullet}$, and $[NYC^{\bullet}GLPGEKYLGNDK + 2H]^{2+\bullet}$ is primarily due to the large distance between the sulfur radical and the protonation site (the two Arg/Lys) leading to favourable radical transfer to the Cys α-carbon.

This effect is even more noticeable with respect to the ECD of triply-charged peptides, in which the three peptides $[NAC^{\bullet}GAPGEKWAGNDK + 3H]^{3+\bullet}$, $[NYC^{\bullet}GLPGERWLGNDR + 3H]^{3+\bullet}$, and $[NYC^{\bullet}GLPGEKYLGNDK + 3H]^{3+\bullet}$ again produce significant peptide backbone fragmentation (64.3 %, 71.4 %, and 71.4 % coverage, respectively), whereas $[NYGLPGC^{\bullet}EKWYGNDK + 3H]^{3+\bullet}$, and $[NYGLPGEKWYGC^{\bullet}NDK + 3H]^{3+\bullet}$ is even lower than their doubly-charged counterparts (28.6 %, and 0 % coverage, respectively). In these cases due to having an addition proton interactions between the protonation sites and sulfur radical are increased resulting in highly favourable electron transfer to the sulfur radical.

Perhaps the most striking feature of these MS^3 ECD mass spectra is the relative abundance of the charge-reduced species. **Figure 6.12** shows the relative intensities of the ECnoD peaks, *i.e.* ratio of the charge reduced precursor ($[M+2H]^{+\bullet\bullet}$ or $[M+3H]^{2+\bullet\bullet}$) to the precursor ion ($[M+2H]^{2+\bullet}$ or $[M+3H]^{3+\bullet}$, respectively), following electron capture by the radical peptides and their unmodified counterparts. In all cases there is an increase in ECnoD for the radical peptide in comparison to its unmodified counterpart, although this increase does not appear to be significant for the two peptides NYCGLPGERWLGNDR and NYCGLPGEKYLGNDK in both double- and triple-charge states, both of which gave considerable backbone fragmentation.

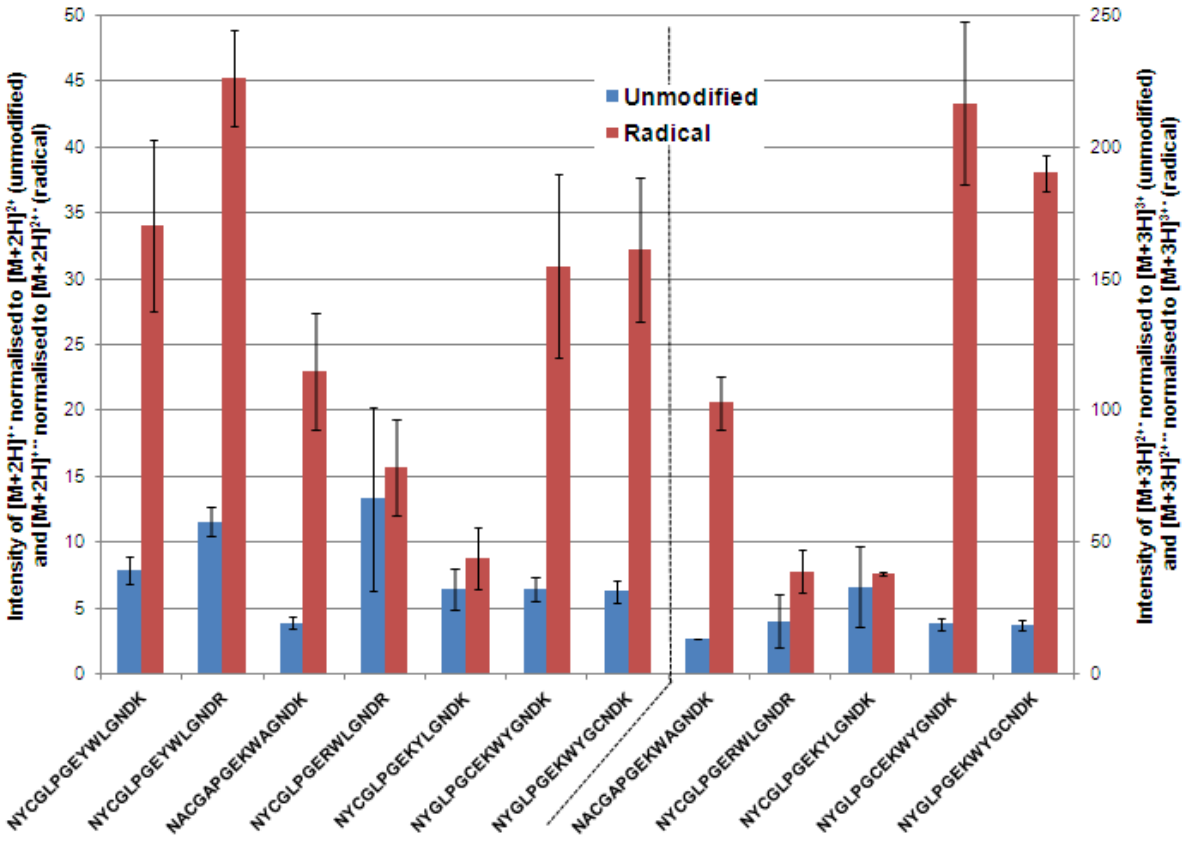

Figure 6.12: Comparison of ECnoD intensity following ECD of hydrogen-abundant and hydrogen-deficient peptide ions

ECnoD intensity following ECD of unmodified (**Blue**) and radical (**Red**) doubly- (**Left**) and triply-charged (**Right**) peptide ions. Error bars constitute standard deviation of n=3. In all cases the presence of the radical results in an increase in ECnoD in comparison to unmodified peptides (this increase is statistically significant to one standard deviation for all but two peptides).

To explain the increase in ECnoD, it is postulated that following initial electron capture at a site of protonation, the electron is favourably transferred through-bond or through-space to the radical site of the sulfur atom thus leading to a full orbital. This transfer may be less favourable if internal structures within the peptide between protonation sites and the peptide backbone are present. These would result in favourable electron transfer to an amide π^* orbital rather than the radical sulfur atom. This may explain the non-significant increase in ECnoD of NYC$^{\bullet}$GLPGERWLGNDR and NYC$^{\bullet}$GLPGEKYLGNDK as noncovalent bonds may be present (MD simulations could not be generated of these radical peptides).

6.2.6 CID of *S*-radicals

As discussed above, CID of the *S*-nitrosopeptide results in a stable hydrogen-deficient peptide radical in which the radical is localised on the sulfur atom, and although it is likely that the radical remains at this site, it is not improbable that migration to the α-carbon occurs [189]. Migration is more likely when further heating of the radical peptide ion takes place, *e.g.* through a second stage of CID, due to potential energy barriers being exceeded. The CID mass spectra of the radical peptide ions, formed following initial CID of the corresponding *S*-nitrosopeptide, shown in **Figure 6.13** (doubly-charged peptide ions) and **Figure 6.14** (triply-charged peptide ions), reveal three important discussion points: the appearance of dominant amino acid side-chain losses, radical (*a*/*c*/*z*) backbone fragment ions, and thermal (*b*/*y*) backbone fragment ions.

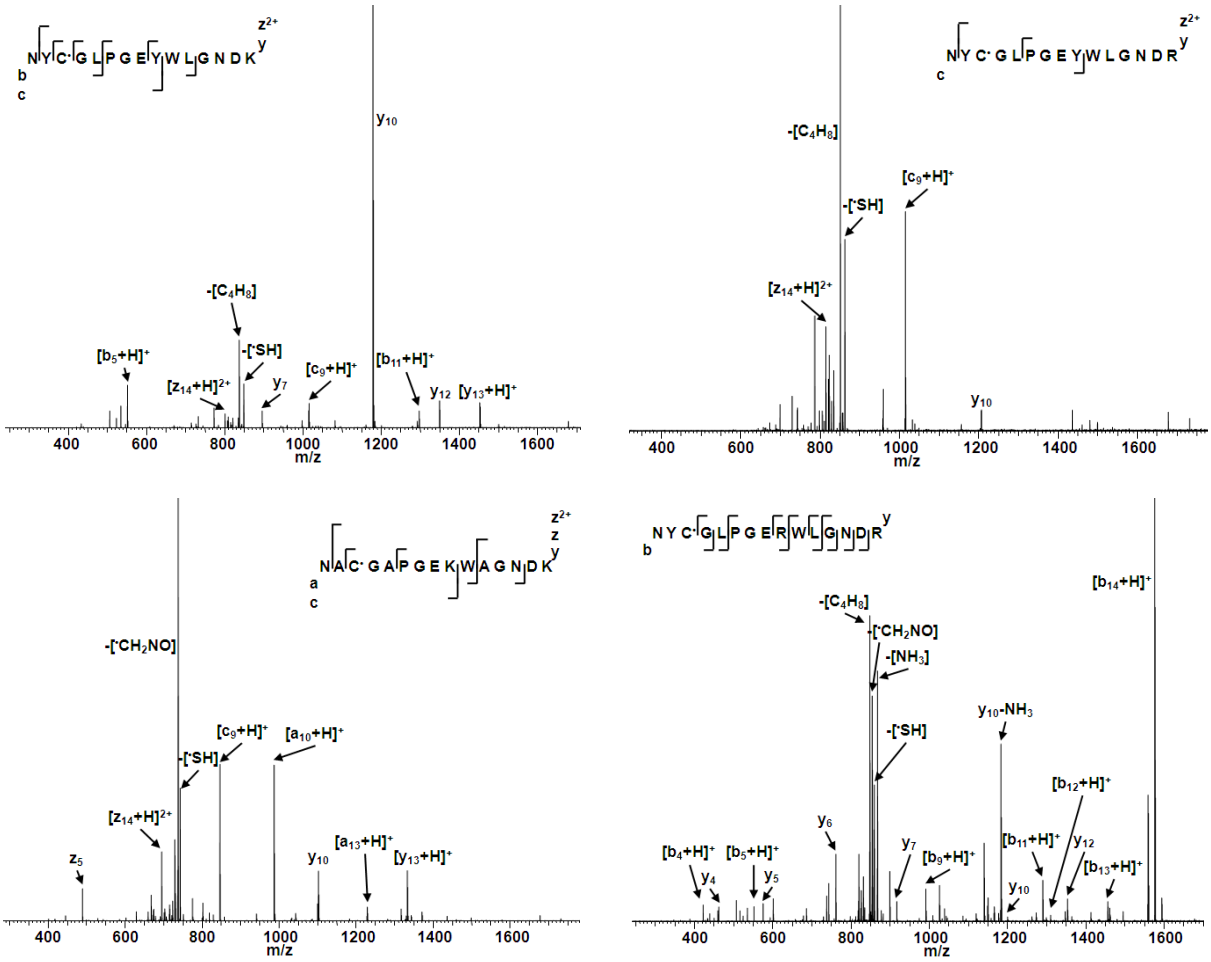

Figure 6.13.1: CID mass spectra of doubly-charged hydrogen-deficient radical peptide ions

CID mass spectra of doubly-charged hydrogen-deficient [NYC$^{\bullet}$GLPGEYWLGNDK + 2H]$^{2+\bullet}$, [NYC$^{\bullet}$GLPGEYWLGNDR + 2H]$^{2+\bullet}$, [NAC$^{\bullet}$GAPGEKWAGNDK + 2H]$^{2+\bullet}$, and [NYC$^{\bullet}$GLPGERWLGNDR + 2H]$^{2+\bullet}$ radical peptide ions. C$^{\bullet}$ denotes radical cysteine, formed from CID of corresponding *S*-nitrosopeptide.

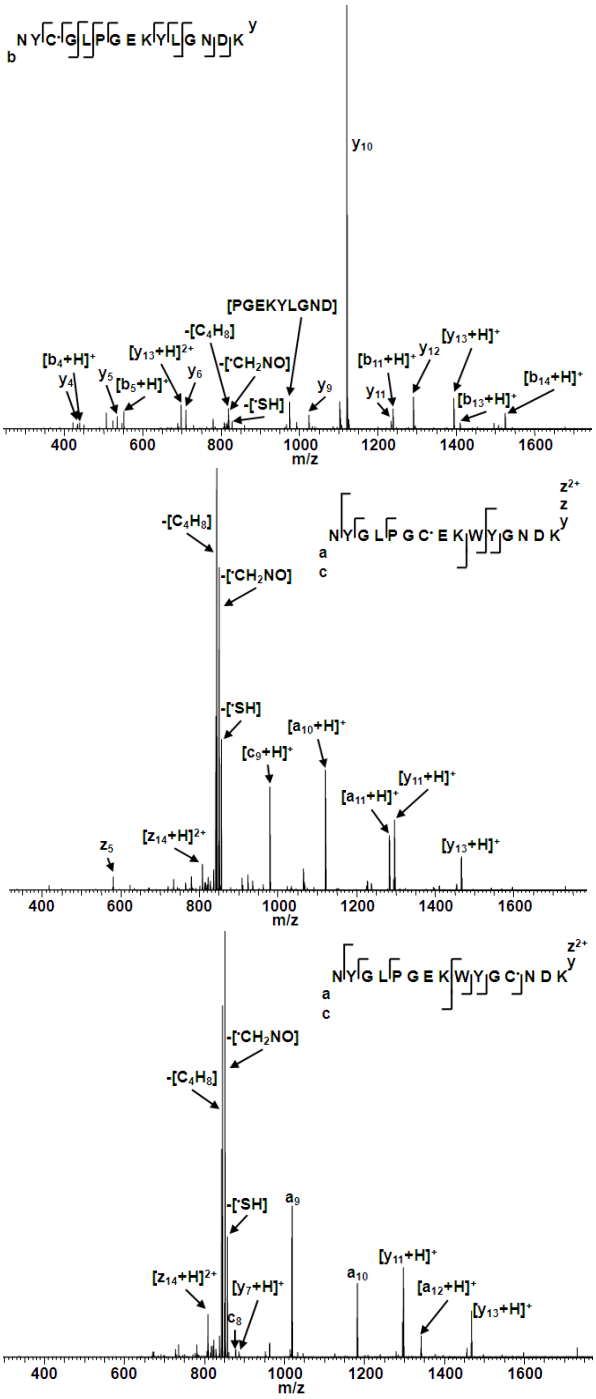

Figure 6.13.2: CID mass spectra of doubly-charged hydrogen-deficient radical peptide ions

CID mass spectra of doubly-charged hydrogen-deficient $[NYC^{\bullet}GLPGEKYLGNDK + 2H]^{2+\bullet}$, $[NYGLPGC^{\bullet}EKWLGNDK + 2H]^{2+\bullet}$, and $[NYGLPGEKWYGC^{\bullet}NDK + 2H]^{2+\bullet}$ radical peptide ions. $C^{\bullet}$ denotes radical cysteine, formed from CID of corresponding *S*-nitrosopeptide.

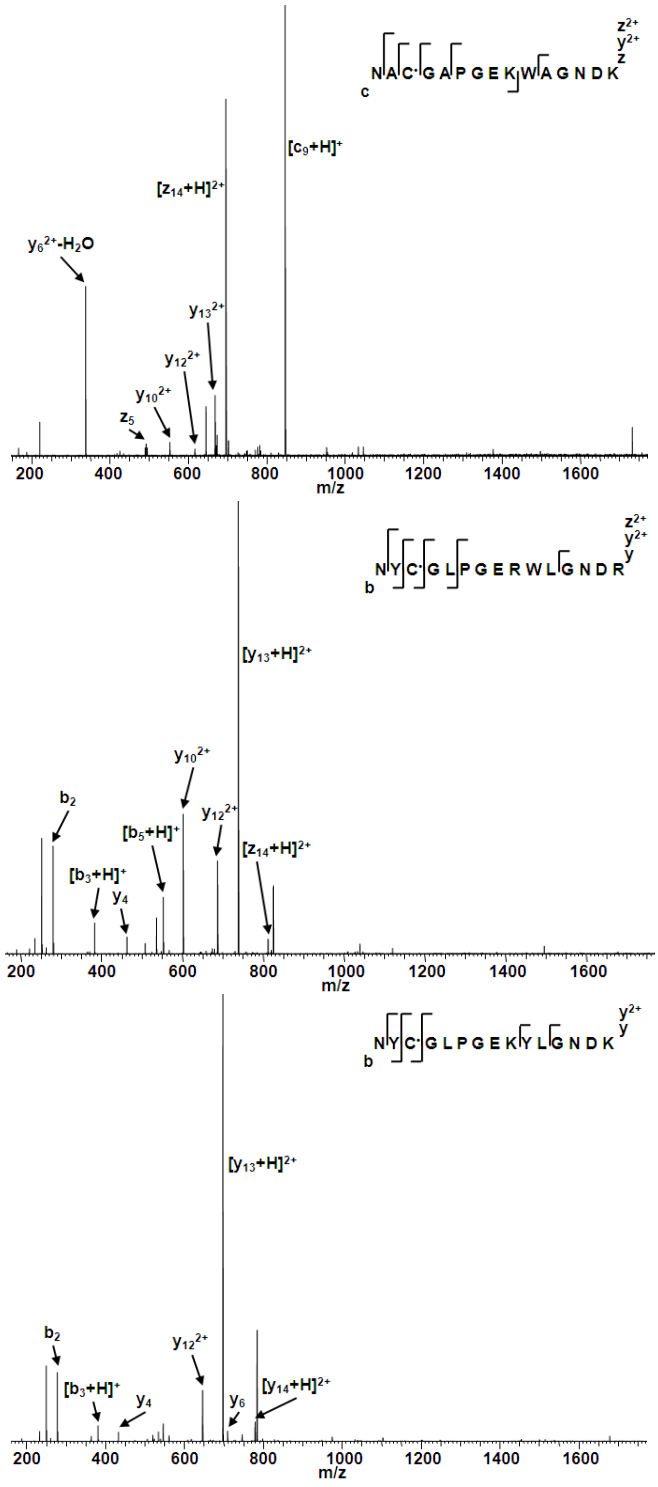

Figure 6.14.1: CID mass spectra of triply-charged hydrogen-deficient radical peptide ions

CID mass spectra of triply-charged hydrogen-deficient $[NAC^{\bullet}GAPGEKWAGNDK + 3H]^{3+\bullet}$, $[NYC^{\bullet}GLPGERWLGNDR + 3H]^{3+\bullet}$, and $[NYC^{\bullet}GLPGEKYLGNDK + 3H]^{3+\bullet}$ radical peptide ions. $C^{\bullet}$ denotes radical cysteine, formed from CID of corresponding *S*-nitrosopeptide.

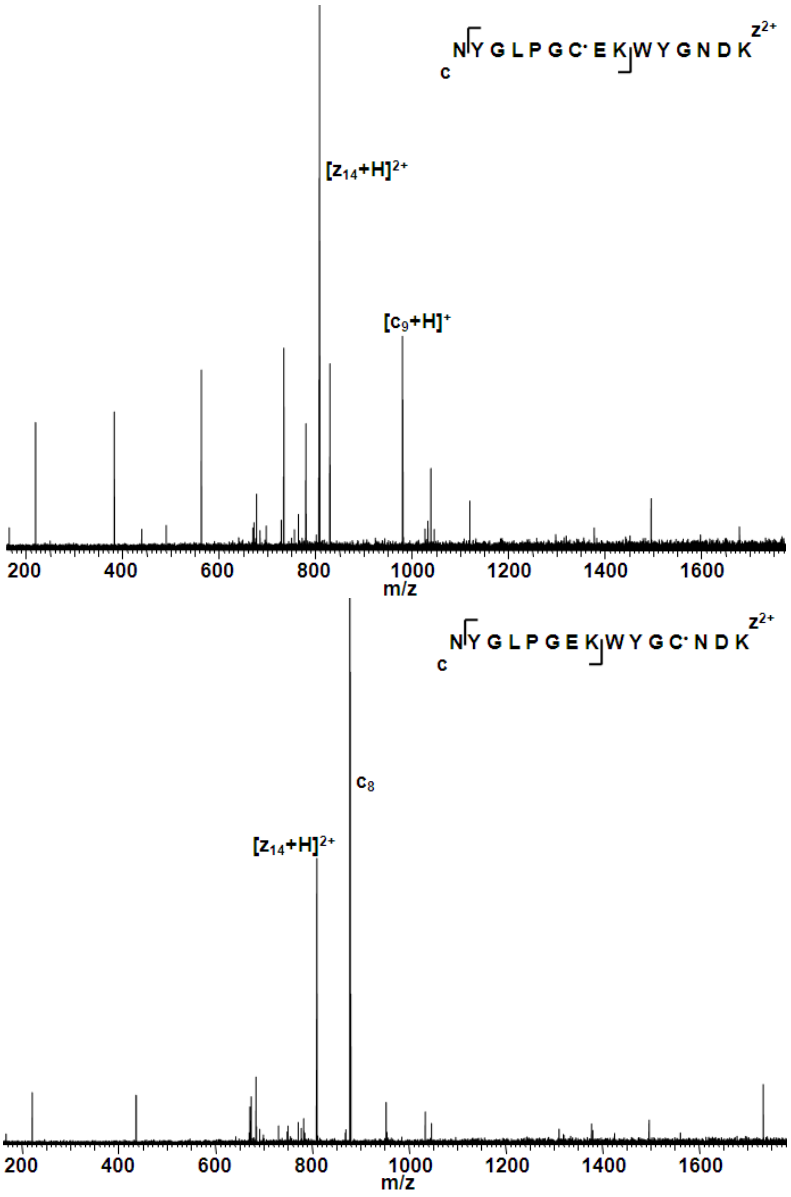

Figure 6.14.2: CID mass spectra of triply-charged hydrogen-deficient radical peptide ions

CID mass spectra of triply-charged hydrogen-deficient [NYGLPGC$^{\bullet}$EKWYGNDK + 3H]$^{3+\bullet}$, and [NYGLPGEKWYGC$^{\bullet}$NDK + 3H]$^{3+\bullet}$ radical peptide ions. C$^{\bullet}$ denotes radical cysteine, formed from CID of corresponding *S*-nitrosopeptide.

6.2.6.1 Amino acid side-chain losses identified from CID of *S*-radicals

CID of all doubly-charged radical peptide ions resulted in neutral losses corresponding to $^{\bullet}SH$, C_4H_8, and $^{\bullet}CH_2NO$. No such losses were observed for the triply-charged radical peptide ions. (The loss of NH_3 was also noted following CID of $[NYC^{\bullet}GLPGERWLGNDR + 2H]^{2+\bullet}$ but is a common loss following thermal heating fragmentation techniques, and is identified following CID of its unmodified peptide counterpart, *i.e.* $[NYCGLPGERWLGNDR + 2H]^{2+}$ (see **Figure 6.9.1**)).

Loss of C_4H_8 is the result of cleavage in the side chain of either leucine or isoleucine (specifically $CH_2C(CH_3)_2$ or $CH_3CHCHCH_3$, respectively) [193], and has been discussed previously by Julian and co-workers [113]. In their work, hydrogen-deficient radical peptide ions were generated by the use of iodinated tyrosine residues which undergo homolysis at a specific wavelength. Loss of C_4H_8 is observed following CID of these hydrogen-deficient radical peptides and also in the ECD of hydrogen-abundant peptides [193]. The proposed mechanism for loss of C_4H_8 from hydrogen-deficient radicals, see **Figure 6.15**, involves initial γ-hydrogen abstraction from the Leu/Ile side chain by a remote radical site followed by homolysis of the Cα-C_β bond. As discussed above, the initial structure of the radical peptide likely comprises the sulfur radical; however, migration to the α-carbon may occur following collisional activation. Either of these radicals may be responsible for the γ-hydrogen abstraction which precedes C_4H_8 loss. The peptides analysed here contain no isoleucine residues, and the site of C_4H_8 loss must be the leucine residues. This conclusion is reinforced by the fact that C_4H_8 loss was not observed following CID of $[NAC^{\bullet}GAPGEKWAGNDK + 2H]^{2+\bullet}$ which does not contain any leucine amino acid residues.

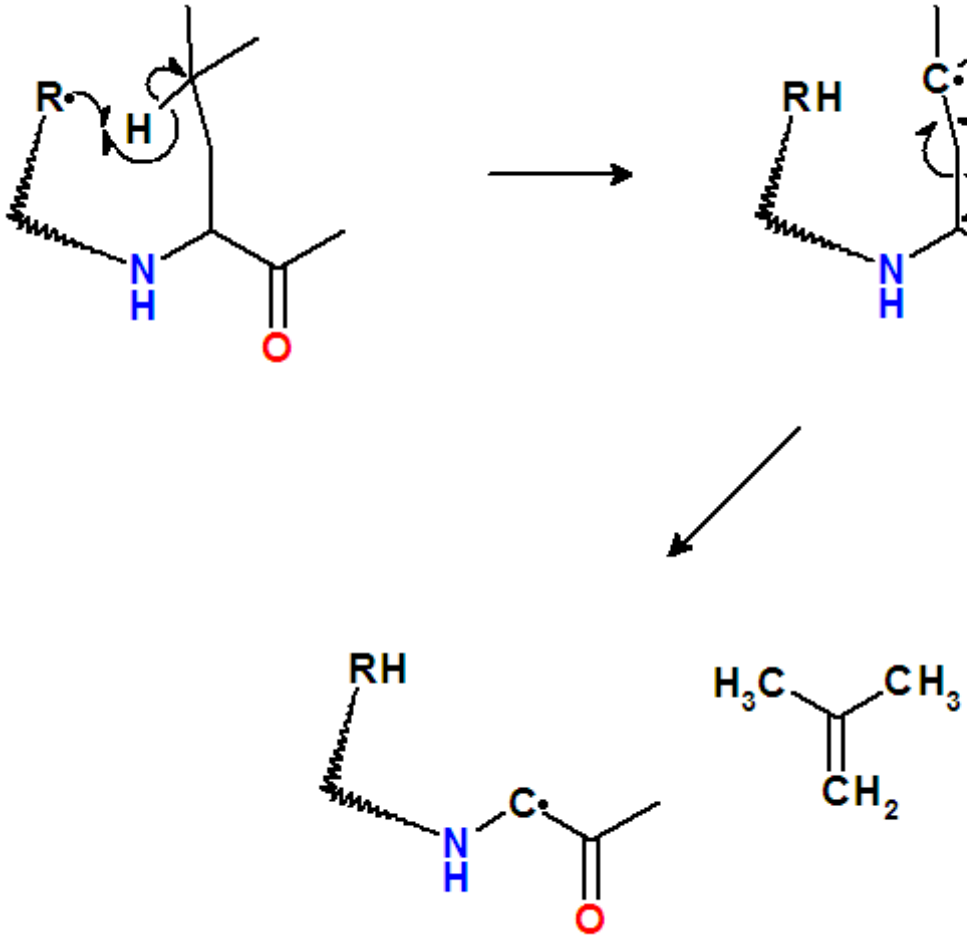

Figure 6.15: Proposed radical mechanism of C_4H_8 neutral loss from Leu

Following γ-hydrogen abstraction of the leucine side chain, homolysis of the Cα-C_β bond results in the formation the captodative-stabilised α-carbon radical peptide ion and $CH_2C(CH_3)_2$.

Loss of $^{\bullet}CH_2NO$ (specifically $^{\bullet}C(O)NH_2$) has also been observed in the fragmentation of hydrogen-deficient radicals from the asparagine side chain [193]. The neutral loss of $^{\bullet}CH_2NO$ from hydrogen-deficient peptide ions has been proposed to follow a two-step mechanism, shown in **Figure 6.16**: initial α-hydrogen-abstraction to form a capodatively stabilised radical α-carbon, followed by homolysis of the C_β-Cγ bond [194].

The asparagine Cα-H has the lowest bond dissociation energy (BDE) of all essential amino acids [195], thus explaining the apparent favoured migration of the radical from the sulfur or backbone α-carbon to the Asn α-carbon. Interestingly, $^{\bullet}CH_2NO$ loss is not identified in CID of either $[NYC^{\bullet}GLPGEYWLGNDK + 2H]^{2+\bullet}$ or $[NYC^{\bullet}GLPGEYWLGNDR + 2H]^{2+\bullet}$ which may suggest that radical migration to the α-carbon or side chain within either asparagine is affected by the location of the protons within the peptide.

The third radically-generated neutral loss is $^{\bullet}SH$ and, although it is never the most abundant neutral loss, is identified in the CID analysis of all doubly-charged radical peptide ions investigated in this work. These losses were also observed in the MS^3 experiments of Hao and Gross [183], but were not following fragmentation of cysteine radical cations (when SH_2 loss was observed) [186]. Loss of $^{\bullet}SH$ can be explained by a similar mechanism to that for loss of the Asn side chain (see **Figure 6.17**): Initial radical migration from the sulfur to the Cys α-carbon, followed by homolysis of the C_β-S bond, resulting in $^{\bullet}SH$ and conversion of the cysteine residue to dehydroalanine. Observation of the $^{\bullet}SH$ loss suggests that radical migration from the sulfur to the Cys α-carbon must take place.

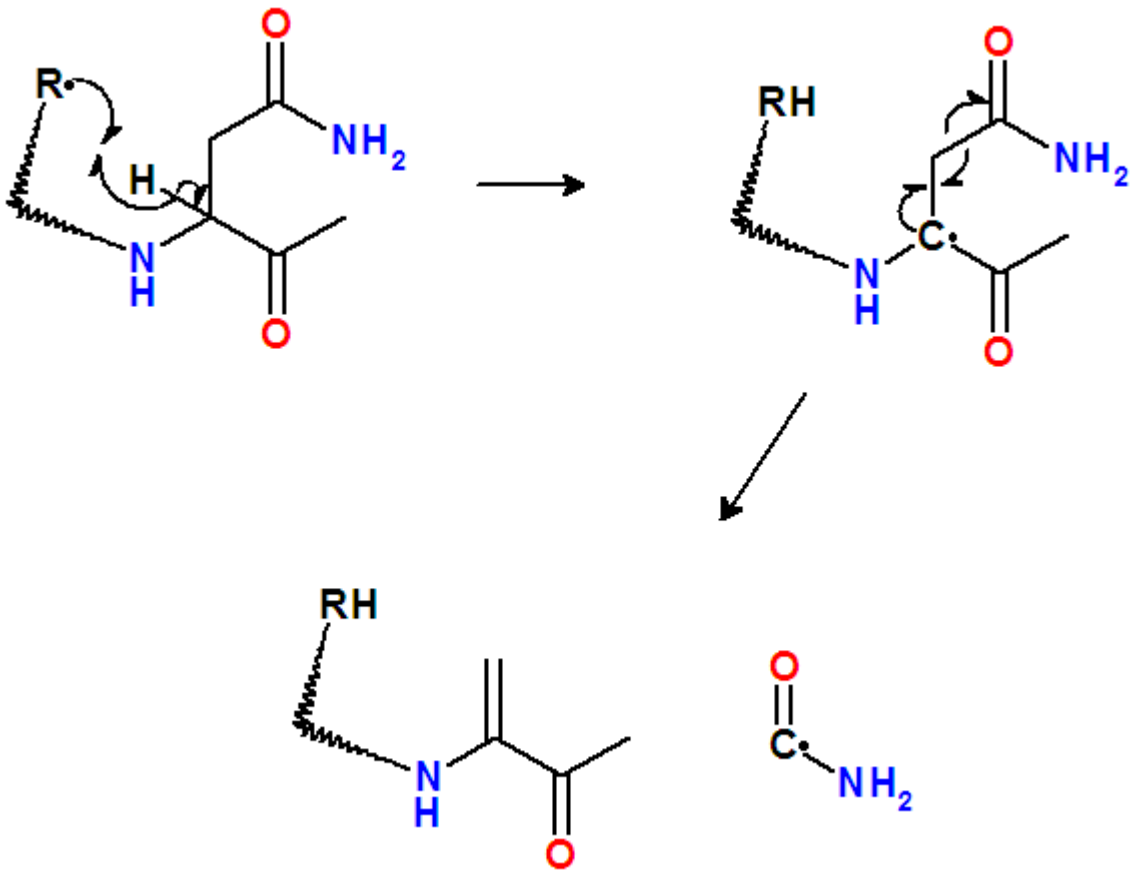

Figure 6.16: Proposed radical mechanism of CH_2NO neutral loss from Asn

Following α-hydrogen abstraction of the asparagine, homolysis of the C_β-C_γ bond results in the formation of dehydroalanine and $^{\bullet}C(O)NH_2$.

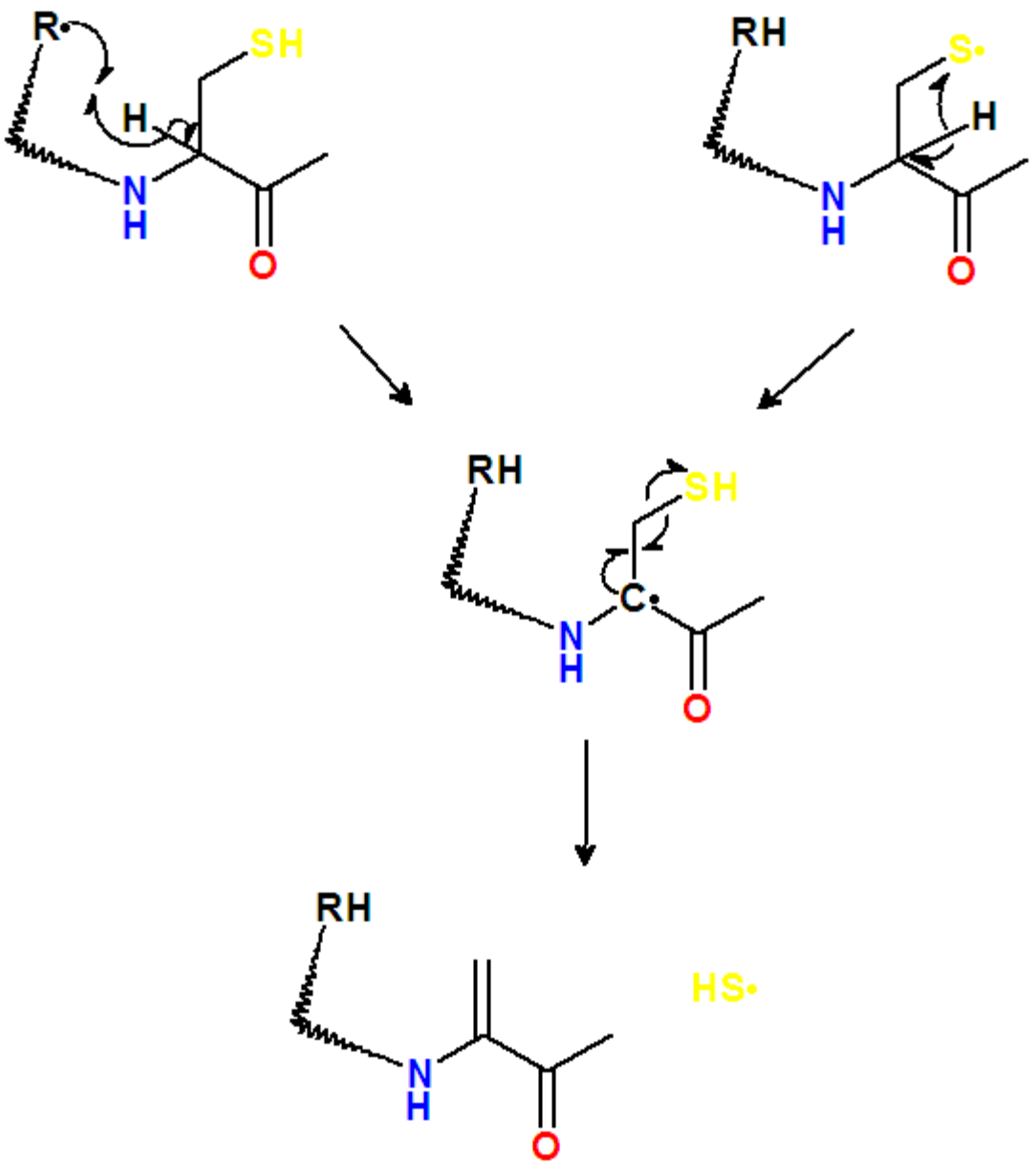

Figure 6.17: Proposed radical mechanism of SH neutral loss from Cys

Following α-hydrogen abstraction of the cysteine from a remote radical site or the radical sulfur atom, homolysis of the C_β-S bond results in the formation of dehydroalanine and $^{\bullet}SH$.

As mentioned above, none of these neutral losses were observed following CID of the triply-charged peptides. The reasoning for this is not simple to ascertain; however, it can be seen that the peptide sequence coverage is decreased with an increase in charge-state suggested that backbone fragmentation is greatly favoured. Also, in the case of $[NYGLPGC^{\bullet}EKWYGNDK + 3H]^{3+\bullet}$, and $[NYGLPGEKWYGC^{\bullet}NDK + 3H]^{3+\bullet}$ the radical peptide stability is very low with lower precursor ion intensity than the other peptides, and certain products may be too unstable for detection.

6.2.6.2 Radical induced backbone cleavage following CID of *S*-radicals

The second point of note in the CID mass spectra of the hydrogen-deficient sulfur radical peptides is the presence of *c*/*z* backbone fragment ions. The *c*/*z* fragment ions are specific and the sites of fragmentation are conserved between peptides. With the exception of $NYC^{\bullet}GLPGERWLGNDR$ and $NYC^{\bullet}GLPGEKYLGNDK$ the formation of c_9 (c_8 in the case of $NYGLPGEKWYGC^{\bullet}NDK$) is identified in all cases, and with the exception of $NYC^{\bullet}GLPGEKYLGNDK$ and $[NYC^{\bullet}GLPGERWLGNDR + 2H]^{2+\bullet}$ z_{14}^{2+} is identified in all cases. As well as these two fragment ions, the formation of z_5 and several *a* ions (a_9, a_{10}, a_{11}, a_{12}, and a_{13}) are identified (it is likely that these *a* ions are the result of a radical mechanism as they are not identified in the CID mass spectra of hydrogen-abundant peptide ions).

In previous work, Hao and Gross [183] observed radical-driven cleavage adjacent to Ser and Thr residues. The peptides studied here do not contain those residues and radical-driven cleavage is observed adjacent to tryptophan and tyrosine (*a* and *c* fragments), and asparagine (*a* and *z* fragments) residues. Consider first the c_9 fragment ions (c_8 in the case of

NYGLPGEKWYGC•NDK). Fragmentation occurs at the Tyr-Trp or Lys-Trp bond. Favourable N-Cα bond fragmentation at tryptophan, as well as tyrosine, residues in radical peptide ions generated following CID of copper (II) ternary complexes has been observed previously by Siu and co-workers [196]. The mechanism proposed is abstraction of a β-hydrogen followed by cleavage of either the N-Cα bond (to give *c* fragments) or the Cα-C_O bond (to give *a* fragments). The C_β-H BDE for tryptophan is the lowest of all essential amino acid residues by >20 kJ mol^{-1} and tyrosine has the fourth lowest (the second lowest of the amino acids contained the peptides studied here) [194]. Further support for this proposal derives from the fact that neither charge state of peptide [NYC•GLPGEKYLGNDK], the only peptide studied which did not contain tryptophan, resulted in any radical-driven backbone fragmentation. This favourable fragmentation pathway also explains the formation of some of the other fragment ions identified, *i.e.* z_5, a_{10}, and a_{11}, which are all adjacent to either or both tyrosine and tryptophan residues.

The z_{14}^{2+} fragment ion is identified following CID of five of the seven doubly charged radical peptide ions, and four of the five triply-charged radical peptide ions. In seven of these cases, fragmentation occurs at the Asn-Tyr bond, which could be explained by β-carbon proton transfer from the tyrosine residue as discussed previously [196]; however, the formation of z_{14}^{2+} is also noted in high abundance for doubly- and triply-charged NAC•GAPGEKWAGNDK, which fragments at the Asn-Ala bond. These data suggest that the presence of the asparagine amino acid and/or adjacent N-terminus is directing the fragmentation. The C_β-H BDE of asparagine is unremarkable, lying at the midpoint of the range of amino acid β BDEs [194]; however, as mentioned above, asparagine does have the lowest Cα-H BDE [195]. Therefore, it is possible that the asparagine α-radical fragments either *via* loss of the side-chain (see **Section 6.2.6.1**) or *via* cleavage of the peptide backbone.

Further evidence to support this proposal is the observation of the a_{13} fragment in the CID mass spectrum of $[NAC^{\bullet}GAPGEKWAGNDK + 2H]^{2+\bullet}$ and the a_{12} fragment in the CID mass spectrum of $[NYGLPGEKWYGC^{\bullet}NDK + 2H]^{2+\bullet}$.

In the case of NYC$^{\bullet}$GLPGERWLGNDR we would expect to see backbone fragmentation due to the presence of the tryptophan residue; however, in this case the charge carrier is the adjacent arginine, rather than lysine as seen in the other peptides. The impact of arginine amino acid residues on radical peptide ions has been explored previously [197], with DFT calculations of GRW radical cations revealing the presence of arginine facilitated radical migration. The CID mass spectra of $[G^{\bullet}RW]^{+}$ and $[GRW]^{+\bullet}$ were very similar and both contained *a* and *c* fragments. The energy barriers for isomerisation between the α-carbon-centred radical, the β-carbon-centred radical, and the γ-carbon-centred radical were comparable to those of dissociation. These observations and calculations thus suggest that CID of NYC$^{\bullet}$GLPGERWLGNDR results in radical migration to the to the arginine α-carbon, and undergoes stabilisation through isomerisation, disfavouring N-Cα bond fragmentation.

6.2.6.3 Thermal backbone fragment ions observed following CID of *S*-radicals

The final point of note in the CID of the hydrogen-deficient radical peptide ions is the variation in the presence and intensities of thermally-driven backbone fragments, *i.e. b*/*y* ions. This disparity can be easily seen in a comparison of $[NYC^{\bullet}GLPGEYWLGNDK + 2H]^{2+\bullet}$ and $[NYC^{\bullet}GLPGEYWLGNDR + 2H]^{2+\bullet}$. The change in BAAR (Lys to Arg) dramatically decreases the abundance thermally-driven backbone fragment ions in favour of radically-

driven fragments (*i.e*. side chain losses and *c*/*z* ions). This observation can be explained by the mobile proton model [73-75].

6.3 Discussion

This chapter has investigated the radical ion chemistry of *S*-nitrosylated peptides. ECD of doubly-charged *S*-nitrosylated peptides resulted in a striking reduction in backbone cleavage when compared to their unmodified counterparts. Greater sequence coverage was obtained for triply-charged *S*-nitrosylated peptides. Nevertheless, these results conclusively show that ECD is not a suitable technique for the localisation of *S*-nitrosylated peptides, but can be used for its detection. The ECD mass spectra were dominated by a peak corresponding to the loss of ˙NO from the charge-reduced precursor which was shown to be formed *via* a radical-based mechanism. This loss can be explained by a modified Cornell or UW mechanism. This S-N bond is exceptionally weak due to electron donation into the π* orbital, and is more competitive than electron transfer to the N-Cα π* orbital. The use of molecular dynamic simulations provides a further technique for analysing peptide gas-phase structures. As identified, when intermolecular bonds were present within the structure between protonation sites and the peptide backbone, there was a greater precedent for N-Cα bonds to fragment over the S-N bond.

The dominant fragmentation pathway in the CID of the *S*-nitrosylated peptides was homolysis of the S-N bond to form a long-lived radical with loss of ˙NO. These radical peptide ions were isolated and subjected to ECD and CID. For ECD, the dominant pathway was electron capture with no subsequent dissociation, *i.e.*, ECnoD. Some backbone cleavage was observed for some species. The results suggest a competition between transfer of the captured electron to the partially-filled sulfur orbital and to an amide π* orbital. CID of the radical peptide ions resulted in losses of amino acid side-chains and both radical-induced and charge-directed backbone fragmentation.

Chapter 7: Electron Capture Dissociation Mass Spectrometry of Noncovalent Phospho-Guanidinium Complexes

7.1 Introduction

CID of phosphorylated peptides will typically result in the loss of H_3PO_4 ([HPO_3+H_2O]), and formation of dehydroalanine (serine) or dehydroamino-2-butyric acid (threonine) residues, with an associated decrease in peptide backbone sequence coverage. ECD analysis of phosphopeptides has been more successful, due to the favourable retention of the PTM on the peptide backbone fragment ions, thus allowing easier PTM localisation [83, 84]. It has been shown that intramolecular salt bridges between acidic phosphate groups and basic amino acid side chains can exist in the gas phase causing an adverse effect on ECD fragmentation and low sequence coverage [89].

The presence of intermolecular salt bridges (*i.e.* between two separate peptides) in the gas phase has also been identified between phosphopeptides and peptides with an RR motif [198]. This was expanded upon by Jackson *et al*. with the use of VLRRRRKRVN and SVSTDpTpSAE in which they observed that CID of this noncovalent complex primarily fragments at the noncovalent bond, resulting in two separate peptides [166]. A minor pathway was identified in which fragmentation within the phosphorylated residue resulted in transfer of the phosphate group [166]. In a follow-up study a comparison between the phosphorylation site on noncovalent bond strength using AAApSAAA-NH_2, AAApTAAA-NH_2 and AAApYAAA-NH_2 showed the phosphotyrosine-guanidinium bond to be the strongest by measuring the intensity of the precursor ion when increasing collisional energy [199].

The use of ECD and ETD was more successful for the identification of the individual peptide sequences as fragmentation occurs favourably at the N-Cα bonds in the peptide backbone with retention of the noncovalent bonds; however, this study only focused on the analysis of a single triply-charged complex containing a phosphoserine peptide (*i.e.* [SFKRRRSSK + GpSSEDLKKEE + 3H]$^{3+}$), and did not explore the behaviour of complexes containing phosphothreonine or phosphotyrosine [200].

In this study a suite of phosphopeptides, *i.e.* AAApSAAA-NH_2, AAApTAAA-NH_2, and AAApYAAA-NH_2, were coupled with the basic peptide VLRRRAVN to further investigate the ECD behaviour of phospho-guanidinium noncovalent complexes. The C-terminus of the phosphopeptides were amidated to ensure that a noncovalent bond was not formed between the guanidinium ion and the C-terminus. This study was undertaken by the use of CID, ECD and AI ECD with attention was focused on the fragmentation behaviour of the noncovalent complexes. These techniques were utilised with varying energies to identify whether the fragmentation pathways, and hence fragment ions, change depending on collisional energy, electron energy or laser power.

7.2 Results

7.2.1 CID and ECD of individual peptides

The CID and ECD mass spectra of doubly- and triply-charged VLRRRAVN are shown in **Figure 7.1**. CID of [VLRRRAVN] resulted in good peptide backbone sequence coverage, with the 5/7 N-C_O bonds fragmenting for the doubly-charged ion and 3/7 N-C_O bonds

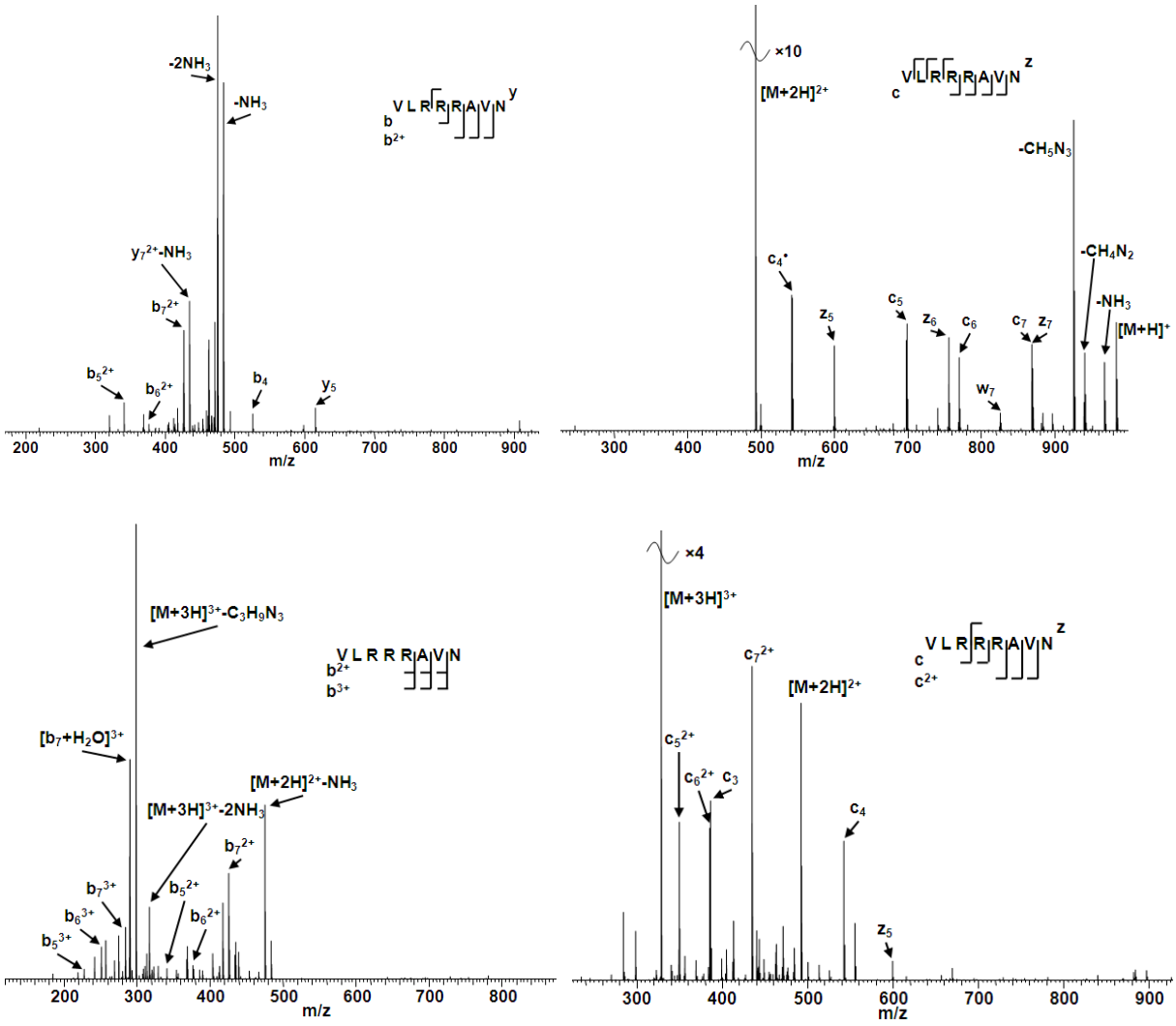

Figure 7.1: CID and ECD mass spectra of doubly- and triply-charged VLRRRAVN

CID (**Left**) and ECD (**Right**) of $[VLRRRAVN + 2H]^{2+}$ (**Upper**) and $[VLRRRAVN + 3H]^{3+}$ (**Lower**) peptide ions.

fragmenting for the triply-charged precursor ion. In both of these CID mass spectra, however, the most abundant peaks corresponded to neutral losses from the arginine side chains. These were the loss of one and two ammonia molecules for the doubly-charged peptide, and the loss of $C_3H_9N_3$ from the triply-charged peptide. $C_3H_9N_3$ loss has been previously shown to be formed following CID of arginine-containing peptides through α-hydrogen rearrangement resulting in $H_2CCHNHC(NH)NH_2$ and H_2 [201].

ECD of the peptide resulted in greater peptide backbone sequence coverage with the doubly-charged peptide undergoing N-Cα fragmentation at all sites (7/7), and the triply-charged peptide resulting in 5/7 N-Cα bonds fragmenting. As for CID, ECD of $[VLRRRAVN + 2H]^{2+}$ resulted in neutral losses from the ammonia side chain. These was assigned to be the loss of CH_5N_3 ($H_2NC(NH)NH_2$) and CH_4N_2 ($HC(NH)NH_2$), both of which have been previously identified to be formed following ECD [112]. Neutral losses were not observed following ECD of $[VLRRRAVN + 3H]^{3+}$.

The phosphopeptides could only be identified as singly-charged ions, and therefore only CID analysis was possible, the mass spectra of which are shown in **Figure 7.2** (ECD of singly-charged ions would result in species with zero charge and therefore undetectable). CID led to poor peptide backbone sequence coverage, and in all cases the most abundant fragment peak corresponded to a neutral loss from the precursor ion. CID of both $[AAApSAAA\text{-}NH_2 + H]^+$, and $[AAApTAAA\text{-}NH_2 + H]^+$ led to the formation of $[M+H]^+\text{-}[H_3PO_4+NH_3]$, and the CID mass spectrum of $[AAApYAAA\text{-}NH_2 + H]^+$ was dominated by $[M+H]^+\text{-}NH_3$. In all these cases, the loss of ammonia is likely to originate from the amidated C-terminus. CID of the phosphotyrosine-containing peptide did not result in the neutral loss of H_3PO_4, as seen for

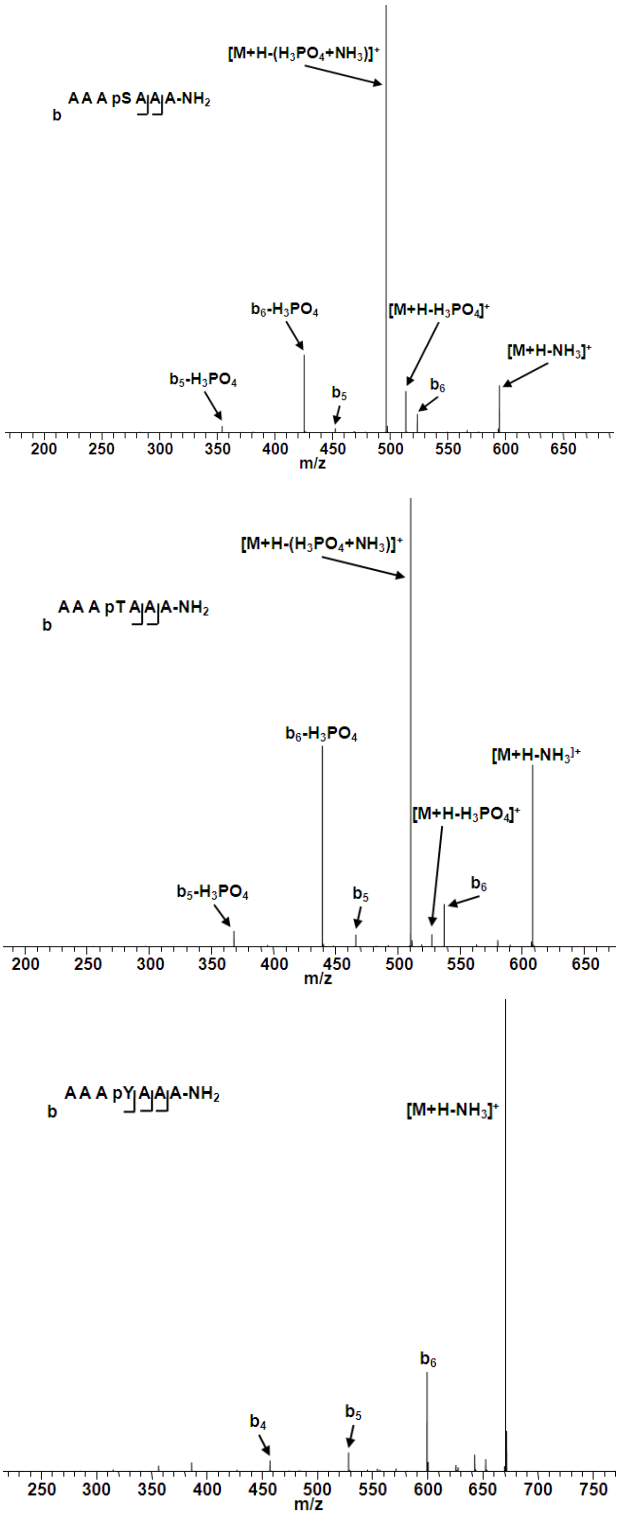

Figure 7.2: CID mass spectra of singly-charged phosphopeptides

CID mass spectra of the singly-charged [AAApSAAA-NH2 + H]$^+$ (**Upper**), [AAApTAAA-NH2 + H]$^+$ (**Middle**), [AAApYAAA-NH2 + H]$^+$ (**Lower**) peptide ions. pS, pT, and pY denotes phosphoserine, phosphothreonine and phosphotyrosine, respectively.

the other two peptides, and can be explained by the inability of the aromatic ring in the phosphotyrosine residue to undergo E2-elimination or an S_N2-neighbouring group participation group reaction [202]. CID of phosphotyrosine can result in the neutral loss of HPO_3, although it has been suggested that this is only observed when basic moieties [203] are present, and was not identified here.

7.2.2 CID and ECD of noncovalent complexes

The two samples were then resuspended in solution, as described in **Section 2.2.9**, with both VLRRRAVN and each phosphopeptide in equimolar concentrations (*i.e.* 2 pmol/μL : 2 pmol/μL) resulting in three samples. As shown in **Figure 7.3**, electrospray of these samples led to the retention and identification of the doubly-charged noncovalent peptide-peptide complex. Herein the species will be referred to as follows:, VLRRRAVN as BP, *i.e.* Basic Peptide; the phosphopeptide as AP, *i.e.* Acidic Peptide, (with subscript S, T, or Y referring to the specific phosphopeptide, *e.g.*AP_S) and the intact noncovalent complex as NCX.

The CID and ECD mass spectra of the doubly-charged phosphoserine containing complex, *i.e.* $[VLRRRAVN + AAApSAAA\text{-}NH_2 + 2H]^{2+}$, are shown in **Figure 7.4**. In the CID mass spectrum, two dominant groups of peaks are present, *i.e.* AP_S-containing and BP-containing, as well as a peak corresponding to the $[NCX + 2H]^{2+}\text{-}H_3PO_4$ ion. The most abundant peak corresponds to the singly-charged BP, suggesting that cleavage of the noncovalent bond is the dominant fragmentation pathway following CID. The loss of water from BP is also observed. The intact singly-charged AP_S is also identified, suggesting that cleavage of the NCX favourably gives the two species. The region of the CID mass spectrum with the AP_S-containing ions appear very similar to CID of $[AP_S + H]^+$ (see **Figure 7.2**), with the dominant

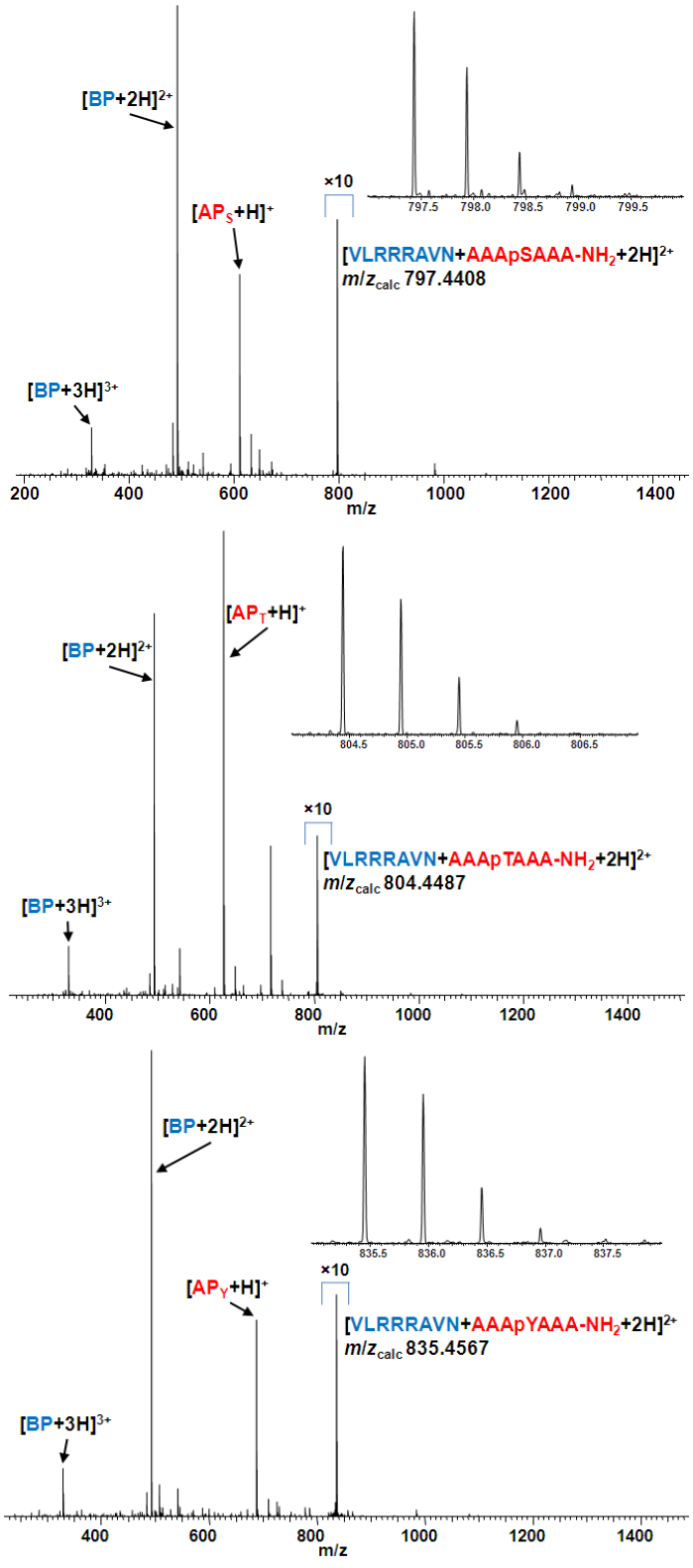

Figure 7.3: Mass spectra of noncovalent complexes

Mass spectra of 2 pmol μL^{-1} VLRRRAVN (BP) and 2 pmol μL^{-1} AAApSAAA-NH_2 (AP_S) (**Upper**), AAApTAAA-NH_2 (AP_T) (**Middle**), or AAApYAAA-NH_2 (AP_Y) (**Lower**). Peaks corresponding to the doubly-charged noncovalent complex are magnified 10x along with the calculated *m/z* and an inset showing the istopic distribution.

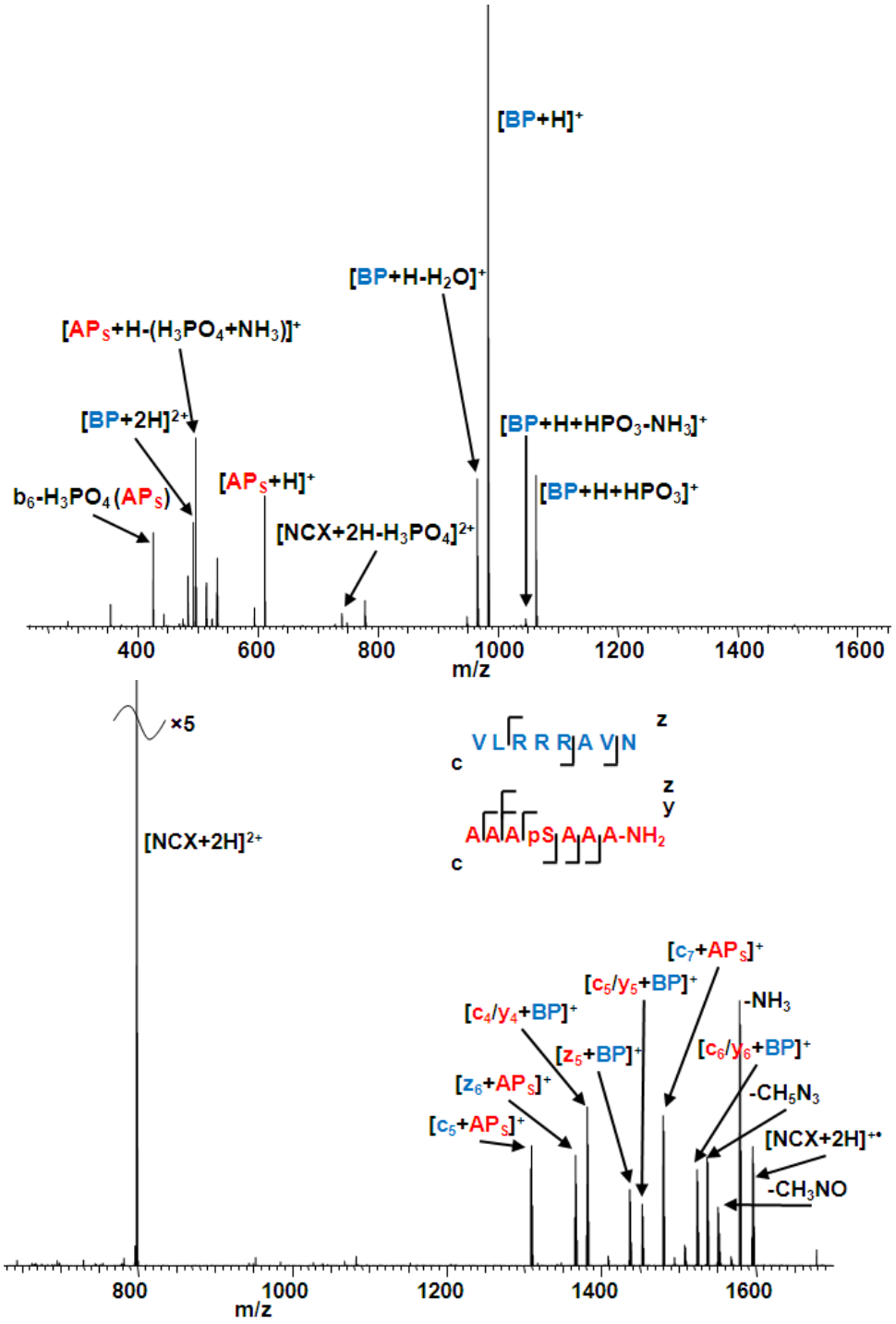

Figure 7.4: CID and ECD mass spectra of phosphoserine containing noncovalent complex

CID (**Upper**) and ECD (**Lower**) mass spectra of the doubly-charged noncovalent complex [VLRRRAVN + AAApSAAA-NH_2 + 2H]$^{2+}$. CID leads in the separation of the complex resulting in the identification of the individual peptides. ECD retains the complex resulting in the identification of fragmentation of the two peptides backbones.

peak being identified as the neutral loss of H_3PO_4 and NH_3. This suggests that within the NCX the AP_S is singly protonated due to the similarity is fragmentation behaviour in the vast majority of cases. Interestingly $[BP + 2H]^{2+}$ is identified, although in low intensity, which suggests that two species are present, *i.e.* one species with both protons on the BP and the other species with one proton on each peptide. Due to the low abundance of $[BP + 2H]^{2+}$ it is postulated that this species is not typically present and is likely to be a result of an increase in proton mobility during CID, explainable by the mobile proton model.

Interestingly, two peaks are identified which show transfer of the phosphorylation group from the AP_S to BP, *i.e.* $[BP + H + HPO_3]^+$ and $[BP + H + HPO_3 - NH_3]^+$. This strongly suggests that the NCX is bound *via* a noncovalent interaction between the phosphate group and the BP, likely the highly basic RRR region. This phenomenon of phosphate transfer following CID between these groups has been previously described previously with the use of quanternary amines [204] and arginine-containing peptides [166, 199]. Therefore the noncovalent bond within this NCX must be extremely strong and can be retained preferentially over the covalent O-P bond within the phosphoserine when CID is performed on the species.

These data suggest that the NCX is bound *via* a phospho-guanidinium noncovalent bond between the phosphoserine and arginine side chains; however, in the CID mass spectrum a peak corresponding to the loss of H_3PO_4 with the retention of the noncovalent complex is identified. This would indicate that the phosphate group is not bound to the BP and can undergo fragmentation whilst the NCX is retained. It is postulated therefore that in a small proportion of species the complex is formed *via* noncovalent bonds elsewhere within the peptides and not the between phospho-guanidinium groups.

A dramatic difference in fragmentation behaviour is noted following ECD. Rather than separation of the noncovalent bond, as shown with CID, ECD results in fragmentation of the peptide backbone with retention of the non-covalent bonds, behaviour previously observed for a triply-charged phosphoserine-containing NCX ([GpSSEDLKKEE + SFKRRRSSK + 3H]$^{3+}$) [200]. The most intense fragment peak corresponds to the neutral loss of ammonia from the charge-reduced precursor ion of the intact complex. Two further neutral losses are identified: CH_5N_3 (arginine side chain) and CH_3NO (asparagine side chain). Seven peaks were identified to be from backbone fragment ions indicating that the complexes remain intact, with four of these peaks originating from fragmentation of the AP_S backbone and three from the BP.

The three BP fragment ions identified all result from cleavage at the N-Cα bond, suggesting that the Cornell or UW mechanism is favoured, with the retention of the AP_S. Due to the location of the fragment ions it is highly likely that the NCX is bound *via* the central RRR region of the BP. Also as no fragmentation occurs in this region, *i.e.* RR + R or R + RR, it is likely that the noncovalent bond is equally connected *via* all three arginine side chains, or transfers through all three. The formation of the noncovalent bond may also decrease the efficiency of Coulombic stabilisation from the arginine side chains to the BP backbone N-Cα bonds (possibly due to conformation and direction of the side chains), hence the lower peptide backbone sequence coverage when compared to non-NCX peptide (see **Figure 7.1**).

ECD of the NCX results in ≤100 % peptide backbone sequence coverage of AP_S; however, for four AP_S fragment ions it is not possible to distinguish whether *c* or *y* ions are identified, as they have the same theoretical mass. All of the fragment ions retain the non-covalent bond, and the location of fragmentation, suggests that it is highly likely that the noncovalent bond is

formed *via* the phosphoserine group, corroborating the CID data. It is shown from the CID data that both peptides are singly protonated, in the vast proportion, and therefore it is likely that the AP_S undergoes fragmentation *via* the Cornell or UW mechanisms resulting in *c*/*z* ions. Due to the close proximity of the arginine side chains from the BP, Coulombic stabilisation of the AP_S backbone N-Cα bonds may be increased explaining the high sequence coverage.

Interestingly, the AP_S could not previously be fragmented *via* ECD as the peptide could not be identified in a multiple-charged state and backbone sequence coverage was extremely limited following CID. Whereas ECD of the AP_S could be undertaken when in the NCX, resulting in ≥50 % backbone sequence coverage (likely 66 % if the *c*/*z* ions are accurate) and identification of the phosphoserine. Therefore it could be suggested that for highly acidic phosphopeptides which cannot be identified in multiple-charge states could be analysed in a NCX with a highly basic peptide, *e.g.* VLRRRAVN, to result in backbone sequence coverage and potentially PTM localisation.

Similar CID and ECD behaviour was observed for the two other noncovalent complexes. CID and ECD mass spectra of the phosphothreonine containing complex are shown in **Figure 7.5**, and mass spectra of the phosphotyrosine containing complex shown in **Figure 7.6**. CID of these two complexes results in the dominant separation of the two peptides, with two populations or peaks being identified within each mass spectrum. In both cases, peaks are observed which show that the phosphate group is transferring to the BP, showing this phenomenon is not peculiar to phosphoserine and guanidinium interactions. Interestingly, CID of neither of these two complexes result in the formation of the $[NCX + 2H]^{2+}$-H_3PO_4 ion

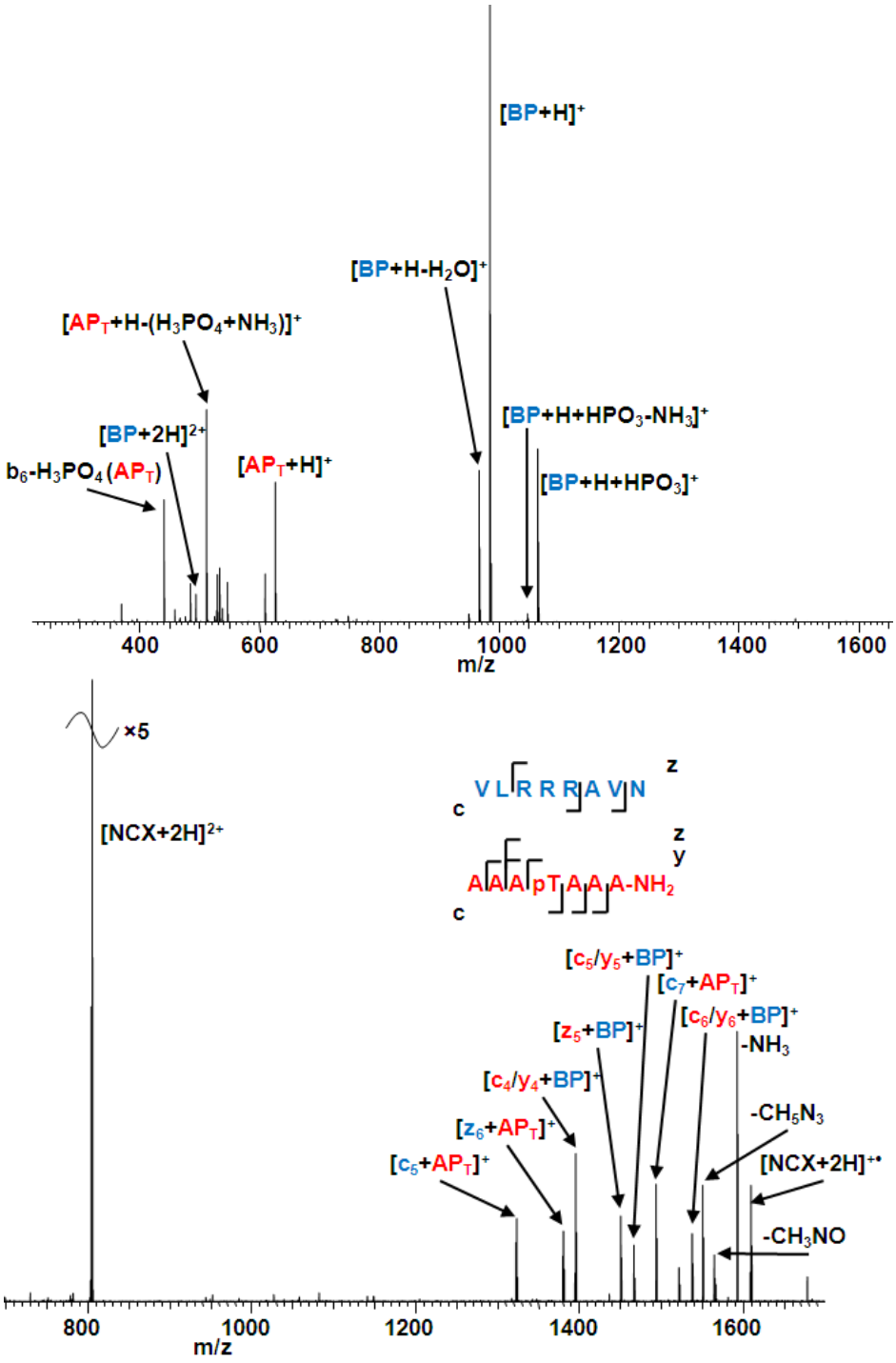

Figure 7.5: CID and ECD mass spectra of phosphothreonine containing noncovalent complex

CID (**Upper**) and ECD (**Lower**) mass spectra of the doubly-charged noncovalent complex [VLRRRAVN + AAApTAAA-NH_2 + 2H]$^{2+}$. CID leads in the separation of the complex resulting in the identification of the individual peptides. ECD retains the complex resulting in the identification of fragmentation of the two peptides backbones.

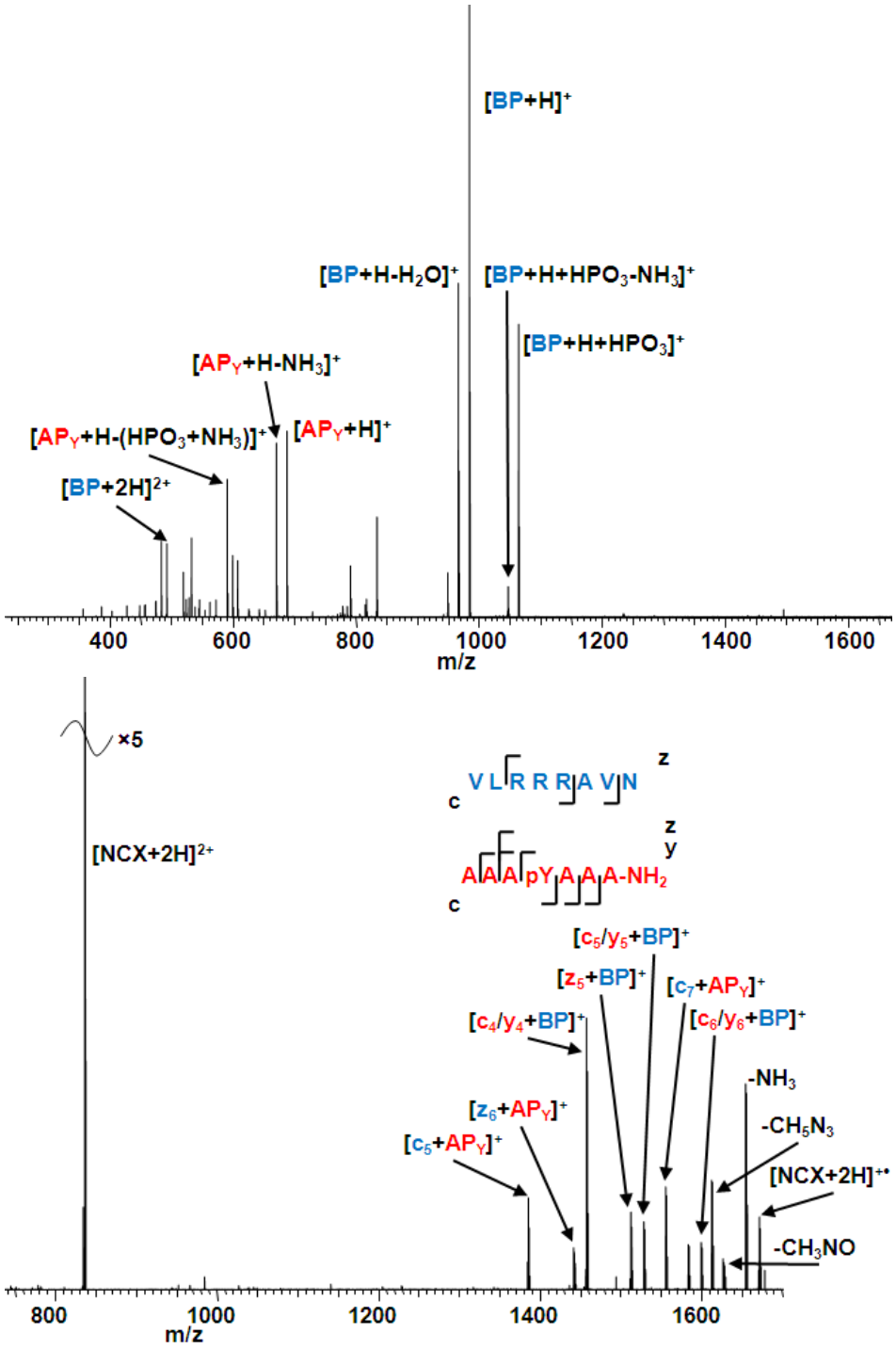

Figure 7.6: CID and ECD mass spectra of phosphotyrosine containing noncovalent complex

CID (**Upper**) and ECD (**Lower**) mass spectra of the doubly-charged noncovalent complex [VLRRRAVN + AAApYAAA-NH_2 + 2H]$^{2+}$. CID leads in the separation of the complex resulting in the identification of the individual peptides. ECD retains the complex resulting in the identification of fragmentation of the two peptides backbones.

seen with the phosphoserine-containing complex, potentially suggesting that complex formation is favoured to occur between the phosphate and guanidinium groups for both phosphothreonine and phosphotyrosine, whereas the interaction may be weaker for phosphoserine.

ECD of the AP_T- and AP_Y-containing NCXs results in backbone fragment ions with the noncovalent bond intact. The BP favourably fragments at the N-Cα bonds with the identification of *c* and *z* ions, whereas the AP_T and AP_Y fragments with the formation of *z* and either *c* or *y* ions (these ions have the same calculated mass).

7.2.3 NCX fragmentation behaviour using CID

These data shown thus far show the potential use of mass spectrometry for the analysis or characterisation of intermolecular noncovalent complexes, and the unique behaviour of ECD resulting in peptide backbone fragmentation allowing peptide sequence identification and localisation of the noncovalent bond. No current studies have directly compared the fragmentation behaviour of these phospho-guanidinium NCXs with the use of ECD. Jackson *et al*. [199] has used CID to investigate NCX bond strength, to identify that the phosphotyrosine-guanidinium noncovalent bond is the strongest, but only investigated the change in $[NCX + nH]^{nH+}$ intensity. Here, the fragmentation behaviour is investigated with the use of variations of CID energy, ECD energy, and laser energy (whilst employing AI ECD analysis). All data shown are from mean values from triplicate studies with each fragment ion intensity being normalised by the total ion intensity within each mass spectrum.

As shown in **Figure 7.7**, there is a strong relationship between CID energy and NCX fragmentation of AP_S containing complexes. The NCX is stable up to a normalised collision energy of <15 %, at which point fragment ions are observed. These fragment ions are shown in the corresponding graph and are identified to be the products of separation of the NCX into the two separate peptide ions. Once this CID threshold is reached, all the fragment ions appear to increase with the fragment ions reaching optimal intensities at ≥25 %. Interestingly, these data show that the formation of $[BP + H]^+$ is largely favoured (~5x) over all other fragment ions, which are all observed in similar intensities.

Similar behaviour is observed for the AP_T-containing NCX, see **Figure 7.8**. The NCX is stable up to a normalised collision energy of <15 %, and optimal fragmentation takes place at ≥25 %, with $[BP + H]^+$ formation favoured over all other fragment ions. This shows a similarity in fragmentation behaviour and noncovalent bond strength between phosphoserine-guanidinium and phosphothreonine-guanidinium groups. The intensity of $[BP + 2H]^{2+}$ is lower for the AP_T-containing NCX than identified for AP_S-containing NCX (~2 % compared to ~6 %) suggesting that the charge-partitioning for the AP_T-containing NCX is more equal between both peptides.

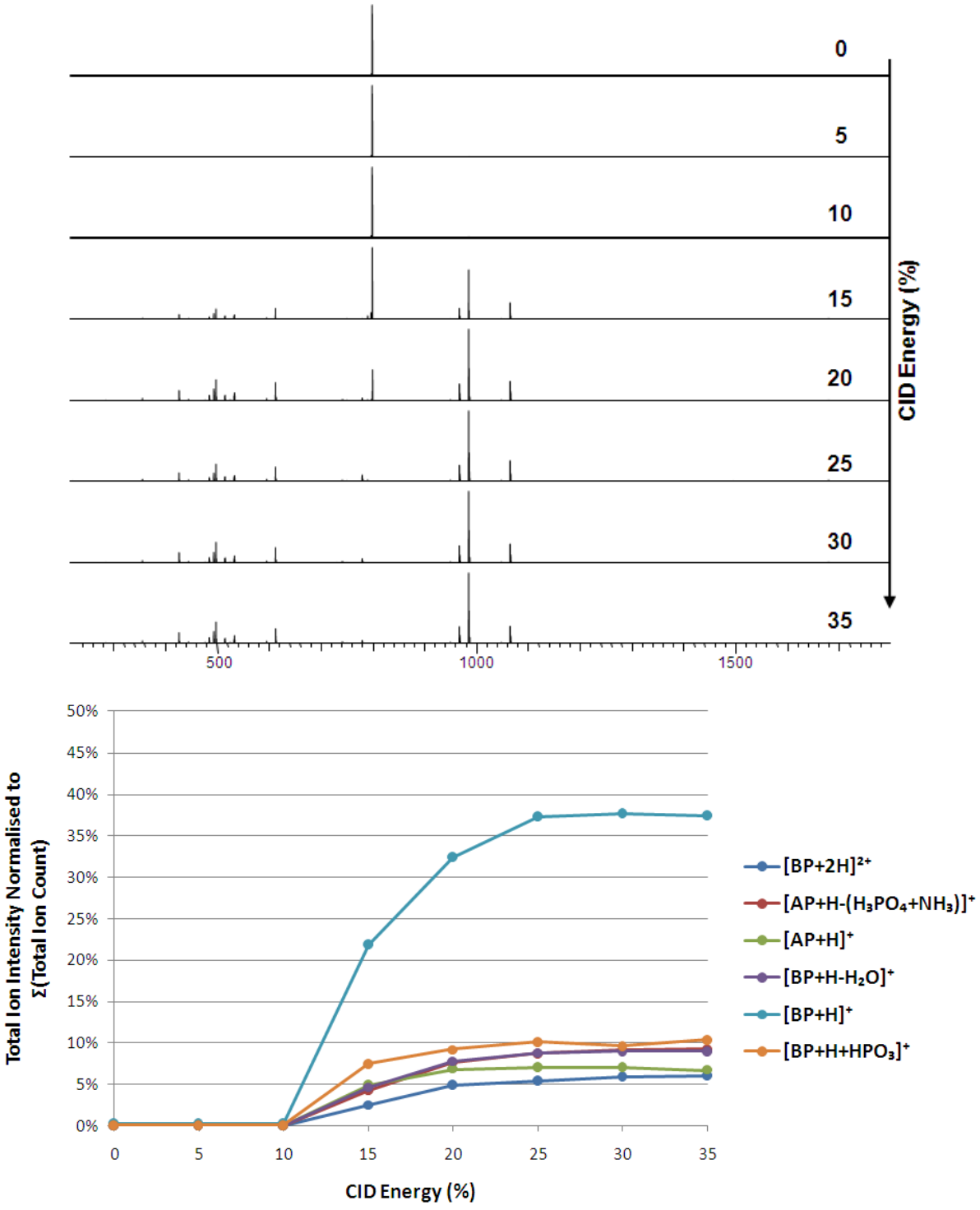

Figure 7.7: Effect of CID energy on AP_S containing NCX fragmentation

Intensity of the thermal-type fragment ions, identified in **Figure 7.4**, normalised to the sum of the total ion count at different CID energies.

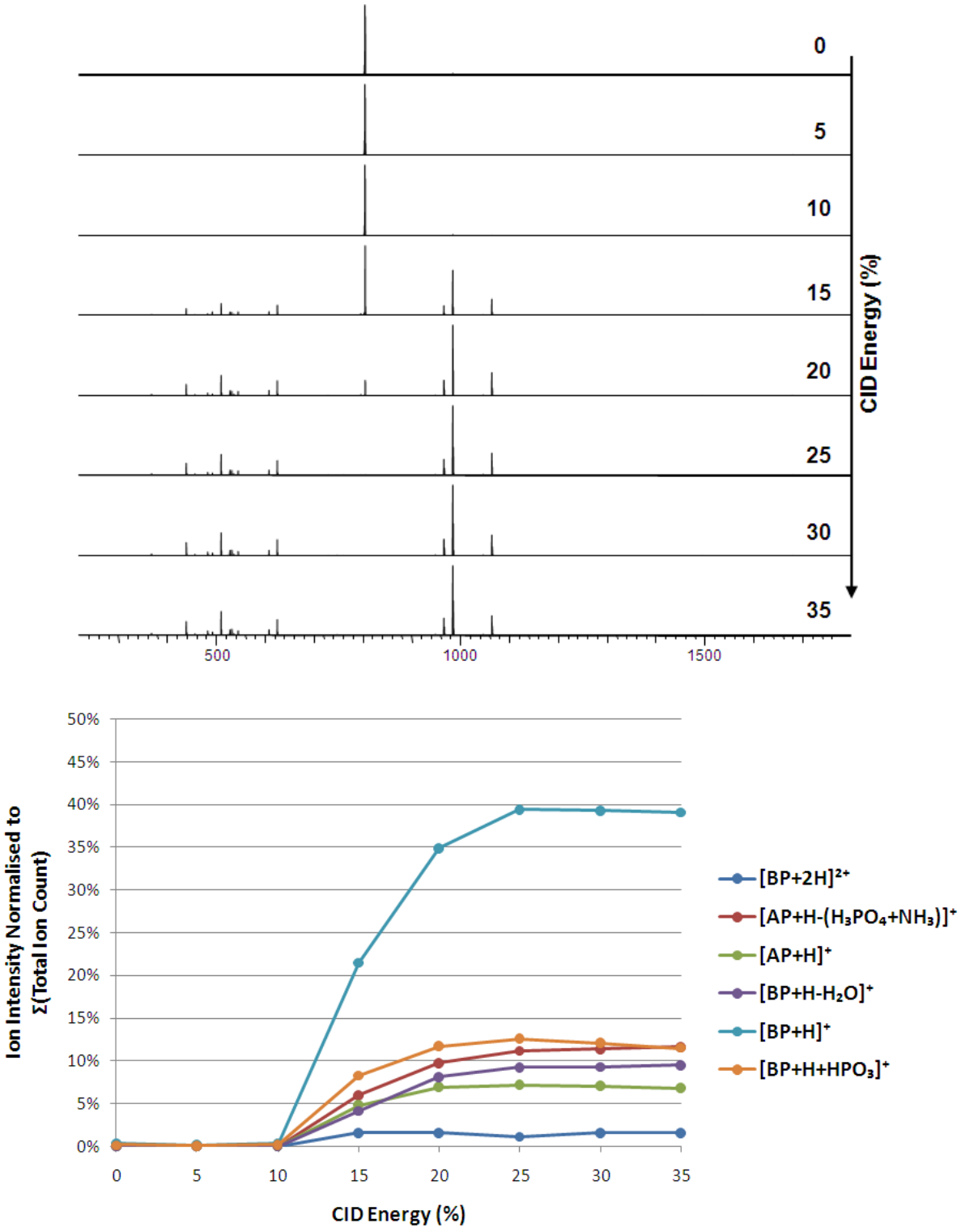

Figure 7.8: Effect of CID energy on AP_T containing NCX fragmentation

Intensity of the thermal-type fragment ions, identified in **Figure 7.5**, normalised to the sum of the total ion count at different CID energies.

Figure 7.9 shows the variation in CID mass spectra with collision energy for the AP_Y-containing NCX. The CID threshold appears to be between 10 % and 15 % normalised collision energy; however, the fragmentation efficiency is much lower than for the AP_S and AP_T NCXs, with the $[NCX + 2H]^{2+}$ precursor peak still being present at a normalised collision energy of 35 %. The most abundant fragment ion corresponds to $[BP + H]^+$, but the intensity of which was ~30% of the total ion count within the mass spectrum (~3x more intense than the other fragment ions), *cf*. ~38 % for the AP_S NCX, and ~40 % for the AP_T NCX. As with the AP_T NCX the intensity of the $[BP + 2H]^{2+}$ is relatively low (~3 %) suggesting an equal charge partitioning between the two peptides. Finally, the intensity of $[BP + H + HPO_3]^+$ and $[BP + H - H_2O]^+$ both become ≥15 % of the total ion count at 25 % and ≥30 % collisional energy, respectively, an observation not seen for the other two NCXs. In the case of the AP_S NCX the most abundant non-$[BP + H]^+$ fragment ion is ~10 % of the mass spectrum and for APT NCX is ~ 12.5 %. This would indicate that the fragmentation behaviour of the AP_Y NCX is distinct from the other two complexes with formation of other fragment ions being favoured.

In all cases, the CID threshold appears to be between 10 % and 15 % normalised collision energy. To ascertain whether each complex has a different CID threshold, these experiments were repeated using single incremental increases of collisional energy in that region. These data, along with a direct comparison of the sum of the identified fragments at the full range of collisional energies, are shown in **Figure 7.10**. These data corroborate the results from the full range of collisional energies, with all NCXs remaining intact at an energy of 10 %, and fragmentation once the energy approaches 15 %. Interestingly, once the CID threshold is reached the fragment ion intensity of the AP_Y NCX remains lower than the other two until 25 % energy, at which point the intensity is the same for as AP_S, and 35 %, at which point all

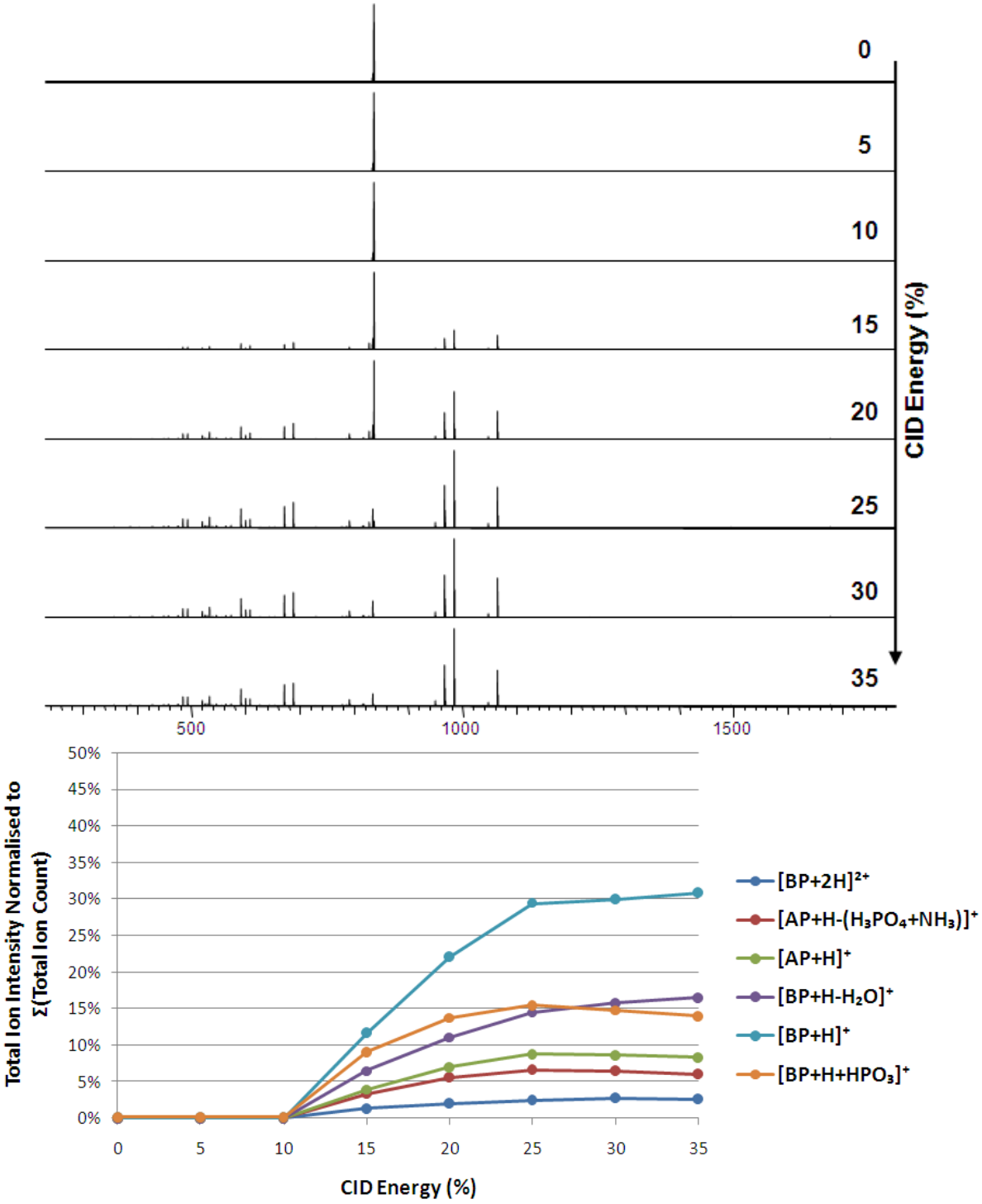

Figure 7.9: Effect of CID energy on AP_Y containing NCX fragmentation

Intensity of the thermal-type fragment ions, identified in **Figure 7.6**, normalised to the sum of the total ion count at different CID energies.

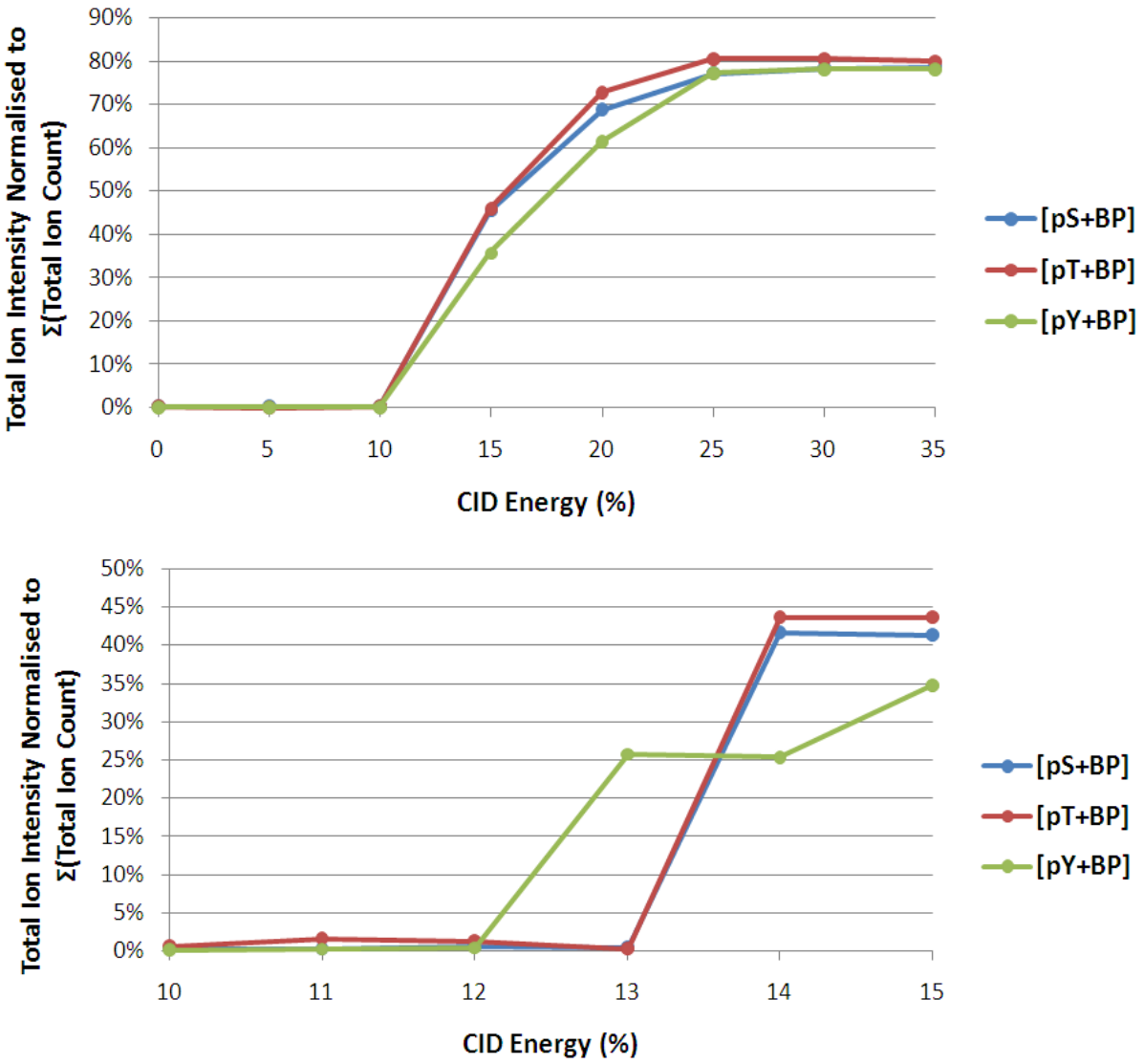

Figure 7.10: Relationship of NCX fragment ion intensity and CID energy

The relationship between CID energy and fragment ion intensities of the phosphoserine, phosphothreonine and phosphotyrosine noncovalent complexes, along with an expanded region indicating the NCX fragmentation threshold.

three have the same fragment ion intensity. This again suggests that the AP_Y NCX fragments in a distinct manner to the other two NCXs, especially at lower collisional energies.

With reference to the threshold energy of CID, the AP_Y NCX fragments at 13 % normalised collision energy, whereas the other two NCXs underwent fragmentation at 14 %. This result suggests that the phosphoserine- and phosphothreonine-guanidinium noncovalent bonds are of very similar strengths, and both of which are stronger than the phosphotyrosine-guanidinium bond. This result appears to contradict previous work which showed the phosphotyrosine-guanidinium bond to be the strongest [199]. In that study the basic peptide used was VLRRRRKRVN, and the high strength of the AP_Y NCX was proposed to be due to the formation of two separate noncovalent bonds: electrostatic interaction between the phosphate group and a guanidinium group, and a cation-π interaction between a guanidinium group and the aromatic ring of the tyrosine side chain. This cation-π interaction has been observed previously in X-ray crystallography with two arginine residues bound to a single phosphotyrosine side chain, one through each noncovalent bond [165]. It is possible that AAApYAAA-NH_2 and VLRRRRKRVN, used previously [199], resulted in both guanidinium-phosphate and cation-π noncovalent bonds due to the presence of the Arg8 residue, whereas in the work presented here, the basic peptide VLRRRAVN is unable to form both noncovalent bonds resulting in a weaker NCX.

7.2.4 NCX fragmentation behaviour using ECD and hot ECD

Unlike previous studies this work used a range of ECD energies to further interrogate any differences in fragmentation behaviour and noncovalent bond strength of the NCXs. The ECD

and hot ECD (HECD), *i.e.* irradiation with hot (3-13 eV) electrons [205], mass spectra of the NCXs are shown in **Figure 7.11**, **7.12** and **7.13**.

In all cases, in the ECD mass spectra, typical ECD behaviour (shown in **Figure 7.4**, **7.5** and **7.6**) is observed up to a cathode potential of between -12 V and -17 V. At cathode potentials ≤-17 V, very few radical-type fragments are identified (expected at m/z >1200) with thermal-type fragments (identified to be fragment ions from the separation of the NCX as identified following CID) being dominant (expected at m/z <1200). When these data are examined graphically it can be seen that this thermal-threshold arises between a cathode potential of -12 V and -17 V, at which point the intensity of the total 'thermal-type' fragments bypasses the intensity of the 'radical-type' fragments, resulting in fragmentation of the phospho-guanidinium (and/or benzyl-guanidinium for AP_Y) noncovalent bonds.

The radical-type fragments observed for the AP_T- and AP_Y-containing NCXs show a similar decrease in intensity; however, there is a higher radical fragmentation efficiency of the AP_Y NCX than expected, with the $[c_5 + AP]^+$ and $[c_6/y_6 + BP]^+$ fragment ions being much more intense than the other ions, at a cathode potential of -12 V. This can be explained by HECD N-Cα fragmentation at electron energies between 3 and 7 eV reaching an efficiency similar to that of ECD, energies likely to be reached at these cathode potentials [205]. The AP_S NCX undergoes fragmentation in a different way to the other two NCXs with radical-type fragments being observed in high intensities up to a cathode potential of 12 V, at which point the thermal-threshold is obtained.

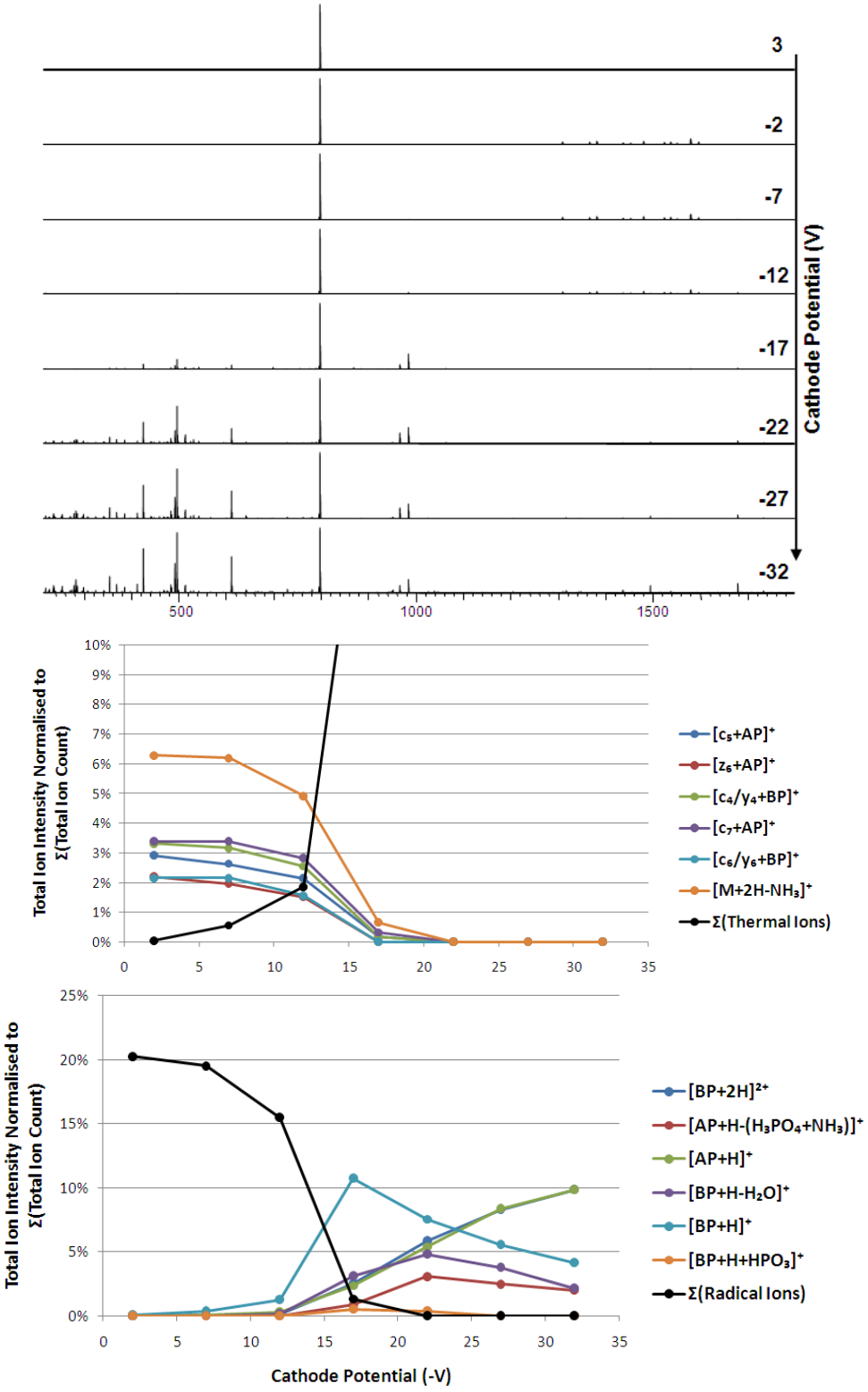

Figure 7.11: Effect of ECD energy on AP_S containing NCX fragmentation

Intensity of the radical- and thermal-type fragment ions normalised to the sum of the total ion count at different ECD energies.

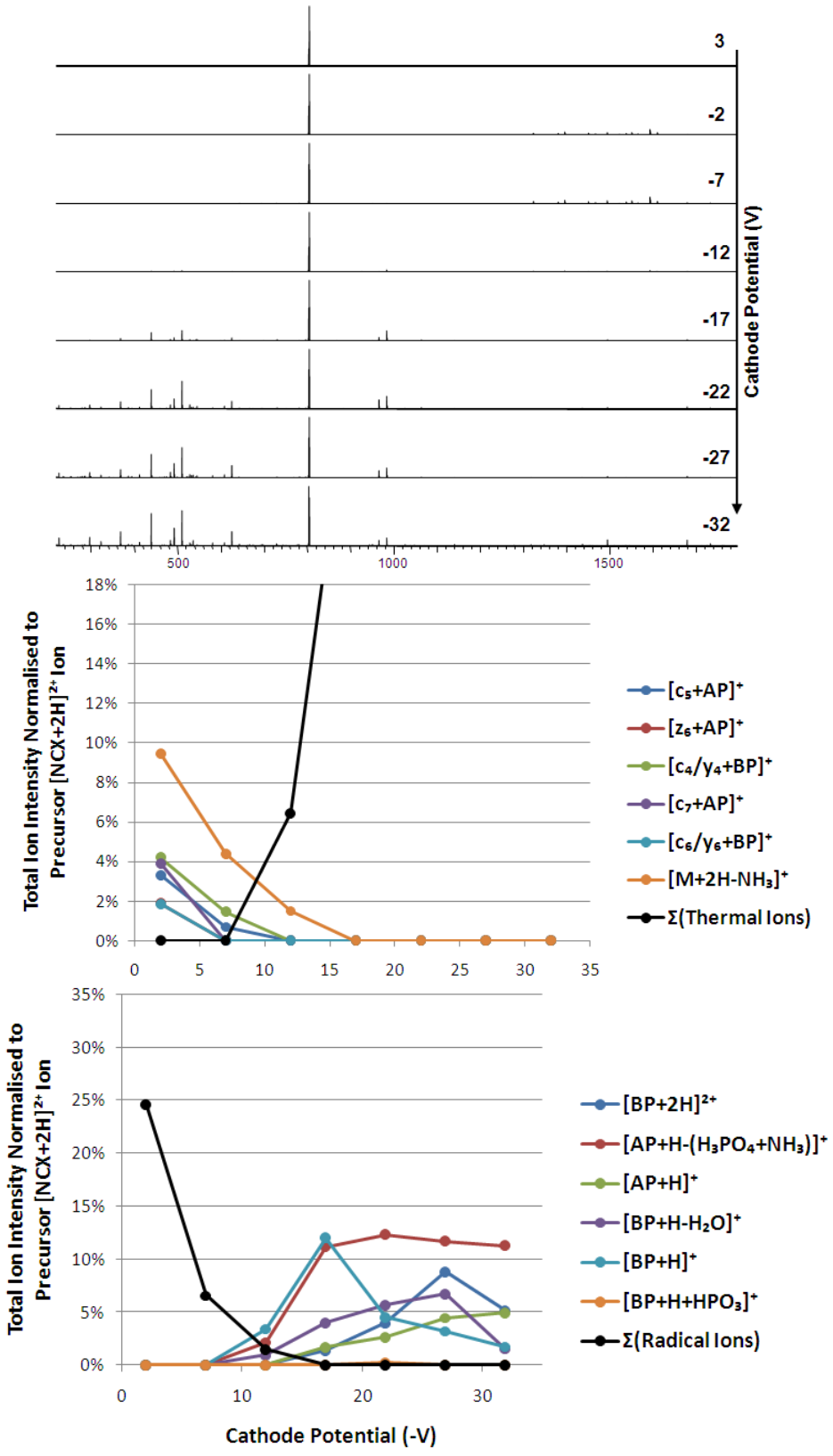

Figure 7.12: Effect of ECD energy on AP_T containing NCX fragmentation

Intensity of the radical- and thermal-type fragment ions normalised to the sum of the total ion count at different ECD energies.

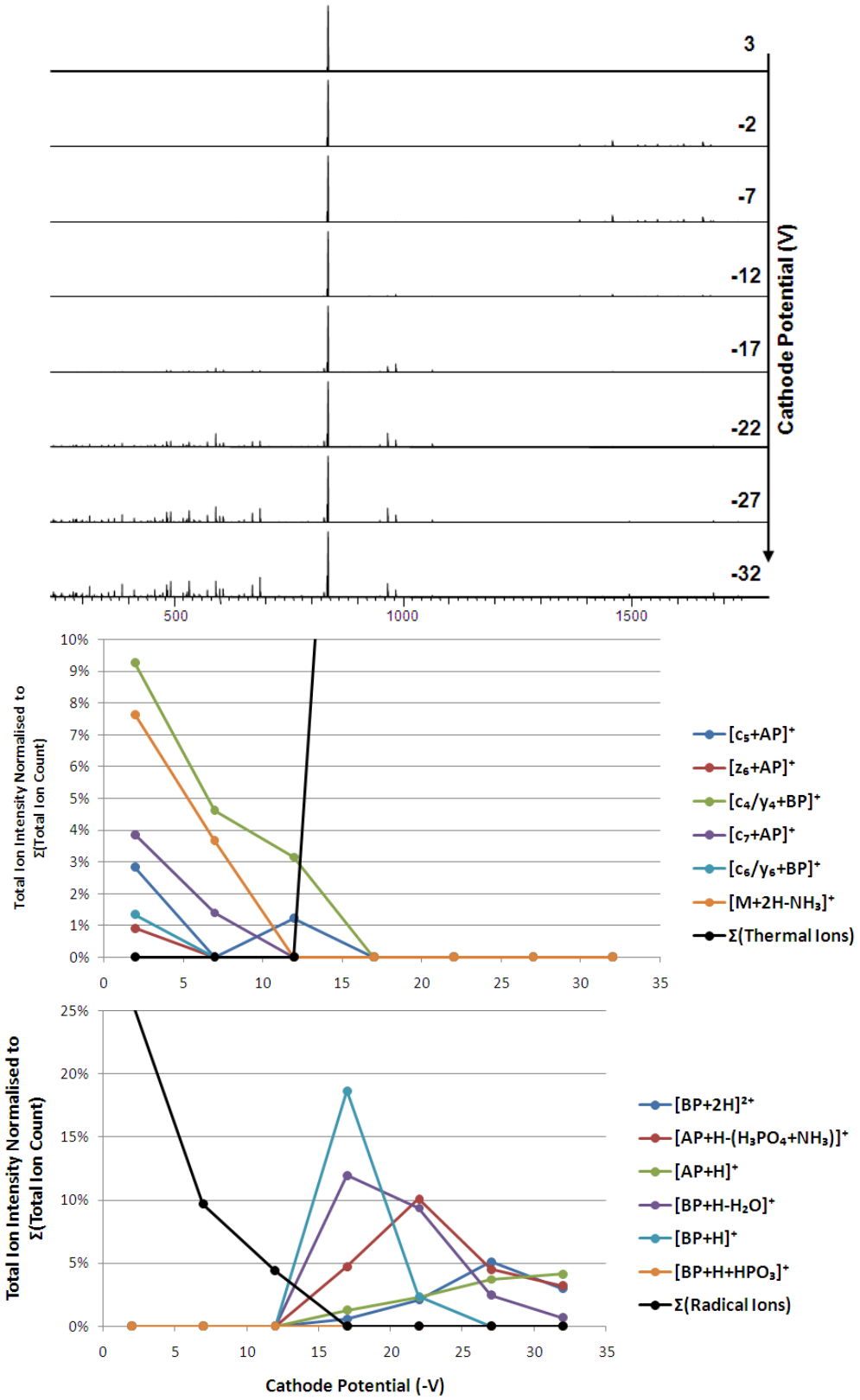

Figure 7.13: Effect of ECD energy on AP_Y containing NCX fragmentation

Intensity of the radical- and thermal-type fragment ions normalised to the sum of the total ion count at different ECD energies.

The thermal-type fragments are identical to those identified following CID of the NCX; however, the intensities of these fragments following HECD differ. For example, when CID was utilised, the most abundant fragment ion observed for all NCXs was the $[BP + H]^+$ peptide ion, and again this is identified to be the most abundant once the thermal-threshold is met leading to separation of the NCX, at a cathode potential of -17 V; however, this ion intensity decreases after this point. For the AP_S- and AP_Y-containing NCXs the behaviour of $[BP + H - H_2O]^+$ appears to mimic the intensity of $[BP + H]^+$, but in a lower level, suggesting that both species are formed in a similar mechanism, and the further loss of water is likely to follow the separation of the NCX. For the AP_T NCX the two appear unlike with the water loss appearing to be more similar to the formation of the $[AP + H - (H_3PO_4 + NH_3)]^+$ ion (which itself is the most intense ion at <-20 V). This similarity is very difficult to explain as the two ions each contain a different peptide, and the neutral losses are not complementary.

Interestingly, HECD (at cathode potentials <-22 V) led to the formation of intense $[AP + H]^+$ and $[BP + 2H]^{2+}$ ions. These ions were both identified with CID of the NCXs, but not at the intensities seen here. This behaviour may be due to the NCX being exerted to higher vibrational energies following electron capture than for the upper limit of CID used in these experiments, resulting in highly mobile protons within the NCXs.

The sum of all radical- and thermal-type fragment ions identified in this work are shown in **Figure 7.14**, along with the associated fragment intensities when ECD and HECD is completed in a stepwise manner from a cathode potential of -10 to -17 V. It can be seen that all three NCXs fragment in differing intensities and efficiencies with optimal fragmentation

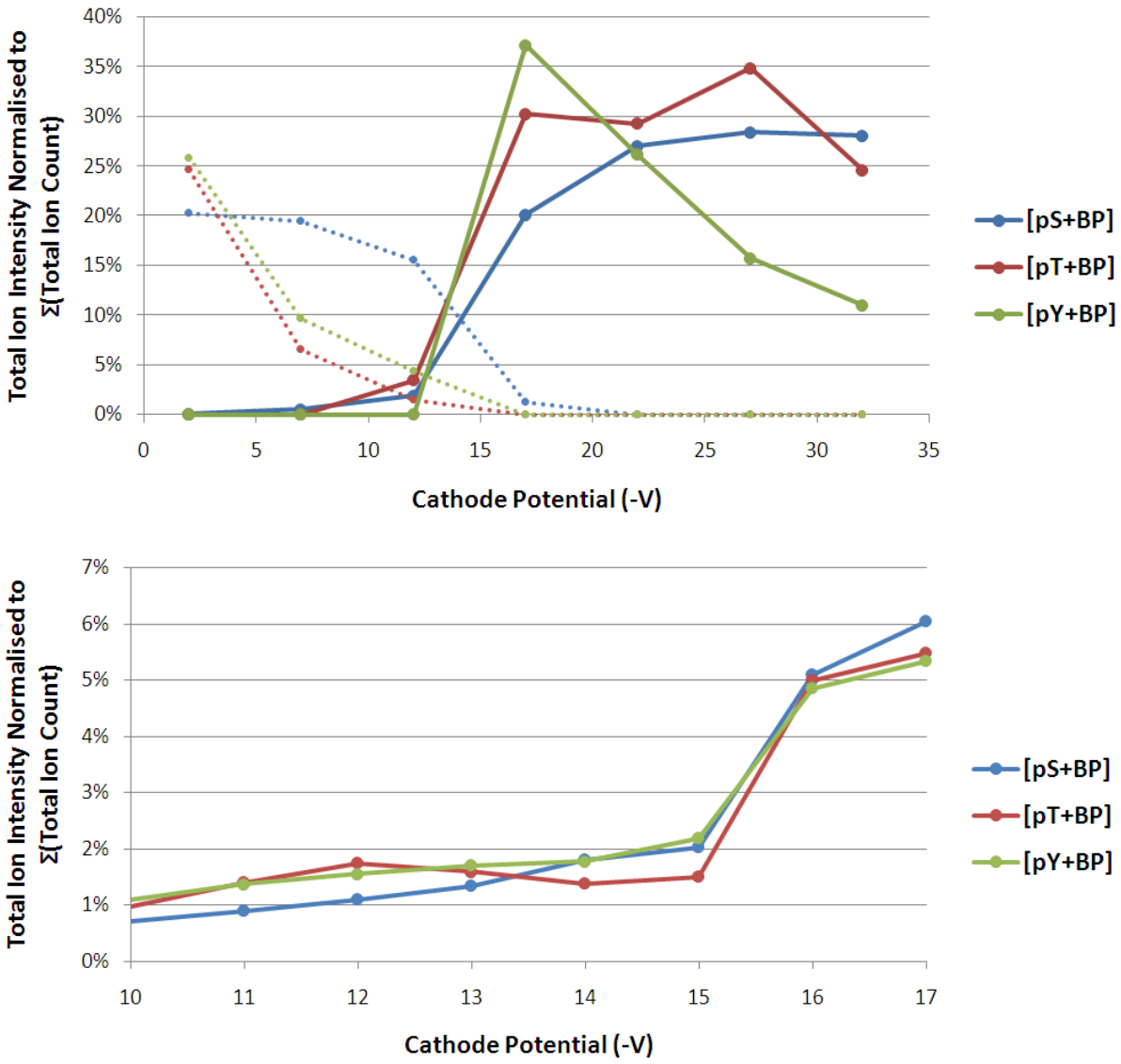

Figure 7.14: Relationship of NCX fragmentation ion intensity and ECD energy

The relationship between ECD energy and fragment ion intensities of the phosphoserine, phosphothreonine and phosphotyrosine noncovalent complexes, along with an expanded region indicating the NCX fragmentation threshold. Thermal-type fragment ion intensities are shown as a solid line, and radical-type fragment ion intensities are shown as a dotted line.

for $[AP_Y + BP + 2H]^{2+}$ taking place at a cathode potential of -17 V, $[AP_T + BP + 2H]^{2+}$ at -27 V, and $[AP_S + BP + 2H]^{2+}$ potentially being higher than the limit researched here. Interestingly, HECD of the AP_T containing NCX results in two maxima, at -17 V and -27 V, which arise due to fragment ions being optimally formed at variable energies, likely due to energetic barriers. These data corroborate the CID data with the observation that the AP_Y-containing NCX is the weakest with thermal fragmentation reaching its maximal efficiency at the lowest cathode potential, and the AP_S-containing NCX is likely the strongest.

The fragment ion intensities observed in the incremental increases in cathode potential are significantly lower than for the other data shown here. The reasoning for this was due to an instrumental change resulting in a decrease in trapping voltage of the ICR cell and hence resulted in a decrease in electron capture efficiency. Nevertheless, it can be seen that all NCXs remain largely intact up to a cathode potential of -16 V at which energy all three NCXs reach their thermal threshold with thermal-type fragment ions being identified.

7.2.5 NCX fragmentation behaviour using AI ECD

The post-laser activation AI ECD mass spectra of the NCXs are shown in **Figure 7.15**, **7.16** and **7.17**, along with the normalised intensities of the observed fragment ions at each laser power. For all NCXs radical-type fragment ions are present within the AI ECD mass spectra up to a laser power of 30 %, at which point the thermal-type fragment ions, which are present at low intensities at a laser power of 10 %, dominate. At the highest laser power utilised in this work no radical-type fragments are identified and the fragmentation efficiency approaches 100 %, with $[NCX + 2H]^{2+}$ being identified in only very minor intensities.

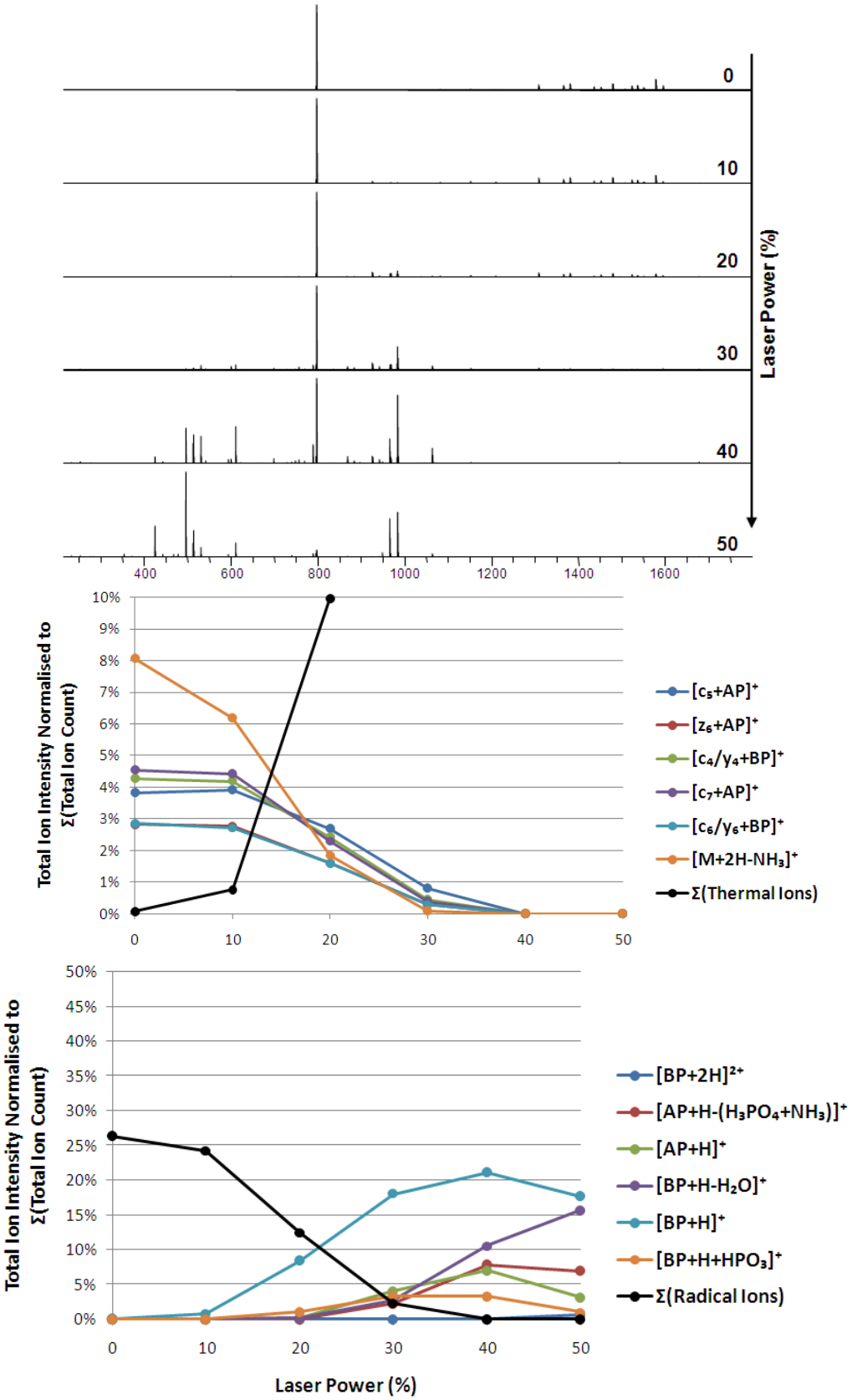

Figure 7.15: Effect of post-laser activation ECD on AP_S containing NCX fragmentation

Intensity of the radical- and thermal-type fragment ions normalised to the sum of the total ion count at different laser activation energies.

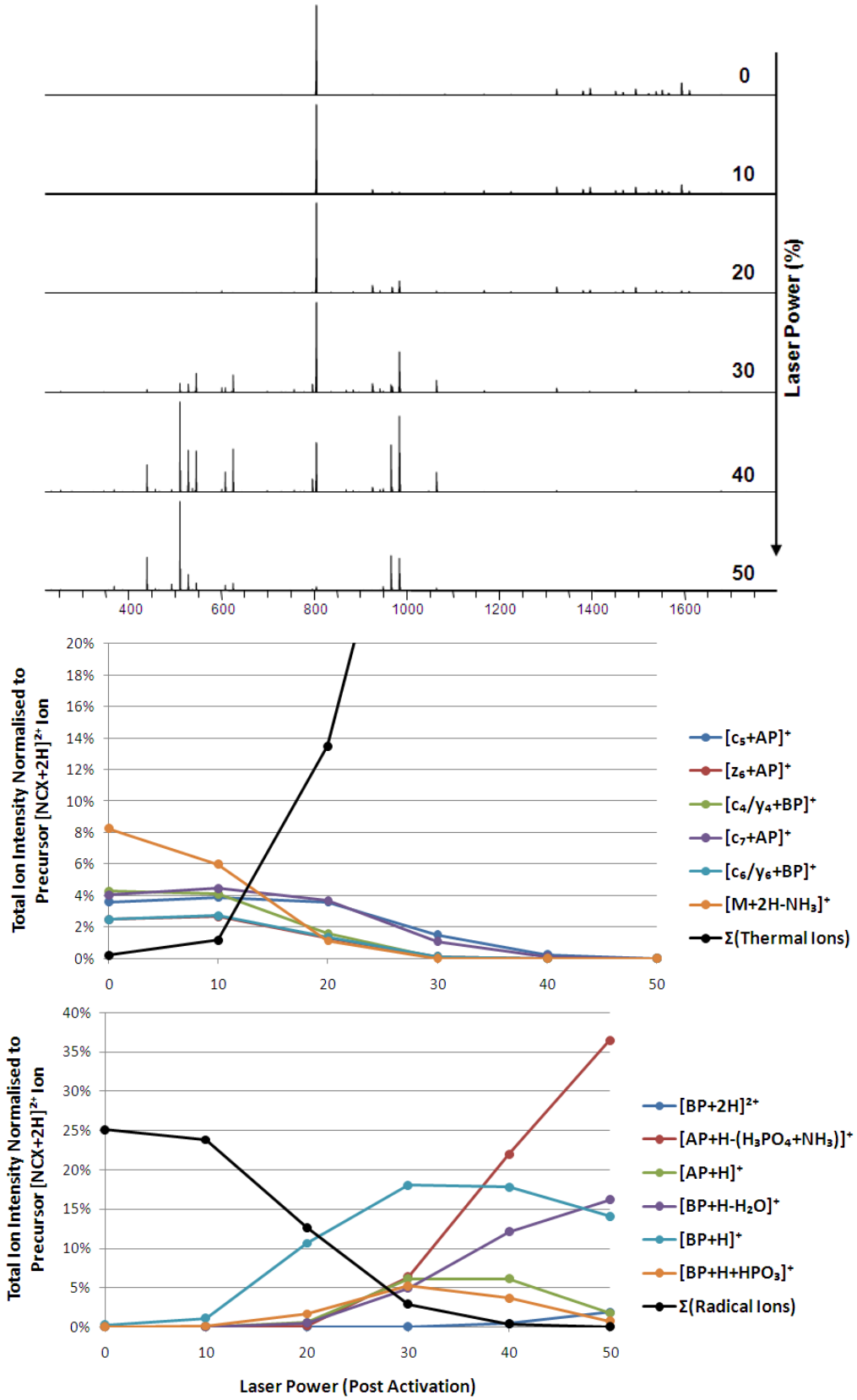

Figure 7.16: Effect of post-laser activation ECD on AP_T containing NCX fragmentation

Intensity of the radical- and thermal-type fragment ions normalised to the sum of the total ion count at different laser activation energies.

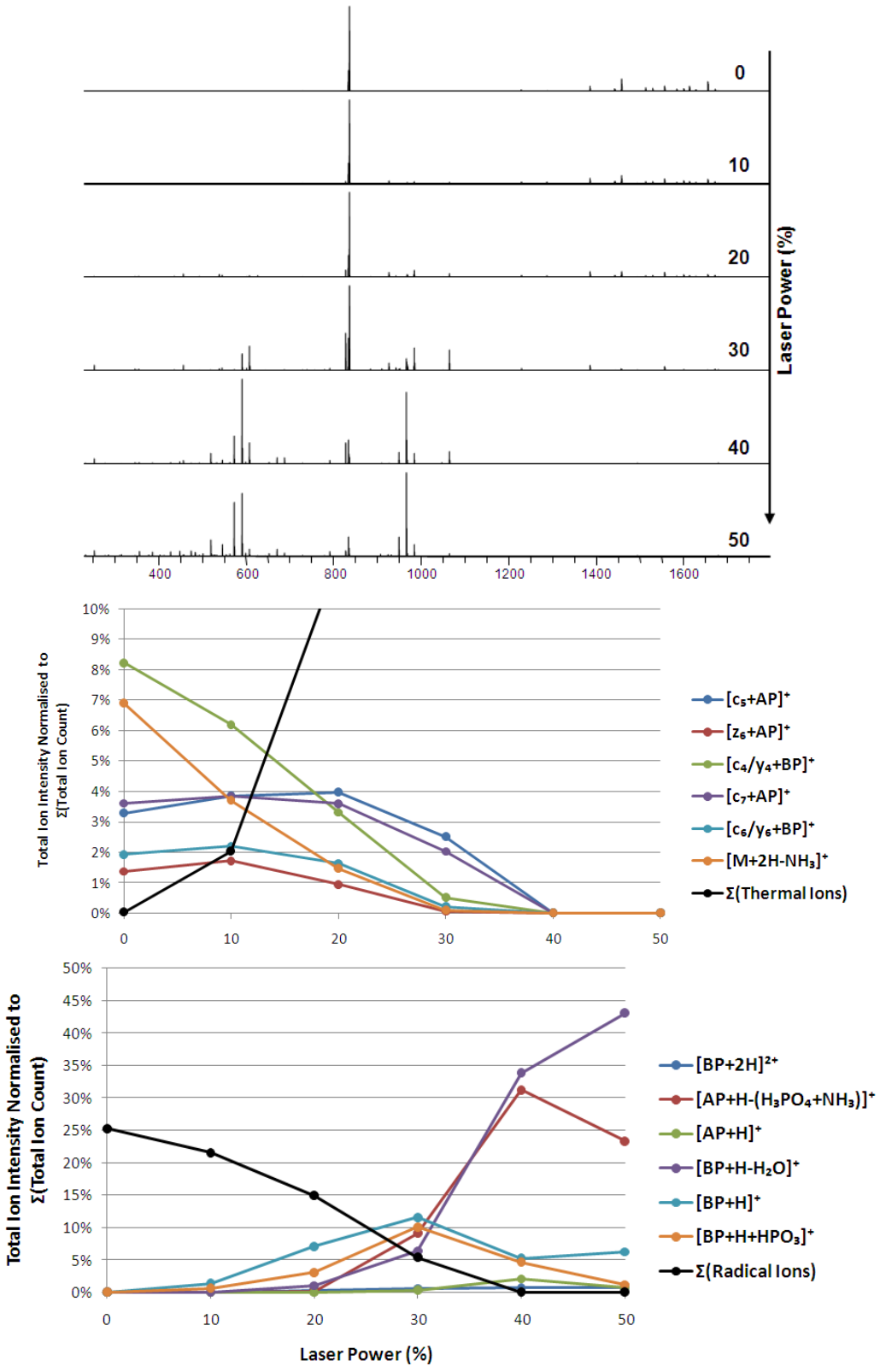

Figure 7.17: Effect of post-laser activation ECD on AP_Y containing NCX fragmentation

Intensity of the radical- and thermal-type fragment ions normalised to the sum of the total ion count at different laser activation energies.

All radical-type fragment ions decrease in intensity with an increase in laser power, with the formation of $[M + 2H – NH_3]^+$ being the most susceptible to decrease following activation, even at low laser power. Ammonia neutral loss is likely to originate from the amidated C-terminus of the phosphopeptides. Data shown above with CID show the charge partitioning to be equal between both peptides. For the APs the proton is likely to be either on the N-terminus or the amidated C-terminus, and on an arginine side chain of the BP. It is proposed that in ECD (therefore 0 % laser power AI ECD) initial electron capture occurs at either the arginine side chain resulting in N-Cα fragmentation (due to the extensive Columbic stabilisation of the RRR region) or the AP termini resulting in NH_3 loss. HECD showed that the charge partitioning was altered, due to the identification of increasing $[BP + 2H]^{2+}$ and $[AP + H]^+$ ions. Therefore it is likely that laser activation also results in a change in proton mobility, with the AP proton having a higher tendency to transfer due to the lower basicity of the termini in comparison to the arginine side chain, and therefore ammonia loss is affected following electron capture. This is backed up by the N-Cα fragments being identified in similar intensities at laser powers ≤20 %, at which point the IRMPD threshold is met.

The thermal-type fragment ions all increase with respect to the laser power, with $[BP + H]^+$ being the most abundant fragment ion in all cases after the IRMPD threshold is reached. At higher laser powers the formation of $[BP + H – H_2O]^+$ continues to increase in intensity in all cases, likely as a secondary fragmentation following formation of $[BP + H]^+$. For the AP_T- and AP_Y-containing NCXs, along with high intensities of $[BP + H – H_2O]^+$, high laser power (>30 %) results in abundant formation of $[AP + H –(H_3PO_4 + NH_3)]^+$.

Direct comparison between the AI ECD analyses of the three NCXs used in this work is shown in **Figure 7.18**, along with a zoomed in region between 5 % and 20 % laser power to identify whether there is, and at what point, the IRMPD threshold arises. The sum of the thermal-type fragments is greater for $[AP_Y + BP + 2H]^{2+}$ than for the other two NCXs, with AI ECD of the AP_S-containing NCX resulting in the least. This result suggests that once the IRMPD threshold is reached, the phosphotyrosine-guanidinium bond is the most susceptible to cleavage, and hence is the weakest. For the stepwise increase of laser power, the range of 5 % to 20 % was chosen as this appears to be the region where the intensity of thermal-type fragment ions is greater than for the radical-type fragments, thus suggesting that the IRMPD threshold occurs at these energies; however, there does not appear to be a specific laser power which induces a dramatic change in dissociation behaviour with a gradual exponential gradient noted. Of the NCXs, again, that the AP_S containing NCX is least susceptible to IRMPD with the lowest intensities identified, with the AP_T and AP_Y complexes being relatively similar in intensities. Again, these observations corroborate those identified from CID and HECD analysis.

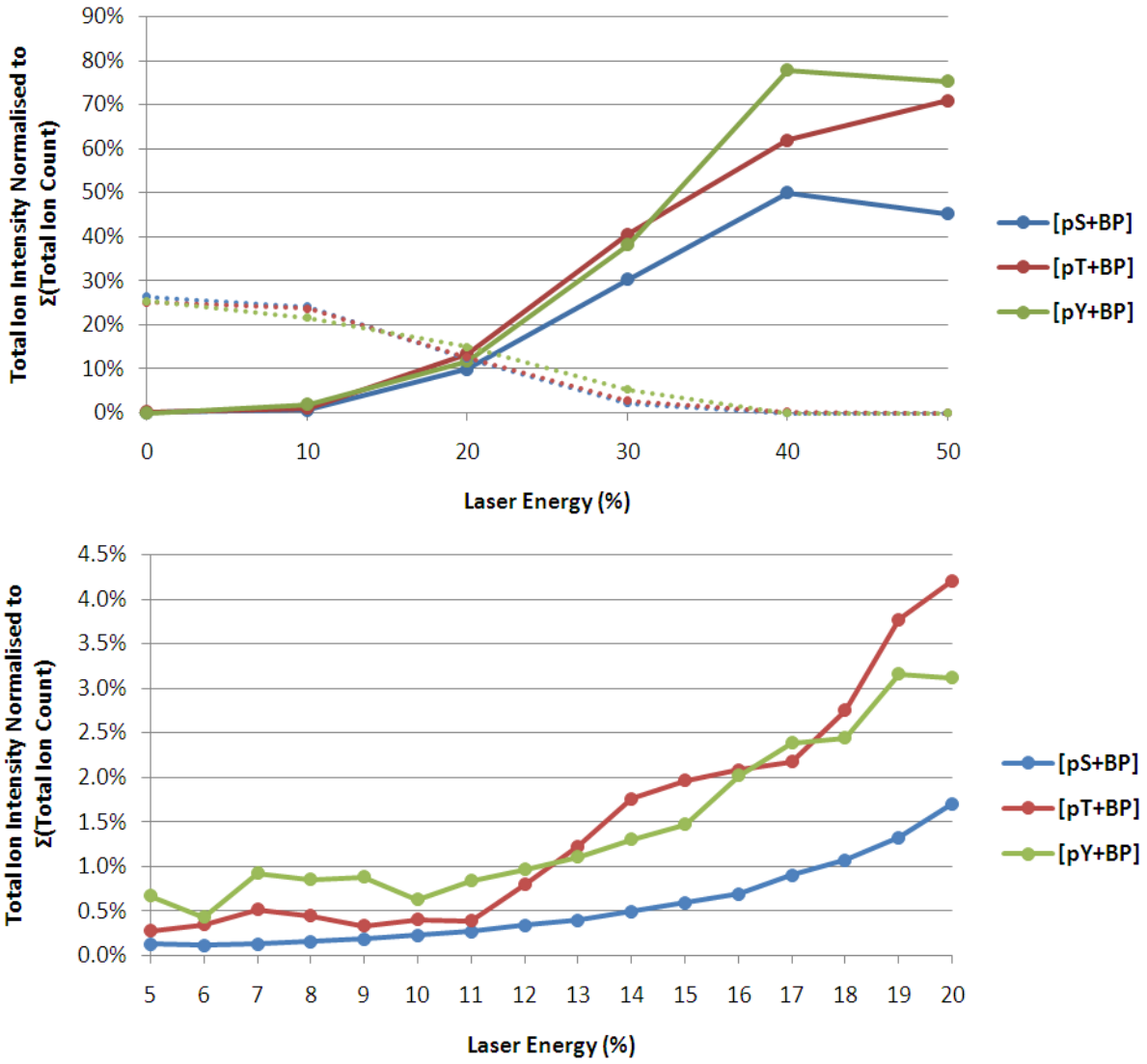

Figure 7.18: Relationship of NCX fragmentation ion intensity and AI ECD energy

The relationship between laser energy and fragment ion intensities of the phosphoserine, phosphothreonine and phosphotyrosine noncovalent complexes, along with an expanded region indicating the NCX fragmentation threshold. Thermal-type fragment ion intensities are shown as a solid line, and radical-type fragment ion intensities are shown as a dotted line.

7.3 Discussion

This area of work shows that phospho-guanidinium bonds exist in the gas-phase between highly basic arginine-rich peptides and acidic phosphoserine, phosphothreonine or phosphotyrosine containing peptides. These noncovalent bonds are labile and thermal-based fragmentation techniques, *e.g.* CID, result in the separation of the two intact peptide chains, whereas the radical-based technique ECD results in peptide backbone fragmentation and retention of the noncovalent bond. Despite obtaining some sequence coverage, it is still relatively low compared to the individual peptides, and thus neither CID nor ECD are truly successful for the identification of the two peptide sequences; however, for the identification and localisation of phosphopeptides can be aided by the formation of a NCX and ECD analysis.

The thermal-type fragment ions were typically identified to be the singly-charged basic peptide along with a neutral loss of water. CID of all three complexes resulted in transfer of the phosphate group requiring favourable fragmentation of a covalent bond over the noncovalent one. Thus it can be concluded that the guanidinium-phosphate bonds with these phosphopeptide complexes are also of an extremely high strength. In the case of the phosphoserine-containing complex, peaks are identified correlating to the intact complex with the neutral loss of the phosphate group. This observation is difficult to explain, although it could be suggested that in this case a noncovalent bond is also formed elsewhere within the peptide complex, which may explain why this forms the strongest noncovalent complex.

The radical-type fragment ions observed all related to the fragmentation of the peptide backbone with the retention of the noncovalent phosphate-guanidinium bond. When fragmentation was identified to be from the basic peptide they were all identified to be *c*/*z* ions and hence proposed to be formed *via* the Cornell or UW mechanism.

Comparisons between the three noncovalent complexes using CID, ECD and AI ECD show that the phospho-guanidinium bonds do not appear to be largely varied, with separation of all three complexes typically occurring at the same energy threshold. Despite this similarity the yield of separation after this threshold appeared highly variable with the phosphoserine-containing complex typically remaining intact at higher energies, explainable by the postulation that a second noncovalent bond may form elsewhere within the complex.

Chapter 8: Conclusions

8.1 Summary

This work has furthered our understanding of the radical-based mechanism of ECD, as well as its uses in proteomics. The key findings are summarised below.

As discussed in the introduction protein tyrosine nitration is a non-signalling PTM which occurs following oxidative and nitrative stress *in vivo*, and thus is of great interest as a biomarker for oxidative stress-related diseases, therefore I have undertaken an extensive study into the behaviour and efficiency of 3-nitrotyrosine analysis when using MS/MS techniques. I have shown that ECD is not a suitable method for the localisation of 3-nitrotyrosine within peptide ions, although the PTM can be easily identified due to the presence of abundant neutral losses. ECD of these peptides occurs *via* the electron predator or hydrogen trap mechanisms, suggesting that the radical is favourably transferred to the 3-nitrotyrosine resulting in the neutral losses of $^{\bullet}OH$, H_2O and NH_3, and inhibiting cleavage of the peptide backbone. The most appropriate method for the analysis of nitrated peptides is CID. The fragmentation of nitrated peptides provides insight into the hierarchy of ECD mechanisms. This finding is discussed further in **Section 8.2**.

The formation of disulfide bonds are crucial for protein structure; however, their presence can result in a decrease in efficiency of certain analytical techniques. To overcome these issues alkylation of the cysteine residues is commonly utilised, but no major study has been completed to identify whether any issues arise from these alkyl groups. I have shown that the use of iodoacetamide and iodoacetic acid, resulting in the formation of carbamidomethylation

and carboxymethylation, respectively, does not affect the fragmentation efficiency and peptide backbone sequence coverage of ECD. It is shown however, that fragmentation does take place in a dominant fashion at the cysteine sulfur atom resulting in the neutral loss of the modification, *i.e.* CH_2CONH_2 or CH_2COOH, following electron capture. This finding can be explained by a modified Cornell or UW mechanism. When examined on a large scale this issue did not result in a decrease in peptide identification. That is, treatment of cysteines with iodoacetamide does not present a problem for global ECD analysis.

Protein cysteine nitrosylation is a critical PTM for protein function and modulation; however, due to the extremely labile nature of the modification, analytical techniques for its detection are relatively poor. I have therefore undertaken an extensive study into the use of ECD for the detection and localisation of *S*-nitrosopeptides. I have shown that the use of ECD for *S*-nitrosopeptide analysis is greatly limited due to the highly favourable fragmentation at the S-N bond resulting in the neutral loss of $^{\bullet}NO$, in place of backbone fragmentation. It is proposed that this favourable fragmentation takes place *via* an adapted Cornell or UW mechanism with electron capture or transfer taking place into the S-N π^* orbital resulting in neutral loss of $^{\bullet}NO$. This finding is discussed further in **Section 8.3**. Following on from this work, it was shown that ECD of hydrogen-deficient radical peptide ions results in an increase in ECnoD, with peptide fragmentation being highly dependent on the peptide gas-phase structure as shown with the use of molecular dynamic simulations. CID of the hydrogen-deficient radical peptide ions resulted in losses of amino acid side-chains and both radical-induced and charge-directed backbone fragmentation dependent on the peptide sequence.

Finally, noncovalent phospho-guanidinium bonds have been shown to be present between arginine-rich species and phosphorylation sites in proteins with the use of X-ray crystallography and as such an extensive study was undertaken to identify how whether these noncovalent complexes can also be successfully identified using MS/MS techniques. I have shown that peptide backbone sequence coverage of gas-phase noncovalent complexes bound through phospho-guanidinium bonds can be increased by the use of ECD in place of CID. Whereas CID results in the separation of the complex with the identification of the two individual peptide chains, ECD results in retention of the noncovalent complex (irrelevant of phosphorylated residue) and fragmentation of the peptides backbones. Of the phosphopeptides studied, it was shown that the phosphoserine-containing noncovalent complex was the strongest, potentially due to two noncovalent bonds being present, and the phosphotyrosine-containing noncovalent complex was the weakest. These results also show the benefit of coupling a highly basic peptide with a phosphopeptide prior to ECD analysis to increase the likelihood and ease of phospho-localisation.

8.2 The Oslo mechanism is the most favourable for peptide ECD

The suitability of ECD for the analysis of 3-nitrotyrosine-containing peptides was investigated and it was shown that ECD proceeded *via* the electron predator or hydrogen trap mechanism. This resulted in the formation of abundant neutral loss species, specifically $^{\bullet}OH$, H_2O, and NH_3, in place of the Cornell or UW mechanisms, in which N-Cα cleavage results in *c*/*z* fragment ions. The observation of water and hydroxyl loss had both been identified experimentally using other electron predators/withdrawing groups and theoretically with intermediate analysis; however, the identification of ammonia loss was novel.

This ammonia loss was shown to originate from the N-terminus of the peptide following electron capture, with the use of a range of analyses, *e.g.* isotopic-labelling, and MS^3 (ECD-IRMPD) being the most critical. When the ammonia loss was further investigated some highly interesting observations were made, especially when ECD analysis was performed on N-terminal acetylated and non-basic amino acid residue (BAAR)-containing peptides. It was seen that the presence of the 3-nitrotyrosine had very little, if any, affect on the ECD behaviour of these peptides. Typically, the addition of 3-nitrotyrosine led to a large decrease in peptide backbone sequence coverage and abundant neutral losses; however, in these cases the peptide backbone sequence coverage remained large and only very minor neutral losses were identified (with ECD of neither leading to ammonia loss). In these doubly-protonated peptides at least one proton must be situated on an amide nitrogen, and hence fragmentation can be explained by the Oslo mechanism, resulting in the observed $a^{\bullet}$/*b*/*y* fragment ions.

These data show that despite containing 3-nitrotyrosine, ECD of N-protonated peptides occurs *via* the Oslo mechanism rather than the predicted electron predator/hydrogen trap mechanisms, and must be the favourable fragmentation pathway. Likewise, as the electron predator/hydrogen trap mechanisms occur for ECD of nitrated peptides which do not have a protonated amide nitrogen, then the Cornell/UW mechanisms must be the least favourable ECD mechanism.

8.3 ECD of *S*-modifications results in an adapted Cornell/UW mechanism

The ECD behaviour of synthetic and biological cysteine-bound modifications was investigated and shown to favourably fragment at the *S*-bound modification site. It is well

documented that ECD of disulfide bonds fragment at the S-S bond [94] which can be explained by the Cornell [1] and UW [95, 96] mechanisms. It is proposed that the favourable fragmentation of other sulfur-bound modifications follow a similar mechanistic pathway: Following electron capture to a high-*n* Rydberg state at a positively charged site, either a H atom is released once the ground Rydberg level is reached to the sulfur atom (akin to the Cornell mechanism) or radical transfer to the sulfur atom takes place before the ground Rydberg level is reached (akin to the UW mechanism). The S-X bond is then cleaved, followed by hydrogen abstraction in the case of the UW mechanism, resulting in RSH and the neutral loss of the modification.

The cysteine modifications analysed in this work, *i.e.* carbamidomethylation, carboxymethylation and nitrosylation, did not all fragment by the same proportion with ECD mass spectra of *S*-nitrosopeptides were typically dominated by peaks corresponding to the neutral loss of $^{\bullet}NO$ and very minor N-Cα backbone fragmentation. This observation is in stark contrast to the carbamidomethylated and carboxymethylated peptides which resulted in no observable decrease in peptide backbone sequence coverage despite peak corresponding to the neutral loss of CH_2CONH_2 and CH_2COOH, respectively, typically being the most abundant fragment. This variation in S-X bond fragmentation is dependent on the chemistry of the sulfur-modification bond with the S-N π* orbital in the *S*-nitrosopeptide being partially filled due to conjugation weakening the bond significantly.

8.4 Inference of data to the 'Hydrogen Trap'

It was discussed in Chapter 1.4.2.5 about what is now referred to as the electron predator and hydrogen trap mechanisms of ECD; however, I suggest that these models and the data presented in the thesis can be expanded upon and provide insight into biological systems. It was previously hypothesised that a successful hydrogen trap must be both an electron predator, *i.e.* EA $\geq$ 1 eV, and be bonded through π orbitals [120], characteristics applicable to 3-nitrotyrosine; however, it can be argued that *S*-nitrosylation also acts in a similar role, despite not having a sufficiently high EA, due to the abstraction of a hydrogen radical and prevention of backbone cleavage.

With respect to these modifications and their behaviour, it is shown that they both, with the use of the molecular models, are largely affected by their gas-phase structure and in-particular their location within space. For example, it is shown that the interaction between the 3-nitrotyrosine residue and the N-terminus directly affects the neutral losses, and hence hydrogen trap behaviour, whereas the *S*-nitrosylation hydrogen trap behaviour, and efficiency, is largely directed by the solvent accessibility.

These behaviours, and especially their dependence on structure, can be extrapolated into *in vivo* systems. It has been shown that *S*-nitrosylation is highly specific to hydrophobic regions within proteins [152] and hence would therefore have a lower solvent accessibility; nevertheless due to the nature of the modification it can be expected that if a protein were to be have a function which produces radicals then these regions may play a role in sequestering or directing the radical to other sites. Unlike *S*-nitrosylation, 3-nitrotyrosine, as discussed in

detail previously, is formed following nitrative and oxidative stress and hence is likely to occur at exposed regions of proteins rather than hydrophobic regions. This could potentially have a major change in protein function if radical species are present within the protein.

8.5 Future work

As it has been shown that through-space and through-bond electron transfer, and hence peptide fragmentation, is highly limited on the number of bonds and distance [106, 107], gas-phase peptide conformation is of utmost importance when considering ECD fragmentation behaviour. Therefore in light of this relationship and the results from chapter four and six in which molecular models using molecular dynamic simulations were generated to aid conclusions and hypotheses, a further investigation into this area would be of high personal and scientific interest.

In chapter four, it was shown how molecular models of polyAla peptides correlated to the experimentally derived data on the importance of the 3-nitrotyrosine site on ammonia loss, as well as corroborating the MS^3 data collected. As well as using the molecular models for this purpose, comparisons were made with experimental data collected through FAIMS, in which one of the peptides was shown to be formed of two stable structures [182] an observation also identified with analysis of the molecular models. This data therefore shows the potential of using molecular dynamic generated models for corroborating experimental data and the similarity between the two.

In the case of chapter six, the molecular models of the *S*-nitrosopeptides were utilised for the development of hypotheses rather than to corroborate experimental data. Here, the proximity between protonation site and modification, and solvent accessibility were analysed to identify how easily electron transfer could occur between different sites. These models were used to explain why different peptides fragmented in varying ways following electron capture. This shows the power of using molecular models for making and reinforcing hypotheses and proposals.

Therefore I would like to further this area by generating a greater range of molecular dynamic simulated models to investigate how much knowledge and insight can be obtained through these means. Also, the observation that FAIMS provides similar data would lead to interesting comparisons between more types of experimental data.

As a side experiment, nitrosylation of a 3-nitrotyrosine containing peptide was completed to identify how an *S*-nitrosylated and nitrated peptide would fragment (data not shown). Interestingly, nitrosylation favourably took place at the tryptophan residue despite residing on the cysteine residue in its non-nitrated peptide counterpart. It would be interesting to identify whether this change of nitrosylation site were to take place on larger nitrated species suggesting a more biological effect, potentially leading to identifiable pathologies of some radical-based diseases.

Finally, from chapter 7, in which it is shown that noncovalent phospho-guanidinium bond strength vary depending on the phosphosite, I would be interested in looking into intact

proteins which undergo changes in phosphorylation sites through mutations to identify whether these result in structural, as well as functional, changes.

References

1. Zubarev, R. A., Kelleher, N. L. & McLafferty, F. W. Electron Capture Dissociation of Multiply Charged Protein Cations. A Nonergodic Process. *Journal of the American Chemical Society*. **120**, 3265-3266 (1998).

2. Syka, J. E. P., Coon, J. J., Schroeder, M. J., Shabanowitz, J. & Hunt, D. F. Peptide and Protein Sequence Analysis by Electron Transfer Dissociation Mass Spectrometry. *Proceedings of the National Academy of Sciences of the United States of America*. **101**, 9528-9533 (2004).

3. Kelleher, N. L., Zubarev, R. A., Bush, K., Furie, B., Furie, B. C., McLafferty, F. W. & Walsh, C. T. Localization of Labile Posttranslational Modifications by Electron Capture Dissociation: The Case of γ-Carboxyglutamic Acid. *Analytical Chemistry*. **71**, 4250-4253 (1999).

4. Jennings, K. R. Collision-Induced Decompositions of Aromatic Molecular Ions. *International Journal of Mass Spectrometry and Ion Physics*. **1**, 227-235 (1968).

5. Haddon, W. F. & McLafferty, F. W. Metastable Ion Characteristics .VII. Collision-Induced Metastables. *Journal of the American Chemical Society*. **90**, 4745-4746 (1968).

6. Axelsson, J., Palmblad, M., Hakansson, K. & Hakansson, P. Electron Capture Dissociation of Substance P Using a Commercially Available Fourier Transform Ion Cyclotron Resonance Mass Spectrometer. *Rapid Communications in Mass Spectrometry*. **13**, 474-477 (1999).

7. Godovac-Zimmermann, J. & Brown, L. R. Perspectives for Mass Spectrometry and Functional Proteomics. *Mass Spectrometry Reviews*. **20**, 1-57 (2001).

8. Peng, J. M. & Gygi, S. P. Proteomics: The Move to Mixtures. *Journal of Mass Spectrometry*. **36**, 1083-1091 (2001).

9. Burnett, G. & Kennedy, E. P. The Enzymatic Phosphorylation of Proteins. *Journal of Biological Chemistry*. **211**, 969-980 (1954).

10. Beckman, J. S. Oxidative Damage and Tyrosine Nitration from Peroxynitrite. *Chemical Research in Toxicology*. **9**, 836-844 (1996).

11. Reiter, C. D., Teng, R. J. & Beckman, J. S. Superoxide Reacts with Nitric Oxide to Nitrate Tyrosine at Physiological pH *via* Peroxynitrite. *Journal of Biological Chemistry*. **275**, 32460-32466 (2000).

12. Radi, R. Nitric Oxide, Oxidants, and Protein Tyrosine Nitration. *Proceedings of the National Academy of Sciences of the United States of America*. **101**, 4003-4008 (2004).

13. Thomson, J. J. A New Method of Chemical Analysis. *Nature*. **86**, 466-469 (1911).

14. Thomson, J. J. Bakerian Lecture: Rays of Positive Electricity. *Proceedings of the Royal Society of London Series a-Containing Papers of a Mathematical and Physical Character*. **89**, 1-20 (1913).

15. Aston, F. W. A Positive Ray Spectrograph. *Philosophical Magazine*. **38**, 707-714 (1919).

16. Aston, F. W. Isotopes and Atomic Weights. *Nature*. **105**, 617-619 (1920).

17. Wolff, M. M. & Stephens, W. E. A Pulsed Mass Spectrometer with Time Dispersion. *Physical Review*. **69**, 691-691 (1946).

18. Cameron, A. E. & Eggers, D. F. An Ion "Velocitron". *Review of Scientific Instruments*. **19**, 605-607 (1948).

19. Hipple, J. A., Sommer, H. & Thomas, H. A. A Precise Method of Determining the Faraday by Magnetic Resonance. *Physical Review*. **76**, 1877-1878 (1949).

20. Comisarow, M. B. & Marshall, A. G. Fourier-Transform Ion-Cyclotron Resonance Spectroscopy. *Chemical Physics Letters*. **25**, 282-283 (1974).

21. Paul, W. & Steinwedel, H. Ein Neues Massenspektrometer Ohne Magnetfeld. *Zeitschrift Fur Naturforschung Section A*. **8**, 448-450 (1953).

22. Makarov, A. Electrostatic Axially Harmonic Orbital Trapping: A High-Performance Technique of Mass Analysis. *Analytical Chemistry*. **72**, 1156-1162 (2000).

23. Kingdon, K. H. A Method for the Neutralization of Electron Space Charge by Positive Ionization at Very Low Gas Pressures. *Physical Review*. **21**, 408-418 (1923).

24. Dempster, A. J. A New Method of Positive Ray Analysis. *Physical Review*. **11**, 316-325 (1918).

25. Munson, M. S. B. & Field, F. H. Chemical Ionization Mass Spectrometry (i) General Introduction. *Journal of the American Chemical Society*. **88**, 2621-2630 (1966).

26. Krone, H. & Beckey, H. D. Field Ionization Mass Spectrometry of Carbohydrates. *Organic Mass Spectrometry*. **2**, 427-432 (1969).

27. Macfarlane, R. D. & Torgerson, D. F. Californium-252 Plasma Desorption Mass-Spectroscopy. *Science*. **191**, 920-925 (1976).

28. Benninghoven, A. & Sichtermann, W. K. Detection, Identification and Structural Investigation of Biologically Important Compounds by Secondary Ion Mass-Spectrometry. *Analytical Chemistry*. **50**, 1180-1184 (1978).

29. Posthumus, M. A., Kistemaker, P. G., Meuzelaar, H. L. C. & Tennoeverdebrauw, M. C. Laser Desorption-Mass Spectrometry of Polar Non-Volatile Bio-Organic Molecules. *Analytical Chemistry*. **50**, 985-991 (1978).

30. Barber, M., Bordoli, R. S., Sedgwick, R. D. & Tyler, A. N. Fast Atom Bombardment of Solids (FAB) - a New Ion-Source for Mass-Spectrometry. *Journal of the Chemical Society-Chemical Communications*. 325-327 (1981).

31. Tanaka, K., Waki, H., Ido, Y., Akita, S., Yoshida, Y., Yoshida, T. & Matsuo, T. Protein and Polymer Analyses Up to *m*/*z* 100 000 by Laser Ionization Time-of-Flight Mass Spectrometry. *Rapid Communications in Mass Spectrometry*. **2**, 151-153 (1988).

32. Karas, M., Bachmann, D., Bahr, U. & Hillenkamp, F. Matrix-Assisted Ultraviolet-Laser Desorption of Nonvolatile Compounds. *International Journal of Mass Spectrometry and Ion Processes*. **78**, 53-68 (1987).

33. Fenn, J. B., Mann, M., Meng, C. K., Wong, S. F. & Whitehouse, C. M. Electrospray Ionization for Mass-Spectrometry of Large Biomolecules. *Science*. **246**, 64-71 (1989).

34. Dole, M., Mack, L. L. & Hines, R. L. Molecular Beams of Macroions. *Journal of Chemical Physics*. **49**, 2240-2249 (1968).

35. Seeley, E. H. & Caprioli, R. M. Molecular Imaging of Proteins in Tissues by Mass Spectrometry. *Proceedings of the National Academy of Sciences of the United States of America*. **105**, 18126-18131 (2008).

36. Zeleny, J. The Electrical Discharge from Liquid Points, and a Hydrostatic Method of Measuring the Electric Intensity at Their Surfaces. *Physical Review*. **3**, 69-91 (1914).

37. Kebarle, P. & Verkerk, U. H. Electrospray: from Ions in Solution to Ions in the Gas Phase, What We Know Now. *Mass Spectrometry Reviews*. **28**, 898-917 (2009).

38. Gomez, A. & Tang, K. Q. Charge and Fission of Droplets in Electrostatic Sprays. *Physics of Fluids*. **6**, 404-414 (1994).

39. Iribarne, J. V. & Thomson, B. A. Evaporation of Small Ions from Charged Droplets. *Journal of Chemical Physics*. **64**, 2287-2294 (1976).

40. Fenn, J. B. Electrospray Wings for Molecular Elephants (Nobel Lecture). *Angewandte Chemie-International Edition*. **42**, 3871-3894 (2003).

41. Emmett, M. R. & Caprioli, R. M. Micro-Electrospray Mass-Spectrometry - Ultra-High-Sensitivity Analysis of Peptides and Proteins. *Journal of the American Society for Mass Spectrometry*. **5**, 605-613 (1994).

42. Wilm, M. & Mann, M. Analytical Properties of the Nanoelectrospray Ion Source. *Analytical Chemistry*. **68**, 1-8 (1996).

43. Karas, M., Bahr, U. & Dulcks, T. Nano-Electrospray Ionization Mass Spectrometry: Addressing Analytical Problems Beyond Routine. *Fresenius Journal of Analytical Chemistry*. **366**, 669-676 (2000).

44. Belov, M. E., Gorshkov, M. V., Udseth, H. R., Anderson, G. A. & Smith, R. D. Zeptomole-Sensitivity Electrospray Ionization - Fourier Transform Ion Cyclotron Resonance Mass Spectrometry of Proteins. *Analytical Chemistry*. **72**, 2271-2279 (2000).

45. Dehmelt, H. G. Spin Resonance of Free Electrons Polarized by Exchange Collisions. *Physical Review*. **109**, 381-385 (1958).

46. Prestage, J. D., Dick, G. J. & Maleki, L. New Ion Trap for Frequency Standard Applications. *Journal of Applied Physics*. **66**, 1013-1017 (1989).

47. de Hoffmann, E. & Stroobant, V., *Mass Spectrometry: Principles and Applications*. Third ed. 2008, West Sussex, UK: John Wiley & Sons Ltd.

48. Douglas, D. J., Frank, A. J. & Mao, D. Linear Ion Traps in Mass Spectrometry. *Mass Spectrometry Reviews*. **24**, 1-29 (2005).

49. Want, E. J., Cravatt, B. F. & Siuzdak, G. The Expanding Role of Mass Spectrometry in Metabolite Profiling and Characterization. *Chembiochem*. **6**, 1941-1951 (2005).

50. March, R. E., McMahon, A. W., Londry, F. A., Alfred, R. L., Todd, J. F. J. & Vedel, F. Resonance Excitation of Ions Stored in a Quadrupole Ion Trap. Part 1. A Simulation Study. *International Journal of Mass Spectrometry and Ion Processes*. **95**, 119-156 (1989).

51. Shi, S. D. H., Hendrickson, C. L. & Marshall, A. G. Counting Individual Sulfur Atoms in a Protein by Ultrahigh-Resolution Fourier Transform Ion Cyclotron Resonance Mass Spectrometry: Experimental Resolution of Isotopic Fine Structure in Proteins. *Proceedings of the National Academy of Sciences of the United States of America*. **95**, 11532-11537 (1998).

52. He, F., Hendrickson, C. L. & Marshall, A. G. Baseline Mass Resolution of Peptide Isobars: A Record for Molecular Mass Resolution. *Analytical Chemistry*. **73**, 647-650 (2001).

53. Williams, D. K. & Muddiman, D. C. Parts-Per-Billion Mass Measurement Accuracy Achieved Through the Combination of Multiple Linear Regression and Automatic Gain Control in a Fourier Transform Ion Cyclotron Resonance Mass Spectrometer. *Analytical Chemistry*. **79**, 5058-5063 (2007).

54. Shi, S. D. H., Drader, J. J., Freitas, M. A., Hendrickson, C. L. & Marshall, A. G. Comparison and Interconversion of the Two Most Common Frequency-to-Mass Calibration Functions for Fourier Transform Ion Cyclotron Resonance Mass Spectrometry. *International Journal of Mass Spectrometry*. **195**, 591-598 (2000).

55. Sleno, L., Volmer, D. A. & Marshall, A. G. Assigning Product Ions from Complex MS/MS Spectra: The Importance of Mass Uncertainty and Resolving Power. *Journal of the American Society for Mass Spectrometry*. **16**, 183-198 (2005).

56. Marshall, A. G. & Rodgers, R. P. Petroleomics: The Next Grand Challenge for Chemical Analysis. *Accounts of Chemical Research*. **37**, 53-59 (2004).

57. Brown, S. C., Kruppa, G. & Dasseux, J. L. Metabolomics Applications of FT-ICR Mass Spectrometry. *Mass Spectrometry Reviews*. **24**, 223-231 (2005).

58. Bogdanov, B. & Smith, R. D. Proteomics by FTICR Mass Spectrometry: Top Down and Bottom Up. *Mass Spectrometry Reviews*. **24**, 168-200 (2005).

59. Shi, S. D. H., Drader, J. J., Hendrickson, C. L. & Marshall, A. G. Fourier Transform Ion Cyclotron Resonance Mass Spectrometry in a High Homogeneity 25 Tesla Resistive Magnet. *Journal of the American Society for Mass Spectrometry*. **10**, 265-268 (1999).

60. Marshall, A. G., Hendrickson, C. L. & Jackson, G. S. Fourier Transform Ion Cyclotron Resonance Mass Spectrometry: A Primer. *Mass Spectrometry Reviews*. **17**, 1-35 (1998).

61. *Finnigan™ LTQ FT™ Hardware Manual*. Revision B ed. 2004: Thermo Electron Corporation. 1-4.

62. Delong, S. E., Mitchell, D. W., Cherniak, D. J. & Harrison, T. M. ζ-Axis Oscillation Sidebands in FT-ICR Mass-Spectra. *International Journal of Mass Spectrometry and Ion Processes*. **91**, 273-282 (1989).

63. Makarov, A., Denisov, E., Kholomeev, A., Baischun, W., Lange, O., Strupat, K. & Horning, S. Performance Evaluation of a Hybrid Linear Ion Trap/Orbitrap Mass Spectrometer. *Analytical Chemistry*. **78**, 2113-2120 (2006).

64. Makarov, A., Denisov, E., Lange, O. & Horning, S. Dynamic Range of Mass Accuracy in LTQ Orbitrap Hybrid Mass Spectrometer. *Journal of the American Society for Mass Spectrometry*. **17**, 977-982 (2006).

65. Makarov, A., Denisov, E. & Lange, O. Performance Evaluation of a High-field Orbitrap Mass Analyzer. *Journal of the American Society for Mass Spectrometry*. **20**, 1391-1396 (2009).

66. *LTQ Orbitrap Velos™ Hardware Manual*. Revision A ed. 2009: Thermo Fisher Scientific. 1-3.

67. Woodin, R. L., Bomse, D. S. & Beauchamp, J. L. Multi-Photon Dissociation of Molecules with Low-Power Continuous Wave Infrared-Laser Radiation. *Journal of the American Chemical Society*. **100**, 3248-3250 (1978).

68. McLuckey, S. A. & Goeringer, D. E. Slow Heating Methods in Tandem Mass Spectrometry. *Journal of Mass Spectrometry*. **32**, 461-474 (1997).

69. Price, W. D., Schnier, P. D. & Williams, E. R. Tandem Mass Spectrometry of Large Biomolecule Ions by Blackbody Infrared Radiative Dissociation. *Analytical Chemistry*. **68**, 859-866 (1996).

70. McCormack, A. L., Jones, J. L. & Wysocki, V. H. Surface-Induced Dissociation of Multiply Protonated Peptides. *Journal of the American Society for Mass Spectrometry*. **3**, 859-862 (1992).

71. Gauthier, J. W., Trautman, T. R. & Jacobson, D. B. Sustained Off-Resonance Irradiation for Collision-Activated Dissociation Involving Fourier-Transform Mass-Spectrometry - Collision-Activated Dissociation Technique That Emulates Infrared Multiphoton Dissociation. *Analytica Chimica Acta*. **246**, 211-225 (1991).

72. Roepstorff, P. & Fohlman, J. Proposal for a Common Nomenclature for Sequence Ions in Mass-Spectra of Peptides. *Biomedical Mass Spectrometry*. **11**, 601-601 (1984).

73. Summerfield, S. G., Whiting, A. & Gaskell, S. J. Intra-Ionic Interactions in Electrosprayed Peptide Ions. *International Journal of Mass Spectrometry and Ion Processes*. **162**, 149-161 (1997).

74. Dongre, A. R., Jones, J. L., Somogyi, A. & Wysocki, V. H. Influence of Peptide Composition, Gas-Phase Basicity, and Chemical Modification on Fragmentation Efficiency: Evidence for the Mobile Proton Model. *Journal of the American Chemical Society*. **118**, 8365-8374 (1996).

75. Wysocki, V. H., Tsaprailis, G., Smith, L. L. & Breci, L. A. Special Feature: Commentary - Mobile and Localized Protons: a Framework for Understanding Peptide Dissociation. *Journal of Mass Spectrometry*. **35**, 1399-1406 (2000).

76. Aebersold, R. & Goodlett, D. R. Mass Spectrometry in Proteomics. *Chemical Reviews*. **101**, 269-295 (2001).

77. Cooper, H. J., Hakansson, K. & Marshall, A. G. The Role of Electron Capture Dissociation in Biomolecular Analysis. *Mass Spectrometry Reviews*. **24**, 201-222 (2005).

78. Tsybin, Y. O., Hakansson, P., Budnik, B. A., Haselmann, K. F., Kjeldsen, F., Gorshkov, M. & Zubarev, R. A. Improved Low-Energy Electron Injection Systems for High Rate Electron Capture Dissociation in Fourier Transform Ion Cyclotron Resonance Mass Spectrometry. *Rapid Communications in Mass Spectrometry*. **15**, 1849-1854 (2001).

79. Cooper, H. J., Hudgins, R. R., Hakansson, K. & Marshall, A. G. Secondary Fragmentation of Linear Peptides in Electron Capture Dissociation. *International Journal of Mass Spectrometry*. **228**, 723-728 (2003).

80. Zubarev, R. A., Horn, D. M., Fridriksson, E. K., Kelleher, N. L., Kruger, N. A., Lewis, M. A., Carpenter, B. K. & McLafferty, F. W. Electron Capture Dissociation for Structural Characterization of Multiply Charged Protein Cations. *Analytical Chemistry*. **72**, 563-573 (2000).

81. Hakansson, K., Cooper, H. J., Emmett, M. R., Costello, C. E., Marshall, A. G. & Nilsson, C. L. Electron Capture Dissociation and Infrared Multiphoton Dissociation

MS/MS of an *N*-Glycosylated Tryptic Peptide to Yield Complementary Sequence Information. *Analytical Chemistry*. **73**, 4530-4536 (2001).

82. Mirgorodskaya, E., Roepstorff, P. & Zubarev, R. A. Localization of *O*-Glycosylation Sites in Peptides by Electron Capture Dissociation in a Fourier Transform Mass Spectrometer. *Analytical Chemistry*. **71**, 4431-4436 (1999).

83. Shi, S. D. H., Hemling, M. E., Carr, S. A., Horn, D. M., Lindh, I. & McLafferty, F. W. Phosphopeptide/Phosphoprotein Mapping by Electron Capture Dissociation Mass Spectrometry. *Analytical Chemistry*. **73**, 19-22 (2001).

84. Stensballe, A., Jensen, O. N., Olsen, J. V., Haselmann, K. F. & Zubarev, R. A. Electron Capture Dissociation of Singly and Multiply Phosphorylated Peptides. *Rapid Communications in Mass Spectrometry*. **14**, 1793-1800 (2000).

85. Guan, Z. Q. Identification and Localization of the Fatty Acid Modification in Ghrelin by Electron Capture Dissociation. *Journal of the American Society for Mass Spectrometry*. **13**, 1443-1447 (2002).

86. Guan, Z. Q., Yates, N. A. & Bakhtiar, R. Detection and Characterization of Methionine Oxidation in Peptides by Collision-Induced Dissociation and Electron Capture Dissociation. *Journal of the American Society for Mass Spectrometry*. **14**, 605-613 (2003).

87. Cooper, H. J., Heath, J. K., Jaffray, E., Hay, R. T., Lam, T. T. & Marshall, A. G. Identification of Sites of Ubiquitination in Proteins: A Fourier Transform Ion Cyclotron Resonance Mass Spectrometry Approach. *Analytical Chemistry*. **76**, 6982-6988 (2004).

88. Cooper, H. J., Tatham, M. H., Jaffray, E., Heath, J. K., Lam, T. T., Marshall, A. G. & Hay, R. T. Fourier Transform Ion Cyclotron Resonance Mass Spectrometry for the Analysis of Small Ubiquitin-Like Modifier (SUMO) Modification: Identification of Lysines in RanBP2 and SUMO Targeted for Modification During the E3 AutoSUMOylation Reaction. *Analytical Chemistry*. **77**, 6310-6319 (2005).

89. Creese, A. J. & Cooper, H. J. The Effect of Phosphorylation on the Electron Capture Dissociation of Peptide Ions. *Journal of the American Society for Mass Spectrometry*. **19**, 1263-1274 (2008).

90. Horn, D. M., Ge, Y. & McLafferty, F. W. Activated Ion Electron Capture Dissociation for Mass Spectral Sequencing of Larger (42 kDa) Proteins. *Analytical Chemistry*. **72**, 4778-4784 (2000).

91. Breuker, K., Oh, H. B., Cerda, B. A., Horn, D. M. & McLafferty, F. W. Hydrogen Atom Loss in Electron-Capture Dissociation: a Fourier Transform-Ion Cyclotron Resonance Study with Single Isotopomeric Ubiquitin Ions. *European Journal of Mass Spectrometry*. **8**, 177-180 (2002).

92. Zubarev, R. A., Haselmann, K. F., Budnik, B., Kjeldsen, F. & Jensen, F. Towards an Understanding of the Mechanism of Electron-Capture Dissociation: a Historical Perspective and Modern Ideas. *European Journal of Mass Spectrometry*. **8**, 337-349 (2002).

93. Savitski, M. M., Kjeldsen, F., Nielsen, M. L. & Zubarev, R. A. Hydrogen Rearrangement to and from Radical *z* Fragments in Electron Capture Dissociation of Peptides. *Journal of the American Society for Mass Spectrometry*. **18**, 113-120 (2007).

94. Zubarev, R. A., Kruger, N. A., Fridriksson, E. K., Lewis, M. A., Horn, D. M., Carpenter, B. K. & McLafferty, F. W. Electron Capture Dissociation of Gaseous Multiply-Charged Proteins is Favored at Disulfide Bonds and Other Sites of High Hydrogen Atom Affinity. *Journal of the American Chemical Society*. **121**, 2857-2862 (1999).

95. Sobczyk, M., Anusiewicz, W., Berdys-Kochanska, J., Sawicka, A., Skurski, P. & Simons, J. Coulomb-Assisted Dissociative Electron Attachment: Application to a Model Peptide. *Journal of Physical Chemistry A*. **109**, 250-258 (2005).

96. Syrstad, E. A. & Turecek, F. Toward a General Mechanism of Electron Capture Dissociation. *Journal of the American Society for Mass Spectrometry*. **16**, 208-224 (2005).

97. McLafferty, F. W., *Mass Spectrometry in the Analysis of Large Molecules*, ed. C.J. McNeal. 1986, New York: John Wiley. 107-120.

98. Simons, J. Mechanisms for S-S and N-Cα Bond Cleavage in Peptide ECD and ETD Mass Spectrometry. *Chemical Physics Letters*. **484**, 81-95 (2010).

99. Turecek, F. & Syrstad, E. A. Mechanism and Energetics of Intramolecular Hydrogen Transfer in Amide and Peptide Radicals and Cation-Radicals. *Journal of the American Chemical Society*. **125**, 3353-3369 (2003).

100. Turecek, F. N-Cα Bond Dissociation Energies and Kinetics in Amide and Peptide Radicals. Is the Dissociation a Non-Ergodic Process? *Journal of the American Chemical Society*. **125**, 5954-5963 (2003).

101. Iavarone, A. T., Paech, K. & Williams, E. R. Effects of Charge State and Cationizing Agent on the Electron Capture Dissociation of a Peptide. *Analytical Chemistry*. **76**, 2231-2238 (2004).

102. Chamot-Rooke, J., Malosse, C., Frison, G. & Turecek, F. Electron Capture in Charge-Tagged Peptides. Evidence for the Role of Excited Electronic States. *Journal of the American Society for Mass Spectrometry*. **18**, 2146-2161 (2007).

103. Dezarnaud-Dandine, C., Bournel, F., Tronc, M., Jones, D. & Modelli, A. σ* Resonances in Electron Transmission (ETS) and X-Ray Absorption (XAS) Spectroscopies of Dimethyl(poly)sulphides $(CH_3)_2S_x$ (x = 1, 2, 3). *Journal of Physics B-Atomic Molecular and Optical Physics*. **31**, L497-L502 (1998).

104. Seydou, M., Modelli, A., Lucas, B., Konate, K., Desfrancois, C. & Schermann, J. P. Electron Attachment to Strongly Polar Clusters - Formamide Molecule and Clusters. *European Physical Journal D*. **35**, 199-205 (2005).

105. Frison, G., van der Rest, G., Turecek, F., Besson, T., Lemaire, J., Maitre, P. & Chamot-Rooke, J. Structure of Electron-Capture Dissociation Fragments from Charge-Tagged Peptides Probed by Tunable Infrared Multiple Photon Dissociation. *Journal of the American Chemical Society*. **130**, 14916-14917 (2008).

106. Sobczyk, M. & Simons, J. Distance Dependence of Through-Bond Electron Transfer Rates in Electron-Capture and Electron-Transfer Dissociation. *International Journal of Mass Spectrometry*. **253**, 274-280 (2006).

107. Sobczyk, M., Neff, D. & Simons, J. Theoretical Study of Through-Space and Through-Bond Electron Transfer Within Positively Charged Peptides in the Gas Phase. *International Journal of Mass Spectrometry*. **269**, 149-164 (2008).

108. Sohn, C. H., Chung, C. K., Yin, S., Ramachandran, P., Loo, J. A. & Beauchamp, J. L. Probing the Mechanism of Electron Capture and Electron Transfer Dissociation Using Tags with Variable Electron Affinity. *Journal of the American Chemical Society*. **131**, 5444-5459 (2009).

109. Laskin, J., Futrell, J. H. & Chu, I. K. Is Dissociation of Peptide Radical Cations an Ergodic Process? *Journal of the American Chemical Society*. **129**, 9598-9599 (2007).

110. Cooper, H. J., Hudgins, R. R. & Marshall, A. G. Electron Capture Dissociation Fourier Transform Ion Cyclotron Resonance Mass Spectrometry of Cyclodepsipeptides, Branched Peptides, and ε-Peptides. *International Journal of Mass Spectrometry*. **234**, 23-35 (2004).

111. Ben Hamidane, H., Vorobyev, A., Larregola, M., Lukaszuk, A., Tourwe, D., Lavielle, S., Karoyan, P. & Tsybin, Y. O. Radical Stability Directs Electron Capture and Transfer Dissociation of β-Amino Acids in Peptides. *Chemistry-a European Journal*. **16**, 4612-4622 (2010).

112. Cooper, H. J., Hudgins, R. R., Hakansson, K. & Marshall, A. G. Characterization of Amino Acid Side Chain Losses in Electron Capture Dissociation. *Journal of the American Society for Mass Spectrometry*. **13**, 241-249 (2002).

113. Moore, B. N., Ly, T. & Julian, R. R. Radical Conversion and Migration in Electron Capture Dissociation. *Journal of the American Chemical Society*. **133**, 6997-7006 (2011).

114. Cooper, H. J. Investigation of the Presence of *b* Ions in Electron Capture Dissociation Mass Spectra. *Journal of the American Society for Mass Spectrometry*. **16**, 1932-1940 (2005).

115. Jones, A. W. & Cooper, H. J. Probing the Mechanisms of Electron Capture Dissociation Mass Spectrometry with Nitrated Peptides. *Physical Chemistry Chemical Physics*. **12**, 13394-13399 (2010).

116. Bakken, V., Helgaker, T. & Uggerud, E. Models of Fragmentations Induced by Electron Attachment to Protonated Peptides. *European Journal of Mass Spectrometry*. **10**, 625-638 (2004).

117. Liu, H. C. & Hakansson, K. Abundant *b*-Type Ions Produced in Electron Capture Dissociation of Peptides Without Basic Amino Acid Residues. *Journal of the American Society for Mass Spectrometry*. **18**, 2007-2013 (2007).

118. Desfrançois, C., Periquet, V., Lyapustina, S. A., Lippa, T. P., Robinson, D. W., Bowen, K. H., Nonaka, H. & Compton, R. N. Electron Binding to Valence and Multipole States of Molecules: Nitrobenzene, Para- and Meta-Dinitrobenzenes. *Journal of Chemical Physics*. **111**, 4569-4576 (1999).

119. Fukuda, E. K. & McIver, R. T. Relative Electron-Affinities of Substituted Benzophenones, Nitrobenzenes, and Quinones. *Journal of the American Chemical Society*. **107**, 2291-2296 (1985).

120. Tureček, F. Electron Predators are Hydrogen Atom Traps. Effects of Aryl Groups on N-Cα Bond Dissociations of Peptide Radicals. *Journal of Mass Spectrometry*. **45**, 1280-1290 (2010).

121. Baba, T., Hashimoto, Y., Hasegawa, H., Hirabayashi, A. & Waki, I. Electron Capture Dissociation in a Radio Frequency Ion Trap. *Analytical Chemistry*. **76**, 4263-4266 (2004).

122. Silivra, O. A., Kjeldsen, F., Ivonin, I. A. & Zubarev, R. A. Electron Capture Dissociation of Polypeptides in a Three-Dimensional Quadrupole Ion Trap: Implementation and First Results. *Journal of the American Society for Mass Spectrometry*. **16**, 22-27 (2005).

123. Ding, L. & Brancia, F. L. Electron Capture Dissociation in a Digital Ion Trap Mass Spectrometer. *Analytical Chemistry*. **78**, 1995-2000 (2006).

124. Chi, A., Bai, D. L., Geer, L. Y., Shabanowitz, J. & Hunt, D. F. Analysis of Intact Proteins on a Chromatographic Time Scale by Electron Transfer Dissociation Tandem Mass Spectrometry. *International Journal of Mass Spectrometry*. **259**, 197-203 (2007).

125. Olsen, J. V.*, et al.* A Dual Pressure Linear Ion Trap Orbitrap Instrument with Very High Sequencing Speed. *Molecular & Cellular Proteomics*. **8**, 2759-2769 (2009).

126. Williams, J. P., Brown, J. M., Campuzano, I. & Sadler, P. J. Identifying Drug Metallation Sites on Peptides Using Electron Transfer Dissociation (ETD), Collision Induced Dissociation (CID) and Ion Mobility-Mass Spectrometry (IM-MS). *Chemical Communications*. **46**, 5458-5460 (2010).

127. Hartmer, R. & Lubeck, M. New Approach for Characterization of Post Translational Modified Peptides Using Ion Trap MS with Combined ETD/CID Fragmentation. *Lc Gc Europe*. 11-13 (2005).

128. Sobczyk, M. & Simons, J. The Role of Excited Rydberg States in Electron Transfer Dissociation. *Journal of Physical Chemistry B*. **110**, 7519-7527 (2006).

129. Swaney, D. L., McAlister, G. C., Wirtala, M., Schwartz, J. C., Syka, J. E. P. & Coon, J. J. Supplemental Activation Method for High-Efficiency Electron-Transfer

Dissociation of Doubly Protonated Peptide Precursors. *Analytical Chemistry*. **79**, 477-485 (2007).

130. Ledvina, A. R.*, et al.* Infrared Photoactivation Reduces Peptide Folding and Hydrogen-Atom Migration following ETD Tandem Mass Spectrometry. *Angewandte Chemie-International Edition*. **48**, 8526-8528 (2009).

131. Perkins, D. N., Pappin, D. J. C., Creasy, D. M. & Cottrell, J. S. Probability-Based Protein Identification by Searching Sequence Databases Using Mass Spectrometry Data. *Electrophoresis*. **20**, 3551-3567 (1999).

132. Geer, L. Y., Markey, S. P., Kowalak, J. A., Wagner, L., Xu, M., Maynard, D. M., Yang, X. Y., Shi, W. Y. & Bryant, S. H. Open Mass Spectrometry Search Algorithm. *Journal of Proteome Research*. **3**, 958-964 (2004).

133. Creese, A. J. & Cooper, H. J. Liquid Chromatography Electron Capture Dissociation Tandem Mass Spectrometry (LC-ECD-MS/MS) Versus Liquid Chromatography Collision-Induced Dissociation Tandem Mass Spectrometry (LC-CID-MS/MS) for the Identification of Proteins. *Journal of the American Society for Mass Spectrometry*. **18**, 891-897 (2007).

134. Good, D. M., Wirtala, M., McAlister, G. C. & Coon, J. J. Performance Characteristics of Electron Transfer Dissociation Mass Spectrometry. *Molecular & Cellular Proteomics*. **6**, 1942-1951 (2007).

135. Swaney, D. L., McAlister, G. C. & Coon, J. J. Decision Tree-Driven Tandem Mass Spectrometry for Shotgun Proteomics. *Nature Methods*. **5**, 959-964 (2008).

136. Walsh, C. T., *Posttranslational Modifications of Proteins: Expanding Nature's Inventory*. 2006, Greenwood Village, CO.: Roberts and Co. Publishers. 6-10.

137. Sokolovsky, M., Riordan, J. F. & Vallee, B. L. Tetranitromethane. A Reagent for Nitration of Tyrosyl Residues in Proteins. *Biochemistry*. **5**, 3582-3589 (1966).

138. Riordan, J. F., Sokolovsky, M. & Vallee, B. L. Tetranitromethane. A Reagent for Nitration of Tyrosine and Tyrosyl Residues of Proteins. *Journal of the American Chemical Society*. **88**, 4104-4105 (1966).

139. Alvarez, B., Rubbo, H., Kirk, M., Barnes, S., Freeman, B. A. & Radi, R. Peroxynitrite-Dependent Tryptophan Nitration. *Chemical Research in Toxicology*. **9**, 390-396 (1996).

140. Abello, N., Kerstjens, H. A. M., Postma, D. S. & Bischoff, R. Protein Tyrosine Nitration: Selectivity, Physicochemical and Biological Consequences, Denitration, and Proteomics Methods for the Identification of Tyrosine-Nitrated Proteins. *Journal of Proteome Research*. **8**, 3222-3238 (2009).

141. Salvemini, D., Doyle, T. M. & Cuzzocrea, S. Superoxide, Peroxynitrite and Oxidative/Nitrative Stress in Inflammation. *Biochemical Society Transactions*. **34**, 965-970 (2006).

142. Ischiropoulos, H. Biological Tyrosine Nitration: A Pathophysiological Function of Nitric Oxide and Reactive Oxygen Species. *Archives of Biochemistry and Biophysics*. **356**, 1-11 (1998).

143. Shishehbor, M. H.*, et al.* Association of Nitrotyrosine Levels with Cardiovascular Disease and Modulation by Statin Therapy. *Journal of the American Medical Association*. **289**, 1675-1680 (2003).

144. Good, P. F., Werner, P., Hsu, A., Olanow, C. W. & Perl, D. P. Evidence for Neuronal Oxidative Damage in Alzheimer's Disease. *American Journal of Pathology*. **149**, 21-28 (1996).

145. Parastatidis, I*., et al.* Fibrinogen β-Chain Tyrosine Nitration Is a Prothrombotic Risk Factor. *Journal of Biological Chemistry*. **283**, 33846-33853 (2008).

146. Gow, A. J., Duran, D., Malcolm, S. & Ischiropoulos, H. Effects of Peroxynitrite-Induced Protein Modifications on Tyrosine Phosphorylation and Degradation. *Febs Letters*. **385**, 63-66 (1996).

147. Kong, S. K., Yim, M. B., Stadtman, E. R. & Chock, P. B. Peroxynitrite Disables the Tyrosine Phosphorylation Regulatory Mechanism: Lymphocyte-Specific Tyrosine Kinase Fails to Phosphorylate Nitrated cdc2(6-20)NH_2 Peptide. *Proceedings of the National Academy of Sciences of the United States of America*. **93**, 3377-3382 (1996).

148. Souza, J. M., Peluffo, G. & Radi, R. Protein Tyrosine Nitration - Functional Alteration or Just a Biomarker? *Free Radical Biology and Medicine*. **45**, 357-366 (2008).

149. Shi, W. Q., Cai, H., Xu, D. D., Su, X. Y., Lei, P., Zhao, Y. F. & Li, Y. M. Tyrosine Phosphorylation/Dephosphorylation Regulates Peroxynitrite-Mediated Peptide Nitration. *Regulatory Peptides*. **144**, 1-5 (2007).

150. Ohmori, H. & Kanayama, N. Immunogenicity of an Inflammation-Associated Product, Tyrosine Nitrated Self-Proteins. *Autoimmunity Reviews*. **4**, 224-229 (2005).

151. Stevens, S. M., Prokai-Tatrai, K. & Prokai, L. Factors That Contribute to the Misidentification of Tyrosine Nitration by Shotgun Proteomics. *Molecular & Cellular Proteomics*. **7**, 2442-2451 (2008).

152. Hess, D. T., Matsumoto, A., Kim, S. O., Marshall, H. E. & Stamler, J. S. Protein *S*-Nitrosylation: Purview and Parameters. *Nature Reviews Molecular Cell Biology*. **6**, 150-166 (2005).

153. Lu, J. M., Wittbrodt, J. M., Wang, K., Wen, Z., Schlegel, H. B., Wang, P. G. & Cheng, J. P. NO Affinities of *S*-Nitrosothiols: A Direct Experimental and Computational Investigation of RS-NO Bond Dissociation Energies. *Journal of the American Chemical Society*. **123**, 2903-2904 (2001).

154. McMillen, D. F. & Golden, D. M. Hydrocarbon Bond-Dissociation Energies. *Annual Review of Physical Chemistry*. **33**, 493-532 (1982).

155. Stamler, J. S., Lamas, S. & Fang, F. C. Nitrosylation: The Prototypic Redox-Based Signaling Mechanism. *Cell*. **106**, 675-683 (2001).

156. Torta, F., Usuelli, V., Malgaroli, A. & Bachi, A. Proteomic Analysis of Protein *S*-Nitrosylation. *Proteomics*. **8**, 4484-4494 (2008).

157. Jaffrey, S. R., Erdjument-Bromage, H., Ferris, C. D., Tempst, P. & Snyder, S. H. Protein *S*-Nitrosylation: A Physiological Signal for Neuronal Nitric Oxide. *Nature Cell Biology*. **3**, 193-197 (2001).

158. Hao, G., Derakhshan, B., Shi, L., Campagne, F. & Gross, S. S. SNOSID, a Proteomic Method for Identification of Cysteine *S*-Nitrosylation Sites in Complex Protein Mixtures. *Proceedings of the National Academy of Sciences of the United States of America*. **103**, 1012-1017 (2006).

159. Bates, S. & Vousden, K. H. p53 in Signaling Checkpoint Arrest or Apoptosis. *Current Opinion in Genetics & Development*. **6**, 12-18 (1996).

160. Hunter, T. The Croonian Lecture 1997. The Phosphorylation of Proteins on Tyrosine: Its Role in Cell Growth and Disease. *Philosophical Transactions of the Royal Society of London Series B-Biological Sciences*. **353**, 583-605 (1998).

161. Cozzone, A. J. Protein-Phosphorylation in Prokaryotes. *Annual Review of Microbiology*. **42**, 97-125 (1988).

162. Ashcroft, M., Kubbutat, M. H. G. & Vousden, K. H. Regulation of p53 Function and Stability by Phosphorylation. *Molecular and Cellular Biology*. **19**, 1751-1758 (1999).

163. Sweet, S. M. M., Bailey, C. M., Cunningham, D. L., Heath, J. K. & Cooper, H. J. Large Scale Localization of Protein Phosphorylation by Use of Electron Capture Dissociation Mass Spectrometry. *Molecular & Cellular Proteomics*. **8**, 904-912 (2009).

164. Cooper, H. J., Akbarzadeh, S., Heath, J. K. & Zeller, M. Data-Dependent Electron Capture Dissociation FT-ICR Mass Spectrometry for Proteomic Analyses. *Journal of Proteome Research*. **4**, 1538-1544 (2005).

165. Gilmer, T.*, et al.* Peptide Inhibitors of src SH3-SH2-Phosphoprotein Interactions. *Journal of Biological Chemistry*. **269**, 31711-31719 (1994).

166. Jackson, S. N., Wang, H. Y. J. & Woods, A. S. Study of the Fragmentation Patterns of the Phosphate-Arginine Noncovalent Bond. *Journal of Proteome Research*. **4**, 2360-2363 (2005).

167. Parr, R. G., Craig, D. P. & Ross, I. G. Molecular Orbital Calculations of the Lower Excited Electronic Levels of Benzene, Configuration Interaction Included. *Journal of Chemical Physics*. **18**, 1561-1563 (1950).

168. Chen, T. C. Expansion of Electronic Wave Functions of Molecules in Terms of United-Atom Wave Functions. *Journal of Chemical Physics*. **23**, 2200-2201 (1955).

169. Kendall, G., Cooper, H. J., Heptinstall, J., Derrick, P. J., Walton, D. J. & Peterson, I. R. Specific Electrochemical Nitration of Horse Heart Myoglobin. *Archives of Biochemistry and Biophysics*. **392**, 169-179 (2001).

170. Mikhailov, V. A. & Cooper, H. J. Activated Ion Electron Capture Dissociation (AI ECD) of Proteins: Synchronization of Infrared and Electron Irradiation with Ion Magnetron Motion. *Journal of the American Society for Mass Spectrometry*. **20**, 763-771 (2009).

171. Sweet, S. M. M., Jones, A. W., Cunningham, D. L., Heath, J. K., Creese, A. J. & Cooper, H. J. Database Search Strategies for Proteomic Data Sets Generated by Electron Capture Dissociation Mass Spectrometry. *Journal of Proteome Research*. **8**, 5475-5484 (2009).

172. Myung, Y. & Han, S. Force Field Parameters for 3-Nitrotyrosine and 6-Nitrotryptophan. *Bulletin of the Korean Chemical Society*. **31**, 2581-2587 (2010).

173. Han, S. An AMBER Force Field for *S*-Nitrosoethanethiol that is Transferable to *S*-Nitrosocysteine. *Bulletin of the Korean Chemical Society*. **31**, 2903-2908 (2010).

174. Feig, M., Karanicolas, J. & Brooks, C. L. MMTSB Tool Set: Enhanced Sampling and Multiscale Modeling Methods for Applications in Structural Biology. *Journal of Molecular Graphics & Modelling*. **22**, 377-395 (2004).

175. Ischiropoulos, H. & Almehdi, A. B. Peroxynitrite-Mediated Oxidative Protein Modifications. *Febs Letters*. **364**, 279-282 (1995).

176. Mikhailov, V. A., Iniesta, J. & Cooper, H. J. Top-Down Mass Analysis of Protein Tyrosine Nitration: Comparison of Electron Capture Dissociation with "Slow-Heating" Tandem Mass Spectrometry Methods. *Analytical Chemistry*. **82**, 7283-7292 (2010).

177. Polášek, M. & Tureček, F. Hydrogen Atom Adducts to Nitrobenzene: Formation of the Phenylnitronic Radical in the Gas Phase and Energetics of Wheland Intermediates. *Journal of the American Chemical Society*. **122**, 9511-9524 (2000).

178. Ben Hamidane, H., Chiappe, D., Hartmer, R., Vorobyev, A., Moniatte, M. & Tsybin, Y. O. Electron Capture and Transfer Dissociation: Peptide Structure Analysis at Different Ion Internal Energy Levels. *Journal of the American Society for Mass Spectrometry*. **20**, 567-575 (2009).

179. Hudgins, R. R., Ratner, M. A. & Jarrold, M. F. Design of Helices that are Stable in Vacuo. *Journal of the American Chemical Society*. **120**, 12974-12975 (1998).

180. Holm, A. I. S.*, et al.* On the Mechanism of Electron-Capture-Induced Dissociation of Peptide Dications from ^{15}N-Labeling and Crown-Ether Complexation. *Journal of Physical Chemistry A*. **111**, 9641-9643 (2007).

181. Heck, A. J. R., Dekoning, L. J., Pinkse, F. A. & Nibbering, N. M. M. Mass-Specific Selection of Ions in Fourier-Transform Ion-Cyclotron Resonance Mass-Spectrometry - Unintentional Off-Resonance Cyclotron Excitation of Selected Ions. *Rapid Communications in Mass Spectrometry*. **5**, 406-414 (1991).

182. Shvartsburg, A. A., Creese, A. J., Smith, R. D. & Cooper, H. J. Separation of a Set of Peptide Sequence Isomers Using Differential Ion Mobility Spectrometry. *Analytical Chemistry*. **83**, 6918-6923 (2011).

183. Hao, G. & Gross, S. S. Electrospray Tandem Mass Spectrometry Analysis of *S*- and *N*-Nitrosopeptides: Facile Loss of NO and Radical-Induced Fragmentation. *Journal of the American Society for Mass Spectrometry*. **17**, 1725-1730 (2006).

184. Wang, Y., Liu, T., Wu, C. & Li, H. A Strategy for Direct Identification of Protein *S*-Nitrosylation Sites by Quadrupole Time-of-Flight Mass Spectrometry. *Journal of the American Society for Mass Spectrometry*. **19**, 1353-1360 (2008).

185. Mikesh, L. M., Ueberheide, B., Chi, A., Coon, J. J., Syka, J. E. P., Shabanowitz, J. & Hunt, D. F. The Utility of ETD Mass Spectrometry in Proteomic Analysis. *Biochimica Et Biophysica Acta-Proteins and Proteomics*. **1764**, 1811-1822 (2006).

186. Ryzhov, V., Lam, A. K. Y. & O'Hair, R. A. J. Gas-Phase Fragmentation of Long-Lived Cysteine Radical Cations Formed *Via* NO Loss from Protonated *S*-Nitrosocysteine. *Journal of the American Society for Mass Spectrometry*. **20**, 985-995 (2009).

187. Sinha, R. K., Maitre, P., Piccirillo, S., Chiavarino, B., Crestoni, M. E. & Fornarini, S. Cysteine Radical Cation: A Distonic Structure Probed by Gas Phase IR Spectroscopy. *Physical Chemistry Chemical Physics*. **12**, 9794-9800 (2010).

188. Osburn, S., Steill, J. D., Oomens, J., O'Hair, R. A. J., van Stipdonk, M. & Ryzhov, V. Structure and Reactivity of the Cysteine Methyl Ester Radical Cation. *Chemistry-a European Journal*. **17**, 873-879 (2011).

189. Osburn, S., Berden, G., Oomens, J., O'Hair, R. & Ryzhov, V. Structure and Reactivity of the *N*-Acetyl-Cysteine Radical Cation and Anion: Does Radical Migration Occur? *Journal of The American Society for Mass Spectrometry*. **22**, 1794-1803 (2011).

190. Li, X. H., Tang, Z. X. & Zhang, X. Z. Natural Bond Orbital Analysis of Some *S*-Nitrosothiols Biological Molecules. *International Journal of Quantum Chemistry*. **110**, 1565-1572 (2010).

191. Viehe, H. G., Janousek, Z., Merenyi, R. & Stella, L. The Captodative Effect. *Accounts of Chemical Research*. **18**, 148-154 (1985).

192. Leymarie, N., Costello, C. E. & O'Connor, P. B. Electron Capture Dissociation Initiates a Free Radical Reaction Cascade. *Journal of the American Chemical Society*. **125**, 8949-8958 (2003).

193. Fung, Y. M. E. & Chan, T. W. D. Experimental and Theoretical Investigations of the Loss of Amino Acid Side Chains in Electron Capture Dissociation of Model Peptides. *Journal of the American Society for Mass Spectrometry*. **16**, 1523-1535 (2005).

194. Sun, Q. Y., Nelson, H., Ly, T., Stoltz, B. M. & Julian, R. R. Side Chain Chemistry Mediates Backbone Fragmentation in Hydrogen Deficient Peptide Radicals. *Journal of Proteome Research*. **8**, 958-966 (2009).

195. Rauk, A., Yu, D., Taylor, J., Shustov, G. V., Block, D. A. & Armstrong, D. A. Effects of Structure on Cα-H Bond Enthalpies of Amino Acid Residues: Relevance to H Transfers in Enzyme Mechanisms and in Protein Oxidation. *Biochemistry*. **38**, 9089-9096 (1999).

196. Siu, C. K., Ke, Y. Y., Orlova, G., Hopkinson, A. C. & Siu, K. W. M. Dissociation of the N-Cα Bond and Competitive Formation of the $[z_n\text{-H}]^{+\bullet}$ and $[c_n\text{+2H}]^{+}$ Product Ions in Radical Peptide Ions Containing Tyrosine and Tryptophan: The Influence of Proton Affinities on Product Formation. *Journal of the American Society for Mass Spectrometry*. **19**, 1799-1807 (2008).

197. Song, T., Ng, D. C. M., Quan, Q. A., Siu, C. K. & Chu, I. K. Arginine-Facilitated α- and π-Radical Migrations in Glycylarginyltryptophan Radical Cations. *Chemistry-an Asian Journal*. **6**, 888-898 (2011).

198. Woods, A. S. The Mighty Arginine, the Stable Quaternary Amines, the Powerful Aromatics, and the Aggressive Phosphate: Their Role in the Noncovalent Minuet. *Journal of Proteome Research*. **3**, 478-484 (2004).

199. Jackson, S. N., Moyer, S. C. & Woods, A. S. The Role of Phosphorylated Residues in Peptide-Peptide Noncovalent Complexes Formation. *Journal of the American Society for Mass Spectrometry*. **19**, 1535-1541 (2008).

200. Jackson, S. N., Dutta, S. & Woods, A. S. The Use of ECD/ETD to Identify the Site of Electrostatic Interaction in Noncovalent Complexes. *Journal of the American Society for Mass Spectrometry*. **20**, 176-179 (2009).

201. Summerfield, S. G., Dale, V. C. M., Despeyroux, D. D. & Jennings, K. R. Charge-Remote Losses of Small Neutrals from Protonated and Group-1 Metal-Peptide Complexes of Peptides. *European Mass Spectrometry*. **1**, 183-194 (1995).

202. Boersema, P. J., Mohammed, S. & Heck, A. J. R. Phosphopeptide Fragmentation and Analysis by Mass Spectrometry. *Journal of Mass Spectrometry*. **44**, 861-878 (2009).

203. Moyer, S. C., VonSeggern, C. E. & Cotter, R. J. Fragmentation of Cationized Phosphotyrosine Containing Peptides by Atmospheric Pressure MALDI/Ion Trap Mass Spectrometry. *Journal of the American Society for Mass Spectrometry*. **14**, 581-592 (2003).

204. Woods, A. S., Moyer, S. C. & Jackson, S. N. Amazing Stability of Phosphate-Quaternary Amine Interactions. *Journal of Proteome Research*. **7**, 3423-3427 (2008).

205. Kjeldsen, F., Haselmann, K. F., Budnik, B. A., Jensen, F. & Zubarev, R. A. Dissociative Capture of Hot (3-13 eV) Electrons by Polypeptide Polycations: An Efficient Process Accompanied by Secondary Fragmentation. *Chemical Physics Letters*. **356**, 201-206 (2002).

Appendix 1

Optical disc containing Perl scripts and spreadsheets containing the theoretical and experimental *m*/*z* values of mass spectra shown.

Appendix 2

Molecular models of doubly- and triply-charged S-nitrosopeptides.

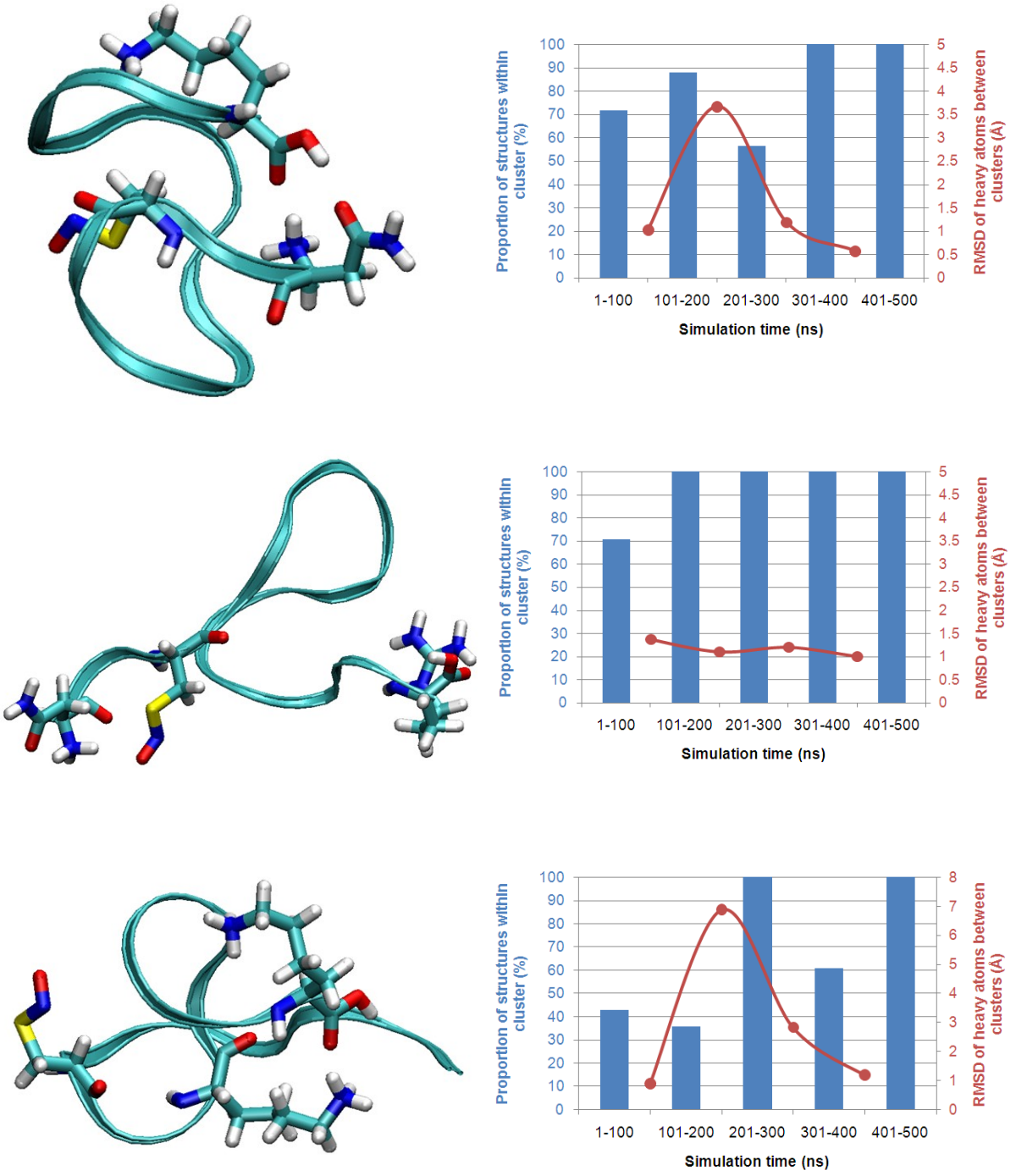

Figure A3.1 (1 of 2): Molecular models of *S*-nitrosopeptides

Representative structures of $[NYC_{NO}GLPGEYWLGNDK + 2H]^{2+}$, $[NYC_{NO}GLPGEYWLGNDR + 2H]^{2+}$, and $[NYGLPGC_{NO}PEKWYGNDK + 2H]^{2+}$.

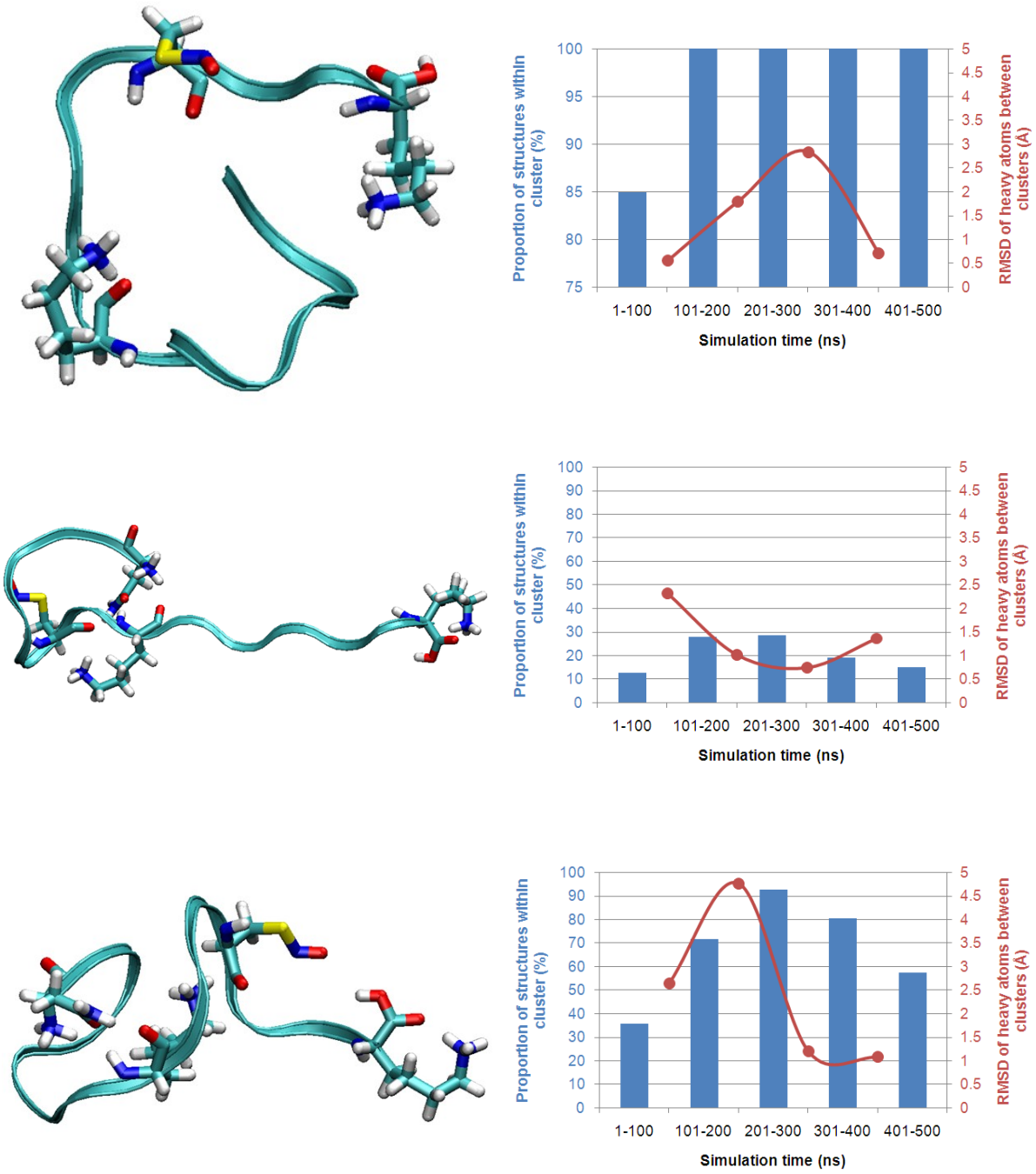

Figure A3.1 (2 of 2): Molecular models of *S*-nitrosopeptides

Representative structures of $[NYGLPGPEKWYGC_{NO}NDK + 2H]^{2+}$, $[NYGLPGC_{NO}PEKWYGNDK + 3H]^{3+}$, and $[NYGLPGPEKWYGC_{NO}NDK + 3H]^{3+}$.

Appendix 3

Journal articles.

1. **Jones, A. W.** & Cooper, H. J. Dissociation techniques in mass spectrometry-based proteomics. *Analyst*. **136**, 3419-3429 (2011).

2. **Jones, A. W.** & Cooper, H. J. Probing the mechanisms of electron capture dissociation mass spectrometry with nitrated peptides. *Physical Chemistry Chemical Physics*. **12(41)**, 13394-13399 (2010).

3. **Jones, A. W.**, Mikhailov, V. A., Iniesta, J. & Cooper, H. J. Electron capture dissociation mass spectrometry of tyrosine nitrated peptides. *Journal of the American Society of Mass Spectrometry*. **21**, 268-277 (2010).

4. Sweet, S. M. M., **Jones, A. W.**, Cunningham, D. L., Heath, J. K., Creese, A. J. & Cooper, H. J. Database search strategies for proteomic data sets generated by electron capture dissociation mass spectrometry. *Journal of Proteome Research*. **20**, 763-771 (2009).